Study of the photon structure at LEP

Habilitation Thesis

Mariusz Przybycień

University of Science and Technology
Al. Mickiewicza 30, Kraków, Poland

Abstract

Two photon physics has become one of the most active fields of research at the recently closed e^+e^- collider LEP. The measurements of the photon structure functions and of the structure of interactions of two virtual photons have been performed at LEP using the process $e^+e^- \to e^+e^-\gamma^{(\star)}\gamma^{(\star)} \to e^+e^-$ X, where X represents a pair of leptons or a hadronic final state. The results obtained by the LEP experiments in single and double tagged measurements are reviewed and compared with similar results available from other e^+e^- colliders. In particular the measurements of the QED and hadronic structure functions of the quasi-real photon as well as the studies of the possible BFKL effects in the intaractions of two virtual photons are discussed in detail. The theoretical framework, needed to understand the experimental results presented in the paper, is given first.

Contents

1 Introduction

The idea that energy can be emitted and absorbed only in discrete portions comes from Planck and was first presented in the year 1900 in his successful theory describing the energy spectrum of the black body radiation. Only five years later Einstein proposed that light can be considered as a flux of particles (light quanta). The notion '*photon*' was introduced by the American chemist G.N.Lewis in the year 1926.

Over the last century we have observed a huge progress in our understanding of both matter and light. The interactions of quarks, leptons and gauge bosons have been successfully described by the Standard Model – a combination of gauge theories. In this model the photon plays a role of a gauge boson of quantum electrodynamics (QED) and mediates the electromagnetic force between charged objects. As the gauge boson of QED, the photon is a massless ($m < 2 \cdot 10^{-16}$ eV) and chargeless ($q < 5 \cdot 10^{-30} e$) particle [1] having no internal structure in the common sense. However, in any quantum field theory, the existence of interactions means also that the quanta themself can develop a structure. This follows from the Heisenberg uncertainty principle written[1] as $\Delta E \Delta t > 1$. For example, the photon can fluctuate for a short period of time into a charged fermion-antifermion pair, $\mathrm{f\bar{f}}$, carrying the same quantum numbers as the photon. The lifetime of this fluctuation increases with the energy of the parent photon E_γ and decreases with the square of the invariant mass of the pair M^2_{pair}: $\Delta t \approx 2E_\gamma / M^2_{\mathrm{pair}}$. When instead of a real photon one has a photon with virtuality Q^2 the fluctuation time is additionally suppressed to $\Delta t \approx 2E_\gamma / (M^2_{\mathrm{pair}} + Q^2)$.

The main subject of this paper are interactions of high energy photons. It is useful to introduce already in this place the commonly used terminology[2]. In the following we call the photon *direct* if it interacts with another object as a whole quantity and we call the photon *resolved* if it interacts through one of the fermions produced in the quantum fluctuation.

If photon fluctuates into a pair of leptons, the process can be completely calculated within QED. However, if it fluctuates into a pair of quarks, then the situation is much more complicated, because of QCD (quantum chromodynamics) interactions. The fact that photons can behave as strongly interacting hadrons, is well known from soft, low energy γp interactions. The properties of those interactions are well described by the Vector Meson Dominance (VMD) model [3] – the photon turns first into a hadronic system with quantum numbers of a vector meson and the hard interaction takes place between partons of the vector meson and a probing object. This contribution to the photon structure usually cannot be calculated perturbatively and has to be parametrized in terms of the parton distribution functions in the photon. Due to similarity to the structure of hadrons (e.g. proton) the contribution is called *hadron-like*. Only when the quark pair has a sufficient relative transverse momentum, the process is perturbatively calculable in QCD, and this contribution to the photon structure we call *point-like*. Of course lepton pairs can give only the point-like contribution to the photon structure, irrespectively of their relative transverse momentum. The contributions to the structure of the photon discussed above are schematically shown in Fig.1, and the photon wave function can be written as [4]:

[1] Throughout the paper we use the convention $c = \hbar = 1$.

[2] An attempt to sort out ambiguities existing in the terminology describing the hard interactions of photons is performed in [2].

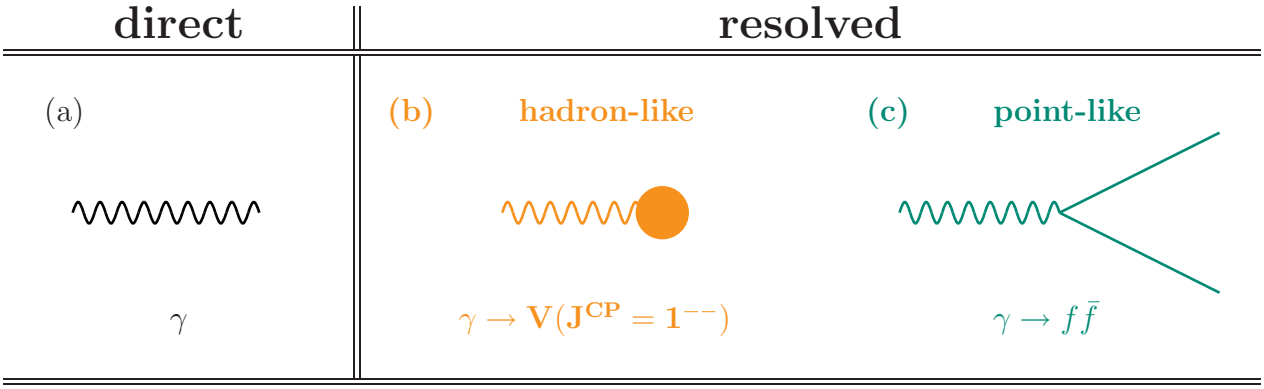

Figure 1: The *direct* photon (a) interacts as a whole quantity. The structure of the photon originates from quantum fluctuations – *resolved* photons: (b) hadron-like (c) point-like.

$$|\gamma\rangle = c_{\rm direct}|\gamma_{\rm direct}\rangle + \sum_{V=\rho^0,\omega,\ldots} c_V|\gamma_V\rangle + \sum_{q=u,d,\ldots} c_q|\gamma_q\rangle + \sum_{l=e,\mu,\tau} c_l|\gamma_l\rangle \tag{1}$$

The coefficients c_V, c_q and c_l depend on the factorization scale used to probe the photon and can be found e.g. in [5]. The coefficient $c_{\rm direct}$ is given by unitarity: $c^2_{\rm direct} = 1 - \sum c_V^2 - \sum c_q^2 - \sum c_l^2$, and in practice is always close to unity. For the rich structure of the photon developed through quantum fluctuations its investigation represents a fundamental test of predictions of both QED and QCD.

Most of the experimental results in the field of particle physics are today obtained from experiments performed at accelerators where beams of high energy elementary particles are collided head on or with stationary targets. However, at present we do not have at our disposal photon beams and most of our knowledge on the structure of the photon comes from e^+e^- or ep colliders where the lepton beams serve as sources of high energy photons (the proton due to its large mass is a much weaker source of photons). The photons are emitted by the lepton beams in the bremsstrahlung process. Consequently the 'photon beams' have no well defined energies, but rather are characterized by broad, continues spectra. The other limitation is that due to the four momentum conservation it is not possible for a beam lepton to emit a real photon in the bremsstrahlung process (although the distribution is peaked at very small virtualities). Therefore in the present day experiments only the structure of quasi-real or virtual photons has been studied.

The main aim of this paper is to present and summarize the results on the structure of the photon and its interactions obtained from the LEP experiments. The classical way to investigate the structure of the photon at e^+e^- colliders is the measurement of the process:

$$e^+(p_1)e^-(p_2) \to e^+(p_1')e^-(p_2')\,X, \tag{2}$$

proceeding via the interaction of two photons, which can be either quasi-real (γ) or virtual ($\gamma^\star$). The terms in parentheses in Eq. 2 represent the four-vectors of the particles as shown in Fig. 3a and X is a given leptonic or hadronic final state. The subdivision of the photon wave function presented in Eq. 1 corresponds to six main event classes in $\gamma\gamma \to$ hadrons interactions, characterized by some transverse momentum scale k_T of the $q\bar{q}$ fluctuation and an unphysical scale k_0 (of order 0.5 GeV) which divides the phase space into perturbative

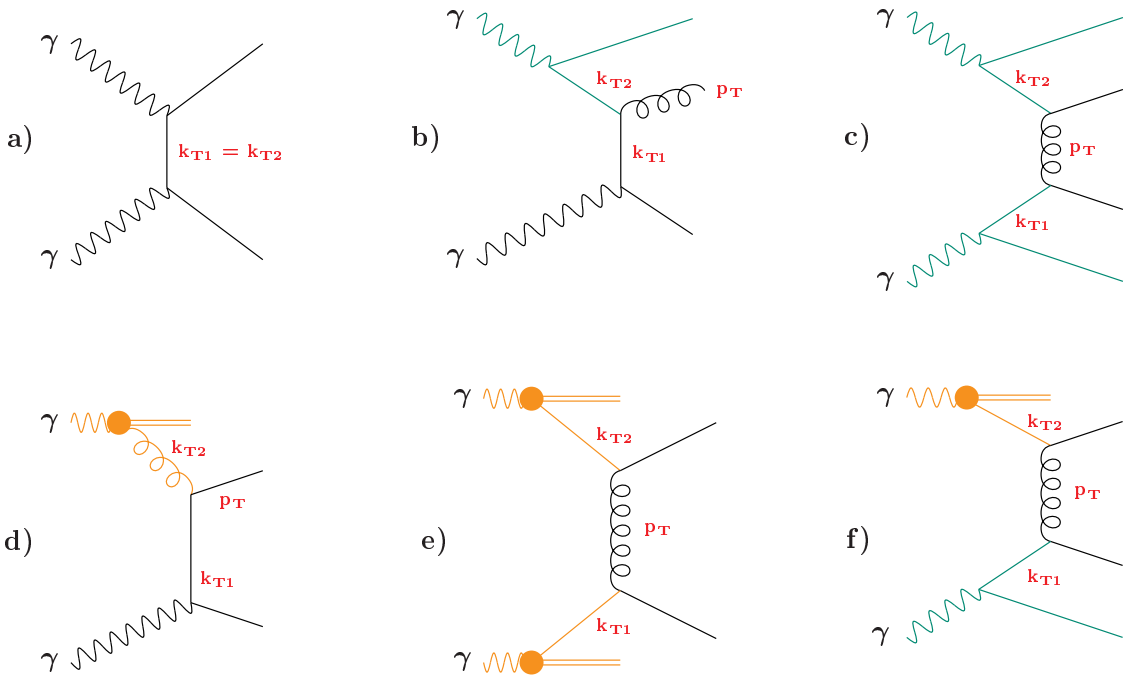

Figure 2: The leading order diagrams corresponding to the six main event classes in the process $\gamma\gamma \to$ hadrons: a) direct $\times$ direct; b) direct $\times$ point-like; c) point-like $\times$ point-like; d) direct $\times$ VMD; e) VMD $\times$ VMD; f) point-like $\times$ VMD.

and non-perturbative regions [4]. They are schematically shown in Fig. 2 and listed below (the quantity p_T represents the maximum transverse momentum in the event):

- direct $\times$ direct – the photons directly produce a quark pair, $(k_0 \ll k_{T1} = k_{T2})$,
- direct $\times$ point-like – the point-like photon splits into a $q\bar{q}$ pair and one of them (or a daughter thereof) interacts directly with the other photon, $(k_0 \ll k_{T2} \ll p_T \ll k_{T1})$,
- point-like $\times$ point-like – both photons perturbatively split into $q\bar{q}$ pairs, and subsequently one parton from each photon takes part in hard interaction, $(k_0 \ll k_{T1}, k_{T2} \ll p_T)$,
- direct $\times$ VMD – a direct photon interacts with the partons of VMD photon, $(k_{T2} < k_0 \ll p_T \ll k_{T1})$,
- VMD $\times$ VMD – both photons turn first into hadrons and then interact like hadrons, $(k_{T1}, k_{T2} < k_0$, arbitrary $p_T)$,
- point-like $\times$ VMD – the point-like photon perturbatively splits into a $q\bar{q}$ pair and and one of these (or a daughter parton thereof) interacts with a parton from VMD photon, $(k_{T2} < k_0 \ll k_{T1} \ll p_T)$,

Lepton pairs, in the above subdivision, can be produced only in the direct $\times$ direct process.

Depending on the virtualities of the photons involved in the process from Eq. 2 the scattered electrons[3] may be observed in the detectors. From the experimental point of view the following three event classes are distinguished. In the case where none of the scattered beam electrons is observed in detector (anti-tagged), the structure of the quasi-real photon has been studied at LEP in terms of total cross-sections, jet production, and heavy quark production. If only one electron is observed (single-tagged), the process can be described as deep-inelastic electron scattering off a quasi-real photon. These events have been studied to measure QED and QCD photon structure functions as well as QCD structure function of the electron. If both electrons are observed (double-tagged), the dynamics of highly virtual photon collisions is probed. The QED and QCD structure of the interactions of two highly virtual photons has also been studied at LEP in terms of the effective structure function of the virtual photon and total cross sections.

In this paper we discuss only the results obtained in single tagged and double tagged measurements. The paper is organized as follows. In Section 2 the kinematics of two photon interactions at e^+e^- colliders is presented and all kinematic quantities used later are defined. The cross section for the process $e^+e^- \to e^+e^- f\bar{f}$ proceeding via the exchange of two photons is discussed in Section 3 and its several important kinematical limits are derived. Section 4 is devoted to the discussion of the deep inelastic electron-photon and electron-electron scattering processes. It starts with the introduction of the photon structure functions. Then the factorization of the e^+e^- cross section into fluxes of transverse and longitudinal photons and the corresponding cross sections for electron photon scattering, expressed in terms of the photon structure functions, is presented. The QED and the hadronic structure functions of the photon are discussed in detail, including the short description of the existing parameterizations of the parton distribution functions in the photon. The structure functions of the electron are defined and the relation between the photon and electron structure functions is given. The interactions of highly virtual photons are discussed in Section 5 in terms of the effective structure function of the virtual photon and the total $\gamma^\star\gamma^\star$ cross sections, focusing on possible BFKL [36] effects in interactions of two highly virtual photons. The short presentation of the Monte Carlo models used in experimental analyses of the photon structure is given in Section 5. In Section 6 the experimental aspects of the two photon physics at LEP are discussed on the example of the OPAL detector. The experimental results on the photon structure obtained by the LEP experiments in single and double tagged measurements are presented in Sections 8 and 9, respectively. When similar results from non LEP experiments exist they are compared with the LEP measurements. The experimental results presented in the paper include the QED and hadronic structure functions of both quasi-real and virtual photons, the structure function of the electron and cross sections for the scattering of two virtual photons with leptonic and hadronic final states. The numerical values of all experimental results presented in the paper are collected in the tables in four appendices. The summary of the studies of the photon and electron structure performed at LEP as well as the prospects of the future measurements are given in Section 10.

There are many review articles which partly overlap or extend the material presented in this paper. The survey in Ref. [6] consists of the short presentations of the most of experimental results on the structure of the photon available at the end of the year 2000. In

[3]Electrons and positrons are generically referred to as electrons.

depth discussion of the photon structure functions and their measurements in deep inelastic electron photon scattering process can be found in Ref. [7]. The thirty years old review by Budnev et al. in Ref. [8], although it lacks new experimental results, still serves as a source of many useful formulas and ideas. A very comprehensive discussions of the theoretical aspects of two photon interactions and especially the approach based on structure functions is given in Ref. [9] and Ref. [11]. The other interesting studies include Refs. [10, 12, 13].

The author of this thesis has been a member of the OPAL Collaboration since 1998. I was engaged primary in physics analyses of LEP2 data. I have concentrated on two photon physics and I made essential contributions to the following OPAL publications:

- OPAL Collaboration, G. Abbiendi et al., *Measurement of the hadronic cross section for the scattering of two virtual photons at LEP*, Eur.Phys.J. **C24** (2002) 17.
- OPAL Collaboration, G. Abbiendi et al., *Measurement of the photon and electron structure functions in deep inelastic* eγ *and* ee *scattering at LEP*, to be published in Eur. Phys. J. **C**.

I have presented on behalf of the OPAL and other LEP collaborations several results on the following conferences:

- *Measurement of the Cross Section for the Process* ee $\rightarrow$ ee$\gamma^\star\gamma^\star \rightarrow$ eeX *at* $\sqrt{s_{\rm ee}} =$ 189 *GeV*, International Conference on The Structure and Interactions of the Photon, Photon 1999, 23 - 27 May, Freiburg in Br., Germany.
- *Measurement of the Cross Section for the Process* ee $\rightarrow$ ee$\gamma^\star\gamma^\star \rightarrow$ eeX *at* $\sqrt{s_{\rm ee}} =$ $189 - 202$ *GeV*, International Conference on The Structure and Interactions of the Photon, Photon 2000, 26 - 31 August, Ambleside, UK.
- *Measurement of the Hadronic Cross Section for the Scattering of Two Virtual Photons at LEP*, International Europhysics Conference on High Energy Physics EPS HEP 2001, 12 - 18 July, 2001, Budapest, Hungary.
- *Measurement of the Hadronic Cross Section for the Scattering of Two Virtual Photons at OPAL*, International Conference on The Structure and Interactions of the Photon, Photon 2001, 2 - 7 September, Ascona, Switzerland.
- *Summary of the Photon Structure Function Measurements at LEP*, 10th International Workshop on Deep Inelastic Scattering (DIS2002), 30 April - 4 May 2002, Kraków, Poland.
- *Measurements of the Photon and Electron Structure Functions at LEP*, XXXIII International Symposium on Multiparticle Dynamics, 5 - 11 September, 2003, Kraków, Poland.

During my stay at CERN as a postdoctoral fellow in the years 1998–2000 I participated in the everyday running of the OPAL experiment. In particular I served as an online expert on shifts at the experiment. I was involved in the work of the luminosity group. I participated in the estimation of the geometrical acceptance of the newly installed small angle 'Far Forward' detector. As a member of the OPAL Two Photon Group I participated in the discussions on several two photon physics analyses and publications on this subject, especially those connected with structure functions measurements.

2 Kinematics

The kinematics of two photon interactions at e^+e^- colliders is illustrated in Fig. 3a. The quantities in parentheses represent the four vectors of the particles. The polar angles θ_i at which the electrons are scattered are measured with respect to the direction of original beam electrons. Throughout the paper, unless said differently, $i = 1, 2$ denotes quantities which are connected with the upper and lower vertex in Fig. 3a, respectively. The virtualities of the radiated photons are given by:

$$Q_i^2 \equiv -q_i^2 = -(p_i - p_i^{'})^2 > 0. \tag{3}$$

In case when the virtualities of the exchanged photons are significantly different, the process can be interpreted as a deep inelastic scattering of the electron off the photon radiated by the other beam electron (Fig. 3b) or directly off the other beam electron (Fig. 3c). The usual dimensionless variables of deep inelastic scattering are defined as:

$$y_{ei} = \frac{q_1 \cdot q_2}{p_i \cdot q_{3-i}}, \qquad x_i = \frac{Q_i^2}{2q_1 \cdot q_2}, \qquad z_i = \frac{Q_i^2}{2q_i \cdot p_{3-i}}, \tag{4}$$

where, in infinite momentum of the target particle frame of reference, x_i (z_i) are fractions of parton momentum with respect to the target photon (electron) and y_{ei} are the energies lost by the inelastically scattered electrons. The e^+e^- centre-of-mass energy squared is given by $s_{ee} = (p_1+p_2)^2$ and the hadronic (or leptonic, if a pair of leptons is produced in the final state) invariant mass (or the two-photon centre-of-mass energy) squared by $W^2 \equiv s_{\gamma\gamma} = (q_1+q_2)^2$. The e^+e^- and $\gamma\gamma$ centre-of-mass energies are related through: $s_{\gamma\gamma} = y_{e1}y_{e2}s_{ee} - Q_1^2 - Q_2^2$. The following useful relation between the above kinematical variables holds: $s_{ee}z_iy_{ei} = Q_i^2$.

Experimentally, the kinematical variables Q_i^2, y_{ei}, x_i and z_i are obtained from the four-vectors of the tagged electrons and the hadronic final state via:

$$Q_i^2 = 4E_b E_i^{'} \sin^2(\theta_i/2), \tag{5}$$

$$y_{ei} = 1 - \frac{E_i'}{E_b}\cos^2(\theta_i/2), \tag{6}$$

$$x_i = \frac{Q_i^2}{Q_1^2 + W^2 + Q_2^2}, \tag{7}$$

$$z_i = \frac{Q_i^2}{y_{ei}s_{ee}} = \frac{E_i^{'}\sin^2(\theta_i/2)}{E_b - E_i^{'}\cos^2(\theta_i/2)}. \tag{8}$$

where E_b and E_i' refer to the energy of the beam electrons and the scattered electrons, respectively, and the mass m_e of the electron has been neglected. If the beams collide head on and have equal energies E_b then $s_{ee} = 4E_b^2$. The two photon centre-of-mass energy, W, can be obtained from the energies, E_h, and momenta, $\vec{p}_h$, of final state particles (h), excluding the scattered electrons, via:

$$W^2 = \left(\sum_h E_h\right)^2 - \left(\sum_h \vec{p}_h\right)^2. \tag{9}$$

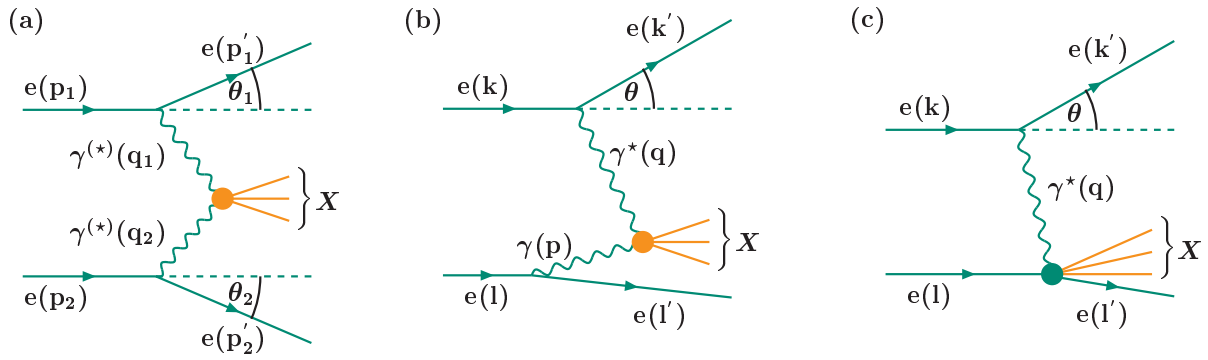

Figure 3: The diagrams corresponding to the process $e^+e^- \to e^+e^- X$, where X represents a given leptonic or hadronic final state, in different versions discussed in the paper: a) general diagram, b) deep inelastic electron photon scattering, c) deep inelastic electron electron scattering.

In single tagged events, using conservation of energy and momentum, and assuming that the untagged electron travels along the beam direction one can calculate W using the formula [16]:

$$W^2 = (p_{\mathrm{b}+} - p_{tag+}) \sum_h p_{h-} - p^2_{tag,T} \tag{10}$$

where $p_\pm = E \pm p_z$ with $p_{\mathrm{b}+}$ and p_{tag+} being calculated for the tagged electron before and after scattering, respectively, and $p_{tag,T}$ being the transverse momentum of the tagged electron. In double tagged events W can be determined from the four-momenta of the beam and the scattered electrons as follows:

$$W^2 = \left(2E_{\mathrm{b}} - E_1' - E_2'\right)^2 - \left(\vec{p}_1{}' + \vec{p}_2{}'\right)^2 \tag{11}$$

For the special case when the virtualities of the exchanged photons are significantly different (deep inelastic scattering) we introduce the following notation (see Fig.2b,c):

$$Q^2 \equiv -q^2 = \max\left(Q_1^2, Q_2^2\right), \qquad P^2 \equiv -p^2 = \min\left(Q_1^2, Q_2^2\right). \tag{12}$$

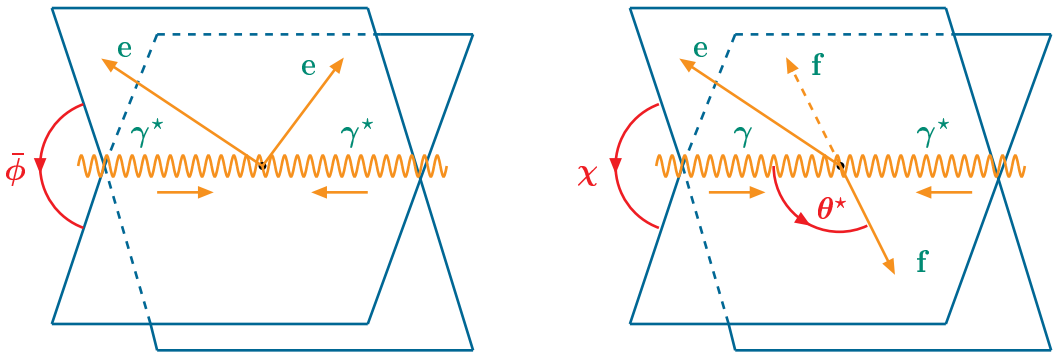

Figure 4: The scattering angles $\bar{\phi}$, $\theta^\star$ and χ defined in the photon-photon centre of mass system. For the precise definitions of the angles see text.

Then the kinematic variables x, z, $y_{\rm e}$ refer to the photon with higher virtuality, and we introduce the notation $\delta = P^2/2(p \cdot q)$. The relation $W^2 = Q^2(1/x - 1) - P^2$, which follows from Eq. 7, is often exploited in the following.

It is useful to define in this section the following additional angles (see Fig. 4). The azimuthal angle $\bar{\phi}$ is defined as the angle between the two scattering planes of the electrons in the photon-photon centre-of-mass system. The polar angle $\theta^\star$ is defined as the angle between the produced fermion or antifermion and the photon-photon axis in the photon-photon centre-of-mass system. The azimuthal angle χ is defined as the angle between the electron scattering plane and the scattering plane of the fermion which in the photon-photon centre-of-mass system is scattered at $\cos\theta^\star < 0$.

3 Cross sections for the process $e^+e^- \to e^+e^- f\bar{f}$

The four main diagrams representing the leading order contributions to the process $e^+e^- \to e^+e^- f\bar{f}$ are shown in Fig. 5. In the kinematical region discussed in this paper – small or medium virtualities Q_i^2 of at least one of the exchanged photons – the dominant contribution stems from the multiperipheral diagram [17]. The contributions from the other types of diagrams or from Z boson exchange become important only at very large photon virtualities and are not considered in the following.

The differential cross-section for the scattering of two unpolarized electrons via the exchange of two photons (multiperipheral diagram from Fig. 5a), integrated over the phase space of produced particles $f\bar{f}$, is given by (derivation of this formula can be found e.g. in [8, 9]):

$$\mathrm{d}^6\sigma = \frac{\mathrm{d}^3\mathrm{p}_1'\mathrm{d}^3\mathrm{p}_2'}{E_1' E_2'} \frac{\alpha^2}{16\pi^4 Q_1^2 Q_2^2} \left[\frac{(q_1\cdot q_2)^2 - Q_1^2Q_2^2}{(p_1\cdot p_2)^2 - m_e^2 m_e^2}\right]^{1/2} \Big(4\rho_1^{++}\rho_2^{++}\sigma_{\mathrm{TT}} + 2\rho_1^{++}\rho_2^{00}\sigma_{\mathrm{TL}} + 2\rho_1^{00}\rho_2^{++}\sigma_{\mathrm{LT}} + \rho_1^{00}\rho_2^{00}\sigma_{\mathrm{LL}} + 2|\rho_1^{+-}\rho_2^{+-}|\tau_{\mathrm{TT}}\cos 2\bar{\phi} - 8|\rho_1^{+0}\rho_2^{+0}|\tau_{\mathrm{TL}}\cos\bar{\phi}\Big) \tag{13}$$

where $\bar{\phi}$ is the angle between the two scattering planes of the electrons in two photon centre-of-mass system (see Fig. 4a) and the four vectors and other kinematical variables are defined in Section 2. The quantities ρ_1^{jk} and ρ_2^{jk}, where $j,k \in (+,-,0)$ denote the photon helicities, are elements of the photon density matrix, which can be expressed in terms of the measurable momenta p_i and p_i' (respectively q_i) and are to that extent entirely known. They take the following form [8]:

$$2\rho_i^{++} = \frac{(2p_i\cdot q_{3-i} - q_1\cdot q_2)^2}{(q_1\cdot q_2)^2 - Q_1^2Q_2^2} + 1 - 4\frac{m_e^2}{Q_i^2}, \qquad \rho_i^{00} = \frac{(2p_i\cdot q_{3-i} - q_1\cdot q_2)^2}{(q_1\cdot q_2)^2 - Q_1^2Q_2^2} - 1,$$
$$|\rho_i^{+-}| = \rho_i^{++} - 1, \qquad |\rho_i^{+0}| = \sqrt{(\rho_i^{00}+1)|\rho_i^{+-}|}. \tag{14}$$

The cross-sections σ_{TT}, σ_{TL}, σ_{LT} and σ_{LL} and the interference terms τ_{TT} and τ_{TL} correspond to specific helicity states of the interacting photons (T – transverse and L – longitudinal).

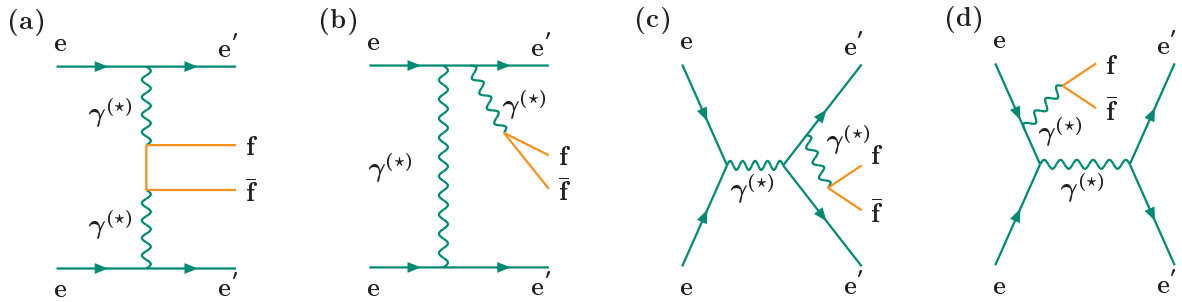

Figure 5: Examples of the diagrams contributing in the leading order to the process $e^+e^- \to e^+e^- f\bar{f}$: a) multiperipheral, b) bremsstrahlung, c) annihilation, d) conversion. In each case only one possible diagram is shown.

They are obtained in QED from doubly virtual box diagram $\gamma^\star(Q_1^2)\gamma^\star(Q_2^2) \to \mathrm{f}\bar{\mathrm{f}}$ and for the case of lepton pair production in the leading order have the following form [8] (Slight modifications with respect to the original formulas given in the reference [8] come from the introduction of additional variables β and $\bar{\beta}$ defined in Eq. 17 and a change in the meaning of the variable T. These modifications are in accord with the modern notation used in the expressions for the photon structre functions introduced in the next section.):

$$
\begin{aligned}
\sigma_{\mathrm{TT}} &= \frac{\pi\alpha^2}{W^2\,X}\left\{(q_1\cdot q_2)L\left[2+\frac{2m^2}{X}-\left(\frac{2m^2}{q_1\cdot q_2}\right)^2-\frac{Q_1^2+Q_2^2}{X}+\frac{Q_1^2\,Q_2^2\,W^2}{2X(q_1\cdot q_2)^2}\right.\right.\\
&\left.\left.+\frac{3}{4}\left(\frac{Q_1^2\,Q_2^2}{X\,(q_1\cdot q_2)}\right)^2\right]-\Delta t\left[1+\frac{m^2}{X}-\frac{Q_1^2+Q_2^2}{X}+\frac{1}{T}\,\frac{Q_1^2Q_2^2}{(q_1\cdot q_2)^2}+\frac{3}{4}\frac{Q_1^2\,Q_2^2}{X^2}\right]\right\}\\
\sigma_{\mathrm{TL}} &= \frac{\pi\alpha^2\,Q_2^2}{W^2X^2}\left\{\Delta t\left[1-\frac{1}{T}\,\frac{Q_1^2}{(q_1\cdot q_2)^2}\left(6m^2-Q_1^2+\frac{3}{2}\frac{Q_1^2\,Q_2^2}{X}\right)\right]\right.\\
&\left.-\frac{L}{q_1\cdot q_2}\left[4m^2X-Q_1^2(W^2+2m^2)+Q_1^2\left(Q_1^2+Q_2^2-\frac{3}{2}\frac{Q_1^2\,Q_2^2}{X}\right)\right]\right\}\\
\sigma_{\mathrm{LT}} &= \sigma_{\mathrm{TL}}(Q_1^2\leftrightarrow Q_2^2)\\
\sigma_{\mathrm{LL}} &= \frac{\pi\alpha^2\,Q_1^2\,Q_2^2}{W^2X^3}\left\{\frac{L}{q_1\cdot q_2}(2W^2X+3Q_1^2\,Q_2^2)-\Delta t\left(2+\frac{1}{T}\,\frac{Q_1^2\,Q_2^2}{(q_1\cdot q_2)^2}\right)\right\}\\
\tau_{\mathrm{TT}} &= -\frac{\pi\alpha^2}{4W^2X}\left\{\frac{2\Delta t}{X}\left[2m^2+\frac{(Q_1^2-Q_2^2)^2}{W^2}+\frac{3}{2}\frac{Q_1^2\,Q_2^2}{X}\right]+\frac{L}{q_1\cdot q_2}\left[\,16m^4\right.\right.\\
&\left.\left.+16m^2(Q_1^2+Q_2^2)-4Q_1^2Q_2^2\left(2+\frac{2m^2}{X}-\frac{Q_1^2+Q_2^2}{X}+\frac{3}{4}\frac{Q_1^2Q_2^2}{X^2}\right)\right]\right\}\\
\tau_{\mathrm{TL}} &= -\frac{\pi\alpha^2\sqrt{Q_1^2\,Q_2^2}}{W^2X^2}\left\{L\left(2m^2-Q_1^2-Q_2^2+\frac{3}{2}\frac{Q_1^2\,Q_2^2}{X}\right)+\Delta t\left(2-\frac{3}{2}\frac{q_1\cdot q_2}{X}\right)\right\}
\end{aligned}
\tag{15}
$$

where m is the lepton mass, and

$$
\begin{aligned}
X &= \frac{(q_1\cdot q_2)^2}{W^2}\,\bar{\beta}^2\,, & \Delta t &= 2(q_1\cdot q_2)\,\beta\bar{\beta}\,,\\
T &= 1-\beta^2\bar{\beta}^2\,, & L &= \ln\frac{1+\beta\bar{\beta}}{1-\beta\bar{\beta}}
\end{aligned}
\tag{16}
$$

with

$$
\beta=\sqrt{1-\frac{4\,m^2}{W^2}}\,,\qquad \bar{\beta}=\sqrt{1-\frac{Q_1^2\,Q_2^2}{(q_1\cdot q_2)^2}}
\tag{17}
$$

Using the relation $q_1\cdot q_2=\frac{1}{2}(W^2+Q_1^2+Q_2^2)$, it is clear that the cross sections and interference terms in Eq. 15 depend only on Q_1^2, Q_2^2, W^2 and the lepton mass m.
It is worth of pointing out here that, in general, although the interference terms τ_{TT} and τ_{TL} are independent of $\bar{\phi}$, even after integration of Eq. 13 over the full range of $\bar{\phi}$ the dependence on the interference terms does not vanish. This follows from strong kinematical correlations

of $\bar{\phi}$ and the variables Q_1^2, Q_2^2 and W^2. In those regions of phase space where the interference terms are large there is no clear relation between the structure function approach discussed in the next section and the individual cross section terms. In such case the total or differential cross sections are the most appropriate quantities to be measured by experiments.

The formulae given in Eq. 15 can be used in the case of quark pair production after multiplying each cross section and interference term by $N_c e_q^4$, with N_c being the number of colours and e_q the quark charge, replacing the lepton mass m by a quark mass m_q and summing over all active flavours. In fixed order perturbation theory the doubly virtual box contribution $\gamma^\star(Q_1^2)\gamma^\star(Q_2^2) \to q\bar{q}$ is referred to as the quark parton model (QPM) approximation. In the case of QED Eq. 15 can be applied irrespective of the virtualities Q_1^2 and Q_2^2, unless they are small enough so that Z boson exchange can be neglected. The situation is different in QCD and depends on the relative sizes of the scales (Q_1^2, Q_2^2, W^2) characterizing the process and a typical hadronic scale, which is of order of Λ. In QCD Λ denotes a scale at which the effective coupling becomes large (see Eq. 50 and discussion after it). If the virtualities of both photons are large compared to Λ ($Q_1^2\,,\, Q_2^2 \gg \Lambda^2$) we have a purely perturbative process where the predictions of Eq. 15 are applicable. Furthermore, if in addition $Q_1^2 \gg Q_2^2$, than the structure of the virtual target photon $\gamma(Q_2^2)$ is resolved by a probe photon $\gamma(Q_1^2)$. In the high energy limit of photon–photon collisions ($Q_1^2\,,\, Q_2^2 \ll W^2$) one can directly study the BFKL [36] dynamics. In that case Eq. 15 constitute a lowest order result. If one of the photons is highly virtual and the other quasi–real ($Q_1^2 \gg \Lambda^2 \gtrsim Q_2^2$) perturbation theory is not reliable due to non-perturbative, long-distance effects. Therefore Eq. 15 are not directly applicable in this case, and the photon structure functions of the quasi–real photon are factorized into non-perturbative parton distribution functions to be fixed by experimental information and a calculable short distance coefficient functions as explained in the next section.

Below we discuss several useful kinematical limits of Eq. 15. They can be applied to both lepton and quark (with appropriate normalization, see above) pairs in the final state. The formulas obtained below will be directly used in the next section to construct photon structure functions in different approximations.

In the general Bjorken limit ($m^2\,, Q_2^2 \ll Q_1^2$) we neglect expressions of order $\mathcal{O}(Q_2^2/Q_1^2)$ and $\mathcal{O}(m^2/W^2)$. In this limit $\sigma_{\rm LL}$ and $\tau_{\rm TL}$ vanish and the remaining quantities have the following form:

$$\begin{aligned}
\sigma_{\rm TT} &= \frac{2\pi\alpha^2}{q_1\cdot q_2}\left\{L\left(1-\frac{1}{2}\frac{Q_1^2\,W^2}{(q_1\cdot q_2)^2}\right)-1+\frac{Q_1^2\,W^2}{(q_1\cdot q_2)^2}-\frac{1}{T}\,\frac{Q_1^2\,Q_2^2}{(q_1\cdot q_2)^2}\right\}\\
\sigma_{\rm TL} &= \frac{2\pi\alpha^2}{q_1\cdot q_2}\,\frac{Q_2^2\,W^2}{(q_1\cdot q_2)^4}\frac{Q_1^4}{T}\\
\sigma_{\rm LT} &= \frac{2\pi\alpha^2}{q_1\cdot q_2}\,\frac{Q_1^2\,W^2}{(q_1\cdot q_2)^2}\\
\tau_{\rm TT} &= -\frac{\pi\alpha^2}{q_1\cdot q_2}\,\frac{Q_1^4}{(q_1\cdot q_2)^2}
\end{aligned} \tag{18}$$

where

$$T = \frac{4m^2}{W^2}+\frac{Q_1^2\,Q_2^2}{(q_1\cdot q_2)^2}\,, \qquad\qquad L = \ln\frac{4}{T}\,. \tag{19}$$

The above expressions further reduce in the limit of $m^2 = 0$ (e.g. light quarks) and $Q_2^2 \ll Q_1^2$:

$$\begin{aligned}
\sigma_{\rm TT} &= \frac{2\pi\alpha^2}{q_1\cdot q_2}\left\{L\left(1-\frac{1}{2}\frac{Q_1^2W^2}{(q_1\cdot q_2)^2}\right)-2+\frac{Q_1^2W^2}{(q_1\cdot q_2)^2}\right\}\\
\sigma_{\rm TL} &= \sigma_{\rm LT} = \frac{2\pi\alpha^2}{q_1\cdot q_2}\,\frac{Q_1^2W^2}{(q_1\cdot q_2)^2}\\
\tau_{\rm TT} &= -\frac{\pi\alpha^2}{q_1\cdot q_2}\,\frac{Q_1^4}{(q_1\cdot q_2)^2}
\end{aligned} \tag{20}$$

where $L = \ln\left(4(q_1\cdot q_2)^2/Q_1^2Q_2^2\right)$. In the Bjorken limit the two-photon processes can be interpreted as deep inelastic scattering and the appropriate cross sections can be described in terms of virtual photon structure functions.

In the case where one photon is real (e.g. $Q_2^2 = 0$), $\bar\beta = 1$ and it follows from Eq. 15 that the terms $\sigma_{\rm TL}$, $\sigma_{\rm LL}$ and $\tau_{\rm TL}$ vanish and the remaining take the following form (the full mass dependence is kept, which is relevant for the heavy quark contribution to the photon structure functions):

$$\begin{aligned}
\sigma_{\rm TT} &= \frac{\pi\alpha^2}{(q_1\cdot q_2)^3}\Big\{\,L\left[2(q_1\cdot q_2)^2+2m^2W^2-4m^4-Q_1^2W^2\right]\\
&\qquad -\frac{\Delta t}{q_1\cdot q_2}\left[(q_1\cdot q_2)^2+m^2W^2-Q_1^2W^2\right]\Big\}\\
\sigma_{\rm LT} &= \frac{\pi\alpha^2Q_1^2}{(q_1\cdot q_2)^4}\left[W^2\Delta t-4m^2(q_1\cdot q_2)L\right]\\
\tau_{\rm TT} &= -\frac{\pi\alpha^2}{2(q_1\cdot q_2)^4}\left[\Delta t(2m^2W^2+Q_1^4)+8m^2(q_1\cdot q_2)(m^2+Q_1^2)L\right]
\end{aligned} \tag{21}$$

where

$$\Delta t = (W^2+Q_1^2)\beta\,, \qquad L = \ln\frac{1+\beta}{1-\beta}\,. \tag{22}$$

If in addition $m^2 \ll Q_1^2$, the Eq. 21 reduce to:

$$\begin{aligned}
\sigma_{\rm TT} &= \frac{\pi\alpha^2}{(q_1\cdot q_2)}\left\{\left[2-\frac{Q_1^2W^2}{(q_1\cdot q_2)^2}\right]\ln\frac{W^2}{m^2}-\frac{W^2+Q_1^2}{q_1\cdot q_2}\left[1-\frac{Q_1^2W^2}{(q_1\cdot q_2)^2}\right]\right\}\\
\sigma_{\rm LT} &= \frac{\pi\alpha^2Q_1^2}{(q_1\cdot q_2)^4}\left[W^2(W^2+Q_1^2)\right]\\
\tau_{\rm TT} &= -\frac{\pi\alpha^2}{2(q_1\cdot q_2)^4}\left[Q_1^4(W^2+Q_1^2)\right]
\end{aligned} \tag{23}$$

Near the mass shell ($Q_i^2 \to 0$) the terms of longitudinal photon scattering vanish. In this limit $\sigma_{\rm TT}$ and $\tau_{\rm TT}$ are transformed into the corresponding quantities for real two photon processes. In particular, at $Q_i^2 = 0$, $\sigma_{\rm TT}$ coincides with the cross section $\sigma_{\gamma\gamma}$ of the $\gamma\gamma \to X$ transition for real non-polarized photons. As a result, at $Q_i^2 \to 0$, we get:

$$\begin{aligned}
\sigma_{\rm TT}(W^2,Q_1^2,Q_2^2) \to \sigma_{\gamma\gamma}(W^2) &= \frac{4\pi\alpha^2}{W^2}\left[\left(1+\frac{4m^2}{W^2}-\frac{8m^4}{W^4}\right)L-\left(\frac{1}{W^2}+\frac{4m^2}{W^4}\right)\Delta t\right]\,,\\
\tau_{\rm TT}(W^2,Q_1^2,Q_2^2) \to \tau_{\gamma\gamma}(W^2) &= -\frac{16\pi\alpha^2m^2}{W^6}(\Delta t+2m^2L)\,,
\end{aligned} \tag{24}$$

where Δt and L are given by Eq. 22 with Q_1^2 set to zero. The other cross sections vanish in the limit $Q_i^2 \to 0$ as:

$$\sigma_{\rm TL} \sim Q_2^2\,, \qquad \sigma_{\rm LT} \sim Q_1^2\,, \qquad \sigma_{\rm LL} \sim Q_1^2 Q_2^2\,, \qquad \tau_{\rm TL} \sim \sqrt{Q_1^2 Q_2^2}\,. \tag{25}$$

The full cross sections and their several limits discussed in this Section will be later used to construct photon structure functions in various approximations.

4 Deep inelastic eγ and ee scattering

In this section we assume that the virtuality of one of the exchanged photons is much smaller than the virtuality of the other photon ($P^2 \ll Q^2$). In that case the subprocess $e\gamma \to e f\bar{f}$ can be interpreted as deep inelastic electron–photon scattering (see Fig. 3b) in which the structure of the quasi–real ($P^2 \lesssim \Lambda^2$) or virtual ($P^2 \gtrsim \Lambda^2$) transverse photon is probed by the virtual photon of both transverse and longitudinal polarizations. Due to experimental (and kinematical) limitations the virtuality of the quasi–real target photon can be kept small but it is always larger than zero. The effect of this small virtuality is usually neglected although it might be important. This problem can be overcome when one interprets the process as deep inelastic scattering of an electron off other, target electron (see Fig. 3c). In such situation the virtual photon probes directly the structure of the real electron. Although the first interpretation (DIS eγ) is most widely used, in the following we discuss both approaches.

4.1 Photon structure functions

In the case of lepton pair production, the cross section presented in the previous section in Eq. 13 is determined by QED and contain full information needed to describe the reaction. On the other hand in the case of quark pair production, QCD corrections are involved and it becomes necessary to parameterize the cross section by means of the photon structure functions. However, to have consistent description of both QED and hadronic structure of the photon we usually express the cross sections for both lepton and quark pair production in terms of structure functions. Usually one introduces structure functions for a spin–averaged target photon. They can be expressed in terms of the photon–photon cross sections σ_{ab} $(a, b = T, L)$ defined in the previous section as follows [8, 9]:

$$\begin{aligned}
F_2^\gamma(x,Q^2,P^2) &= \frac{Q^2}{4\pi^2\alpha}\frac{1}{\bar{\beta}}\Bigg[\sigma_{\rm TT}(x,Q^2,P^2)+\sigma_{\rm LT}(x,Q^2,P^2) \\
&\quad -\frac{1}{2}\sigma_{\rm LL}(x,Q^2,P^2)-\frac{1}{2}\sigma_{\rm TL}(x,Q^2,P^2)\Bigg] \\
2xF_T^\gamma(x,Q^2,P^2) &= \frac{Q^2}{4\pi^2\alpha}\,\bar{\beta}\left[\sigma_{\rm TT}(x,Q^2,P^2)-\frac{1}{2}\sigma_{\rm TL}(x,Q^2,P^2)\right] \\
F_L^\gamma(x,Q^2,P^2) &= \frac{Q^2}{4\pi^2\alpha}\,\bar{\beta}\left[\sigma_{\rm LT}(x,Q^2,P^2)-\frac{1}{2}\sigma_{\rm LL}(x,Q^2,P^2)\right]
\end{aligned} \tag{26}$$

where $\bar{\beta} = \sqrt{1 - Q^2\,P^2/(p\cdot q)^2}$ and we made use of Eq. 7 to express the cross sections σ_{ab} as functions of x, Q^2 and P^2. This choice of variables is conveniently used for the presentation of the photon structure functions. The following relation holds between the above structure functions: $F_L^\gamma = \bar{\beta}^2\,F_2^\gamma - 2xF_T^\gamma$. The expressions in Eq. 26 are generally valid for arbitrary P^2 and Q^2, although they have a meaningful interpretation as structure functions of a target photon probed by deeply virtual photon only in the limit $P^2 \ll Q^2$. Since the fluxes of transverse and longitudinal photons are different it is useful to introduce structure functions

of transverse ($a = T$) and longitudinal ($a = L$) target photons:

$$F_2^{\gamma_a}(x, Q^2, P^2) = \frac{Q^2}{4\pi^2\alpha}\,\frac{1}{\bar{\beta}}\Big[\,\sigma_{Ta}(x, Q^2, P^2) + \sigma_{La}(x, Q^2, P^2)\Big]$$

$$\begin{aligned} 2xF_T^{\gamma_a}(x, Q^2, P^2) &= \frac{Q^2}{4\pi^2\alpha}\,\bar{\beta}\,\sigma_{Ta}(x, Q^2, P^2) \\ F_L^{\gamma_a}(x, Q^2, P^2) &= \frac{Q^2}{4\pi^2\alpha}\,\bar{\beta}\,\sigma_{La}(x, Q^2, P^2) \end{aligned} \tag{27}$$

They are related to each other via $F_L^{\gamma_a} = \bar{\beta}^2\,F_2^{\gamma_a} - 2xF_T^{\gamma_a}$. The expressions for a spin-averaged target photons given in Eq. 26 are related to the structure functions of polarized photons given in Eq. 27 via $F_i^{\gamma} = F_i^{\gamma_T} - \frac{1}{2}F_i^{\gamma_L}$, where $i = 2, L, T$.

It is well known that for $P^2 = 0$ the cross section for the process ee $\to$ ee$\gamma\gamma^\star \to$ eeX can be factorised into a product of the flux of target photons of transverse polarization and the cross section for deep inelastic eγ scattering [7]. One can also show [9] that in the Bjorken limit ($Q^2 \to \infty$, $p\cdot q \to \infty$, x – fixed, what means that the quantity $\delta = P^2/2p\cdot q = xP^2/Q^2$ is small and can be neglected) the factorization holds for virtual target photons as well. Neglecting the terms of order $\mathcal{O}(\sqrt{\delta})$, changing appropriately the variables and integrating over azimuthal angles of the scattered electrons one can rewrite the cross section given in Eq. 13 in the factorised form [9]:

$$\frac{d\sigma(\mathrm{ee}\to\mathrm{eeX})}{dxdQ^2dydP^2} = \hat{f}^T_{\gamma^\star/e}(y, P^2)\frac{d\sigma(\mathrm{e}\gamma_\mathrm{T}\to\mathrm{eX})}{dxdQ^2} + \hat{f}^L_{\gamma^\star/e}(y, P^2)\frac{d\sigma(\mathrm{e}\gamma_\mathrm{L}\to\mathrm{eX})}{dxdQ^2} \tag{28}$$

where y is the fractional momentum of the target photon with respect to the beam electron. The fluxes of transverse and longitudinal target photons in the equivalent photon approximation (EPA) are given by [18]:

$$\hat{f}^T_{\gamma^\star/e}(y, P^2) = \frac{\alpha}{2\pi}\left[\frac{1+(1-y)^2}{y}\frac{1}{P^2} - 2y\frac{m_e^2}{P^4}\right] \tag{29}$$

$$\hat{f}^L_{\gamma^\star/e}(y, P^2) = \frac{\alpha}{2\pi}\frac{2(1-y)}{y}\frac{1}{P^2} \tag{30}$$

The cross sections for deep inelastic electron–photon scattering expressed in terms of the polarized photon structure functions $F_2^{\gamma_a}$ and $F_L^{\gamma_a}$ read:

$$\frac{d\sigma(\mathrm{e}\gamma_\mathrm{a}\to\mathrm{eX})}{dxdQ^2} = \frac{2\pi\alpha^2}{xQ^4}\left[\left(1+(1-y_\mathrm{e})^2\right)F_2^{\gamma_a}(x, Q^2, P^2) - y_\mathrm{e}^2F_L^{\gamma_a}(x, Q^2, P^2)\right] \tag{31}$$

In the limit of small virtualities of target photons ($P^2 \approx 0$) the contribution from the longitudinal target photons vanish and the cross section for the process ee $\to$ ee$\gamma\gamma^\star \to$ eeX can be written as a product of the flux of transversally polarized photons and the cross section for deep inelastic electron photon scattering:

$$\frac{d^4\sigma}{dxdQ^2dzdP^2} = \frac{2\pi\alpha^2}{x^2Q^4}\left[\left(1+(1-y_\mathrm{e})^2\right)F_2^{\gamma}(x, Q^2, P^2) - y_\mathrm{e}^2F_L^{\gamma}(x, Q^2, P^2)\right]\hat{f}^T_{\gamma^\star/e}(z/x, P^2) \tag{32}$$

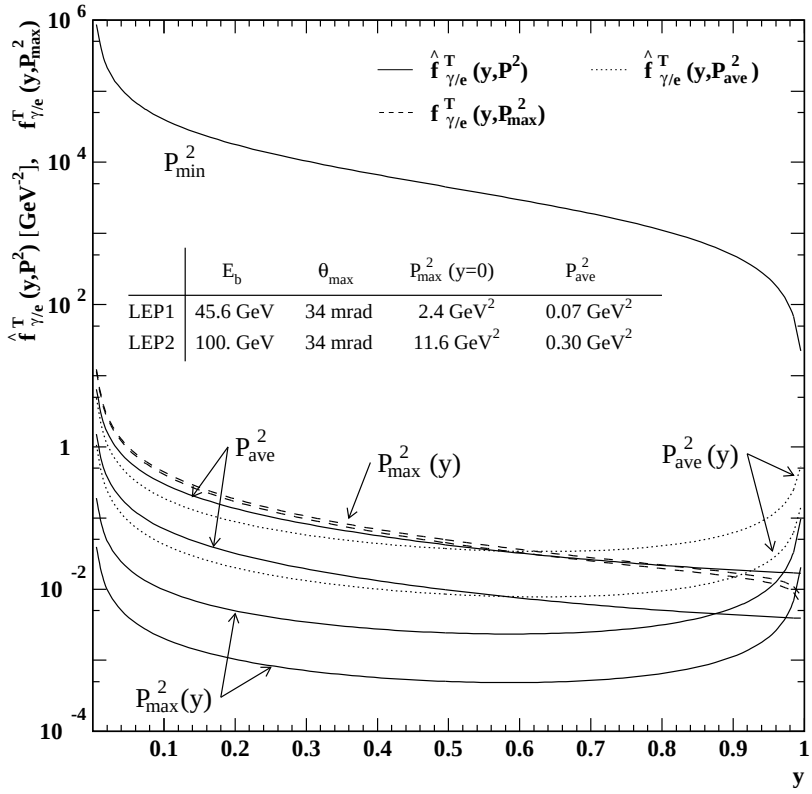

Figure 6: Comparison of EPA ($\hat{f}^T_{\gamma^\star/\mathrm{e}}$) and the Weizsäcker–Williams approximation ($f^T_{\gamma^\star/e}$). The chosen beam energies, minimum tagging angle, the values of $P^2_{\mathrm{max}}(y=0)$ and the values of P^2_{ave} averaged over the full range of P^2 and the range of $10^{-4} < y < 1$ are also shown.

The flux of equivalent photons as well as the structure functions depend in principle on the virtuality of the target photon. However, in experiments the virtuality of the target photon is usually unknown and one has to calculate structure functions assuming some effective target virtuality, P^2_{eff}, and integrate the flux over the range of possible virtualities. In practice, this effective virtuality P^2_{eff} is usually obtained from Monte Carlo simulation or from the best fit of the structure function predictions to the data. The integration of EPA over the possible range of P^2 leads to the Weizsäcker–Williams approximation [19]:

$$\begin{aligned} f^T_{\gamma^\star/e}(y, P^2_{\mathrm{max}}) &= \int_{P^2_{\mathrm{min}}(y)}^{P^2_{\mathrm{max}}} dP^2 \hat{f}^T_{\gamma^\star/e}(y, P^2) = \\ &= \frac{\alpha}{2\pi}\left[\frac{1+(1-y)^2}{y}\ln\left(\frac{P^2_{\mathrm{max}}(1-y)}{m_e^2 y^2}\right) - 2\frac{1-y}{y} + 2y\frac{m_e^2}{P^2_{\mathrm{max}}}\right] \end{aligned} \tag{33}$$

where

$$P^2_{\mathrm{min}}(y) = \frac{m_e^2 y^2}{1-y} \qquad \text{and} \qquad P^2_{\mathrm{max}}(y) = (1-y)E^2\theta^2_{\mathrm{max}} \tag{34}$$

The lower boundary of the integration P^2_{min} follows from the four vector conservation and the upper boundary is determined by the experimental acceptance. In practical applications

we often choose a constant value of $P_{\max}$ (equal to the minimum virtuality of probe photons) and fill the missing phase space by a model prediction. In Fig. 6 we show the predictions of EPA and the Weizsäcker-Williams approximation for two typical situations during LEP1 and LEP2 data taking periods. The chosen beam energies are 45 GeV and 100 GeV, respectively, and in both cases the minimum tagging angle had been chosen at 34 mrad. Predictions of EPA are shown at $P^2_{\min}$, $P^2_{\max}(y)$ and at average values of virtuality $P^2_{\rm ave}(y)$ depending on y and at the virtuality $P^2_{\rm ave}$ averaged over y in the range $10^{-4} < y < 1$. The predictions of the Weizsäcker-Williams approximation is shown for the integration range given by Eqs. 34. For the LEP1 case the Weizsäcker–Williams approximation is close to the EPA prediction at $P^2_{\rm ave}$. But this is already not the case for the LEP2 energies, and follows from only a very weak dependence of the Weizsäcker–Williams approximation on the upper boundary of the P^2 integration range.

Let us return to the discussion of the cross section of Eq. 32. For small values of the variable $y_{\rm e}$, accessible at LEP energies, the term proportional to F_L^γ can be neglected. Integrating Eq. 32 over P^2 we get:

$$\frac{d^3\sigma}{dxdQ^2dz} \approx \frac{2\pi\alpha^2}{x^2Q^4}\left(1+(1-y_{\rm e})^2\right) F_2^\gamma(x,Q^2,P^2_{\rm eff}) f_{\gamma^\star/e}(z/x,P^2_{\max}) \tag{35}$$

where only a weak dependence of F_2^γ on P^2 has been assumed. The effective value of $P^2_{\rm eff}$ has been chosen in such a way that the following relation is fulfilled:

$$\langle F_2^\gamma(P^2)\rangle = F_2^\gamma(P^2_{\rm eff}) \tag{36}$$

One can integrate Eq. 35 over z changing the variables according to $y_e = Q^2/(zs_{ee}) \equiv \chi/z$ and using the relation:

$$\begin{aligned}\frac{1}{x}\int_{z_{min}}^{x} dz\left(1+(1-\chi/z)^2\right) f_{\gamma^\star/e}\left(z/x,P^2_{\max}\right) = \\ = \int_\eta^1 dy\left(1+(1-\eta/y)^2\right) f_{\gamma^\star/e}(y,P^2_{\max}) \equiv \mathcal{K}(\eta,b)\end{aligned} \tag{37}$$

where $z_{min}=\chi$, $\eta \equiv y_{min} = z_{min}/x = \chi/x$ and $b = P^2_{\max}/m_e^2$. The function $\mathcal{K}(\eta,b)$ has the following form:

$$\begin{aligned}\mathcal{K}(\eta,b) = \frac{\alpha}{2\pi}\Bigg[-\frac{1}{6}\pi^2(\eta+2)^2 - \ln(\eta)(\eta+2)^2\ln\left(\frac{b}{\eta}\right) + (10-4\eta-3\eta^2)\ln(\eta) \\ - \frac{1}{2}(3\eta+19)(\eta-1) + 2(\eta+3)(\eta-1)\ln(b(1-\eta)) + (\eta+2)^2 Li_2(\eta)\Bigg]\end{aligned} \tag{38}$$

where $Li_2(x) = -\int_0^x \frac{\ln|1-t|}{t}\,dt$ is the dilogarithm function. Usually we assume that $P^2_{\rm eff}=0$ and in consequence the formula given in Eq. 35 can be rewritten in the form:

$$\frac{d^2\sigma_{ee}}{dxdQ^2} \approx \frac{2\pi\alpha^2}{xQ^4} F_2^\gamma(x,Q^2)\mathcal{K}\left(\frac{Q^2}{xs},\frac{P^2_{\max}}{m_e^2}\right) \tag{39}$$

which can be directly used to obtain the photon structure function F_2^γ from the measured differential cross section $d^2\sigma_{ee}/dx\,dQ^2$.

4.2 QED structure functions of the photon

The QED structure functions of the photon can be defined for any type of lepton pairs in the final state of the process $e\gamma \to e l\bar{l}$. However, measurements exist only for muon pairs and therefore we will use the muon mass in the numerical results presented in this paragraph.

The leading order formulae for the QED structure functions $F^{\gamma}_{2,\mathrm{QED}}$ and $F^{\gamma}_{\mathrm{L,QED}}$ keeping the full dependence on the virtuality of the quasi-real photon P^2 can be obtained from Eq. 26 together with the cross sections listed in Eq. 15. They are however very long and will be not written down here. Much more compact formulae can be derived in the limit $2xP^2/Q^2 \ll 1$, but keeping the terms of order $\mathcal{O}(P^2/m^2)$. They are referred to as the Bethe-Heitler expressions for the virtual photon and have the following form [20]:

$$\begin{aligned} F^{\gamma}_{2,\mathrm{BH}}(x,Q^2,P^2) = \frac{\alpha}{\pi}x\Bigg\{ & \left[x^2+(1-x)^2\right]\ln\frac{1+\beta\bar{\beta}}{1-\beta\bar{\beta}} - \beta + 6\beta x(1-x) \\ & + \left[2x(1-x) - \frac{1-\bar{\beta}^2}{1-\beta^2} - (1-\beta^2)(1-x)^2\right]\frac{\beta\bar{\beta}(1-\beta^2)}{1-\beta^2\bar{\beta}^2} \\ & + (1-\beta^2)(1-x)\left[\frac{1}{2}(1-x)(1+\beta^2) - 2x\right]\ln\frac{1+\beta\bar{\beta}}{1-\beta\bar{\beta}}\Bigg\} \end{aligned} \tag{40}$$

$$F^{\gamma}_{\mathrm{L,BH}}(x,Q^2,P^2) = \frac{\alpha}{\pi}x^2(1-x)\left[\beta - \frac{1}{2}(1-\beta^2)\ln\frac{1+\beta\bar{\beta}}{1-\beta\bar{\beta}}\right] \tag{41}$$

where β and $\bar{\beta}$ are given in Eq. 17. Neglecting in addition the terms of order $\mathcal{O}(m^2/W^2)$ we arrive at the Bjorken limit discussed in Section 3. The structure functions in this limit can be constructed using Eq. 26 and the cross sections listed in Eq. 18. A very compact formula for $F^{\gamma}_{2,\mathrm{QED}}$ is obtained in the Bjorken limit combined with the restriction $P^2 \ll W^2$:

$$\begin{aligned} F^{\gamma}_{2,apr}(x,Q^2,P^2) = \frac{\alpha}{\pi}x\Bigg\{ & \left[x^2+(1-x)^2\right]\ln\frac{W^2}{m^2+P^2x(1-x)} - 1 \\ & + 8x(1-x) + \frac{P^2(1-x)}{m^2+P^2x(1-x)}\Bigg\} \end{aligned} \tag{42}$$

The predictions of the exact formula for $F^{\gamma}_{2,\mathrm{QED}}$ and of the approximations discussed above are shown in Fig. 7 for different values of $P^2 = 0, 0.01, 0.1$ and 1 GeV^2 and a moderate value of $Q^2 = 10$ GeV^2. Both, exact and approximate $F^{\gamma}_{2,\mathrm{QED}}$ are strongly suppressed with P^2. They agree with each other for small values of P^2, but start to differ for $P^2 \gtrsim 0.1$ GeV^2. The formula from Eq. 42 gives already rather bad approximation in the whole x range, whereas the other two approximations underestimate the exact result only in the large x region. This ends the discussion of the QED structure functions of the virtual photon and the rest of the paragraph is devoted to the QED structure functions of the real photon.

The differential cross-section given in Eq. 13 can be expressed in terms which have the same angular dependence with respect to the azimuthal angles χ and $\bar{\phi}$ (see Fig. 4 for the definition) and combinations thereof, using 13 structure functions as shown in [85]. In the case of the final state of the process $e^+e^- \to e^+e^- f\bar{f}$ being a pair of leptons it is experimentally possible to measure a triple differential cross section. By integrating over

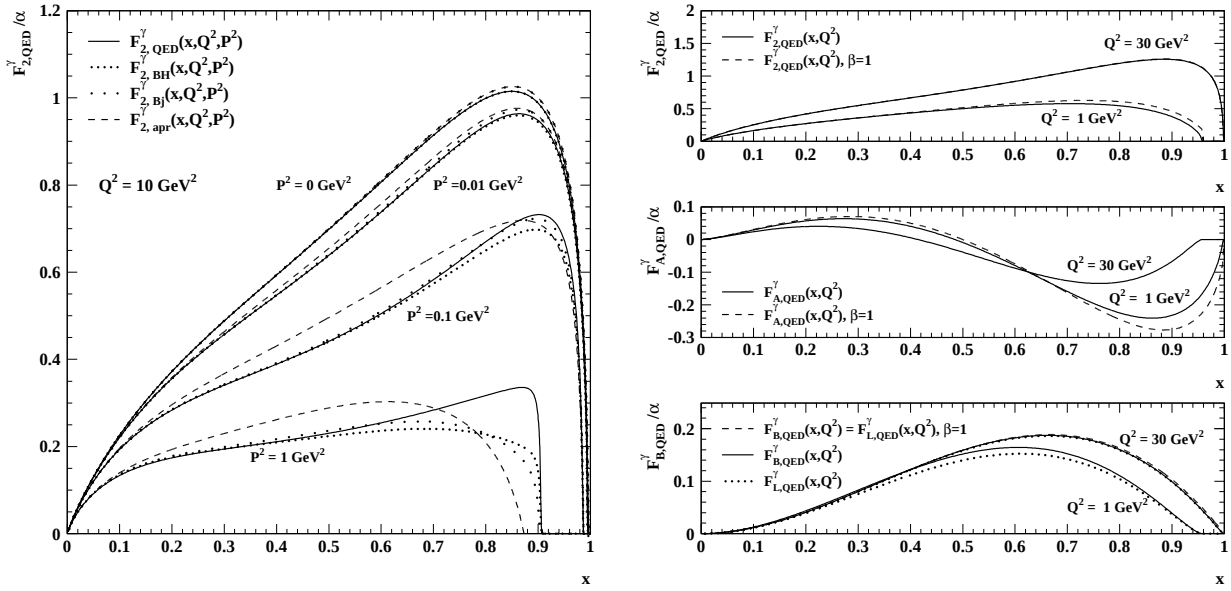

Figure 7: The structure function $F^{\gamma}_{2,\mathrm{QED}}$ for $\mu^+\mu^-$ final states based on double virtual box calculation (solid) and its approximations discussed in the text: the Bethe-Heitler expression (dense dots), the Bjorken limit (rare dots), the formula given in Eq. 42 (dash). The curves are plotted for $Q^2 = 10$ GeV^2 and for several values of $P^2 = 0, 0.01, 0.1, 1$ GeV^2.

Figure 8: The structure functions of the real photon $F^{\gamma}_{2,\mathrm{QED}}$, $F^{\gamma}_{\mathrm{A,QED}}$, $F^{\gamma}_{\mathrm{B,QED}}$ and $F^{\gamma}_{\mathrm{L,QED}}$ for $\mu^+\mu^-$ final states at $Q^2 = 1$ GeV^2 and 30 GeV^2 with full mass dependence (solid and dots) and in the leading logarithmic approximation discussed in the text (dash).

all angular dependences except the χ dependence, the cross section for deep inelastic eγ scattering can be written as:

$$\frac{d^3\sigma(\mathrm{e}\gamma \to \mathrm{eff})}{dx dQ^2 d\chi/2\pi} = \frac{2\pi\alpha^2}{xQ^4}\left(1+(1-y_\mathrm{e})^2\right)\Bigg[\; F^{\gamma}_{2,\mathrm{QED}} - (1-\epsilon(y_\mathrm{e}))F^{\gamma}_{\mathrm{L,QED}} - \rho(y_\mathrm{e})F^{\gamma}_{\mathrm{A,QED}}\cos\chi + \frac{1}{2}\epsilon(y_\mathrm{e})F^{\gamma}_{\mathrm{B,QED}}\cos 2\chi\Bigg] \tag{43}$$

where the functions $\rho(y_\mathrm{e}) = (2-y_\mathrm{e})\sqrt{1-y_\mathrm{e}}/(1+(1-y_\mathrm{e})^2)$ and $\epsilon(y_\mathrm{e}) = 2(1-y_\mathrm{e})/(1+(1-y_\mathrm{e})^2)$ are both close to unity for small values of y_e accessed at LEP. The above cross section is based on the structure functions of the real photon, $P^2 = 0$. The structure functions $F^{\gamma}_{2,\mathrm{QED}}$ and $F^{\gamma}_{\mathrm{L,QED}}$ can be obtained from the Eq. 26 and the cross sections given in Eq. 21. The structure functions $F^{\gamma}_{\mathrm{A,QED}}$ and $F^{\gamma}_{\mathrm{B,QED}}$ are new. They are proportional to the cross sections for the target photon to interact with different polarization states of the virtual photon: transverse–longitudinal interference (A) and interference between the two transverse polarizations (B). The formulae for the structure functions $F^{\gamma}_{\mathrm{A,QED}}$, $F^{\gamma}_{\mathrm{B,QED}}$, $F^{\gamma}_{\mathrm{L,QED}}$ and $F^{\gamma}_{2,\mathrm{QED}}$, which keep the full dependence on the lepton mass up to terms of order $\mathcal{O}(m^2/W^2)$, taken from [84] read:

$$F^{\gamma}_{\mathrm{A,QED}}(x,Q^2) = \frac{4\alpha}{\pi}x\sqrt{x(1-x)}(1-2x)\left\{\beta\left[1+(1-\beta^2)\frac{1-x}{1-2x}\right]\right.$$

$$
\begin{aligned}
&+\frac{3x-2}{1-2x}\sqrt{1-\beta^2}\arccos\left(\sqrt{1-\beta^2}\right)\Bigg\}\\
F^{\gamma}_{\mathrm{B,QED}}(x,Q^2) &= \frac{4\alpha}{\pi}x^2(1-x)\left\{\beta\left[1-(1-\beta^2)\frac{1-x}{2x}\right]\right.\\
&\left.+\frac{1}{2}(1-\beta^2)\left[\frac{1-2x}{x}-\frac{1-x}{2x}(1-\beta^2)\right]\ln\frac{1+\beta}{1-\beta}\right\}\\
F^{\gamma}_{\mathrm{L,QED}}(x,Q^2) &= \frac{\alpha}{\pi}x^2(1-x)\left[\beta-\frac{1}{2}(1-\beta^2)\ln\frac{1+\beta}{1-\beta}\right]\\
F^{\gamma}_{\mathrm{2,QED}}(x,Q^2) &= \frac{\alpha}{\pi}x\left\{\left[x^2+(1-x)^2\right]\ln\frac{1+\beta}{1-\beta}-\beta+8\beta x(1-x)-\beta(1-\beta^2)(1-x)^2\right.\\
&\left.+(1-\beta^2)(1-x)\cdot\left[\frac{1}{2}(1-x)(1+\beta^2)-2x\right]\ln\frac{1+\beta}{1-\beta}\right\} \qquad (44)
\end{aligned}
$$

where $\beta=\sqrt{1-\frac{4m^2}{W^2}}=\sqrt{1-\frac{4m^2}{Q^2}\frac{x}{1-x}}$. These are in fact the familiar massive Bethe-Heitler expressions for the real photon. The structure functions in the leading logarithmic approximation can be obtained from Eq. 44 in the limit $\beta\to 1$. They have the following form:

$$
\begin{aligned}
F^{\gamma}_{\mathrm{A,QED}}(x,Q^2) &= \frac{4\alpha}{\pi}x\sqrt{x(1-x)}(1-2x)\\
F^{\gamma}_{\mathrm{B,QED}}(x,Q^2) &= F^{\gamma}_{\mathrm{L,QED}}(x,Q^2)=\frac{4\alpha}{\pi}x^2(1-x)\\
F^{\gamma}_{\mathrm{2,QED}}(x,Q^2) &= \frac{\alpha}{\pi}x\left\{\left[x^2+(1-x)^2\right]\ln\frac{W^2}{m^2}-1+8x(1-x)\right\} \qquad (45)
\end{aligned}
$$

The formulae for $F^{\gamma}_{\mathrm{2,QED}}$ and $F^{\gamma}_{\mathrm{L,QED}}$ in the leading logarithmic approximation are related to the cross sections listed in Section 3 through the Eq. 26 and the cross sections given in Eq. 23. In the above approximation only $F^{\gamma}_{\mathrm{2,QED}}$ has a non-trivial dependence on Q^2. It must be noted, that although in the above leading logarithmic approximation the structure functions $F^{\gamma}_{\mathrm{B,QED}}$ and $F^{\gamma}_{\mathrm{L,QED}}$ are accidentally described by the same function of x, they involve different photon helicity structures. In $F^{\gamma}_{\mathrm{B,QED}}$ the photons are purely transverse. The comparison of the structure functions $F^{\gamma}_{\mathrm{A,QED}}$, $F^{\gamma}_{\mathrm{B,QED}}$, $F^{\gamma}_{\mathrm{2,QED}}$ and $F^{\gamma}_{\mathrm{L,QED}}$ obtained with mass dependent terms (Eq. 44) and in the leading logarithmic approximation (Eq. 45) is shown in Fig. 8 for two values of $Q^2=1$ GeV^2 and 30 GeV^2. The approximation is rather good in the case of $F^{\gamma}_{\mathrm{2,QED}}$, but for the structure functions $F^{\gamma}_{\mathrm{A,QED}}$ and $F^{\gamma}_{\mathrm{B,QED}}$ the difference between the exact and approximate formulas is significant especially in the high x region and for low values of Q^2. One can also see that the structure functions $F^{\gamma}_{\mathrm{B,QED}}$ and $F^{\gamma}_{\mathrm{L,QED}}$ are very close to each other in the whole x and Q^2 ranges considered here, also when the mass dependent terms are taken into account. Therefore the measurement of $F^{\gamma}_{\mathrm{B,QED}}$ gives a good estimate of the longitudinal structure function $F^{\gamma}_{\mathrm{L,QED}}$ which is not measured by experiments.

4.3 Hadronic structure functions of the photon

The hadronic structure of the photon follows from the quantum fluctuation of the photon into a pair of quarks. In general both the real and the virtual photon possess a parton

content. One expects that the parton distributions of the virtual photon in the limit of $P^2 = 0$ smoothly transform into the parton distributions of the real photon. Formally the treatments of the real and the virtual photons are similar, although they differ in the boundary conditions used for the calculation of the parton distribution functions. In the following we discuss the more general case, the virtual photon, pointing out the differences with respect to the real photon. The discussion is concentrated on transverse (real and virtual) photons and only a short notice on the longitudinal photons will be given at the end of this paragraph. That means we require that $P^2 \ll Q^2$ to guarantee that the physical cross sections are dominated by the transverse target photon contributions. The discussion presented in this paragraph is mainly based on the following publications [23, 27, 74, 101].

The predictions for the structure functions F_2^γ and F_L^γ in the quark parton model (QPM) approximation can be obtained from the formulae for the QED structure functions discussed in the previous paragraph by formally multiplying them by $N_c \sum_{k=1}^{n_f} e_{q_k}^4$, where N_c is the number of colours, e_{q_k} is the electric charge of the flavour q_k and the sum runs over all active flavours n_f. As an example let us rewrite here the leading logarithmic results, which in case of QED were given in Eq. 45. They take the following form:

$$F_{2,\mathrm{QPM}}^\gamma(x,Q^2) = \frac{N_c\,\alpha}{\pi} \sum_{k=1}^{n_f} e_{q_k}^4 x \left\{ \left[x^2 + (1-x)^2\right] \ln \frac{W^2}{m_{q_k}^2} - 1 + 8x(1-x) \right\}$$
$$F_{\mathrm{L,QPM}}^\gamma(x,Q^2) = \frac{4N_c\,\alpha}{\pi} \sum_{k=1}^{n_f} e_{q_k}^4 x^2(1-x) \tag{46}$$

The above QPM result for F_2^γ is valid for the real photon. In case of the virtual photon, its virtuality P^2 can act as the regulator and no quark masses have to be introduced. Taking the limit $P^2/Q^2 \to 0$ in Eq. 40 whenever possible we obtain [21, 22]:

$$F_{2,\mathrm{QPM}}^\gamma(x,Q^2,P^2) = \frac{N_c\,\alpha}{\pi} \sum_{k=1}^{n_f} e_{q_k}^4 x \left\{ \left[x^2 + (1-x)^2\right] \ln \frac{Q^2}{x^2\,P^2} - 2 + 6x(1-x) \right\} \tag{47}$$

The structure function $F_{\mathrm{L,QPM}}^\gamma$ does not need a regulator and remains unchanged. It should be noted that the virtual photon structure functions are kinematically constrained within $0 \le x \le (1 + P^2/Q^2)^{-1}$ [22]. It is also worth of pointing out here that the QPM results already predict a logarithmic evolution of the photon structure function F_2^γ with Q^2. This is in contrast to the behaviour of the proton (or hadron in general) structure function F_2^p, in case of which the scaling violations appear only due to the QCD corrections. The reason of this different behaviour is the point-like coupling of the photon to quarks. It leads to the rise of F_2^γ towards large values of x, where the proton structure function F_2^p decreases. This point-like coupling also results in the positive scaling violation of F_2^γ for all values of x, whereas F_2^p exhibits positive scaling violations at small values of x (caused by quark pairs production from gluons) and negative scaling violations at large values of x (caused by gluon radiation). In case of the photon, the direct production of quark pairs at large values of x is more efficient than the loss of quarks in that region due to gluon radiation.

Due to the QCD corrections the leading order QED results given in Eq. 46 and Eq. 47 are not sufficient. For the purpose of the following discussion it is useful to decompose the

hadronic photon structure functions into parts corresponding to light $F_{i,l}^{\gamma}$ and heavy $F_{i,h}^{\gamma}$ quarks:

$$F_i^{\gamma}(x,\, Q^2,\, P^2) = F_{i,l}^{\gamma}(x,\, Q^2,\, P^2) + F_{i,h}^{\gamma}(x,\, Q^2,\, P^2) \tag{48}$$

where $i = 2, L$. In terms of the parton distribution functions in the photon, the structure functions for the light quarks are given in next-to-leading order (NLO) QCD in the modified minimal subtraction factorization scheme ($\overline{\rm MS}$) by (see e.g. [27]):

$$\begin{aligned} F_{i,l}^{\gamma}(x,\, Q^2,\, P^2) = 2x \sum_{k=1}^{3} e_{q_k}^2 \Bigg\{ & q_k^{\gamma}(x, Q^2, P^2) + \frac{\alpha}{2\pi} e_{q_k}^2 C_{i,\gamma}(x) + \\ & \frac{\alpha_s(Q^2)}{2\pi} \int_x^1 \frac{dy}{y} \left(C_{i,q}\left(\frac{x}{y}\right) q_k^{\gamma}(y,\, Q^2,\, P^2) + C_{i,g}\left(\frac{x}{y}\right) g^{\gamma}(y,\, Q^2,\, P^2) \right) \Bigg\} \end{aligned} \tag{49}$$

where the quark $q_k^{\gamma}(x,\, Q^2,\, P^2)$ and gluon $g^{\gamma}(x,\, Q^2,\, P^2)$ parton densities provide the hadron-like contributions of the photon to F_2^{γ}, while $C_{i,\gamma}$ provides the point-like contribution. Note that due to charge conjugation invariance $\bar{q}_k^{\gamma}(x, Q^2, P^2) = q_k^{\gamma}(x, Q^2, P^2)$. The running strong coupling constant $\alpha_s(Q^2)$ in NLO is given by:

$$\frac{\alpha_s(Q^2)}{4\pi} \simeq \frac{1}{\beta_0 \ln Q^2/\Lambda^2} - \frac{\beta_1}{\beta_0^3} \frac{\ln\ln Q^2/\Lambda^2}{(\ln Q^2/\Lambda^2)^2} \tag{50}$$

with $\beta_0 = 11 - 2n_f/3$, $\beta_1 = 102 - 38n_f/3$. For Q^2 values much larger than Λ^2, the effective coupling is small and a perturbative description in terms of quarks and gluons interacting weakly makes sense. For Q^2 of order of Λ^2 we can not make such a picture, since quarks and gluons will arrange themselves into strongly bound clusters (hadrons). The value of Λ is not predicted by the theory: it is a free parameter to be determined from experiment. It is of order of typical hadronic mass with a value somewhere in the range 0.1 – 0.5 GeV. The Wilson coefficient functions $C_{i,q}$, $C_{i,g}$ and $C_{i,\gamma}$ are given by [28, 29, 101]:

$$C_{2,q}(x) = \frac{4}{3}\left[\frac{1+x^2}{(1-x)_+} \left(\ln\frac{1-x}{x} - \frac{3}{4} \right) + \frac{1}{4}(9+5x) \right], \qquad C_{L,q}(x) = \frac{8}{3}x\,, \tag{51}$$

$$C_{2,g}(x) = \frac{1}{2}\left\{ [x^2 + (1-x)^2] \ln\frac{1-x}{x} - 1 + 8x(1-x) \right\}, \quad C_{L,g}(x) = 2x(1-x)\,, \tag{52}$$

$$C_{2,\gamma}^{\overline{MS}}(x) = \frac{3}{1/2} C_{2,g}(x)\,, \qquad C_{L,\gamma}^{\overline{MS}}(x) = \frac{3}{1/2} C_{L,g}(x)\,. \tag{53}$$

The regularized function $(1-x)_+^{-1}$ in $C_{2,q}$ is defined by the so called *plus prescription*:

$$\int_0^1 dx \frac{f(x)}{(1-x)_+} \equiv \int_0^1 dx \frac{f(x) - f(1)}{(1-x)} \tag{54}$$

In next-to-leading order there exist a freedom in the definition of terms belonging to the parton density functions and the terms which are included in the hard scattering matrix elements. The different choices, called factorization schemes, make that physics quantities, like F_2^{γ}, calculated in fixed order perturbation theory can differ by finite terms (see e.g. [95]). These ambiguities disappear only when the calculations are performed to all orders. There

are two commonly used factorization schemes for the photon structure function: the $\overline{MS}$ scheme and the DIS$_\gamma$ scheme. In the original DIS scheme, introduced for the proton, all higher order corrections have been absorbed into the definition of the quark distribution functions, so that F_2^p was proportional in all orders in α_s to the quark distribution functions. In case of photon, in the DIS$_\gamma$ scheme only the $C_{2,\gamma}$ term has been absorbed into the NLO ($\overline{MS}$) quark densities, so that:

$$q^\gamma_{k,DIS_\gamma} = q^\gamma_{k,\overline{MS}} + \frac{\alpha}{2\pi} e^2_{q_k} C^{\overline{MS}}_{2,\gamma}, \quad C^{DIS_\gamma}_{2,\gamma} = 0 \tag{55}$$

$$g^\gamma_{DIS_\gamma} = g^\gamma_{\overline{MS}} \tag{56}$$

Note that $C_{L,\gamma}$ is the same in the $\overline{MS}$ and DIS$_\gamma$ schemes. The LO expressions for F_i^γ can be obtained from Eq. 49 dropping all higher order terms $C_{q,g,\gamma}$ and the term proportional to β_1 in Eq. 50.

The above discussion applies only to the light quarks u, d, s. Due to the large scale introduced by the heavy quark masses, their contribution to the photon structure function have to be calculated in fixed order perturbation theory and can be expressed as a sum of a point-like (pl) and a hadron-like (hl) parts:

$$F^\gamma_{i,h}(x,Q^2,P^2) = F^{\gamma,pl}_{i,h}(x,Q^2,P^2) + F^{\gamma,hl}_{i,h}(x,Q^2,P^2) \tag{57}$$

This is schematically shown in Fig. 9. The point-like contribution can be approximated by the Bethe-Heitler formula (the lowest order QED result for doubly virtual box diagram) given in Eq. 41 multiplied by $N_c\, e_q^4$. The relevant expressions for $F^{\gamma,pl}_{2,h}$ and $F^{\gamma,pl}_{L,h}$ read:

$$\begin{aligned} F^{\gamma,pl}_{2,h}(x,Q^2,P^2) = N_c \frac{e_q^4\,\alpha}{\pi} x \Bigg\{ & [x^2+(1-x)^2] \ln\frac{1+\beta\bar{\beta}}{1-\beta\bar{\beta}} - \beta + 6\beta x(1-x) \\ & + \left[2x(1-x) - \frac{1-\bar{\beta}^2}{1-\beta^2} - (1-\beta^2)(1-x)^2\right] \frac{\beta\bar{\beta}(1-\beta^2)}{1-\beta^2\bar{\beta}^2} \\ & + (1-\beta^2)(1-x)\left[\frac{1}{2}(1-x)(1+\beta^2) - 2x\right] \ln\frac{1+\beta\bar{\beta}}{1-\beta\bar{\beta}} \Bigg\} \end{aligned} \tag{58}$$

$$F^{\gamma,pl}_{L,h}(x,Q^2,P^2) = N_c \frac{e_q^4\,\alpha}{\pi} x^2(1-x)\left[\beta - \frac{1}{2}(1-\beta^2)\ln\left(\frac{1+\beta\bar{\beta}}{1-\beta\bar{\beta}}\right)\right] \tag{59}$$

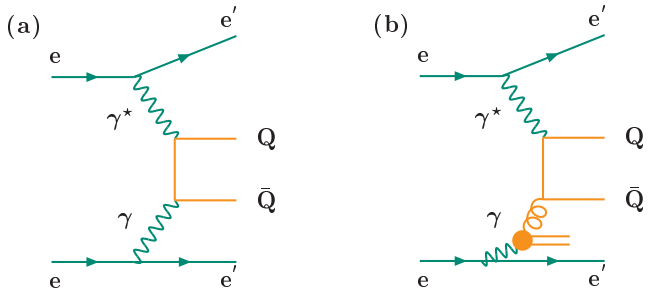

Figure 9: Leading order diagrams of the point-like (a) and hadron-like (b) contribution to the heavy quark structure function of the photon $F^\gamma_{2,h}$.

In principle one should use here the NLO formulas. However the NLO expressions have been only calculated so far for the real photon and they were found to make only a small correction comparable to the ambiguities due to different choices of the mass of heavy flavours [26]. The resolved heavy quark contribution to the photon structure functions is calculated via the process $\gamma^\star g \to Q\bar{Q}$ shown in Fig. 9b with $f_i^{\gamma^\star g\to Q\bar{Q}}(x, Q^2, P^2)$ given by Eq. 58 or Eq. 59 and with $e_q^2\alpha$ replaced by $e_q^2\alpha_s(\mu_F^2)/6$:

$$F_{i,h}^{\gamma,hl}(x,\, Q^2,\, P^2) = \int_{z_{min}}^{z_{max}} \frac{dz}{z} z g^\gamma(z, \mu_F^2, P^2) f_i^{\gamma^\star g\to Q\bar{Q}}\left(\frac{x}{z},\, Q^2,\, P^2\right) \tag{60}$$

where $z_{min} = x(1 + 4m_Q^2/Q^2 + P^2/Q^2)$ and $z_{max} = (1 + P^2/Q^2)^{-1}$. Here g^γ represents the gluon distribution function in the appropriate order, and the factorization scale μ_F^2 can be chosen as $\mu_F^2 \simeq 4m_h^2$ [24] or $\mu_F^2 = Q^2 + 4m_h^2$ [25] (in the later case the relation $\mu_F^2 \gg P^2$ is fulfilled also for large P^2).

The quark, gluon and photon distribution functions in the transverse photon, denoted by q_k^γ, g^γ and Γ^γ, respectively, obey the following inhomogeneous Dokshitzer-Gribov-Lipatov-Altarelli-Parisi (DGLAP) [51] evolution equations for the massless parton densities:

$$\begin{aligned}
\frac{\partial q_i^\gamma}{\partial \ln Q^2} &= \bar{P}_{q\gamma} \otimes \Gamma^\gamma + 2\sum_{k=1}^{n_f} \bar{P}_{qq} \otimes q_k^\gamma + \bar{P}_{qg} \otimes g^\gamma \\
\frac{\partial g^\gamma}{\partial \ln Q^2} &= \bar{P}_{g\gamma} \otimes \Gamma^\gamma + 2\sum_{k=1}^{n_f} \bar{P}_{gq} \otimes q_k^\gamma + \bar{P}_{gg} \otimes g^\gamma \\
\frac{\partial \Gamma^\gamma}{\partial \ln Q^2} &= \bar{P}_{\gamma\gamma} \otimes \Gamma^\gamma + 2\sum_{k=1}^{n_f} \bar{P}_{\gamma q} \otimes q_k^\gamma + \bar{P}_{\gamma g} \otimes g^\gamma
\end{aligned} \tag{61}$$

where the explicit dependence of the distribution functions on x, Q^2 and P^2 has been omitted. The symbol $\otimes$ stands for the convolution integral:

$$(f \otimes g)(x) = \int_x^1 \frac{dy}{y} f\left(\frac{x}{y}\right) g(y)\,. \tag{62}$$

The Altarelli-Parisi evolution kernels $\bar{P}_{ij}$ are generalized splitting functions:

$$\bar{P}_{ij}(y, \alpha, \alpha_s) = \sum_{l,m=0}^{\infty} \frac{\alpha^l \alpha_s^m}{(2\pi)^{l+m}} P_{ij}^{(l,m)}(y)\,. \tag{63}$$

Since the electromagnetic coupling constant is small we can neglect terms of order $\mathcal{O}(\alpha^2)$ as well as the dependence of α on Q^2 in the evolution equations given in Eq. 61. The parton distribution functions q^γ and g^γ are already of order $\mathcal{O}(\alpha)$ and therefore we can set $l = 0$ in all generalized evolution kernels $\bar{P}_{ij}$ which are multiplied by these parton densities. In case of $\bar{P}_{q\gamma}$, $\bar{P}_{g\gamma}$ and $\bar{P}_{\gamma\gamma}$ the only contributions of order $\mathcal{O}(\alpha)$ come from setting $l = 1$ in Eq. 63. The terms proportional to $P_{\gamma q}$ and $P_{\gamma g}$ are necessarily of order $\mathcal{O}(\alpha^2)$ and can be dropped.

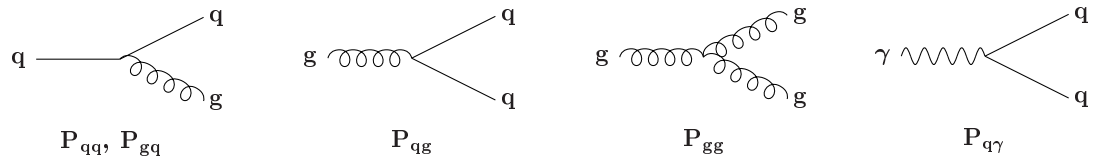

Figure 10: Diagrams illustrating the DGLAP splitting functions in the leading order.

In consequence the evolution equation for the photon distribution Γ^γ decouples and can be solved separately (see e.g. [23]). The remaining evolution equation can be written as:

$$\frac{\partial q_k^\gamma}{\partial \ln Q^2} = \frac{\alpha}{2\pi} P_{q\gamma} + \frac{\alpha_s(Q^2)}{2\pi}\left[P_{qq}\otimes q_k^\gamma + P_{qg}\otimes g^\gamma\right],$$
$$\frac{\partial g^\gamma}{\partial \ln Q^2} = \frac{\alpha}{2\pi} P_{g\gamma} + \frac{\alpha_s(Q^2)}{2\pi}\left[\sum_{k=1}^{n_f} P_{gq}\otimes q_k^\gamma + P_{gg}\otimes g^\gamma\right]. \tag{64}$$

The hadronic splitting functions $P(x,Q^2)$ receive the following LO and NLO QCD contributions:

$$P(y,Q^2) = P^{(0)}(y) + \frac{\alpha_s(Q^2)}{2\pi} P^{(1)}(y) \tag{65}$$

In the LO QCD the following parton splittings occur: $q\to qg$, $q\to gq$, $g\to q\bar{q}$, $g\to gg$. They are schematically shown in Fig. 10 and are described by the following formulae [30,31]:

$$P^{(0)}_{q\gamma}(y) = N_c\, e^4_{q_k}[y^2+(1-y)^2], \qquad P^{(0)}_{q_iq_k}(y) = \delta_{ik}\left[\frac{4}{3}\frac{1+y^2}{(1-y)_+} + 2\delta(1-y)\right],$$
$$P^{(0)}_{qg}(y) = \frac{1}{2}\left[y^2+(1-y)^2\right], \qquad P^{(0)}_{gq}(y) = \frac{4}{3}\frac{1+(1-y)^2}{y}, \qquad P^{(0)}_{g\gamma}(y) = 0,$$
$$P^{(0)}_{gg}(y) = 6\left[\frac{1-y}{y} + \frac{y}{(1-y)_+} + y(1-y) + \left(\frac{11}{12} - \frac{n_f}{18}\right)\delta(1-y)\right]. \tag{66}$$

The expressions for the splitting functions in NLO can be found e.g. in [31, 32].

For completeness let us make a short notice on the longitudinal target photon. Formally one can apply all the considerations of this paragraph to longitudinal photons setting $\Gamma^{\gamma_L}(x,Q^2,P^2) = 0$ [33]. This condition follows from the the fact that to order $\mathcal{O}(\alpha)$ there is no transverse photon inside the longitudinal target photon. In consequence the quark and gluon distribution functions of the longitudinal photon satisfy homogeneous evolution equations [33].

4.4 Parton distribution functions in the photon

There are many parameterizations of parton distribution functions in the photon available today, constructed in the leading and/or next-to-leading order. Most of them are valid only for the real photon, but few have been also constructed for the virtual photon ($P^2 \gtrsim \Lambda^2$).

Below we discuss shortly the main features of the most popular parameterizations. If not said explicitly a parameterization is valid for the real photon and is constructed in DIS_γ factorization scheme. The names of the parameterizations are usually constructed from the first letters of the names of their authors. For more details the reader is referred to the original publications or to the summary given e.g. in [7].

1. **DG – Drees and Grassie [92]:** This is the oldest parameterization of parton distributions in the photon. The parameterization is based on the solution of the leading order evolution equations. The x dependent input parton distributions, with free parameters, were assumed at $Q_0^2 = 1$ GeV^2 and fitted to the only data available at that time from PLUTO at $Q_0^2 = 5.3$ GeV^2 [122]. Due to limited statistics further assumptions have been made: $q_d^\gamma = q_s^\gamma$, $q_u^\gamma = q_c^\gamma$, and the input gluon distribution function has been set to zero, which means that gluons are generated purely dynamically. The charm and bottom quarks are treated as massless, and are included only for $Q^2 > 20$ GeV^2 and $Q^2 > 200$ GeV^2, respectively, by means of the number of flavours n_f used in the evolution equations. The user can choose from three independent sets constructed for $n_f = 3, 4, 5$.

2. **LAC – Levy, Abramowicz, Charchuła [93]:** The parameterisation is based on the solution of the leading order evolution equations. The input parton distributions of the form:

$$\begin{aligned} xq_0(x, Q_0^2) &= Ae_q^2 x \frac{x^2 + (1-x)^2}{1 - B\ln(1-x)} + Cx^D(1-x)^E \\ xg_0(x, Q_0^2) &= C_g x^{D_g}(1-x)^{E_g} \end{aligned} \tag{67}$$

were assumed at $Q_0^2 = 4$ GeV^2 (sets LAC1 and LAC2) or at $Q_0^2 = 1$ GeV^2 (set LAC3) and were fitted to the available data. The sets LAC1 and LAC2 differ in the gluon distribution function – in LAC2 the parameter D_g is set to zero. The first and second terms in the quark distribution function correspond to the point-like and hadron-like parts, respectively. The charm quark is treated as massless and its contribution is only included for $W^2 > 4m_c^2$. No parton distribution for the bottom quark is available.

3. **WHIT – Watanabe, Hagiwara, Izubuchi, Tanaka [94]:** The parametrisation is based on the solution of the leading order evolution equations. The initial parton distributions for three light flavours are assumed at $Q_0^2 = 4$ GeV^2. The contribution from charm quarks ($m_c = 1.5$ GeV) is added according to the Bethe–Heitler formula for $Q^2 < 100$ GeV^2 or by using the massive–quark evolution equations for $Q^2 > 100$ GeV^2. No parton distribution function for bottom quarks is available. The parametrisation is essentially a study of the sensitivity of the photon structure function to the gluon content of the photon. The initial gluon distribution is parametrized by the simple formula $xg_0(x, Q_0^2)/\alpha = A_g(C_g+1)(1-x)^{C_g}$. The available data are not accurate enough to determine the gluon parameters A_g and C_g. Therefore the authors provide six parton distributions which have systematically different gluon contents: WHIT1-3 ($A_g = 0.5$) and WHIT4-6 ($A_g = 1$) and in both cases $C_g = 3, 9, 15$.

4. **GRV – Glück, Reya, Vogt [74]:** The parton distribution functions are available in leading order and in next-to-leading order. They are evolved from low starting scales ($Q_0^2 = 0.25$ GeV^2 in LO and $Q_0^2 = 0.3$ GeV^2 in NLO) using a VMD input based on measurement

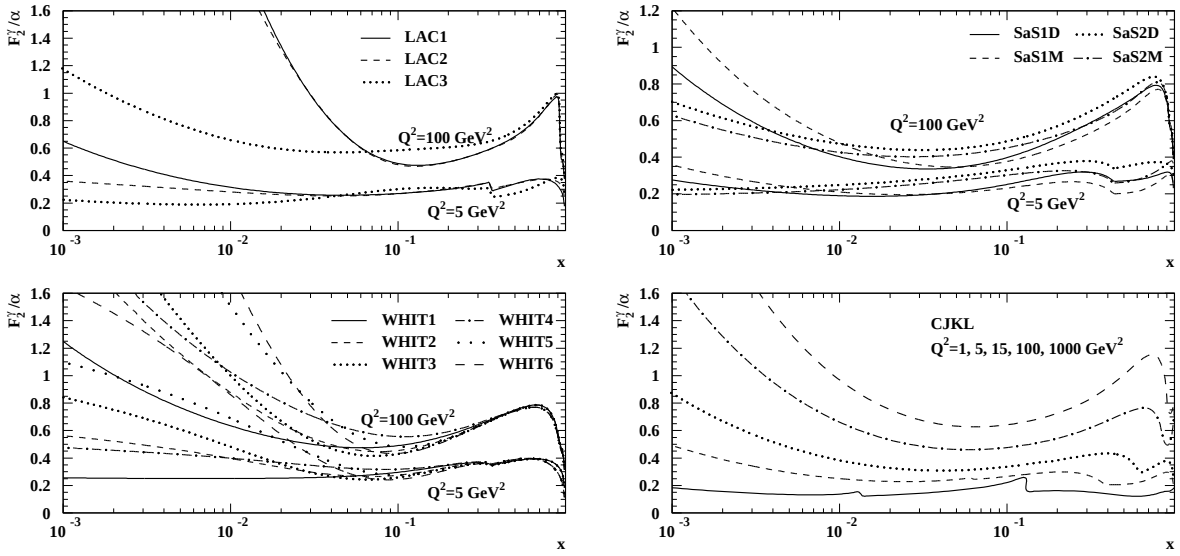

Figure 11: The photon structure function F_2^γ divided by the fine structure constant obtained from different parton distribution functions. Shown are predictions from different sets of LAC, WHIT and SaS parameterizations at two values of $Q^2 = 5, 100$ GeV^2 and from the CJKL parameterization for $Q^2 = 1, 5, 15, 100, 1000$ GeV^2.

of the pion structure function of the form $q(x, Q_0^2) = g(x, Q_0^2) = \kappa(4\pi\alpha/f_\rho^2) f_\pi(x, Q_0^2$ where $xf_\pi \sim x^a(1-x)^b$ and $1/f_\rho^2 = 2.2$. The similarity of the ρ and π mesons is assumed and a proportionality factor $1 \leq \kappa \leq 2$ is used to account for the inclusion of ω, ϕ and other high mass vector mesons. The point-like contribution is chosen to vanish at the input scale and for higher virtualities is generated dynamically using the full evolution equations. The charm and bottom quarks are included via the Bethe-Heitler formula with $m_c = 1.5$ GeV and $m_b = 4.5$ GeV.

5. **AFG – Aurenche, Fontannaz, Guillet [95]:** The parametrisation is available only in the next-to-leading order. Similarly as in the GRV parametrisation the point-like contribution vanishes at the low starting scale chosen at $Q_0^2 = 0.5$ GeV^2 and the purely hadron-like input is based on VMD arguments, where a coherent sum of low mass vector mesons ρ, ω and ϕ is used. The evolution is performed in the massless scheme for three flavours for $Q^2 < m_c^2 = 2$ GeV^2 and for four flavours for $Q^2 > m_c^2$. No parton distribution function for bottom quarks is available. The AFG parton distributions are constructed in the $\overline{MS}$ factorization scheme.

6. **CJKL – Cornet, Jankowski, Krawczyk, Lorca [96]:** This is the most recent parameterization. A global, three parameter fit to all data available today is performed based on the leading order evolution equations. The idea of radiatively generated parton distributions similar to the one used in GRV parameterization is exploited. The starting scale is chosen at $Q_0^2 = 0.25$ GeV^2. However, input densities of the ρ^0 meson are not approximated by the pionic ones, but instead the valence-like and gluon densities of the form $xv^\rho(x, Q_0^2) = N_v x^\alpha (1-x)^\beta$ and $xg(x, Q_0^2) = N_g x^\alpha (1-x)^\beta$ are used. All sea quark distri-

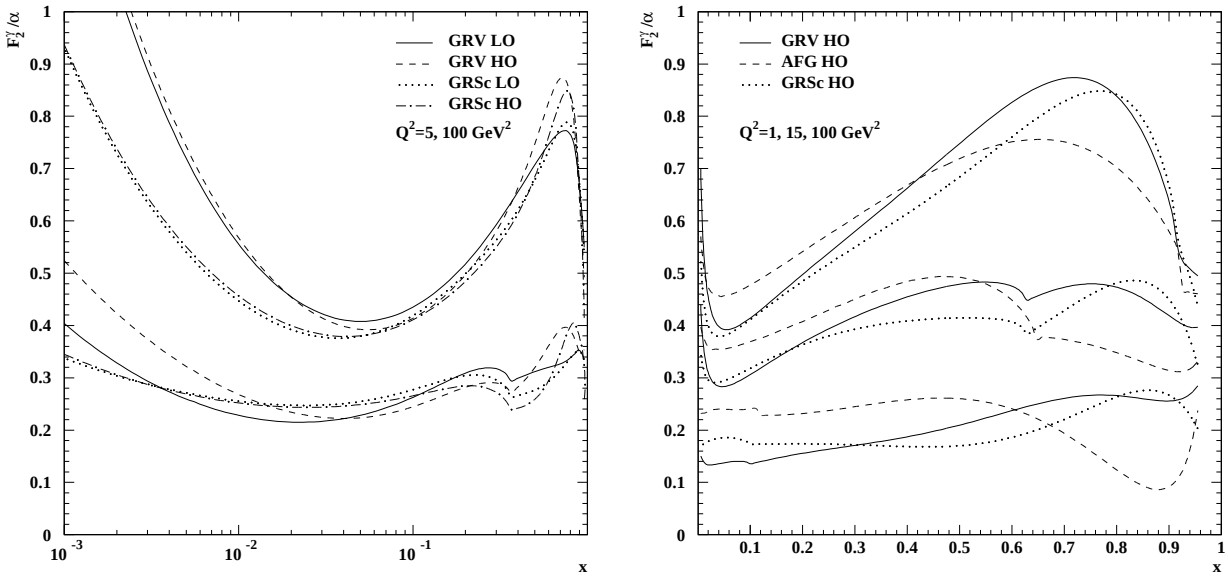

Figure 12: The photon structure function F_2^γ divided by the fine structure constant obtained from different parton distribution functions. Predictions of LO and HO GRV and GRSc parameterization for two values of $Q^2 = 5, 100$ GeV^2 are shown on the left and the comparison of HO predictions from GRV, GRSc and AFG parameterizations at $Q^2 = 1, 15, 100$ GeV^2 is shown on the right.

butions are neglected at the input scale. The special treatment of heavy quarks based on the $ACOT(\chi)$ prescription [97], originally introduced for the proton structure function is adopted to the photon structure function for the first time. It means essentially an improvement of the treatment of the threshold region $W \approx 2m_h$ where usually the Bethe-Heitler formula is used.

7. **GRS – Glück, Reya, Stratmann [101]:** The parameterization is an extension of the phenomenologically successful GRV photon densities [74] to non-zero P^2 in LO and NLO. Similarly as in GRV, at low input scale $Q_0^2 \approx 0.25$ GeV^2, the parton densities of real photons are given by a VMD inspired input. A simple prescription which smoothly interpolates between $P^2 = 0$ and $P^2 \gg \Lambda^2$ is used:

$$f^{\gamma(P^2)}(x, Q^2 = \tilde{P}^2) = \eta(P^2) f^{\gamma(P^2)}_{non-pert}(x, \tilde{P}^2) + [1 - \eta(P^2)] f^{\gamma(P^2)}_{pert}(x, \tilde{P}^2) \tag{68}$$

with $\tilde{P}^2 = \max(P^2, \mu^2)$ and $\eta(P^2) = (1 - P^2/m_\rho^2)^{-2}$ where m_ρ is some effective mass in the vector meson propagator. The VMD-like non-perturbative input is taken to be proportional to the GRV pion densities $f^{\gamma(P^2)}_{non-pert}(x, \tilde{P}^2) = \kappa(4\pi\alpha/f_\rho^2) f^\pi(x, \tilde{P}^2)$. Heavy quarks do not take part in the Q^2 evolution and they must be taken into account using Bethe-Heitler formula. For real photons it is known up to NLO and can be found in [26]. For non-zero P^2 they are available only in LO and the relevant cross sections are given in Eq. 15.

8. **GRSc – Glück, Reya, Schienbein [27]:** The parton distribution functions are constructed for the real photon in LO and NLO and for the virtual photon in LO, which within

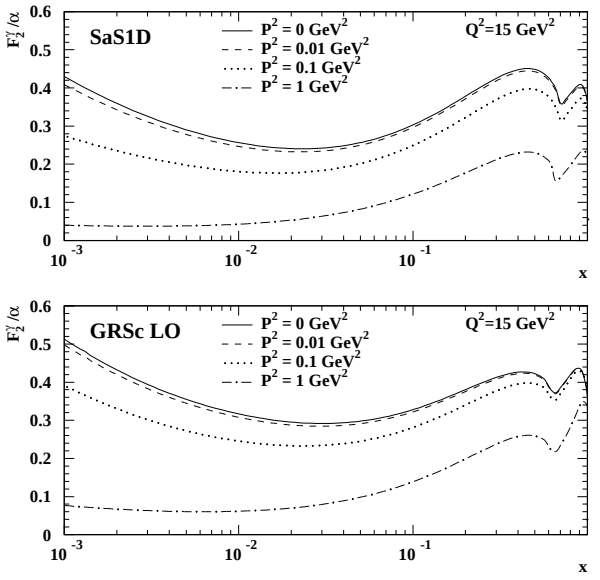

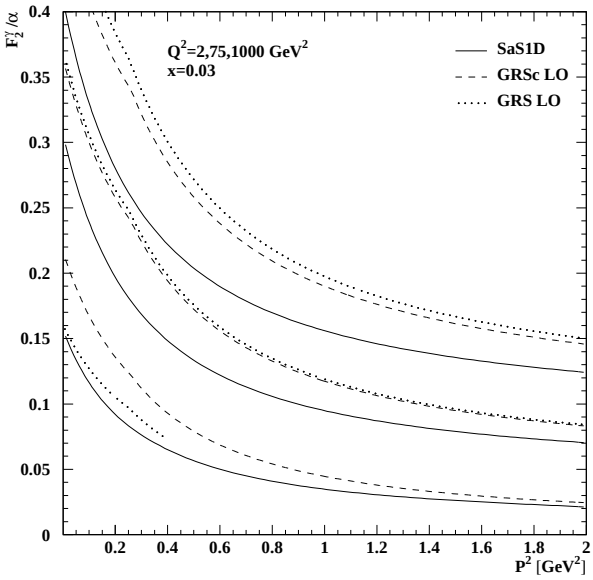

Figure 13: The photon structure function F_2^γ divided by the fine structure constant of the virtual photon. The predictions of SaS1D and GRSc parameterizations for $Q^2 = 15$ GeV^2 and for different virtualities of the target photons $P^2 = 0, 0, 01, 0.1, 1$ GeV^2.

Figure 14: The P^2 dependence of F_2^γ/α predicted by SaS1D, GRSc and GRS parameterizations at a medium $x = 0.03$ and three values of $Q^2 = 2, 75, 1000$ GeV^2.

sufficient accuracy may be also used in NLO. A consistent set of boundary conditions have been formulated, which allow for a calculation of $f^\gamma(x,\, Q^2,\, P^2)$ also in NLO QCD as well as for a smooth transition from the virtual to the real photon. The parameterization is based on the same general ideas as the GRV parameterization. However, in contrast to GRV, the coherent sum of vector mesons is used in VMD to describe the hadronic components of the photon, with the recently updated parton distribution of the pion [101]. The charm quark mass has been changed to $m_c = 1.4$ GeV.
In case of virtual photons it is assumed that the effects of the photon virtuality are entirely taken into account by the flux factors, which are valid for $Q^2 \gg P^2$. In consequence, in contrast to GRS parameterization, all partonic cross sections are calculated as if $P^2 = 0$. In particular, the process $\gamma\gamma^\star \to q\bar{q}$ is used to evaluate $C_\gamma(x)$, instead of the process $\gamma^\star\gamma^\star \to q\bar{q}$ and charm contribution for $P^2 > 0$ is based on the Bethe-Heitler formula for the real photon.

9. **SaS – Schuler, Sjöstrand [102,103]:** The parameterization is based on the solution of the leading order evolution equations for three massless flavours. Two sets were constructed with different starting scales: $Q_0^2 = 0.36$ GeV^2 (SaS1) and $Q_0^2 = 4$ GeV^2 (SaS2). Each set is available in the $\overline{MS}$ (set M) and DIS_γ (set D) factorization schemes. The set SaS2 contains a larger VMD contribution in comparison to the set SaS1, which is necessary in order to fit the data due to a much larger starting scale Q_0^2.
The extension to non-zero P^2 is based on a dispersion-integral in the mass of $q\bar{q}$ fluctuations, which links perturbative and non-perturbative contributions [102, 103]. The $q\bar{q}$ fluctuations

are separated into a discrete sum of vector meson states and a high mass continuous perturbative spectrum from the point-like contribution. Both terms are suppressed by different P^2-dependent terms.
The contributions from the charm ($m_c = 1.3$ GeV) and bottom ($m_b = 4.6$ GeV) quarks are taken into account via the Bethe–Heitler formula taking into account full P^2 dependence.

The parameterizations of the parton distribution functions discussed above are used to construct the photon structure function F_2^γ. They are compared below for several values of the probe and target photon virtualities.

In Fig. 11 the structure function F_2^γ for the real photon constructed from the parton distribution functions predicted by different sets of LAC, WHIT and SaS parameterizations are shown for two values of $Q^2 = 5$ and 100 GeV^2, and by the CJKL parameterization for $Q^2 = 1, 5, 15, 100, 1000$ GeV^2. The predictions of LAC and WHIT parameterizations are very similar at large values of x. However, they start to differ significantly at low values of x where the value of the starting scale Q_0^2 and the shape of the input distribution of gluons become important.

The structure functions F_2^γ for the real photon constructed from parton distribution functions predicted by the leading order (LO) and next-to-leading order (HO) GRV and GRSc parameterizations are shown in Fig. 12 for two values of $Q^2 = 5, 100$ GeV^2. At the lower value of Q^2 the LO and HO GRV predictions are rather different in whole x range. In case of GRSc the LO and HO predictions are very similar for $x < 0.1$ and differ only at large values of x. With increasing Q^2 the LO and HO predictions of both parameterizations tend to be very similar at low values of x but they still differ significantly at high values of x. In Fig. 12 we also show the comparison of the predictions for F_2^γ for the real photon obtained from all available next-to-leading order parameterizations GRV, GRSc and AFG for three values of $Q^2 = 1, 15$ and 100 GeV^2. The predictions are quite different for large values of x where the data are not very precise.

In Fig14 we show the structure function F_2^γ for the virtual photon obtained from the parton distribution functions predicted by SaS, GRSc and GRS parameterizations. The x dependence of SaS1D and GRSc parameterizations at $Q^2 = 15$ GeV^2 and for several values of $P^2 = 0, 0.01, 0.1, 1$ GeV^2 are shown on the left. Clearly the suppression of F_2^γ with increasing P^2 and especially the hadron-like contribution are visible. On the right, the P^2 dependence of F_2^γ predicted by SaS1D, GRSc and GRS parameterizations for three values of $Q^2 = 2, 75, 1000$ GeV^2 and at moderately small value of $x = 0.03$ are shown. Once more a strong suppression of F_2^γ with increasing P^2 is visible.

4.5 Hadronic structure of the electron

At present beam energies the splitting of the electron induced reactions into the flux of quasi-real transverse photons in the electron and the distribution of partons inside the photon is quite a good approximation. However, at future colliders, contributions from W and Z bosons as well as from γ-Z interference will play more and more significant role. Therefore instead of measuring separate structure functions of each of intermediate bosons (which

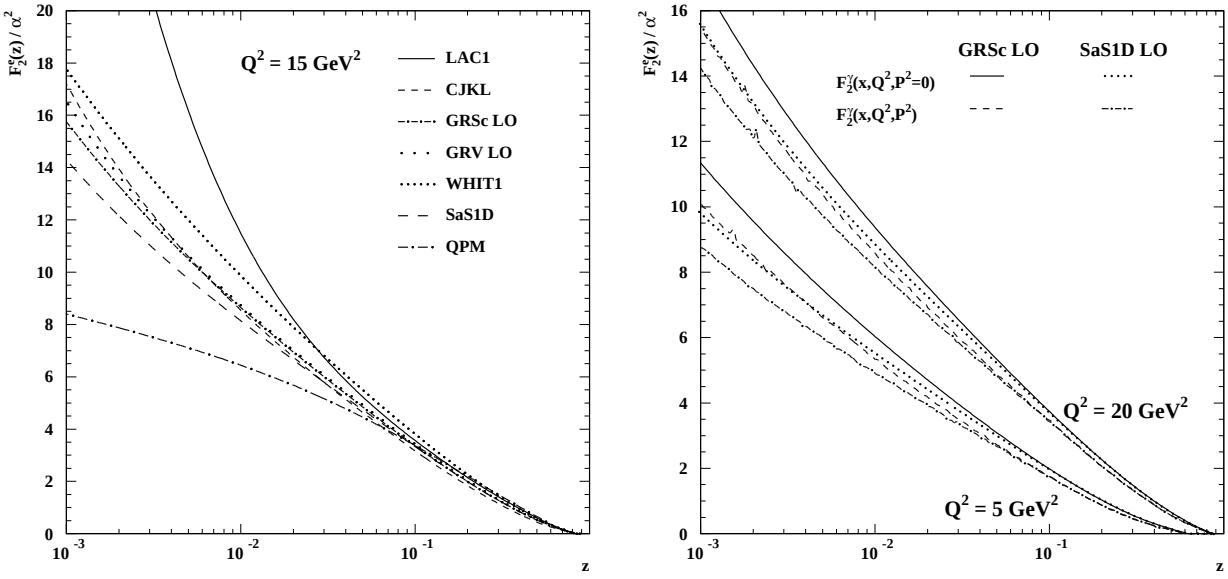

Figure 15: The electron structure function F_2^e divided by the fine structure constant squared obtained from different parton distribution functions in the photon using the Eq. 70. In all parameterizations of F_2^γ used, the P^2 dependence is either neglected or set to $P^2 = 0$.

Figure 16: The electron structure function F_2^e divided by the fine structure constant squared obtained from the parton distribution functions in the photon predicted by SaS1D and GRSc LO parameterizations in two cases: P^2 set to zero in F_2^γ and with full P^2 dependence of F_2^γ and of the photon flux and for two different values of $Q^2 = 5, 20$ GeV^2.

from experimental point of view might be even not possible) it seems more reasonable to measure the electron structure functions. The concept of the hadronic structure of the electron has been introduced only recently in Refs. [104, 105], where the evolution equations in Q^2 have been constructed and the asymptotic solutions have been found for the quark and gluon content of the electron in the leading logarithmic approximation. At LEP energies the measurements of the electron structure function and the photon structure function are roughly equivalent. The cross section for the deep inelastic scattering of an electron off a target electron expressed in terms of the electron structure functions F_2^e and F_L^e reads:

$$\frac{d^2\sigma}{dz\,dQ^2} = \frac{2\pi\alpha^2}{z\,Q^4}\left[\left(1+(1-y_e)^2\right)F_2^e(z,Q^2) - y_e^2 F_L^e(z,Q^2)\right] \tag{69}$$

Neglecting the term proportional to F_L^e we can directly use this formula to extract the electron structure function F_2^e from the differential cross section. Comparing Eq. 69 with Eq. 32 one finds the following relation between the electron F_a^e and the photon F_a^γ $(a = 2, L)$ structure functions:

$$F_a^e(z,Q^2;P^2_{\max}) \equiv \int_z^1 dx \int_{P^2_{\min}(z/x)}^{P^2_{\max}} dP^2\,\frac{z}{x^2}F_a^\gamma(x,Q^2,P^2)\hat{f}_{\gamma^*/e}(z/x,P^2) \tag{70}$$

From the theoretical point of view, the measurement of the electron structure function, even at present energies, has some advantages [106, 107]. The target photons used to measure the

photon structure function, are always off-shell. Treating the photons as real is an approximation. From the measurements of the QED structure function of the photon we know that the precise information about this small but finite virtuality of the target photons is essential in a correct description of the data by QED predictions. In the case of hadronic structure function of the photon the dependence on the virtuality of target photons in not measured nor completely known theoretically. The photon structure function also depends on the form of the equivalent photon formula and this is still being discussed in literature [147]. The above problems do not appear in the concept of the electron structure function which only weakly depends on $P^2_{\max}$. The most important drawback of the electron structure function is that its shape is dominated by the strongly peaked flux of target photons. In Fig. 15 we present a comparison of the electron structure functions F_2^e constructed from different parameterizations of the photon structure function F_2^γ using the formula given in Eq. 70, as a function of z and for $Q^2 = 15$ GeV^2. When calculating the curves in Fig. 15, the dependence of F_2^γ on P^2 has been neglected ($P^2 = 0$), which means that the virtuality of the photon radiated by the target electron enters only through the photon flux (Eq. 29) and through the upper limit of integration $P^2_{\max} = 4.5$ GeV^2 (typical value at LEP2). One can see that the shape of F_2^e is dominated by the strongly peaked EPA formula. The sensitivity of the electron structure function F_2^e to the dependence of the photon structure function F_2^γ on P^2 has been investigated in Fig. 16. The predictions based on GRSc LO [27] and SaS1D [102] parameterizations are shown for two different situations: with the full dependence of F_2^γ on P^2 and with P^2 set to zero in F_2^γ. One can see that the difference between these two situations is of the same order as the difference between the parameterizations themself.

5 Structure and interactions of virtual photons

In the previous Section we discussed in detail the interactions of virtual photons with quasi-real or slightly virtual photons. The cross section for this process has been expressed in terms of the structure functions of the quasi-real photon. In the present Section we shall extend our discussion to the interactions of two highly virtual photons ($Q^2, P^2 \gg \Lambda^2$). From the experimental point of view this means that we will consider double-tagged events, i.e. events with both final state electrons scattered at sufficiently large polar angles θ_i to be observed in a detector.

5.1 The cross section

The differential cross-section given in Eq. 13, in the limit $Q_i^2 \gg m_e^2$, reduces to:

$$\mathrm{d}^6\sigma = \frac{\mathrm{d}^3\mathrm{p}_1'\mathrm{d}^3\mathrm{p}_2'}{E_1' E_2'}\,\mathcal{L}_{\mathrm{TT}}\left(\sigma_{\mathrm{TT}} + \epsilon_1\sigma_{\mathrm{LT}} + \epsilon_2\sigma_{\mathrm{TL}} + \epsilon_1\epsilon_2\sigma_{\mathrm{LL}} + \frac{1}{2}\epsilon_1\epsilon_2\tau_{\mathrm{TT}}\cos 2\bar{\phi} - \sqrt{2\epsilon_1(\epsilon_1+1)}\sqrt{2\epsilon_2(\epsilon_2+1)}\tau_{\mathrm{TL}}\cos\bar{\phi}\right) \tag{71}$$

where $\epsilon_i \equiv \rho_i^{00}/2\rho_i^{++}$ and the photon helicities ρ_i^{00} and ρ_i^{++} are given in Eq. 14. The values of ϵ_i are close to unity in the kinematic region accessed at LEP (low values of y_{ei}). The luminosity function $\mathcal{L}_{\mathrm{TT}}$ describes the flux of the incoming transversely polarized photons. Comparing Eq. 71 with the general formula for the cross section given in Eq. 13 we find that $\mathcal{L}_{\mathrm{TT}}$ is given by:

$$\mathcal{L}_{\mathrm{TT}} = \frac{\alpha^2}{16\pi^4 Q_1^2 Q_2^2}\left[\frac{(q_1\cdot q_2)^2 - Q_1^2Q_2^2}{(p_1\cdot p_2)^2 - m_{\mathrm{e}}^2 m_{\mathrm{e}}^2}\right]^{1/2} 4\rho_1^{++}\rho_2^{++} \tag{72}$$

The sum of the cross sections and interference terms given in parentheses in Eq. 71 represents the cross section for the reaction $\gamma^\star\gamma^\star \to$ hadrons (leptons):

$$\sigma_{\gamma^\star\gamma^\star} = \sigma_{\mathrm{TT}} + \sigma_{\mathrm{TL}} + \sigma_{\mathrm{LT}} + \sigma_{\mathrm{LL}} + \frac{1}{2}\tau_{\mathrm{TT}}\cos 2\bar{\phi} - 4\tau_{\mathrm{TL}}\cos\bar{\phi} \tag{73}$$

where we made use of the approximation $\epsilon_i \approx 1$. The cross section for the process $\mathrm{e^+e^-} \to \mathrm{e^+e^-}$ hadrons can be then written as a product of a term describing the flux of the incoming photons and the cross-section for the interaction of the virtual photons. Depending on the relative size of virtualities of the interacting photons the process can be divided into two classes. When the virtualities of the photons differ significantly, $Q^2 \gg P^2 \gg \Lambda^2$, the process can be considered as a deep inelastic scattering of the electron off the virtual photon. In this case the considerations of the previous Section apply and the cross section can be expressed in terms of virtual photon structure functions defined in analogy to the structure functions of the quasi-real photon. However, experimentally one can access only an effective structure function $F_{\mathrm{eff}}^{\gamma} = (Q^2/4\pi^2\alpha)\bar{\beta}^{-1}\,\sigma_{\gamma^\star\gamma^\star}$ which is proportional to the cross section $\sigma_{\gamma^\star\gamma^\star}$ defined in Eq. 73. Making further assumptions, that σ_{LL} is negligible, $\sigma_{\mathrm{TL}} = \sigma_{\mathrm{LT}}$, and that the

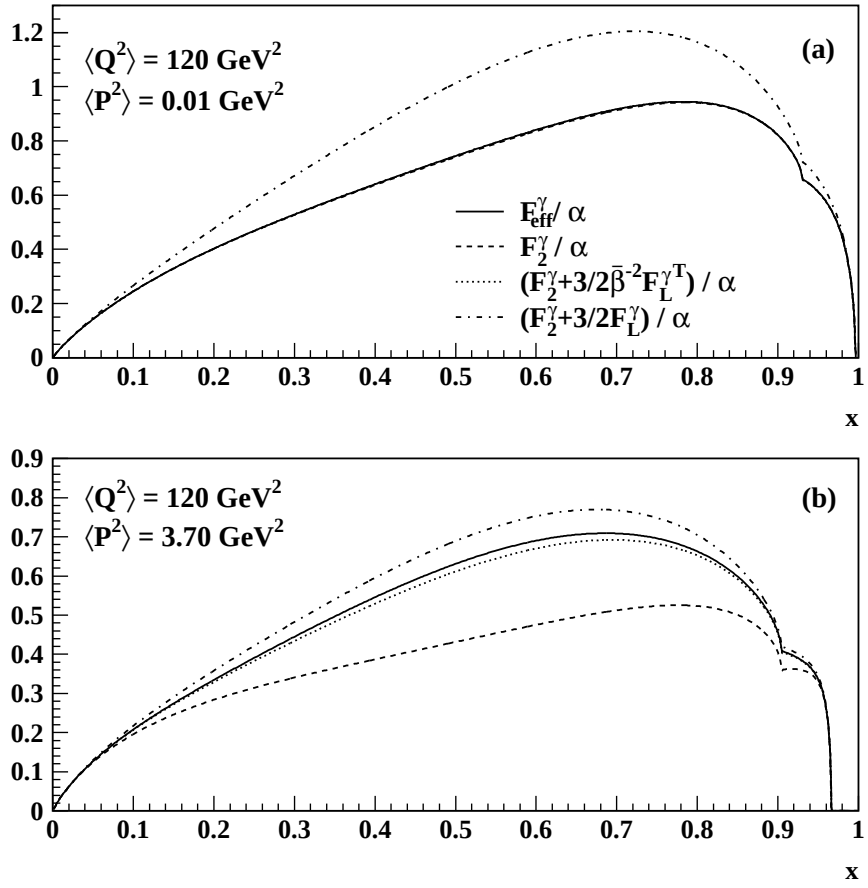

Figure 17: Comparison of the effective structure function $F_{\rm eff}^{\gamma}$ with F_2^{γ} and the approximations given in Eq. 74 for two cases: (a) $\langle Q^2\rangle = 120$ GeV^2, $\langle P^2\rangle = 0.01$ GeV^2 and (b) $\langle Q^2\rangle = 120$ GeV^2, $\langle P^2\rangle = 3.7$ GeV^2 assuming the QPM ($m_{\rm u} = m_{\rm d} = m_{\rm s} = 0.325$ GeV and $m_{\rm c} = 1.5$ GeV). To a good approximation the quantity measured for the virtual photon is the effective structure function given by $(F_{\rm eff}^{\gamma} = F_2^{\gamma} + 3/2F_L^{\gamma})/\alpha$.

interference terms do not contribute, one can relate $F_{\rm eff}^{\gamma}$ to the known structure functions F_2^{γ} and F_L^{γ}:

$$F_{\rm eff}^{\gamma} = F_2^{\gamma} + \frac{3}{2}\bar{\beta}^{-2}F_L^{\gamma T} \simeq F_2^{\gamma} + \frac{3}{2}F_L^{\gamma} \tag{74}$$

In Fig. 17 we compare the effective structure function $F_{\rm eff}^{\gamma}$, calculated in QPM, directly from the cross section $\sigma_{\gamma^\star\gamma^\star}$ with neglected interference terms and using the approximations given in Eq. 74. One can see that for the quasi-real photon the effective structure function $F_{\rm eff}^{\gamma}$ is equal to F_2^{γ} and is well in agreement with the first relation given in Eq. 74. However, the second approximation in Eq. 74 is significantly worse. On the other hand in case of virtual photon the effective structure function $F_{\rm eff}^{\gamma}$ is close to the combination of F_2^{γ} and F_L^{γ} given in Eq. 74, but very different from F_2^{γ}.

In the case when the virtualities of the interacting photons are of the same order, the usual interpretation in terms of the photon structure functions is not meaningful and the most appropriate quantity which can be measured is just the cross section.

5.2 DGLAP and/or BFKL dynamics?

The second topic extensively studied both theoretically and experimentally is the dynamics of interactions of highly virtual photons. The interaction of two virtual photons has been argued to be a 'golden' process to study the parton dynamics, because it does not require (for sufficiently large photon virtualities) any non-perturbative input in theoretical calculation. The discussion in this paragraph is based on the following publications [37–39]. Many processes in QCD can be described by a fixed order expansion in the strong coupling constant α_s. However, hadronic processes at high-energy colliders often involve more than one energy scale, and in consequence in perturbative QCD α_s gets multiplied by a large logarithm of the relevant scales. In such a case fixed order calculations must be replaced with leading-log calculations in which such terms are resumed.
In Fig. 18 we show schematically the 'map' of deep inelastic electron photon scattering in (x, Q^2) plane. If one of the colliding hadronic objects is much smaller than the other one (in our case the photons with higher and lower virtuality, respectively) then in order to correctly treat such collision it is necessary to resum terms proportional to $(\alpha_s \ln Q^2/Q_0^2)^n$, because the smallness of α_s is compensated by the large size of $\ln Q^2/Q_0^2$. This procedure leads to DGLAP [51] evolution equations introduced in Section 4. DGLAP evolution, up in Q^2, describes the change of parton density with increasing spatial resolution of about $1/Q$ (see Fig. 18). The evolution is self-contained in a given x interval and in particular does not involve knowledge of the parton densities at lower values of x. The cross section is proportional to the quark distribution at scale Q^2, which is related to the qark distribution at another scale Q_0^2 via:

$$\begin{aligned} xq(x,Q^2) = xq(x,Q_0^2) &+ \alpha_s \ln\frac{Q^2}{Q_0^2}\int_x^1 dy_1 \frac{x}{y_1} P_{qq}\left(\frac{x}{y_1}\right) q(y_1,Q_0^2) \\ &+ \alpha_s \ln\frac{Q^2}{Q_0^2}\int_x^1 dy_1 \frac{x}{y_1} P_{qg}\left(\frac{x}{y_1}\right) g(y_1,Q_0^2) + ... \end{aligned} \tag{75}$$

where the splitting functions P_{qq} and P_{qg} are given in the leading order by Eq. 66. In an appropriate gauge Eq. 75 can be interpreted as the first (with one rung only) in a series of ladder diagrams shown in Fig. 19, whose rungs are strongly ordered in transverse momenta:

$$Q_1^2 \gg k_{T,n}^2 \gg k_{T,n-1}^2 \gg \cdots \gg k_{T,1}^2 \gg Q_2^2 \tag{76}$$

For high energy scattering, i.e. at small x, the ladder becomes long, and because the domination of the splitting function $P_{gg}(y) \sim 1/y$ in this region, it consists mainly of gluons. The dominant terms in perturbative QCD expansion are of the form $(\alpha_s \ln(1/x) \ln(Q^2/Q_0^2))^n$. Their resummation is referred to as the double leading logarithmic approximation (DLLA). The region of its applicability is shown in Fig. 18. In this case in addition to the strong ordering of the transverse momenta (see Eq. 76), also the fractional longitudinal momenta[4] x_i' where $i = 1, ..., n$, of the gluons along the ladder are strongly ordered:

$$x_1 \equiv x_n' \ll x_{n-1}' \ll \cdots \ll x_1' \equiv x_2 \tag{77}$$

[4]In Eq. 77 and in Fig. 19 we use x_i' to denote the fractional longitudinal momenta of partons along the ladder to avoid a conflict in notation with the symbols x_1 and x_2 used throughout the paper to denote the Bjorken scaling variables of DIS electron photon scattering process.

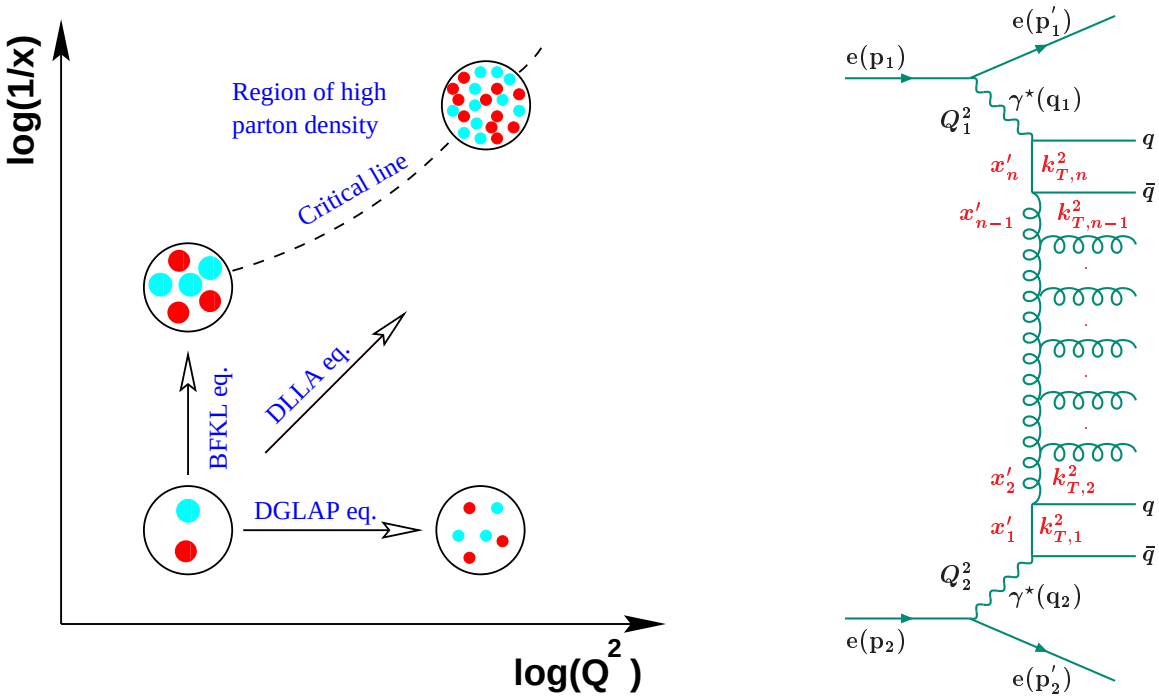

Figure 18: The $(x,\, Q^2)$ regions of validity of the various evolution equations. In DGLAP evolution with increasing Q^2 the partonic constituents of the photon are resolved more finely. The BFKL evolution towards small values of x allows to access regions of growing gluon densities, but the resolution in transverse plane remains at approximately $1/Q$. Simultaneous evolution in x and Q^2 leads to DLLA evolution equations. Perturbative QCD is applicable below the critical line.

Figure 19: The ladder diagram corresponding to the interaction of two virtual photons. The ladders start and end with quark boxes, and can have gluon or quark rungs. The fractional longitudinal momenta and the transverse momenta squared of each rung are denoted as x'_i and $k_{T,i}$, respectively, with $i = 1, ..., n$.

The DLLA leads to a gluon density strongly rising towards low x, like $xg(x, Q^2) \sim x^{-\lambda}$ with an effective power $\lambda \approx \sqrt{(12\alpha_s/\pi)\ln(1/x)\ln(Q^2/Q_0^2)}$ [40].

When the partons at the ends of the ladder have similar transverse momenta, $Q_1^2 \approx Q_2^2$, there is no phase space left for the transverse momenta to be strongly ordered along the ladder, and the strong ordering in k_T is replaced by a diffusion pattern. In perturbative expansion all terms proportional to $(\alpha_s \ln(1/x))^n \approx (\alpha_s \ln(W^2/Q^2))^n$ need to be resumed. This is done by the Balitski-Fadin-Kuraev-Lipatov (BFKL) equation [36]. In the appropriate gauge each term corresponds to the n-rung ladder diagram (Fig. 19) in which gluon emissions are strongly ordered in longitudinal momenta. The basic quantity in this approximation is the unintegrated (over the gluon transverse momentum) gluon density distribution $\mathcal{G}(x,\, k_T^2)$ related to the usual gluon distribution $g(x, Q^2)$ via:

$$\mathcal{G}(x,\, k_T^2) = x\, \frac{\partial g(x,\, Q^2)}{\partial \ln Q^2}\bigg|_{Q^2=k_T^2} \tag{78}$$

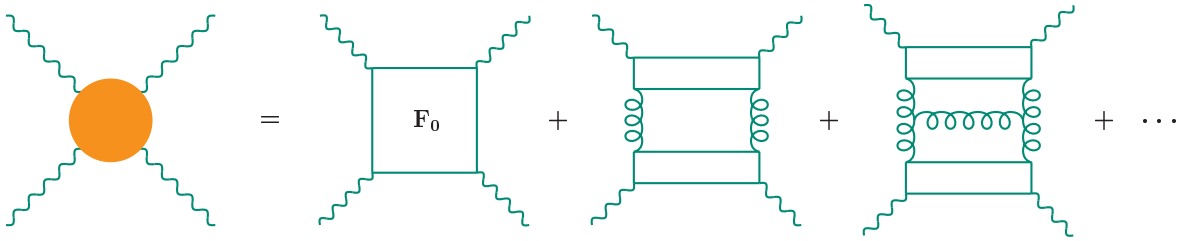

Figure 20: The contributions to the $\gamma^\star\gamma^\star$ cross section: box digram (F_0), one gluon exchange, next in the set of ladder diagrams, ...

The unintegrated gluon distribution $\mathcal{G}(x,\, Q^2)$ satisfies the following leading logarithmic ($\ln 1/x$) BFKL evolution equation [36]:

$$\frac{\partial \mathcal{G}(x,\, k_T^2)}{\partial \ln 1/x} = 3\frac{\alpha_s(k_T^2)}{\pi} k_T^2 \int_{k_{T0}}^{\infty} \frac{dk_T'^2}{k_T'^2} \left[\frac{\mathcal{G}(x,\, k_T'^2) - \mathcal{G}(x,\, k_T^2)}{|k_T'^2 - k_T^2|} + \frac{\mathcal{G}(x,\, k_T^2)}{\sqrt{4k_T'^4 + k_T^4}} \right] \tag{79}$$

where k_{T0} is the lower limit cut-off, which is necessary if the running coupling constant effects are taken into account. The BFKL evolution equation takes us to smaller values of x where the gluon density increases while the transverse size that is probed remains the same. Eventually we reach the critical line where recombination effects must be incorporated via perturbative QCD. Finally we enter the region of high parton density where we can not use normal methods of perturbation theory. At higher Q^2 we can evolve further in x before reaching the critical line.

When the running of α_s is neglected and $k_{T0}^2 = 0$ the BFKL equation can be solved analytically giving at small x the following dependence of the gluon distribution:

$$xg(x, Q^2) \sim \frac{x^{1-\alpha_{I\!P}}}{\sqrt{\ln\,(1/x)}} \tag{80}$$

where $\alpha_{I\!P} = 1 + \lambda = 1 + (3\alpha_s/\pi)4\ln 2$ is the bare QCD pomeron. The value λ is usually said to be 0.5, though this requires $\alpha_s = 0.18$, which happens only at high Q^2. When the running coupling constant effects are taken into account the small x behaviour of parton distributions is $xg(x, Q^2) \sim x^{-\lambda}$, with $\lambda \approx 0.5$ as in the fixed coupling case.

Recently, much attention has been given to the BFKL pomeron especially for small x deep inelastic electron proton scattering at HERA. The onset of BFKL effects has been searched for in the measurements of the proton structure function $F_2^{\rm p}$ and the analysis of hadronic final states [47]. The situation is so far inconclusive, with the strongest hint for BFKL effects in the data coming from the analysis of forward π^0 production.

It has been argued [45, 48–50] that the e^+e^- colliders offer an excellent opportunity to test the BFKL predictions through the measurement of the total cross section for the process $\gamma^\star\gamma^\star \to$ hadrons. The cross section $\sigma_{\gamma^\star\gamma^\star}$ can be expressed in terms od ladder diagrams squared as shown in Fig. 20. The diagram denoted as F_0 represents the lowest order contribution called the 'box diagram' or QPM contribution. The contribution of the next in line diagram is often called 'one gluon exchange' contribution. For sufficiently large photon virtualities Q_1^2 and Q_2^2 (more than few GeV^2), this BFKL calculations can be carried out

without non-perturbative input. If additionally $Q_1^2 \simeq Q_2^2$ then the evolution in Q^2 is suppressed, allowing for a clean test of BFKL effects.

The original LO-BFKL calculations [45] predicted an increase of $\sigma_{\gamma^\star\gamma^\star}$ by a factor 20 or more compared to calculations without BFKL effects, or with only DGLAP (Q^2) evolution [51]. Since then the LO-BFKL calculations have been improved by including charm quark mass effects, running of the strong coupling constant α_s and the contribution of the longitudinal photon polarization states. Recently, it has become clear that the Next-to-Leading Order (NLO) corrections to the BFKL equation are large and effectively reduce the value of λ. A phenomenological determination of the Higher Order (HO) effects was presented in Ref. [50] and the resulting BFKL scattering cross-sections were shown to increase by a factor 2-3 only, relative to the calculations without BFKL effects. Since then theoretically motivated improved higher order calculations have been performed [38, 42, 43, 52–55], and give similar results.

For the comparison of the data to BFKL calculations the following additional kinematic quantity, which is a measure of the length of the gluon ladder, is defined [45]:

$$Y \equiv \ln\left(\frac{s_{\rm ee} y_{\rm e1} y_{\rm e2}}{\sqrt{Q_1^2 Q_2^2}}\right) = \ln\left(\frac{W^2 + Q_1^2 + Q_2^2}{\sqrt{Q_1^2 Q_2^2}}\right) \simeq \ln\left(\frac{W^2}{\sqrt{Q_1^2 Q_2^2}}\right) \equiv \overline{Y}\,, \tag{81}$$

where the approximation requires $W^2 \gg Q_i^2$.

6 Monte Carlo generators

In the analysis of the data collected by experiments at high energy colliders a crucial role is played by Monte Carlo generators. They are based on our knowledge of the physics processes taking place during a collision of elementary particles. The usual output from a Monte Carlo program is a collection of four momenta of particles produced in the interaction. At this stage, often called hadron (or more generically generator) level, we have an exact information on the whole final state. However, in the real experiments this information is disturbed by detector effects like resolution and acceptance. Therefore to be able to compare Monte Carlo predictions with measurements we need to pass the output from a generator through as accurate as possible simulation of the detector. The detector simulation is based on our best knowledge of the geometry and of response of its different parts to incident particles. All the information about the response of the detector to the input from a generator we usually call the detector level (of the Monte Carlo simulation). This detector level information is passed through the same reconstruction and analysis chains as the real data. Having information on the generator and detector levels we are able to use Monte Carlo programs to correct the data for detector acceptance and resolution effects and get insight into pure physics.

Usually even in a single analysis, several Monte Carlo generators are compared to the data or used to correct the data for detector effects. Most relevant to the measurements presented in this paper are the programs which are used to model two-photon interactions for double-tagged, single-tagged and anti-tagged events. The main features of the Monte Carlo programs used for analyses of LEP data are briefly described here. For further details the reader is referred to the original publications. An overview can be found e.g. in [7,14,15].

PHOJET [35]: The general purpose Monte Carlo program, which is based on the Dual Parton Model [80] combined with the QCD improved parton model to give an almost complete description of hadron-hadron, photon-hadron and photon-photon interactions at high energies. It contains both hard and soft processes. The hard processes are calculated in LO perturbative QCD, and soft processes are modeled based on γp, pp and p$\bar{\text{p}}$ data assuming Regge factorization. Originally only (quasi-)real photons were considered, but recently the program has been extended to match the deep inelastic electron photon scattering as well as the scattering of two virtual photons. Both photons are allowed to fluctuate into a hadronic state before they interact. The $\gamma^\star\gamma$ or $\gamma^\star\gamma^\star$ cross-sections are obtained from the $\gamma\gamma$ cross-section by extrapolating in Q^2 on the basis of the Generalized Vector Meson Dominance model using the description of Ref. [56]. In particular, it is worth pointing out here, that the program is not based on the cross section formula for deep inelastic electron-photon scattering and always produces the same x and Q^2 distributions, independent of the input structure function. Events are generated for both soft and hard partonic processes. A cut-off on the transverse momentum of the scattered partons in the photon-photon centre-of-mass system of 2.5 GeV is used to separate the two classes of events. For this reason the generation of events with W below 5 GeV is known to be incomplete. The hadronisation is based on the Lund string model as implemented in JETSET [79].

HERWIG [59]: The general purpose Monte Carlo program, which has been upgraded to electron photon scattering during the LEP2 Workshop [14]. The most recent version

HERWIG5.9+k_t (dyn) incorporates improvements in modeling of the intrinsic transverse momentum of the quarks within the photon. This version uses a modified transverse momentum distribution, k_t, for the quarks inside the photon, with the upper limit dynamically (dyn) adjusted according to the hardest scale in the event, which is of order Q^2. In HERWIG the photon flux is based on the EPA [18]. The hard interaction is simulated as eq→eq scattering, with the incoming quark generated according to a set of parton distribution functions. The incoming quark is subject to an initial state paron shower, which is designed in such a way that the hardest emission is matched to the sum of the matrix elements for the higher order resolved processes ($g \to q\bar{q}$, $q \to qg$ and $\gamma \to q\bar{q}$). The parton shower uses the transverse momentum as evolution parameter and obeys angular ordering. This procedure dynamically separates events into point-like and hadron-like events, which can be different from the choice made in the parton distribution functions. For hadron like events the photon remnant gets a transverse momentum k_t with respect to the direction of the incoming photon, generated from a Gaussian distribution. The hadronisation is based on the cluster model.

PYTHIA [57]: The general purpose Monte Carlo program, which can generate hard or soft processes between leptons, hadrons and photons. In case of deep inelastic electron photon scattering, the quarks are generated according to parton distribution functions of the photon. The flux of the quasi-real photons has to be externally provided, and the corresponding electron is only modeled in the collinear approximation. The program is based on the leading order matrix element for the process eq→eq. Higher order QCD processes are generated via parton showers, using the parton virtuality as the evolution parameter. The separation into point-like and hadron-like events is taken from the parton distribution functions. For hadron-like events the photon remnant gets a transverse momentum k_t generated from a Gaussian distribution, and for point-like events the transverse momentum follows a power like behaviour, dk_t^2/k_t^2, with $k_{t,max} = Q^2$ as the upper limit. The hadronisation is based on the Lund string model.

TWOGAM [61]: The Monte Carlo program developed by the DELPHI Collaboration for the simulation of two photon processes. TWOGAM generates three different subprocesses: QPM, QCD resolved photon processes and non-perturbative soft processes described by the Vector Meson Dominance model [3]. The normalization of the QPM process is determined by the quark masses. The normalizations of the VMD is fixed by the cross section for the scattering of two real photons. The partons generated according to a chosen parton distribution function in the photon, undergo a hard $2 \to 2$ scattering process. No parton showers are included. The hadronisation is based on the Lund string model. TWOGAM was recently upgraded to take into account QED soft and hard radiation from initial and final state electrons.

Vermaseren [73]: The Monte Carlo program, which has become a standard calculation of the process $e^+e^- \to e^+e^- f\bar{f}$ proceeding via $\gamma\gamma$ interactions. It uses the subset of the exact $2 \to 4$ matrix element in which the electron and positron do not annihilate. The full dependence on the mass of final state fermion and an P^2 is kept.

BDK [66–68]: The program is an extension of the Vermaseren program and includes the QED radiative corrections to the process. It mainly serves to the estimation of the radiative corrections to be applied to data corrected for acceptance with a different Monte Carlo program which does not contain QED radiative corrections.

GALUGA [65]: The Monte Carlo program, which contains a full implementation of the cross section given in Eq.13. It is not used as an event generator, but due to its flexibility is often used to calculate cross sections and photon fluxes in a user defined phase space.

7 The OPAL detector at LEP

The **L**arge **E**lectron **P**ositron (LEP) collider was an e^+e^- storage ring located at CERN. It had a circumference of 27 km and was located 100 m underground. Four experiments: OPAL, ALEPH, DELPHI and L3, were situated at symmetrical collision points around the ring. During the first phase of operation (LEP1), in the years 1989–1995, the centre-of-mass energy of the electron and positron beams was close to the mass of the Z^0 gauge boson at 91 GeV. The energy was increased for the LEP2 phase: first to 161 GeV to produce W^+W^- pairs and then in steps up to 209 GeV by the end of operation in the year 2000.

A schematic view of the OPAL (**O**mni **P**urpose **A**pparatus for **L**EP) detector is shown in Fig.21. A detailed description of the OPAL detector can be found in Ref. [69]. Here only a brief account is given of the main components relevant to the measurements in two photon physics.
The right-handed OPAL coordinate system is defined with the z axis pointing in the direction of the e^- beam and the x axis pointing towards the centre of the LEP ring. The polar angle θ, the azimuthal angle ϕ and the radius r are the usual spherical coordinates.

The central tracking system is located inside a solenoid magnet which provides a uniform axial magnetic field of 0.435 T along the beam axis. The central tracking system consists of a two-layer silicon micro-vertex detector [70], a high precision vertex drift chamber, a large volume jet chamber with 159 layers of axial anode wires, and a set of z–chambers for accurately measuring track coordinates along the beam direction. The transverse momenta p_{T} of tracks with respect to the z direction of the detector are measured with a precision of $\sigma_{p_{\mathrm{T}}}/p_{\mathrm{T}} = \sqrt{0.02^2 + (0.0015 \cdot p_{\mathrm{T}})^2}$ (p_{T} in GeV) in the central region, $\theta > 753$ mrad. The jet chamber also provides energy loss, $\mathrm{d}E/\mathrm{d}x$, measurements which are used for particle identification.

The central detector is surrounded in the barrel region ($|\cos\theta| < 0.82$) by a lead glass electromagnetic calorimeter (ECAL) and a hadronic sampling calorimeter (HCAL). Outside the HCAL, the detector is surrounded by muon chambers. There are similar layers of detectors in the endcaps ($0.81 < |\cos\theta| < 0.98$). The barrel section consists of a cylindrical array of 9440 lead-glas blocks with a depth of 24.6 radiation lengths. The endcap sections (EE) consist of 1132 lead-glas blocks with a depth of more than 22 radiation lengths. The lectromagnetic energy resolution of the EE calorimeter is about $15\%/\sqrt{E}$ (E in GeV) at polar angles above 350 mrad, but deteriorates closer to the edge of the detector.

The small angle region from 47 to 140 mrad around the beam pipe on both sides of the interaction point is covered by the forward detectors (FD) and the region from 25 to 59 mrad by the silicon-tungsten luminometers (SW) [71]. During the LEP2 phase the lower boundary of the SW acceptance was effectively 33 mrad due to the installation of a low-angle shield to protect the central detector from synchrotron radiation. The FD consists of cylindrical lead-scintillator calorimeters with a depth of 24 radiation lengths divided azimuthally into 16 segments. The electromagnetic energy resolution is approximately $18\%/\sqrt{E}$ (E in GeV). The SW detector consists of two cylindrical small angle calorimeters encircling the beam pipe at approximately ± 2.5 m from the interaction point. Each calorimeter is made of a stack of 18 tungsten plates, interleaved with 19 layers of silicon sampling wafers and

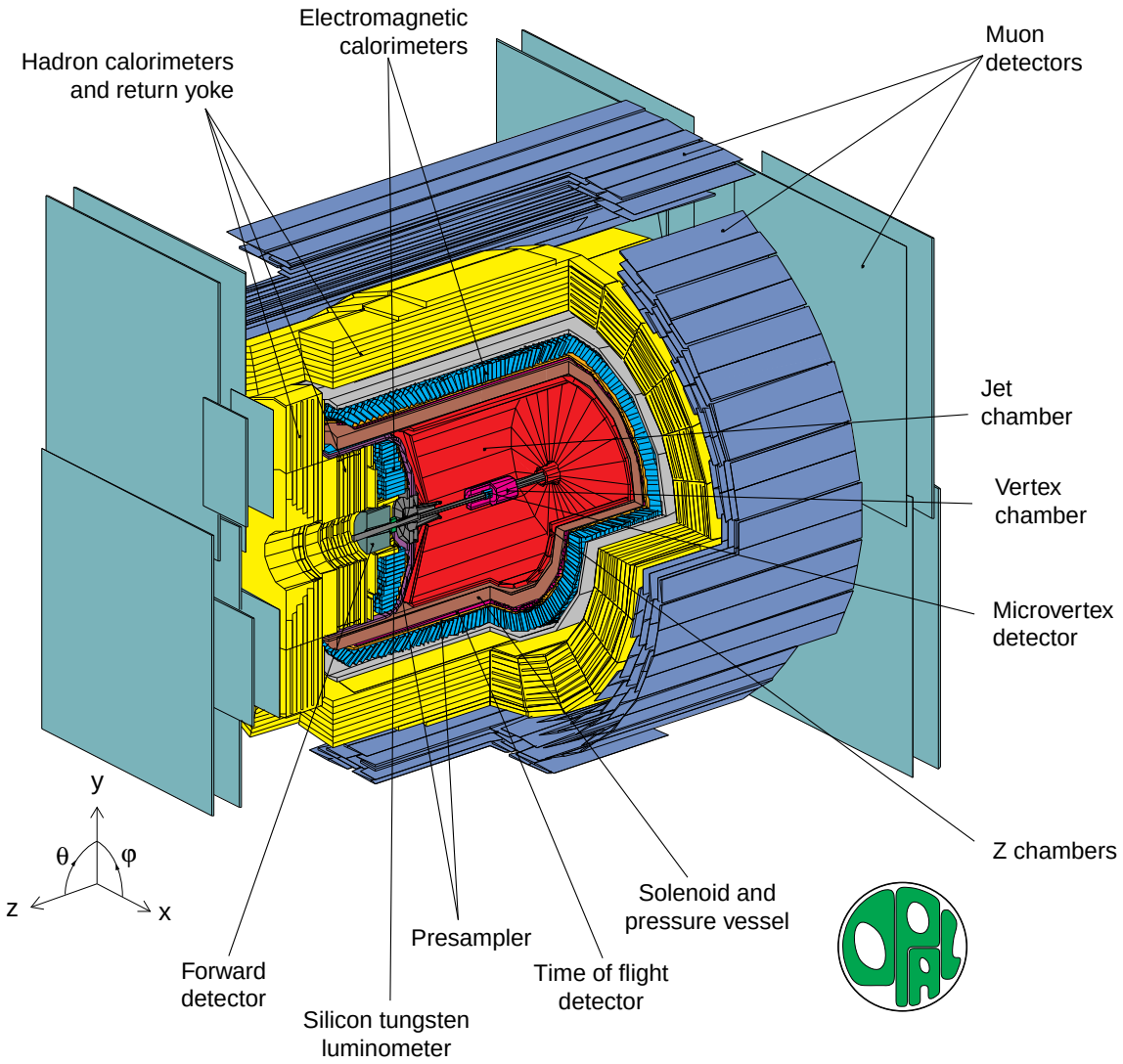

Figure 21: Schematic view of the OPAL detector. Main components discussed in the text are indicated.

mounted as two interlocking C–shaped modules around the LEP beam pipe. The depth of the detector amounts to 22 radiation lengths. Each silicon layer consists of 16 wedge-shaped silicon detectors. The sensitive area of the calorimeter fully covers radii between 81 and 142 mm from the beam axis. The electromagnetic energy resolution is approximately $25\%/\sqrt{E}$ (E in GeV) on both sides. At LEP2 energies it was found that the energy resolution is almost constant with energy due to the energy leakage and dead material.
Small angle detectors were primary used in the luminosity measurement, which was based on the tagging of electrons and positrons scattered at small angles in the Bhabha process.

The other three experiments were constructed based on the similar general concepts, although they differ in technical and constructional solutions. For details see: ALEPH [108], DELPHI [109], L3 [110]. Also the geometrical (and in consequence kinematical) acceptances of different subdetectors differ slightly between the experiments.

8 Studies of the photon and electron structure in DIS

8.1 QED structure functions of the photon

The measurements of the QED photon structure functions at e^+e^- colliders are possible by studying the reaction $e^+e^- \to e^+e^- l^+l^-$, where l = e, μ, τ, in deep inelastic electron photon scattering regime, where one of the beam electrons scatters at sufficiently large polar angle to be observed in a detector, and the other remains undetected. Although from the theoretical point of view, all lepton channels are equally well suited for this purpose, from the experimental side the most clean measurement can be performed with $\mu^+\mu^-$ final state. The process has large cross section and is almost background free. For e^+e^- final state the cross section is even higher, but the number of different Feynman diagrams contributing to this process makes the analysis in terms of the photon structure functions more difficult. The $\tau^+\tau^-$ final state suffers from low statistics and can be only identified by detecting the products of τ decays. This makes the analysis quite difficult, because of large backgrounds from $q\bar{q}$ production or $\mu^+\mu^-$ final state, depending on whether the hadronic or leptonic decay channels of τ are used for its detection. The results presented in this section were obtained from the measurement of the process $e^+e^- \to e^+e^- \mu^+\mu^-$. In principle the measurement can serve as a test of QED to order $\mathcal{O}(\alpha^4)$. However, the experimental uncertainties are rather large and the precision tests of QED are not the aim of the measurement. At e^+e^- colliders this measurement rather serves as a test of experimental methods used in more difficult analyses like the hadronic structure function of the photon.

The measurements of the QED structure functions of the photon at LEP base on data collected during LEP1 phase and correspond in each experiment to an integrated luminosity close to 100 pb^{-1}. The photon structure function $F^{\gamma}_{2,\mathrm{QED}}$ has been measured at LEP by OPAL [111], DELPHI [112] and L3 [113] experiments. The above measurements by OPAL and DELPHI replaced the earlier measurements at lower statistics published in [117] and in [118]. There exist a preliminary measurement by ALEPH [119], which however is not going to be published and therefore is not considered here. Prior to LEP the measurements of $F^{\gamma}_{2,\mathrm{QED}}$ were performed by the CELLO [114], PLUTO [115] and TPC/2γ [116] experiments.

The measurements of the structure function $F^{\gamma}_{2,\mathrm{QED}}$ performed by the above experiments are compared to the QED predictions in Fig. 22, and the values of $F^{\gamma}_{2,\mathrm{QED}}$ together with available errors are listed in Tables 14, 15 and 16. If the average virtuality of the target photon $\langle P^2 \rangle$ in the measurement is provided by the experiment, it is used in the QED prediction. The value of $\langle P^2 \rangle$ is usually obtained from a Monte Carlo program or from the best fit of the QED prediction to the data. All LEP experiments provide $\langle P^2 \rangle$ of their measurements and non of the experiments prior to LEP does it. In the later case $P^2 = 0$ was assumed in the QED calculation. The value of the average virtuality of the probe photon $\langle Q^2 \rangle$ or the range of Q^2 used for $F^{\gamma}_{2,\mathrm{QED}}$ measurement is given in Fig. 22 in parentheses close to the name of the experiment. In the case when $\langle Q^2 \rangle$ is provided, the measurement is compared to the QED prediction for $F^{\gamma}_{2,\mathrm{QED}}(x, \langle Q^2 \rangle, \langle P^2 \rangle)$. In the case when the range of experimental Q^2 acceptance only is provided, the prediction for $\langle F^{\gamma}_{2,\mathrm{QED}}(x, Q^2, \langle P^2 \rangle) \rangle$ averaged over given Q^2 range is used instead. The data are generally in a good agreement with QED predictions. Only the measurement by TPC/2γ is systematically below the QED prediction. The reason

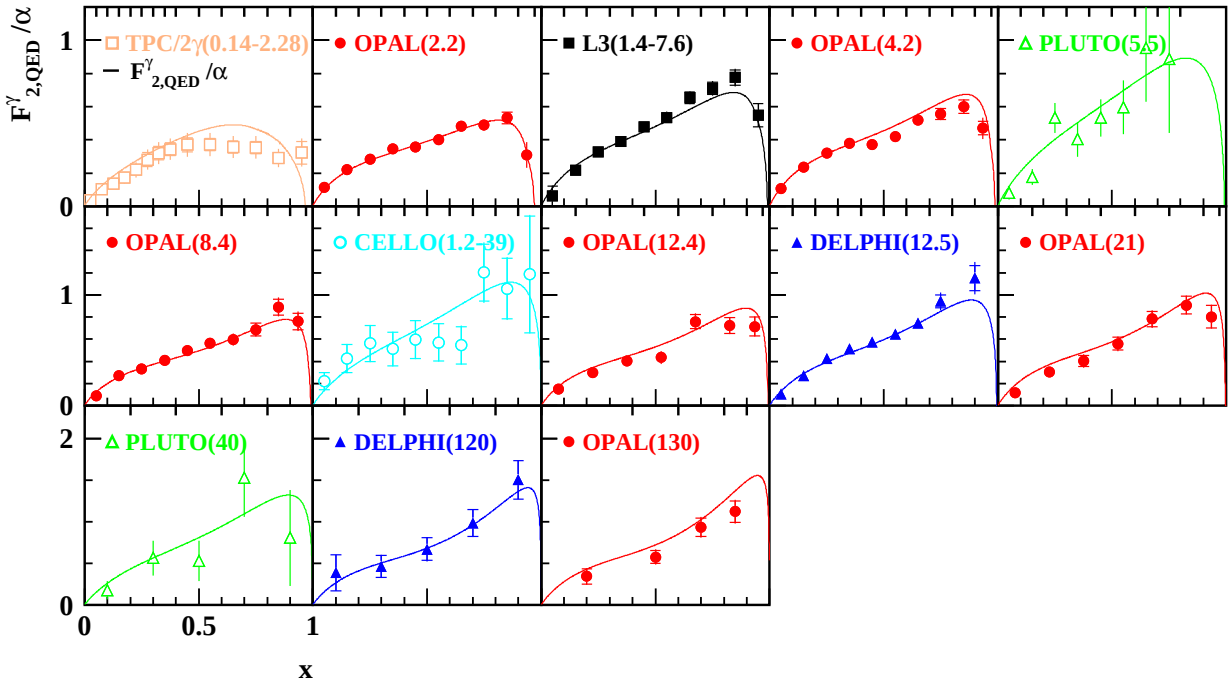

Figure 22: Compilation of all available measurements of $F^{\gamma}_{2,\mathrm{QED}}$ as a function of x. The measured values of $F^{\gamma}_{2,\mathrm{QED}}/\alpha$ are compared to the QED predictions. The statistical error is given by the inner error bars, and the total errors as full error bars. The numbers in parentheses denote the average virtuality of the probe photon $\langle Q^2 \rangle$ or the range of Q^2 in the measurement. The QED predictions shown correspond to $F^{\gamma}_{2,\mathrm{QED}}(x, \langle Q^2 \rangle, \langle P^2 \rangle)$ or to $\langle F^{\gamma}_{2,\mathrm{QED}}(x, Q^2, \langle P^2 \rangle) \rangle$ and use the average $\langle P^2 \rangle$ value of the measurement if provided by the experiment or $P^2 = 0$ as discussed in the text.

of this disagreement may be due to the averaging procedure used for the QED prediction as well as due to assumption that $P^2 = 0$, which might be of great importance especially because of low virtuality of the probe photon in this measurement.

Another way of presentation of $F^{\gamma}_{2,\mathrm{QED}}$ is as a function of Q^2, which is done in Fig. 23. Data are grouped into bins of x of size of 0.1 (only the highest x bin is slightly narrower due to the upper kinematical limit) and central values $\langle x \rangle$ shown in the figure. To separate the measurements in each bin of x an offset N indicated in the figure was added to each measurement and QED prediction. The QED predictions shown in the figure represent an average $F^{\gamma}_{2,\mathrm{QED}}$ in the x bin under study with $P^2 = 0$. All data points for which $\langle P^2 \rangle$ is known are corrected to $P^2 = 0$ by multiplying by the ratio of $F^{\gamma}_{2,\mathrm{QED}}$ (or $\langle F^{\gamma}_{2,\mathrm{QED}} \rangle$) calculated at $P^2 = 0$ and at $P^2 = \langle P^2 \rangle$. If for a particular measurement the range of Q^2 is given then for each data point at given x a separate average value of Q^2 has been calculated based on QED predictions for $F^{\gamma}_{2,\mathrm{QED}}$. This has the most significant influence on TPC/2γ data where the points at high values of x have been measured at effectively higher values of Q^2 than the points at low values of x. The agreement between the measurements and the QED predictions is very good in whole explored range of average photon virtualities $0.43 < \langle Q^2 \rangle < 130\mathrm{GeV}^2$.

The process $\mathrm{e^+e^-} \to \mathrm{e^+e^-}\,\mu^+\mu^-$ has such a clear experimental signature that it is possible to measure the triple differential cross section given in Eq. 43. The shape of the

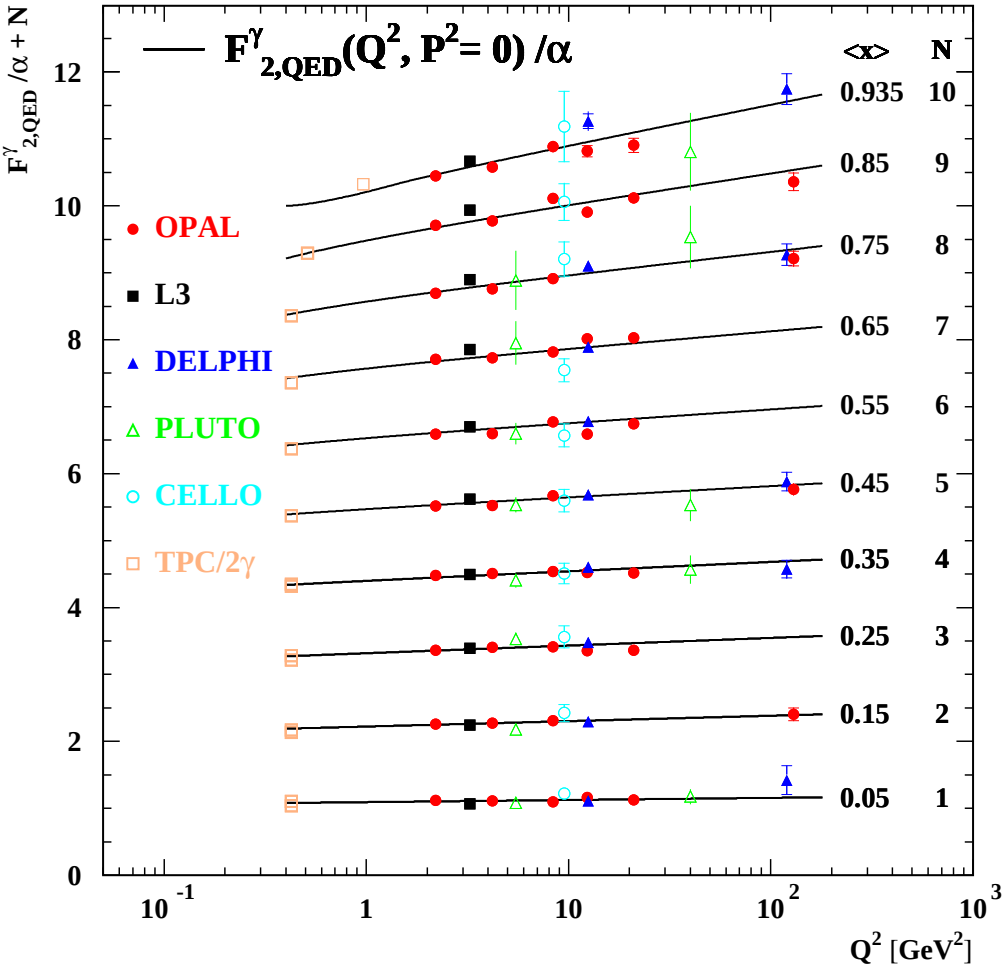

Figure 23: Compilation of all available measurements of $F^{\gamma}_{2,\mathrm{QED}}$ as a function of Q^2. The measured values of $F^{\gamma}_{2,\mathrm{QED}}/\alpha$ are compared to the QED predictions. The statistical error is given by the inner error bars, and the total errors as full error bars. The LEP data have been corrected for the effect of non-zero P^2. The curves represent the QED predictions for $P^2 = 0$. The average values of $\langle x \rangle$ and the offset N are indicated on the right side of the figure.

distribution of the azimuthal angle χ (for the definition see Section 2):

$$\frac{dN}{d\chi} = A\left(1 + \frac{F^{\gamma}_{\mathrm{A,QED}}}{F^{\gamma}_{2,\mathrm{QED}}}\cos\chi + \frac{1}{2}\frac{F^{\gamma}_{\mathrm{B,QED}}}{F^{\gamma}_{2,\mathrm{QED}}}\cos 2\chi\right) \tag{82}$$

can be used to determine the ratios of the structure functions for the real photon. Measuring in addition the structure function $F^{\gamma}_{2,\mathrm{QED}}$ for the real photon, it is possible to obtain directly $F^{\gamma}_{\mathrm{A,QED}}$ and $F^{\gamma}_{\mathrm{B,QED}}$. The structure functions $F^{\gamma}_{\mathrm{A,QED}}$ and $F^{\gamma}_{\mathrm{B,QED}}$ themself or/and scaled by the structure function $F^{\gamma}_{2,\mathrm{QED}}$ have been measured at LEP by OPAL [111], DELPHI [112] and L3 [113] experiments. There exist no other measurements of these quantities. The LEP results are listed in Tables 17 and 18. The measured ratios of the structure functions $F^{\gamma}_{\mathrm{A,QED}}/F^{\gamma}_{2,\mathrm{QED}}$ and $\frac{1}{2}F^{\gamma}_{\mathrm{B,QED}}/F^{\gamma}_{2,\mathrm{QED}}$ are compared in Fig. 24 between the experiments and with theoretical predictions given by Eq. 44. The average virtuality of each measurement

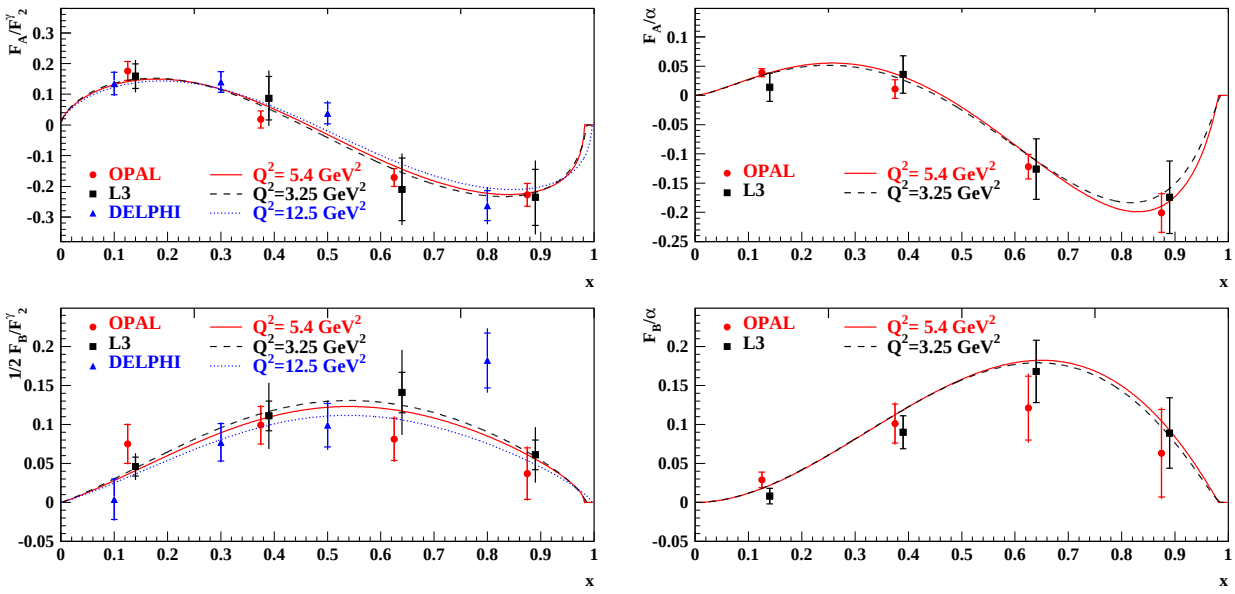

Figure 24: The structure function ratios $F^{\gamma}_{\mathrm{A,QED}}/F^{\gamma}_{2,\mathrm{QED}}$ and $\frac{1}{2}F^{\gamma}_{\mathrm{B,QED}}/F^{\gamma}_{2,\mathrm{QED}}$ measured by the OPAL, L3 and DELPHI experiments are compared to the predictions of QED. The statistical error is given by the inner error bars, and the total errors as full error bars. The tick marks at the top of the figures indicate the bin boundaries of the OPAL measurement. The QED curves are drawn for each Q^2 value separately.

Figure 25: The structure functions $F^{\gamma}_{\mathrm{A,QED}}$ and $F^{\gamma}_{\mathrm{B,QED}}$ measured by the OPAL and L3 experiments are compared to the predictions of QED. The meaning of symbols as in Fig. 24.

is indicated in the figure, and the QED curves are drawn separately for each of them. The measurements agree well within the relatively large statistical errors between each other and with QED predictions. For example, in case of the OPAL measurement, the QED predictions for the full range in x of $F^{\gamma}_{\mathrm{A,QED}}/F^{\gamma}_{2,\mathrm{QED}} = -0.027$ and $\frac{1}{2}F^{\gamma}_{\mathrm{B,QED}}/F^{\gamma}_{2,\mathrm{QED}} = 0.078$ are well in agreement with the measured values $F^{\gamma}_{\mathrm{A,QED}}/F^{\gamma}_{2,\mathrm{QED}} = -0.036 \pm 0.027 \pm 0.004$ and $\frac{1}{2}F^{\gamma}_{\mathrm{B,QED}}/F^{\gamma}_{2,\mathrm{QED}} = 0.061 \pm 0.013 \pm 0.004$.
The strength of the χ dependence varies with the scattering angle $\cos\theta^{\star}$ of the muons in the photon-photon centre-of-mass system. Reducing the acceptance of $\cos\theta^{\star}$ enhances the χ dependence, but to obtain a result for $F^{\gamma}_{\mathrm{A,QED}}$ and $F^{\gamma}_{\mathrm{B,QED}}$ which is valid for the full range of $\cos\theta^{\star}$ the measurement has to be extrapolated using the predictions of QED. The measurements performed by L3 and DELPHI are obtained in the range $|\cos\theta^{\star}| < 0.7$ and $|\cos\theta^{\star}| < 0.94$, respectively, and extrapolated to the full range in $\cos\theta^{\star}$. The OPAL measurements are valid in the full angular range $|\cos\theta^{\star}| < 1$.
The structure functions $F^{\gamma}_{\mathrm{A,QED}}$ and $F^{\gamma}_{\mathrm{B,QED}}$ have been extracted from the above ratios by OPAL and L3 only. They are compared between each other and with the QED predictions in Fig. 25. The agreement between both experiments and with QED predictions is good. Although the errors are large, it is clear from the measurements that both structure functions $F^{\gamma}_{\mathrm{A,QED}}$ and $F^{\gamma}_{\mathrm{B,QED}}$ are different from zero and are not flat. As explained in Section 4, the measurement of $F^{\gamma}_{\mathrm{B,QED}}$ is a good estimate of the longitudinal structure function $F^{\gamma}_{\mathrm{L,QED}}$ which has been not directly measured sofar.

8.2 Hadronic structure function of the photon

The first measurement of the hadronic structure function of the photon F_2^γ has been performed by the PLUTO experiment [122]. Since then many other measurements have become available, with most precise results coming from the LEP experiments. The structure function F_2^γ is extracted from the differential cross section for deep inelastic electron photon scattering process (Eq. 39). From the experimental point of view the measurements are based on single tagged events with a hadronic final state. The most recent OPAL measurement of F_2^γ at low-x has been performed by the author of this paper. This section is divided into three parts. It starts with a more detailed description of the recent OPAL analyses at low-x and at high Q^2, in particular the event selection criteria, the background sources and the description of data by Monte Carlo models is reviewed. In the second part all available measurements of F_2^γ from LEP and from other experiments are presented and compared between each other and with some recent parameterisations. In last the measurement of the charm structure function $F_{2,c}^\gamma$ of the photon is discussed.

8.2.1 Measurement of F_2^γ by the OPAL experiment at low-x

In this section we present the recent OPAL measurement of F_2^γ [143]. The data sample used in the analysis corresponds to an integrated luminosity of 592.7 pb^{-1} accumulated by the OPAL experiment in 1998 (168.5 pb^{-1}), 1999 (208.3 pb^{-1}) and 2000 (215.9 pb^{-1}) at e^+e^- centre-of-mass energies $\sqrt{s_{ee}} = 189 - 209$ GeV with a luminosity weighted average of $\sqrt{s_{ee}} = 198$ GeV.

Event selection and background estimation

As explained above, the measurement of the hadronic structure function F_2^γ of the photon is based on single tagged events with a hadronic final state. Such events were selected with the following set of cuts (see Section 7 for more details on the OPAL detector):

1. An electron candidate should be observed in one of SW detectors, with energy $E' > 0.75E_b$ and polar angle in the range $34 < \theta < 55$ mrad. The angle θ is measured with respect to the original beam direction. The calorimeter cluster with the highest energy is taken as the electron candidate. The high energy threshold for the electron candidate is needed to reject electron candidates from beam–gas interactions (off-momentum electrons).

2. An anti-tag cut is applied for possible electron candidates in the hemisphere opposite to the tag electron – there must be no cluster with energy $E_a > 0.25E_b$ in SW detector on the opposite side.

3. In order to remove events with scattered electrons in FD or in the central electromagnetic calorimeter, we require that there is no single cluster in these detectors with an energy above $0.25E_{\mathrm{b}}$.

4. At least 3 tracks ($N_{\mathrm{ch}} \geq 3$) must be found in the tracking system. A track is required to have a minimum transverse momentum of 120 MeV, and to fulfill standard quality cuts as given in [72].

5. The visible invariant mass, W_{vis}, is required to be in the range of 2.5 GeV up to $0.64E_{\mathrm{b}}$. The upper limit is dictated by the high background of annihilation events at large W_{vis} values. The quantity W_{vis} is reconstructed from tracks measured in the central tracking detectors and the position and energy of clusters measured in the electromagnetic and hadronic calorimeters, as well as in the forward detectors FD and SW. A matching algorithm [72] is used to avoid double counting of the particle momenta in the calorimeters and tracking chambers.

6. To reduce the remaining background due to beam–gas interactions, the z position of the primary vertex $|\langle z_0 \rangle|$ is required to be less than 4 cm from the nominal interaction point. Here $\langle z_0 \rangle$ is calculated as the error weighted average of the z coordinates of all tracks at the point of closest approach to the origin in the $r - \phi$ plane. We also require that the distance d_0 of the primary vertex from the beam axis should be less than 0.5 cm.

7. In order to ensure that the event is well contained in the detector and to reduce background from beam–gas interactions, the total energy measured in the event must be less than $2.2E_{\mathrm{b}}$.

The numbers of events selected in each data taking period together with the numbers of signal events after subtracting the background contributions described below are given in Table 1. Only signal events, but split into two ranges of Q^2 used for F_2^γ measurement, are given in Table 2. The average measured virtuality $\langle Q^2 \rangle$ is also given for each Q^2 range and each data taking period.
Trigger efficiencies were evaluated from the data using sets of separate triggers and found to be larger than 99% for the events within the selection cuts.

Several Monte Carlo generators have been compared to the data or have been used to correct the data for detector effects. For details on Monte Carlo programs mentioned below see Section 6. To simulate the signal events we use HERWIG 5.9+k_{t} (dyn) [59], a general purpose Monte Carlo program that includes deep inelastic electron photon scattering. The version uses a modified transverse momentum distribution, k_{t}, for the quarks inside the photon, with the upper limit dynamically (dyn) adjusted according to the hardest scale in the event, which is of order Q^2. In order to have an additional model that contains different assumptions for modeling the hard scattering and the hadronisation process the Monte Carlo program PHOJET 1.05 was also used to simulate signal events. PHOJET simulates hard interactions through perturbative QCD and soft interactions through Regge phenomenology, and the hadronisation is modeled by PYTHIA [57]. Several HERWIG and PHOJET samples were generated (with the integrated luminosity more than five times that of the data) using

year / luminosity	1998 / 168.5 pb^{-1}	1999 / 208.3 pb^{-1}	2000 / 215.9 pb^{-1}
Data selected	7003	8414	8384
Data signal	6447 ± 84	7745 ± 92	7657 ± 92
HERWIG signal	6538 ± 16	7738 ± 19	8010 ± 20
Backgrounds			
$\gamma^\star\gamma \to \tau^+\tau^-$	349 ± 7.7	416 ± 9.3	446 ± 9.7
$\gamma^\star\gamma \to e^+e^-$	146 ± 5.0	174 ± 6.0	200 ± 6.7
$\gamma^\star\gamma^\star \to$ hadrons	27 ± 0.6	32 ± 0.7	32 ± 0.7
$Z_0/\gamma^\star \to$ hadrons	25 ± 0.9	36 ± 1.6	38 ± 2.0
4–fermion eeqq	6 ± 0.5	7 ± 0.6	8 ± 0.6

Table 1: The numbers of selected events and signal events (selected events corrected for background) in the data compared to the signal predictions from the HERWIG program. The expected numbers of background events for the dominant sources according to Monte Carlo are also listed. The errors given are only statistical.

year	Q^2 range [GeV^2]	OPAL		HERWIG		
		events	$\langle Q^2\rangle$ [GeV^2]	events	$\langle Q^2\rangle$ [GeV^2]	$\langle Q^2_{tru}\rangle$ [GeV^2]
1998	7 – 13	2576 ± 53	11.0	2653 ± 10	11.0	9.4
	13 – 27	3870 ± 65	17.7	3884 ± 12	17.7	18.3
1999	7.5 – 14	3050 ± 57	11.9	2824 ± 12	12.0	10.1
	14 – 30	4695 ± 72	19.3	4914 ± 15	19.4	19.9
2000	8 – 15	2876 ± 56	12.8	3008 ± 12	12.9	10.8
	15 – 33	4780 ± 73	20.7	5002 ± 16	20.8	21.6

Table 2: The numbers of signal events in the data compared to the signal predictions from the HERWIG program split into two bins in Q^2. The average $\langle Q^2\rangle$ values at the detector level and true values of average $\langle Q^2_{tru}\rangle$ predicted by HERWIG are listed.

the GRV LO [74] parameterisation of F_2^γ, taken from the PDFLIB library [81], as the input structure function. This version assumes massless charm quarks. Since PHOJET is not based on the cross-section formula for deep inelastic electron photon scattering, the program always produces the same x and Q^2 distributions independent of the input structure function. Therefore the x distribution of PHOJET, for the use in unfolding procedure, was reweighted to match that from HERWIG using GRV LO. This is not an important limitation, because the main emphasis lies on the alternative hadronisation model. The result of the unfolding procedure is expected to be almost independent of the actual underlying x distribution of the Monte Carlo sample used. The number of expected signal events predicted by HERWIG are listed in Table 1. The same events, but split into two bins of Q^2 together with average measured and true $\langle Q^2\rangle$ values are listed in Table 2. The measured values of $\langle Q^2\rangle$ in data and MC simulation agree well. The true values of $\langle Q^2\rangle$ are slightly different because of the cuts applied - at the true level only cuts defining the bins in Q^2 are applied. The average values of Q^2 for the F_2^γ measurement are obtained as the luminosity weighted average of the true values listed in Table 2.

The dominant background comes from the reaction $e^+e^- \to e^+e^- \tau^+\tau^-$ proceeding via the multiperipheral process shown in Fig. 3b, with $e^+e^- \to e^+e^- e^+e^-$ giving a smaller contribution. These were simulated using the Vermaseren program [73]. The process $Z^0 \to$ hadrons also contributes significantly and was simulated using PYTHIA. The next largest background comes from non-multiperipheral four-fermion events with $eeq\bar{q}$ final states (denoted by 4-fermion eeqq) and was simulated with GRC4f [62]. Because our aim is to measure the structure function of the quasi-real photon, events stemming from the interaction of two virtual photons with hadronic final states are also treated as background. These events were generated using PHOJET 1.10 with the virtualities of both photons to be above 4.5 GeV^2. The contributions to the background from all other Standard Model processes was found to be negligible. The expected numbers of events from the dominant background sources for each data taking period are listed in Table 1.

None of the Monte Carlo programs used in this analysis contain radiative corrections to the deep inelastic scattering process. These are dominated by initial state radiation from the deeply inelastically scattered electron. The final state radiation is experimentally to a large extent absorbed in the scattered electron energy measurement, due to the granularity of the calorimeters. The Compton scattering process contributes very little, and the radiative corrections due to radiation of photons from the electron that produced the quasi-real target photon where shown to be small [82].

In this analysis the radiative corrections have been evaluated using the TWOGAM 2.04 Monte Carlo program [61], which includes initial state and final state radiation from both electron lines. The calculations are performed using mixed variables, which means that Q^2 is calculated from electron variables, while W^2 is calculated from hadronic variables. The value of x is found from W^2 and Q^2, exactly as for experimental analysis. Samples of TWOGAM with radiative corrections switched on and off corresponding to the three average centre-of-mass energies of the data were generated separately. To each sample the experimental restrictions on the electron energy and polar angle, the minimum and maximum invariant mass and the anti-tag energy and angle were applied. The predicted ratio of the differential cross section for each bin of the analysis is used to correct the data, i.e. the measured F_2^γ (as well as the corresponding differential cross section $\mathrm{d}\sigma/\mathrm{d}x$) are multiplied by the ratio of the non-radiative to the radiative cross sections. The radiative corrections with statistical errors, weighted with the luminosity of the data samples, are given in Table 3. In Fig. 26 we show the value of the radiative corrections for the two ranges of Q^2 as a function of x for different subprocesses generated by TWOGAM as well as for the weighted average. Also the relative contribution of the individual subprocesses to the total cross section is shown in bottom plots. The radiative corrections are largely insensitive to the choice of F_2^γ used in the calculation.

Several theoretical models exist for how F_2^γ should behave as a function of P^2 [92, 100, 102]. They all predict a decrease of $F_2^\gamma(x, Q^2, P^2 \neq 0)$ with P^2 which is strongest at low values of x. The size of the effect was studied using the GRSc [100] and SaS1D [102, 103] parameterisations. A stand alone analytical program has been used to calculate average values of P^2 for each pair of (x, Q^2) values considered in the measurement. The ratio of $F_2^\gamma(x, Q^2, P^2 = 0)$ and $F_2^\gamma(x, Q^2, \langle P^2 \rangle)$ was used to obtain correction factors for the P^2 effect in case of F_2^γ and $\mathrm{d}\sigma/\mathrm{d}x$ measurements. The errors on the correction factors are taken to be the difference between the predictions from the GRSc and from the SaS 1D parameteri-

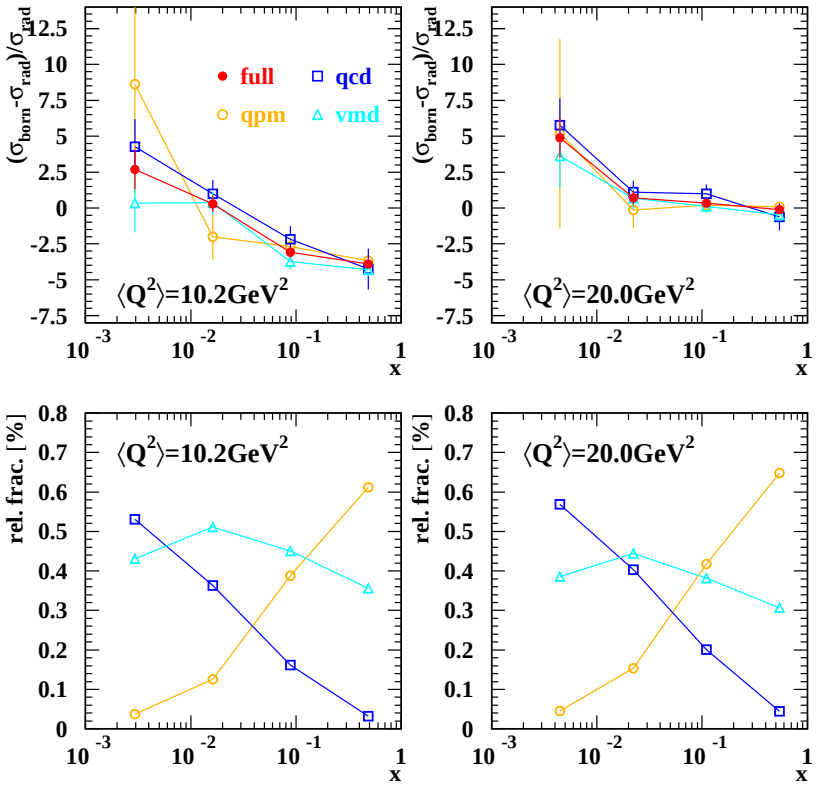

Figure 26: QED radiative corrections estimated with TWOGAM 2.04 Monte Carlo program in the phase space used for F_2^γ measurement in the latest OPAL analysis [143]. The relative difference of non-radiative and radiative with respect to the radiative cross section is shown for two ranges of Q^2 as a function of x for different subprocesses generated by TWOGAM as well as for the weighted average. The relative contribution of the individual subprocesses to the total cross section is shown in bottom plots.

sations. Luminosity weighted average values of $\langle P^2\rangle$ and the correction factors are given in Table 3.

Properties of single-tagged $\gamma^\star\gamma$ events

Scattered electrons in single tagged events are recorded on both sides of the OPAL detector. As the detector is fully symmetric there should be no statistically significant difference in any aspect between the events with electrons recorded on the left and on the right side. This has been checked to be the case.

A HERWIG Monte Carlo sample is used to correct the data for acceptance and resolution effects, and the PHOJET Monte Carlo is used to determine the systematic uncertainty on this correction due to the different hadronisation model. A comparison is made of data distributions with predictions from HERWIG and PHOJET. Variables calculated from the scattered electrons as well as variables calculated from the hadronic final state are studied. All Monte Carlo distributions shown here are normalized to the luminosity in data.

$\langle Q^2 \rangle$ [GeV^2]	x range	radiative cor. [%]	bin-centre cor. [%]	P^2 effect	
				$\langle P^2 \rangle$ [GeV^2]	cor. [%]
10.2	0.0009 - 0.0050	2.68 ± 1.37	3.61 ± 0.57	0.033 ± 0.005	9.81 ± 1.58
	0.0050 - 0.0273	0.74 ± 0.57	-0.23 ± 0.62	0.042 ± 0.003	11.67 ± 0.83
	0.0273 - 0.1496	-2.43 ± 0.35	-7.50 ± 0.82	0.075 ± 0.004	14.86 ± 0.18
	0.1496 - 0.8187	-3.38 ± 0.25	10.55 ± 0.62	0.095 ± 0.002	10.75 ± 0.41
20.0	0.0015 - 0.0074	4.88 ± 1.43	2.25 ± 0.35	0.033 ± 0.001	9.37 ± 0.42
	0.0074 - 0.0369	1.52 ± 0.51	-1.43 ± 0.63	0.052 ± 0.004	13.21 ± 0.38
	0.0369 - 0.1827	0.61 ± 0.30	-7.70 ± 0.87	0.092 ± 0.004	15.27 ± 0.14
	0.1827 - 0.9048	0.21 ± 0.20	6.06 ± 0.90	0.116 ± 0.002	9.24 ± 0.30

Table 3: The values of the corrections which have been applied to data, averaged over different data taking periods, are listed. For a given bin in Q^2 and x the correction is the difference of the corrected and non corrected cross sections as a percentage of the non corrected cross section. Average values of P^2 in each bin are also given. For the details of how the correction have been estimated and the meaning of the errors see text.

In Fig. 27 the energy scaled by the beam energy, azimuthal and polar angles of the tagged electrons are shown. All distributions are reasonably well described by the sum of the signal as predicted by HERWIG or PHOJET and the estimated background from other physics processes. In Fig. 27 also distributions are shown which characterize the hadronic final state: the number of tracks, $N_{\rm ch}$, the hadronic energy, $E_{\rm had}$, and the visible hadronic invariant mass, $W_{\rm vis}$. All the distributions are again reasonably well described by the sum of the signal as predicted by HERWIG and the estimated background from other physics processes. The description by the PHOJET Monte Carlo is somewhat less good.

In Fig. 28 we show the distributions of the missing longitudinal, Δp_z, and transverse, Δp_T momentum. The sum runs over all visible tracks and calorimeter deposits and include the scattered electron and the electron lost in the beam pipe (for which the momentum of the respective beam was assumed). Fig. 28 also shows the missing longitudinal and transverse momenta for the hadronic final state alone. Finally Fig. 28 shows the distribution of the transverse component of the energy out of the tagging plane. In all HERWIG plus background describes these distributions reasonably well, while the description is less good for PHOJET plus background.

In Fig. 29 we show the distributions of the following kinematical variables: the virtuality of the probe photon, Q^2, and the dimensionless scaling variables defined in Section 2, $y_{\rm e}$, z and x for tagged events. All these distributions are well described by the sum of the signal as predicted by HERWIG or PHOJET and the background processes.

Finally Fig. 30 shows the distributions of the energy and transverse energy flows in single tagged events averaged over all selected events. The polar angle in the definition of pseudorapidity, $\eta = -\ln\tan\theta/2$, is always measured with respect to the direction of that original beam electron which produced the tag electron in the detector. The azimuthal angle of the particles is always calculated with respect to the electron tagging plane. The Monte Carlo predictions are obtained as the weighted sums of HERWIG or PHOJET and the background processes, which are close to the predictions of HERWIG or PHOJET alone, within the cuts used in this analysis. In all HERWIG gives a good description of the data

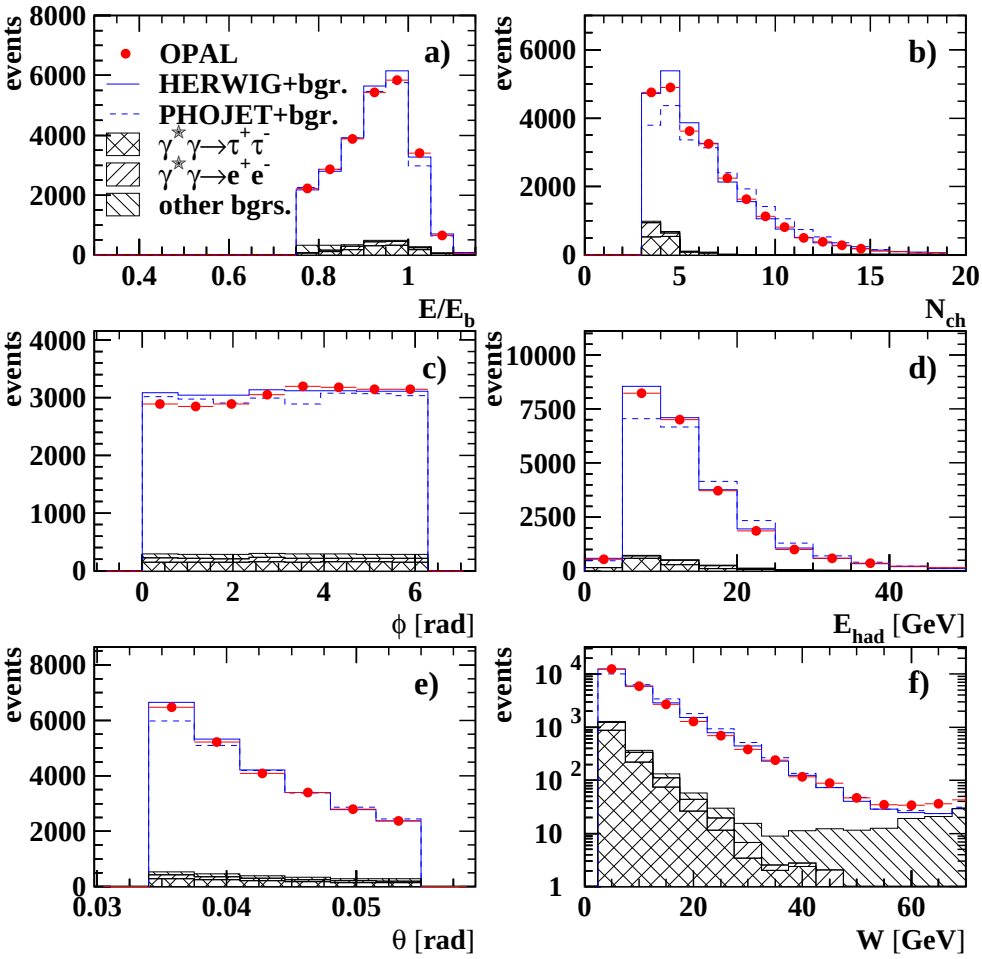

Figure 27: Distributions of a) the electron energy normalized to the energy of the beam electrons, b) the number of charged tracks, c) the electron azimuthal angle, d) the visible hadronic energy, e) the electron polar angle, f) the visible hadronic invariant mass, for selected single tagged events. The histograms are the predictions from HERWIG and PHOJET with background added and for the background itself. The errors are statistical only.

while PHOJET gives only a fair description. In particular, PHOJET predicts to much energy in the central region of pseudorapidity. Also in the azimuthal angle PHOJET underestimate the hadronic energy spread in the direction opposite that of the tagged electron.

Results

The aim of the analysis is the extraction of the photon structure function F_2^γ from the differential cross section given in Eq. 39. To measure the differential cross section $\mathrm{d}\sigma_{\mathrm{ee}}/\mathrm{d}x\,\mathrm{d}Q^2$ we perform a two dimensional unfolding using the GURU program [90]. As the variables for the unfolding we have chosen x and Q^2. For backward compatibility we use the same bins in x as in the previous OPAL paper [75]. In the variable Q^2 we use four bins between 4.5 GeV^2 and 50 GeV^2 with the two inner bins equal to the ranges used for F_2^γ measurement and given

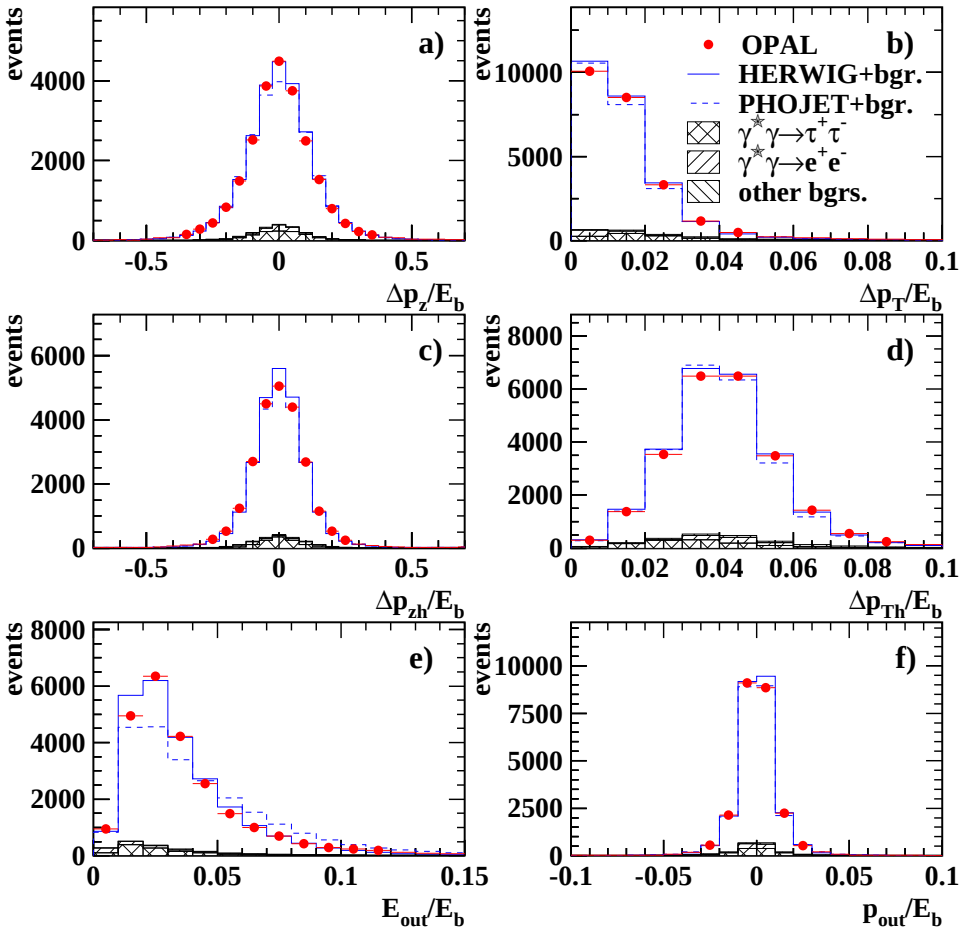

Figure 28: Distributions of missing transverse (Δp_T) and longitudinal (Δp_z) momentum for all particles (a,b), for hadrons only (c,d), and the scalar and vector sum of the energy component out of the tag plane (e,f), with HERWIG and PHOJET predictions and background estimates. All quantities shown are normalized to the energy of the beam electron. The errors are statistical only.

in Table 2. We obtain the photon structure function F_2^γ by dividing the differential cross sections $\mathrm{d}\sigma_{\mathrm{ee}}/\mathrm{d}x\,\mathrm{d}Q^2$ by the flux calculated according to the Eq. 38 and the appropriate kinematical term. The unfolded F_2^γ and the cross section $\mathrm{d}\sigma/\mathrm{d}x$ are further corrected for the QED radiative effects and for the P^2 effect. Bin-centre correction has been in addition applied to F_2^γ. Bin-centre correction is calculated as the average of GRV LO and SaS1D predictions for the correction from the average F_2^γ over the bin in x and the range of Q^2 to the value of F_2^γ at the nominal $(x,\langle Q^2\rangle)$ position. The luminosity weighted average values of bin-centre corrections and the nominal values of x and $\langle Q^2\rangle$ are given in Table 3. The errors on the bin-centre correction are obtained as a half of the difference between the predictions of GRV LO and SaS1D parameterisations.

The systematic error of the measurement has been evaluated taking into account several contributions. All changes of selection cuts, except the change of the cut on N_{ch}, are applied to the data. The list of systematic checks include:

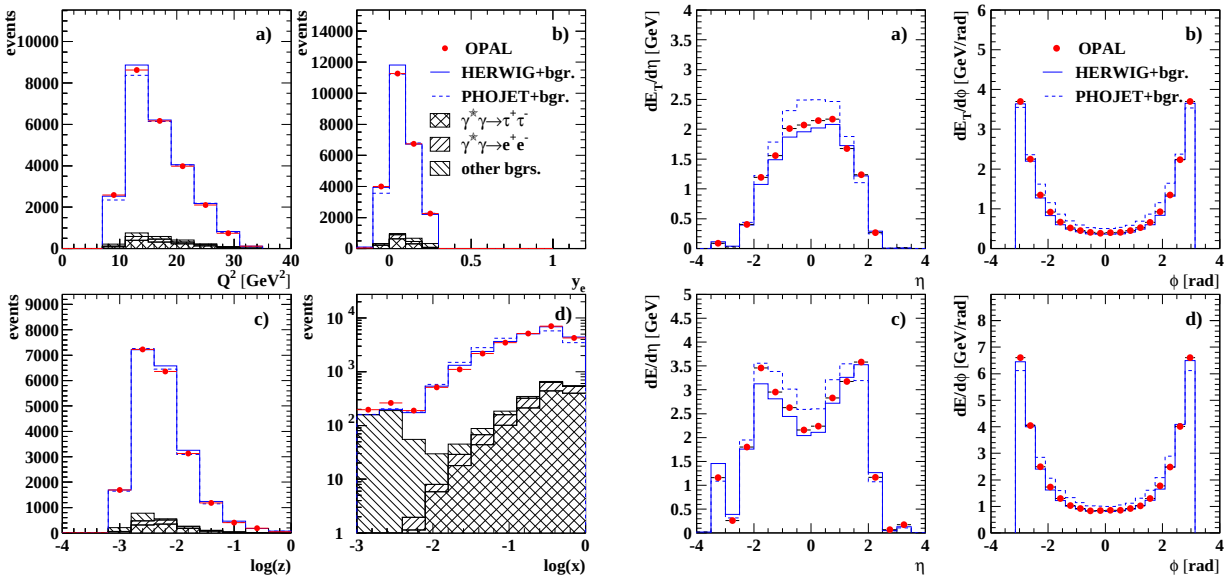

Figure 29: Distribution of kinematic quantities: a) Q^2, b) y_e, c)log(z) and d) log(x). The histograms are the predictions from HERWIG and PHOJET with background added and for the background itself. The errors are statistical only.

Figure 30: Distribution of transverse energy (a,b) and energy (c,d) flows in single tagged events versus pseudorapidity η and azimuthal angle ϕ. The polar angle in the definition of pseudorapidity is always calculated with respect to the direction of that beam electron which produced the tagged electron. The azimuthal angle is calculated with respect to the electron tagging plane. The histograms are the weighted sums of predictions of HERWIG or PHOJET and background processes. The errors are statistical only.

1. The dependence on the Monte Carlo model used in the unfolding has been estimated by repeating the unfolding using the PHOJET sample. Half of the difference between the results of unfolding based on HERWIG and on PHOJET has been taken as the systematic error, both for the positive and negative error.

2. The error due to a possible shift of the energy scale of the SW detectors was taken into account by scaling the electron energy by $\pm 1\%$, in accord with the uncertainty in the scale observed in single-tagged events, which is conservative because the differences observed for Bhabha events were much smaller.

3. The uncertainty in the description of the energy scale of the central electromagnetic calorimeter ECAL was taken into account by varying the energy scale by $\pm 3\%$ [75].

4. The uncertainty of the position of SW detectors in the plane perpendicular to the z-axis has been estimated changing the lower cut on θ by ± 0.2 mrad. This was estimated using back-to-back topology of Bhabha events.

5. The uncertainty in the description of the interaction point was estimated by changing the cut on $|\langle z_0 \rangle|$ by ± 1.0 cm and the cut on the distance of the primary vertex from the beam axis was changed by ± 0.1 cm.

6. The uncertainty in the measurement of hadronic energy was estimated by changing the lower cut on W ± 0.2 GeV and the upper cut by ± 3 GeV.

7. The cut on the number of charged tracks has been changed from $N_{\rm ch} \geq 3$ to $N_{\rm ch} \geq 4$. This change has been applied simultaneously to data and Monte Carlo.

8. The number of bins used for the measured variable can be different from the number of bins used for the true variable (though it should be at least as large). The standard result has 6 bins in the measured x variable. This was increased to 8 to estimate the systematic effects of unfolding.

The final results for F_2^γ and the cross section $\mathrm{d}\sigma/\mathrm{d}x$ are the average of the results obtained from unfolding using HERWIG and PHOJET. The total systematic error was obtained by adding in quadrature errors coming from the above contributions. The sum has been performed separately for positive and negative contributions. The errors from the QED radiative correction, correction for the P^2 effect as well as of the bin-centre correction have been added in quadrature to the total systematic error. In Table 5 we present the individual contributions to the total systematic error. The numbers are given as percentage of the nominal value, and are averaged over the different data taking periods. The main contribution to the systematic error comes from the modeling of the hadronic final state as predicted by HERWIG and PHOJET. In the lower Q^2 range the results are also quite sensitive to the precise determination of the position of SW detectors, and in the higher Q^2 range the energy scale in SW detectors plays a more significant role.

In Fig. 31 we present the measurements of the photon structure function in two bins of Q^2, and compare it with the results of the previous OPAL publication [75]. For this figure the P^2 correction, which is about 10%, was not applied, such that these measurements can be compared. The results agree well with the previous data. In Figs. 32 the measurement is presented including the correction for the target photon virtuality. The results are compared to predictions from structure functions based on different parton distribution functions. The results are compatible with a rise of F_2^γ with decreasing x. In Table 4 we give the measured differential cross sections for the process $\mathrm{e^+e^-} \to \mathrm{e^+e^-}\gamma^\star\gamma \to \mathrm{e^+e^-X}$ and the photon structure function F_2^γ as a function of x in two bins of Q^2. The discussion of the results presented here, together with the results on F_2^γ from other experiments will be given in Section 8.2.3.

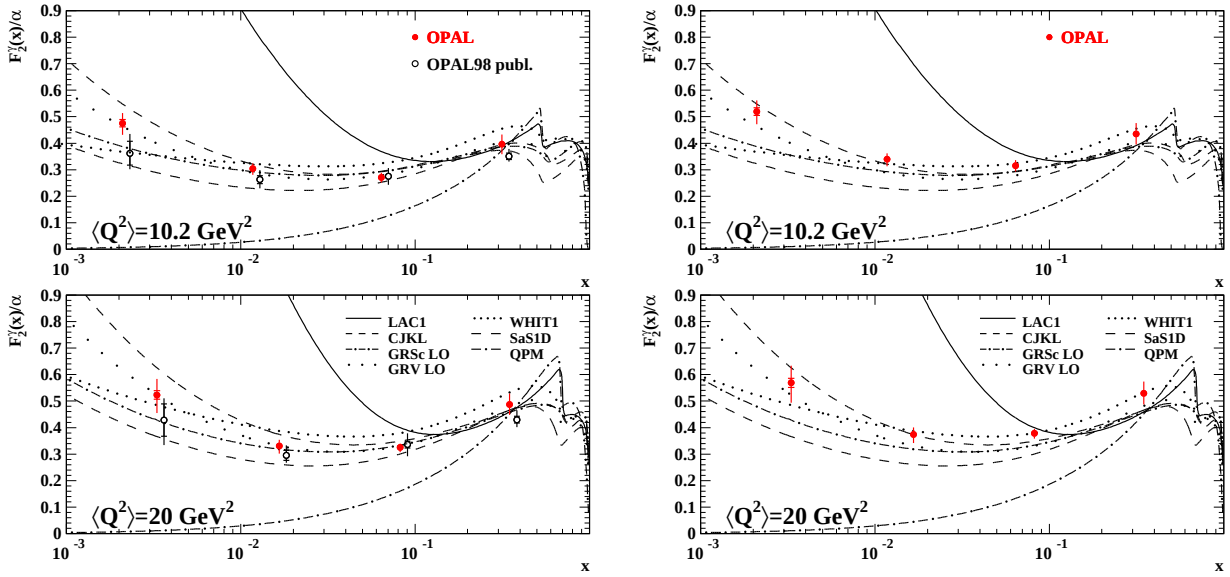

Figure 31: Photon structure function F_2^γ measured by the OPAL experiment in this analysis (full circle), not corrected for the target photon virtuality P^2, compared to the previously published result (open circle), shown in two bins of Q^2. For each point, the inner error bars show the statistical error and the full error bars show the total error. Predictions of different parameterisations of F_2^γ are shown as curves.

Figure 32: Photon structure function F_2^γ measured by the OPAL experiment, corrected for the virtuality of the target photon P^2, shown in two bins of Q^2. For each point, the inner error bars show the statistical error and the full error bars show the total error. Predictions of different parameterisations are shown as curves.

$\langle Q^2 \rangle$ [GeV^2]	x		$\mathrm{d}\sigma/\mathrm{d}x$ [pb]	F_2^γ/α
	range	bin-centre		
10.2	0.0009 - 0.0050	0.0021	$2098 \pm 62\ ^{+171}_{-192}$	$0.519 \pm 0.015\ ^{+0.040}_{-0.045}$
	0.0050 - 0.0273	0.0117	$682 \pm 14\ ^{+49}_{-57}$	$0.340 \pm 0.007\ ^{+0.021}_{-0.026}$
	0.0273 - 0.1496	0.0639	$215 \pm 4\ ^{+14}_{-15}$	$0.315 \pm 0.005\ ^{+0.020}_{-0.021}$
	0.1496 - 0.8187	0.3143	$74 \pm 1\ ^{+8}_{-7}$	$0.435 \pm 0.008\ ^{+0.040}_{-0.040}$
20.0	0.0015 - 0.0074	0.0033	$768 \pm 24\ ^{+80}_{-94}$	$0.569 \pm 0.017\ ^{+0.063}_{-0.073}$
	0.0074 - 0.0369	0.0166	$287 \pm 6\ ^{+20}_{-24}$	$0.374 \pm 0.008\ ^{+0.026}_{-0.031}$
	0.0369 - 0.1827	0.0821	$110 \pm 2\ ^{+4}_{-6}$	$0.379 \pm 0.006\ ^{+0.016}_{-0.019}$
	0.1827 - 0.9048	0.3483	$43 \pm 1\ ^{+4}_{-4}$	$0.530 \pm 0.008\ ^{+0.043}_{-0.042}$

Table 4: Results on the measurements of $\mathrm{d}\sigma/\mathrm{d}x$ and F_2^γ/α for two different values of photon virtuality $\langle Q^2 \rangle$. In each case the first error is statistical and the second systematic. The values of the cross section are the average values in the bin, and the values of F_2^γ are corrected to the bin centre.

Table 5: Systematic errors for F_2^γ/α as a function of x in bins of Q^2. The statistical error and the contributions to the systematic error from each of the sources are listed as a percentages of F_2^γ/α.

$\langle Q^2 \rangle$ [GeV^2]	x bin centre	F_2^γ/α	total error		$\theta_{\min}-$	$\theta_{\min}+$	$E_{\mathrm{SW}}+$	$E_{\mathrm{SW}}-$	$E_{\mathrm{had}}+$	$E_{\mathrm{had}}-$	$W_{\min}-$	$W_{\min}+$	$W\max+$	W_{ma}
			stat.	sys.										
10.2	0.0021	0.519	2.9	$^{+7.7}_{-8.7}$	4.72	−4.36	−0.65	−0.56	1.22	−1.54	−2.20	0.32	0.14	−0.
	0.0117	0.340	2.1	$^{+6.3}_{-7.6}$	4.99	−4.74	−1.10	0.53	0.89	−0.97	−1.79	−0.91	0.08	−0.
	0.0639	0.315	1.6	$^{+6.3}_{-6.7}$	5.25	−5.14	−1.71	2.01	0.43	−0.23	1.47	−2.60	0.02	−0.
	0.3143	0.435	1.8	$^{+9.2}_{-9.2}$	5.67	−5.55	−2.28	3.41	0.03	0.41	7.53	−4.28	−0.02	0.
20.0	0.0033	0.569	3.0	$^{+11.1}_{-12.8}$	−0.24	0.23	2.82	−4.25	2.20	−2.29	−3.67	0.64	0.15	−0.
	0.0166	0.374	2.1	$^{+7.0}_{-8.3}$	−0.27	0.26	2.78	−3.78	1.49	−1.59	−1.88	−0.35	0.08	−0.
	0.0821	0.379	1.6	$^{+4.2}_{-5.0}$	−0.30	0.31	2.81	−3.17	0.47	−0.56	1.68	−1.90	0.02	−0.
	0.3483	0.530	1.5	$^{+8.1}_{-7.9}$	−0.34	0.36	2.85	−2.86	−0.56	0.49	5.17	−3.60	−0.02	0.

$\langle Q^2 \rangle$ [GeV^2]	x bin centre	F_2^γ/α	total error		MC model	unfol. bins	bin centre	P^2 corr.	rad. corr.	$N_{\mathrm{ch}} > 3$	$\lvert z_0\rvert-$	$\lvert z_0\rvert+$	$\lvert d_0\rvert-$	$\lvert d_0$
			stat.	sys.										
10.2	0.0021	0.519	2.9	$^{+7.7}_{-8.7}$	±5.20	−0.98	±0.57	±1.58	±1.37	−1.23	−1.90	1.25	−0.23	0.1
	0.0117	0.340	2.1	$^{+6.2}_{-7.6}$	±2.65	−0.74	±0.62	±0.83	±0.57	−0.66	−2.41	1.56	−0.31	0.2
	0.0639	0.315	1.6	$^{+6.3}_{-6.7}$	±0.63	−0.28	±0.82	±0.18	±0.35	0.19	−3.05	1.97	−0.42	0.3
	0.3143	0.435	1.8	$^{+9.2}_{-9.2}$	±4.37	−0.08	±0.62	±0.41	±0.25	0.81	−3.62	2.39	−0.54	0.4
20.0	0.0033	0.569	3.0	$^{+11.1}_{-12.8}$	±10.02	−0.68	±0.35	±0.42	±1.43	−0.16	−2.18	1.34	−0.38	0.1
	0.0166	0.374	2.1	$^{+7.0}_{-8.3}$	±5.61	−0.50	±0.63	±0.38	±0.51	−0.38	−2.50	1.53	−0.45	0.2
	0.0821	0.379	1.6	$^{+4.2}_{-5.0}$	±1.06	−0.13	±0.87	±0.14	±0.30	−0.70	−2.95	1.82	−0.57	0.2
	0.3483	0.530	1.5	$^{+8.1}_{-7.9}$	±5.47	0.33	±0.90	±0.30	±0.20	−0.96	−3.41	2.15	−0.69	0.3

8.2.2 Measurement of F_2^γ by the OPAL experiment at high Q^2

The OPAL measurements of the hadronic structure function of the photon F_2^γ have been recently extended to an average Q^2 of $\langle Q^2 \rangle = 780$ GeV^2 using data collected at e^+e^- centre-of-mass energies from 183 to 209 GeV, with a luminosity weighted average of $\sqrt{s_{ee}} = 197.1$ GeV, taken in the years 1997-2000. The measurement is based on single tagged events with the scattered beam electron recorded at very high polar angles in the electromagnetic endcap calorimeters (EE). Here only the main results of the analysis will be given, and for more details the reader is referred to Ref. [140].

The single tagged events are selected by applying cuts on the scattered electrons and on the hadronic final state. The scattered electron is required to have energy $E' > 0.7E_b$ and polar angle in the range $230 < \theta < 500$ mrad. To remove electron candidates originating from energetic electromagnetic clusters stemming, e.g., from hadronic final states in the reaction $Z^0/\gamma^\star \to$ hadrons, an isolation cut is applied which requires that less than 3 GeV is deposited in cone of 500 mrad half-angle around the electron candidate. To ensure that the virtuality of the quasi-real photon is small, the highest energy electromagnetic cluster in the hemisphere opposite to the one containing the scattered electron must have an energy $E_a < 0.25E_b$. The number of tracks must be at least four, of which at least two tracks must not be identified as electrons. The visible invariant mass is required to be in the range $2.5 < W_{vis} < 60$ GeV. The quality of the description of the data by Monte Carlo models in this kinematical region is shown in Fig. 33. The data distributions of the energy and polar angle of the scattered electron are well described by both HERWIG and Vermaseren Monte Carlo models. For the variables related to the hadronic final state, the number of tracks N_{trk} and the visible hadronic invariant mass W_{vis}, there are apparent differences in shape.

The data have been unfolded using three bins in x spanning the range $0.15 - 0.98$ and for $400 < Q^2 < 2350$ GeV^2. The central values have been obtained using HERWIG and the RUN program [91] for the unfolding. Each data point is corrected for radiative effects using the RADEG program [89]. Bin-centre corrections are also applied as given by the average of the GRSc [100], SaS 1D [102], and WHIT1 [94] predictions for the correction from the average F_2^γ over the bin to the value of F_2^γ at the nominal x position at the bin centre. The measured F_2^γ/α, shown in Fig. 34 together with several theoretical predictions, exhibits a flat behaviour. It can be seen that in this high Q^2 regime the differences between these predictions are moderate, particularly in the central x-region. All these predictions are compatible with the data to within about 20%, with the WHIT1 parameterisation, which predicts the flattest behaviour, being closest to the data. The QPM curve, which models only the point-like component of F_2^γ, is calculated for four active flavours with masses of 0.325 GeV for light quarks and 1.5 GeV for charm quarks. This prediction shows a much steeper behaviour in x and is disfavoured by the data.

The same data have been used in [140] to measure F_2^γ at lower Q^2 but still only for $x > 0.1$. They are used together with the high Q^2 measurement presented above to study the evolution of F_2^γ with Q^2. The results are shown in Fig. 35. The data in Fig. 35a exhibit positive scaling violations in F_2^γ for the x ranges $0.10 - 0.25$ and $0.25 - 0.60$. For the range $0.60 - 0.85$, the data are compatible with the predicted scaling violations. To quantify the slope for medium values of x, where data are available at all values of Q^2, the data were

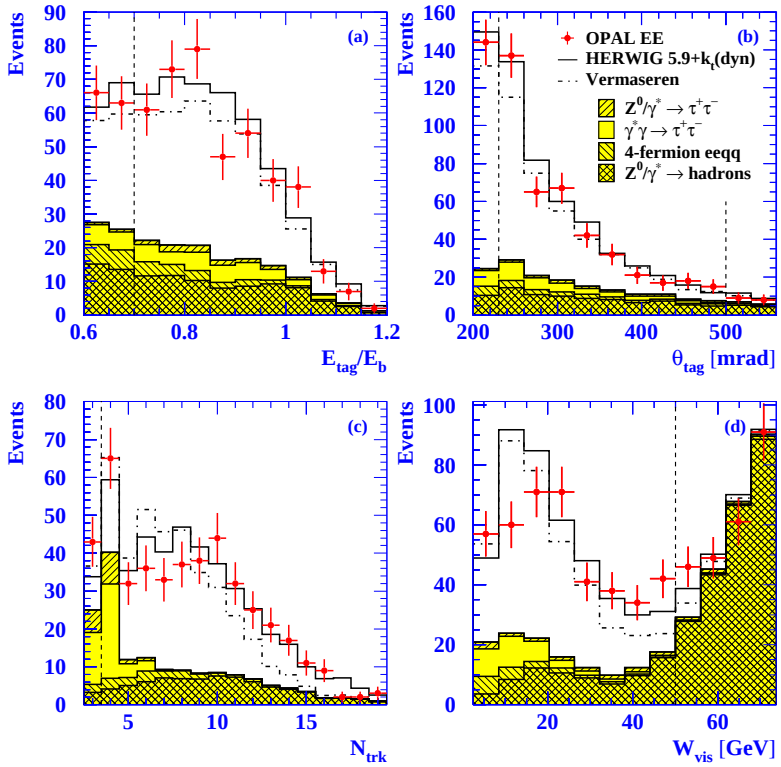

Figure 33: Comparison of OPAL data distributions of the single tagged events recorded in the central electromagnetic calorimeter (EE) with Monte Carlo predictions. The open histograms are the sum of the signal prediction and the contributions of the major background sources, shown for both HERWIG (solid line) and Vermaseren (dash-dotted line) models. The Monte Carlo predictions are normalised to the data luminosity. The distributions are: a) $E_{\rm tag}/E_{\rm b}$, the energy of the scattered electron as a fraction of the energy of the beam electrons; b) $\theta_{\rm tag}$, the polar angle of the scattered electron; c) $N_{\rm trk}$, number of tracks; d) $W_{\rm vis}$, the measured invariant mass of the hadronic final state. The errors given are only statistical.

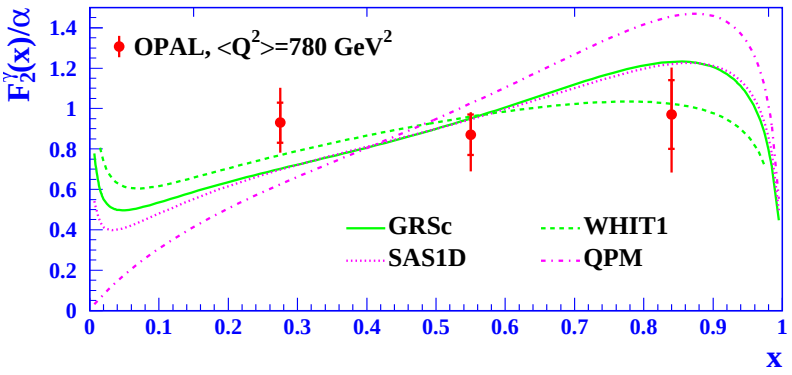

Figure 34: The measured F_2^γ/α as a function of x for $\langle Q^2 \rangle = 780$ GeV^2. The data are compared to the predictions from GRSc (full line), SaS1D (dotted line), WHIT1 (dashed line) and QPM (dot-dashed line) parameterisations of F_2^γ/α. The inner error bars represent the statistical errors and the outer error bars represent the statistical and systematic errors added in quadrature.

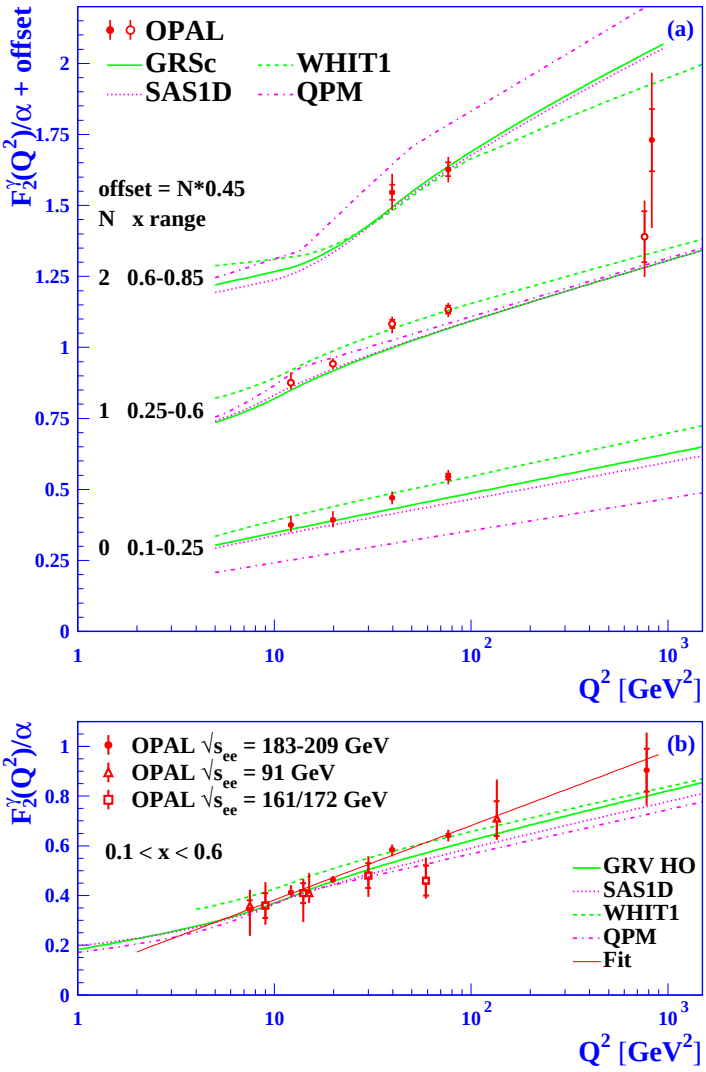

Figure 35: The evolution of F_2^γ/α as a function of Q^2 for several bins of x, (a) $0.10 - 0.25$, $0.25 - 0.60$ and $0.60 - 0.85$ and (b) for the central region $0.10 - 0.60$. The inner error bars represent the statistical errors and the outer error bars represent the statistical and systematic errors added in quadrature. In (a) the data are compared to the predictions from GRSc (full line), SaS1D (dotted line), WHIT1 (dashed line) and QPM (dot-dashed line) parameterisations of F_2^γ/α. In (b) GRSc has been replaced by the higher order prediction from GRV and, in addition, the result of the fit discussed in the text is shown.

fitted in the region $0.1 < x < 0.6$, with a linear function of the form $a + b \ln Q^2$, where Q^2 is in GeV^2, resulting in:

$$F_2^\gamma(Q^2)/\alpha = (0.08 \pm 0.02^{+0.05}_{-0.03}) + (0.13 \pm 0.01^{+0.01}_{-0.01}) \ln (Q^2/\mathrm{GeV}^2)$$

with a correlation between the two parameters of -0.98 and a χ^2/ndf of 10/3.

The data, together with the fit result, are shown in Fig. 35b. The result of the fit is in agreement and has significantly reduced errors on the parameters a and b compared to the

previous OPAL measurement of the Q^2 evolution of F_2^γ, published in [138]:

$$F_2^\gamma(Q^2)/\alpha = (0.16 \pm 0.05^{+0.17}_{-0.16}) + (0.10 \pm 0.02^{+0.05}_{-0.02}) \ln(Q^2/\mathrm{GeV}^2)$$

Both for the measurement of F_2^γ at $\langle Q^2 \rangle = 780$ GeV^2 and for the investigation of the Q^2 evolution of F_2^γ, the quark parton model (QPM) is not in agreement with the data. It shows a much steeper rise than the data as a function of x for $\langle Q^2 \rangle = 780$ GeV^2 and also a different behaviour in the Q^2 evolution. In contrast the leading order GRSc, SaS 1D and WHIT1 parameterisations and the higher order GRV parameterisation of F_2^γ are much closer to the data. This means that the corresponding parton distribution functions of the photon are adequate to within about 20% at large values of x and at $\langle Q^2 \rangle$ scales of about 780 GeV^2.

8.2.3 World results on the measurements of F_2^γ

In this section all presently available results on F_2^γ from LEP experiments as well as from experiments at other e^+e^- colliders are collected. The structure function F_2^γ is presented as a function of both x and Q^2. The range of $\langle Q^2 \rangle$ covered by the various experiments is $0.24 < \langle Q^2 \rangle < 780$ GeV^2, and the measurements reach as low x as approximately 10^{-3}. Of special interest is the low-x behaviour of F_2^γ in comparison to the proton structure function F_2^p. The large span of of the measurements as a function of Q^2 allows the investigation of the evolution of F_2^γ with Q^2. The results presented here are only the published results from the non LEP experiments and the published or preliminary (which are likely to be published soon) results from the LEP experiments. The following measurements are taken into account: AMY [123, 124], JADE [125], PLUTO [126, 127, 145], TASSO [128], TPC/2γ [129], TOPAZ [130], ALEPH [131], DELPHI [133], L3 [135, 136] and OPAL [137–140, 143]. Numerical values of all measurements of F_2^γ together with available errors are collected in Tables 20-24.

A summary of all measurements of F_2^γ as a function of x is shown in Fig. 36. The value of $\langle Q^2 \rangle$ for each measurement is given in parentheses close to the name of the experiment. The data are compared to the predictions of the GRV HO and SaS1D parameterisations of F_2^γ, drawn for the average Q^2 of the measurements shown in a particular plot. The parameterisations reflect the general behaviour of the data, however, there are regions where the agreement is not good. For example, the TPC/2γ data show quite unexpected shape in the low x region. This strange behaviour might be due to underestimated systematic errors in the TPC/2γ measurements. The measurements from the TOPAZ experiment rise faster towards low values of x than newer and more precise data from LEP. Also the measurements by TASSO and JADE, in spite of large errors, seem to be systematically shifted with respect to the theoretical predictions and newer LEP measurements. To get a quantitative estimation of the agreement between predictions of F_2^γ and the data we use simple χ^2 method:

$$\chi^2 = \sum_{i=1}^{\mathrm{ndf}} \left(\frac{F_{2,i}^\gamma - F_{2,par}^\gamma}{\sigma_i} \right)^2 \tag{83}$$

where the sum runs over all data points. The term $F_{2,i}^\gamma$ denotes the i-th measured value of F_2^γ and σ_i is its total error. The theoretical prediction $F_{2,par}^\gamma$ of a given parameterisation

is approximated by $F_2^\gamma(\langle x\rangle, \langle Q^2\rangle, 0)$ or $\langle F_2^\gamma(x, \langle Q^2\rangle, 0)\rangle$ depending on whether the measured value of F_2^γ is given at a point $\langle x\rangle$ or averaged over a bin in x. If systematic errors quoted by an experiment are asymmetric, than the value chosen depends on whether the prediction lies below or above the measured value. The above procedure does not take into account the correlations of the errors between the data points and the experiments. However, as mentioned in [7], because there are common sources of errors, it is most likely that by using this method the experimental errors are overestimated, and when using a more precise method, the predictions which are not compatible with the data would give even worse approximations of the data.
The data are compared to the predictions of GRV LO, GRV HO, GRSc, SaS1D, SaS 1M and the most recent CJKL parameterisations of F_2^γ. The results of this comparison are listed in Table 6. The number of data points used in the comparison depends on the lowest value of Q^2 for which a parameterisation of F_2^γ is valid. All measurements prior to LEP, but the TPC/2γ data points, are well described by the selected parameterisations. The TPC/2γ measurements which show an unexpected behaviour as a function of x are disfavoured by all parameterisations. The LEP measurements by OPAL, ALEPH and L3 are in good agreement with the predictions. In all cases the best value of χ^2/ndf give the ALEPH measurements. The measurements by the DELPHI experiment, which tend to rise faster towards lower values of x, than other measurements, give the worst agreement with the predictions. The data from most of experiments separately as well as combined data points from all experiments are in best agreement with the CJKL parameterisation, which is the most recent parameterisation available. The data at higher values of Q^2 are better described by the existing parameterisations than the data at lower values of Q^2.

The same data as in Fig. 36 are shown as a function of Q^2 in Fig. 37. The data are compared to the predictions of the GRV HO and SaS1D parameterisations of F_2^γ. The measurements are separated into bins of x, with bin boundaries of 0.001, 0.01, 0.1, 0.2, 0.3, 0.4, 0.6, 0.8, 0.99, and central values $\langle x\rangle$ indicated in the figure. To separate the measurements in different bins of x, an offset value N has been added to each measurement and theoretical prediction. The theoretical predictions are obtained as the average F_2^γ/α in the bin. The general behaviour of the data is followed by the predictions. As expected, the photon structure function F_2^γ exhibits positive scaling violations for all values of x, with the slope slightly increasing with increasing x. The kinks in the theoretical predictions are caused by the charm threshold. The charm quark contribution to F_2^γ gets larger at higher values of Q^2.
To study the Q^2 evolution of F_2^γ usually data are fitted in the medium range of x, with a linear function of the form $a + b \ln Q^2$, where Q^2 is in GeV^2. The recent fit of that form to the OPAL data in the region $0.1 < x < 0.6$ and $7.5 < Q^2 < 780$ GeV^2, was discussed in the previous section, and reads:

$$F_2^\gamma(Q^2)/\alpha = (0.08 \pm 0.02^{+0.05}_{-0.03}) + (0.13 \pm 0.01^{+0.01}_{-0.01}) \ln (Q^2/\mathrm{GeV}^2)$$

A similar study has been performed by the L3 experiment in [136]. The data were fitted in two regions of x, $0.01 < x < 0.1$ and $0.1 < x < 0.2$, using the Q^2 range of $1.2 - 30$ GeV^2. The results of the fit are:

$$F_2^\gamma(Q^2)/\alpha = (0.13 \pm 0.01 \pm 0.02) + (0.080 \pm 0.009 \pm 0.009) \ln (Q^2/\mathrm{GeV}^2) \quad \text{in} \quad 0.01 < x < 0.1$$
$$F_2^\gamma(Q^2)/\alpha = (0.04 \pm 0.08 \pm 0.08) + (0.13 \pm 0.03 \pm 0.03) \ln (Q^2/\mathrm{GeV}^2) \qquad \text{in} \quad 0.1 < x < 0.2$$

Exp. name	ndf	χ^2/ndf					
		GRV LO	GRV HO	GRSc	SaS1D	SaS 1M	CJKL
AMY	8	0.75	1.15	0.73	0.98	0.91	0.65
JADE	8	1.01	1.16	1.01	1.09	1.00	0.79
PLUTO	13	0.50	0.46	0.60	0.60	0.51	1.22
TASSO	5	0.97	0.76	1.16	1.03	0.85	1.29
TOPAZ	8	2.02	2.41	1.87	2.53	2.03	1.77
TPC/2γ	19/15/11	4.67	4.27	7.02	2.09	4.06	2.43
ALEPH	27	0.41	0.68	0.48	1.09	0.59	0.35
DELPHI	28	2.96	2.59	3.42	5.69	3.75	1.80
L3	28	2.16	1.96	1.52	3.62	2.03	0.94
OPAL	26	1.54	2.03	1.79	3.91	1.83	1.02
All	170/166/162	1.91	1.93	2.08	2.83	2.03	1.16
$Q^2 > 4$ GeV^2	137	1.42	1.56	1.48	2.72	1.66	1.13

Table 6: Quantitative comparison of predictions of selected parameterizations with measurements of F_2^γ. Listed are the number of data points (ndf) and the values of χ^2/ndf calculated using Eq. 83 for the individual experiments, for all data points (All) and for the measurements with $Q^2 > 4$ GeV^2. The number of data points used in the comparison depends on the lowest value of Q^2 for which a parameterisation of F_2^γ is valid. The TPC/2γ measurement at $\langle Q^2 \rangle = 0.24$ GeV^2 is outside the validity of all the parameterisations listed here. The minimum Q^2 for the GRSc parameterisation is $Q_0^2 = 0.5$ GeV^2 and for the CJKL parameterisation is $Q_0^2 = 1$ GeV^2. This reduces the number of TPC/2γ data points used in the comparison to 15 and 11, for GRSc and CJKL parameterisations, respectively.

with χ^2/ndf of 0.69 and 0.13, respectively. The results of the fit are in agreement with the recent L3 measurement [146] of F_2^γ at $Q^2 = 120$ GeV^2. There is also a nice agreement between OPAL and L3 measurements.

8.2.4 Charm structure function of the photon

The first measurement of the photon structure function F_2^γ for heavy quarks has been performed by the OPAL experiment in [141]. This measurement has been later extended to the full LEP statistics [142]. The production of charm quarks has been studied in deep inelastic electron-photon scattering using data collected at e^+e^- centre-of-mass energies $\sqrt{s_{ee}} = 183 - 209$ GeV, with a luminosity weighted average of $\sqrt{s_{ee}} = 196.6$ GeV. The charm quarks have been identified by full reconstruction of charged $D^\star$ mesons using their decays into $D^0\pi$ with D^0 observed in two decay modes.with charged particle final states, $K\pi$ and $K\pi\pi\pi$. Fig. 38 shows the difference between the $D^\star$ and D^0 candidate masses for both decay channels combined. A clear peak is observed around the mass difference between the $D^\star$ and the D^0 meson, which is $\Delta m_0 = 0.1454$ GeV [1]. In Fig. 38 we also show a fit of a Gaussian for the signal and a power law function of the form $a(\Delta m - m_\pi)^b$, for the back-

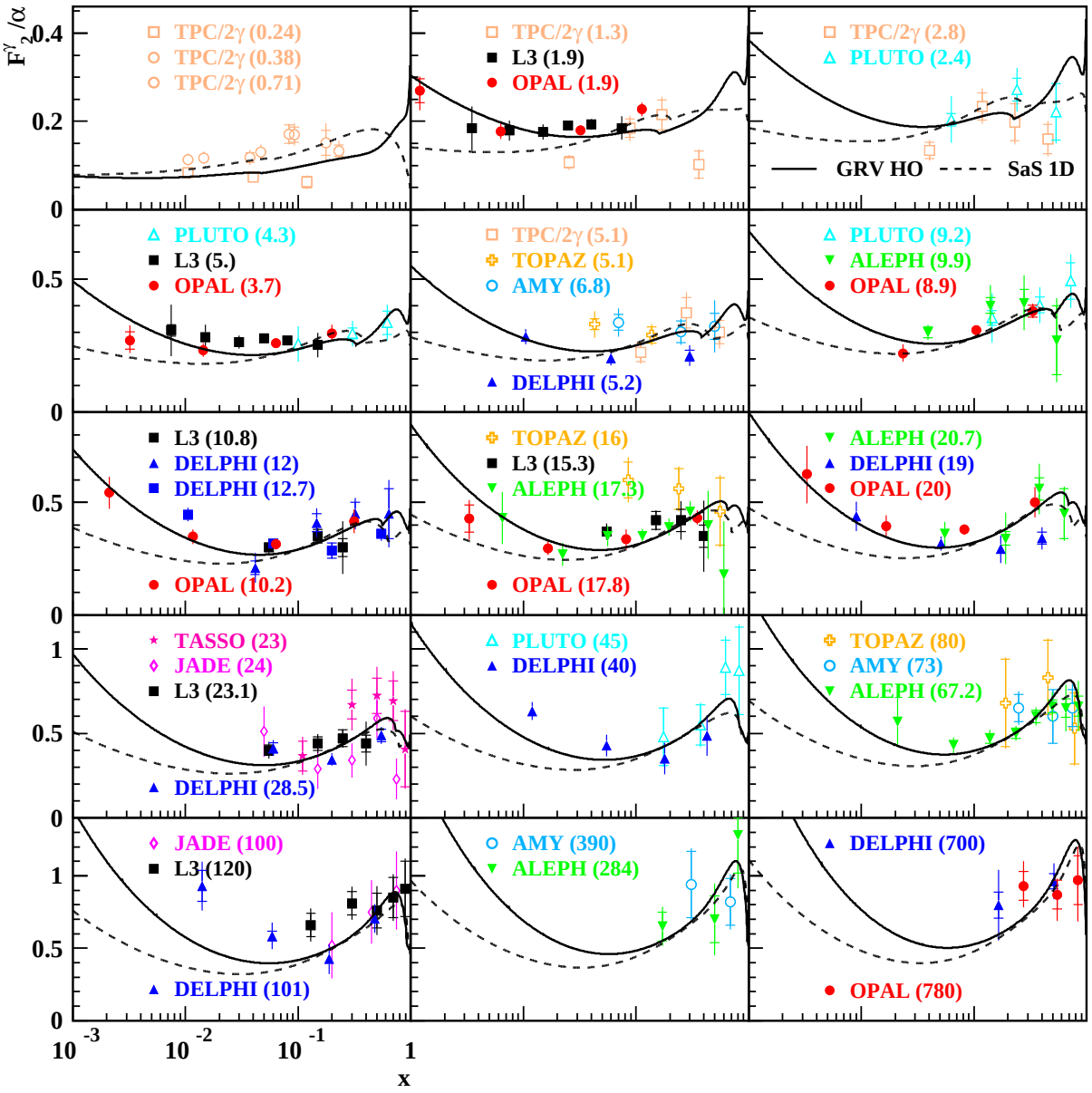

Figure 36: Compilation of all available measurements of F_2^γ as a function of x. The measured values of F_2^γ/α are compared to predictions from the GRV HO and SaS1D parameterisations of the parton distribution functions. The curves are drawn for the average Q^2 of the measurements shown in a particular plot. The statistical error is given by the inner error bars, and the statistical and systematic errors added in quadrature (or the total error) as full error bars. The numbers in parentheses close to the name of experiment denote average $\langle Q^2 \rangle$ of the measurement.

ground contribution. An absolute prediction of the combinatorial background measured from the data using events with a wrong charge pion for the $D^\star \to D^0\pi$ decays. The cross section $\sigma^{D^\star}$ for production of charged $D^\star$ in the reaction $e^+e^- \to e^+e^-D^\star X$ has been measured in a restricted kinematical region where $p_t^{D^\star} > 1$ GeV for an electron scattering angle of 33–55 mrad, or $p_t^{D^\star} > 3$ GeV for 60–120 mrad, $|\eta^{D^\star}| < 1.5$ and $5 < Q^2 < 100$ GeV^2 in two bins of

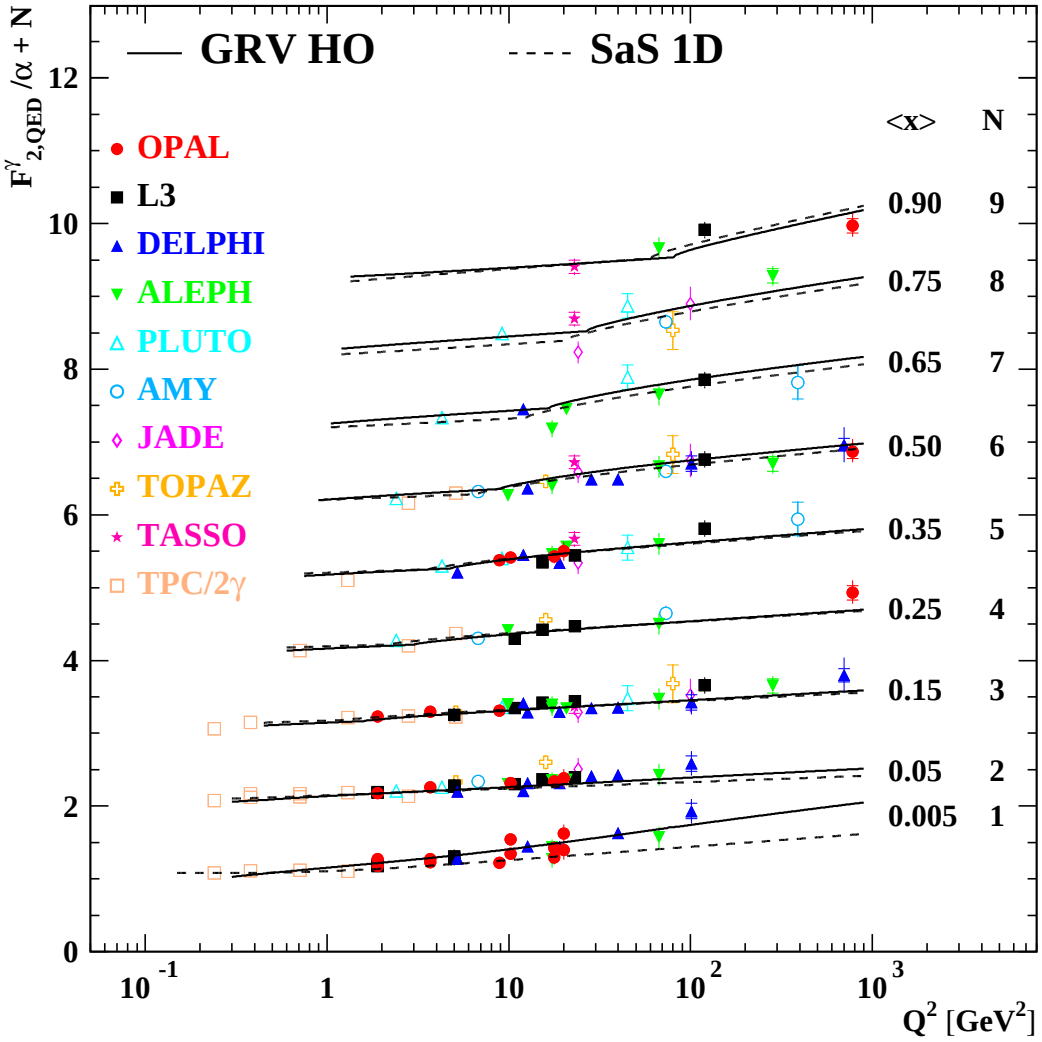

Figure 37: Compilation of all available measurements F_2^γ as a function of Q^2 in several bins of the variable x. The measured values of F_2^γ/α are compared to the predictions based on the GRV HO and SaS1D parameterisations of the parton distribution functions. The statistical error is given by the inner error bars, and the statistical and systematic errors added in quadrature (or the total error) as full error bars. The bin boundaries in x are 0.001, 0.01, 0.1, 0.2, 0.3, 0.4, 0.6, 0.8, 0.99, with central values $\langle x \rangle$ indicated in the figure. To separate the measurements in different bins of x, an offset N shown in the figure has been added to each measurement and theoretical prediction.

x, $0.0014 < x < 0.1$ and $0.1 < x < 0.87$. Within errors the cross section can be described by the HERWIG model. From $\sigma^{D^\star}$ the charm production cross section $\sigma(\mathrm{e^+e^-} \to \mathrm{e^+e^-c\bar{c}X})$ and the charm structure function of the photon $F_{2,c}^\gamma$ are obtained by extrapolation in the same bins of x and Q^2, using Monte Carlo. The results of the measurement are presented in Fig. 39 and listed in Table 26. For $x > 0.1$, the perturbative QCD calculation at NLO agrees perfectly with the measurement. For $x < 0.1$ the point-like component, however calculated, lies below the data. Subtracting the NLO point-like prediction, a measured value for the hadron-like part of $0.154 \pm 0.059 \pm 0.029$ is obtained.

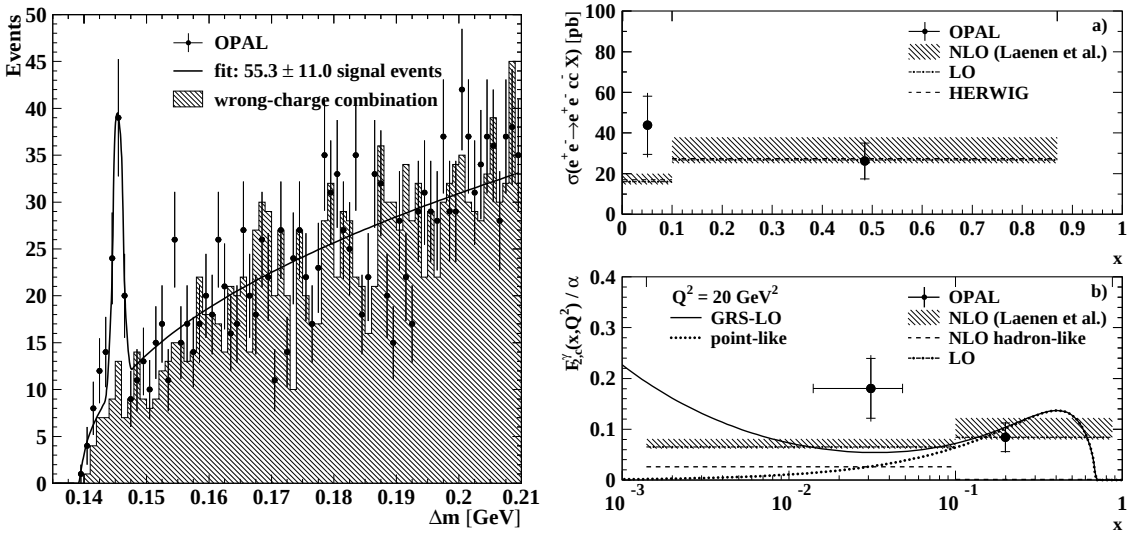

Figure 38: Distribution of the difference, Δm, between the $D^\star$ and D^0 candidate masses for both decay channels combined. The data are shown as points with statistical errors. The histogram represents the combinatorial background estimated using events with a wrong charge pion for the $D^\star \to D^0\pi$ decays. The curve is the result of the fit to a Gaussian signal plus a power-law background function, as explained in the text.

Figure 39: OPAL results for (a) the cross section $\sigma(\mathrm{e^+e^-} \to \mathrm{e^+e^-\,c\bar{c}\,X})$, with $5 < Q^2 < 100$ GeV^2 and (b) for the charm structure function of the photon divided by the fine structure constant, $F_{2,c}^{\gamma}(x,Q^2)/\alpha$, at $Q^2 = 20$ GeV^2. The data points are the results obtained with the HERWIG Monte Carlo model. The outer error bar is the total error and the inner error bar the statistical error. The data points in (b) are placed at those x values that correspond to the average predicted $F_{2,c}^{\gamma}$ within a bin. The data are compared to the calculation of [26] performed in LO and NLO. The band for the NLO calculation indicates the theoretical error from uncertainties in the charm quark mass and renormalisation and factorization scales. In (a) the cross section prediction of the HERWIG Monte Carlo model is also given; (b) also shows the prediction of the GRS-LO parameterisation for the structure function at $Q^2 = 20$ GeV^2 and its point-like component separately.

8.3 Hadronic structure function of the electron

The measurements of the hadronic structure function of the electron F_2^e have been performed so far only by the OPAL [143] and DELPHI [144] experiments. The OPAL analysis has been performed by the author of this paper. In the following we present the results obtained by both experiments and compare them with theoretical predictions.

The OPAL analysis is essentially an extension of the analysis of the photon structure function F_2^γ presented in Section 8.2.1. In particular, exactly the same data and Monte Carlo samples have been used in both analyses. Therefore for the list of selection cuts, the discussion of the background processes and the quality of description of the data by the Monte Carlo models the reader is referred to Section 8.2.1. Here only some additional information on the differences between the measurements of F_2^γ and F_2^e will be given.

Phase space for the measurement of $d\sigma_{ee}/dz$	
OPAL	DELPHI
$E' > 0.75E_b$	$E' > 0.3E_b$
$34 < \theta < 55$ mrad	$35 < \theta < 155$ mrad
$W > \sqrt{3}$ GeV	$W > 3$ GeV

Table 7: Phase space used for the measurements of the cross section $d\sigma_{ee}/dz$ for the process $e^+e^- \to e^+e^-$ hadrons, by OPAL and DELPHI experiments.

The variable z, in opposite to the variable x, is calculated with respect to the beam particle (electron) of fixed and known momentum. It is informative to see the distribution of single tagged events in the kinematical plane (z, Q^2). As an example we show in Fig. 40 the distribution of single tagged events, selected in the year 1999, in the (z, Q^2) plane together with several lines representing fixed values of different kinematical variables.

One of the arguments in favour of measuring the electron structure function F_2^e is a much better reconstruction of the variable z than the variable x. This can be seen in Fig. 41 where the migrations of events in the (x,Q^2) and (z,Q^2) planes as well as the smearings of the variables x and z are shown. The plots in Fig. 41 are based on the HERWIG model. The similar plots obtained from PHOJET show the same general features. The base of an arrow is at the average generated values of x and Q^2 (z and Q^2) for a given bin. The head of the arrow is at the average reconstructed x and Q^2 (z and Q^2). The migration between different Q^2 bins is small. Also the migration between different z bins is rather small. However, the migration between different x bins is very large, and any attempt to measure x distribution requires an unfolding method. The same feature can be seen on the plots showing the smearings of the variables x and z. The variable z is fully determined by the energy and polar angle of the scattered beam electron, which are usually well reconstructed, whereas the measurement of the variable x requires additional information on the hadronic final state, which is not fully measured nor well modeled.

Due to small migrations in the variable z the measurement of the differential cross section $d\sigma_{ee}/dz$, does not require an unfolding procedure and a simple bin-by-bin correction is sufficient. As one can see from Fig. 40 the phase space available for the measurement is not easily divisible into rectangle bins in z and Q^2 unless one chooses very small bins (especially in small z region) or decides to fulfill the missing phase space regions using a model. The statistics does not allow to choose sufficiently small bins. As we do not want to bias the measurement assuming any model we decided to measure the cross section as a function of z in the phase space region defined by the cuts imposed by the experimental conditions. They are listed in Table 7. The bins in z have been chosen to be equidistant in the logarithmic scale and are given in Table 9.

The measured cross section $d\sigma_{ee}/dz$ is further corrected for the QED radiative effects, which were estimated using the TWOGAM 2.04 program, in a similar way as for the measurement of F_2^γ. The calculations are performed using mixed variables, which means that z and Q^2 are calculated from electron variables, while W^2 is calculated from hadronic variables. Samples of TWOGAM with radiative corrections switched on and off corresponding to the

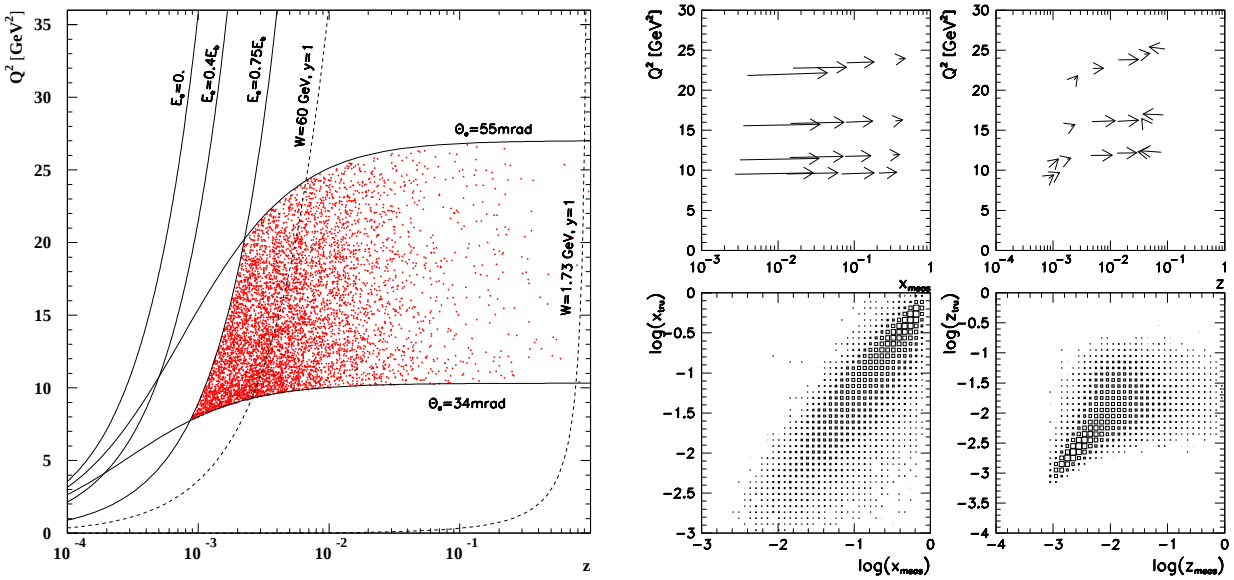

Figure 40: Kinematical plane (z,Q^2) with single tagged events selected by the OPAL experiment in the year 1999. Several lines representing fixed values of different kinematical variables are plotted. The beam energy used for the lines is $E_\mathrm{b} = 99$ GeV.

Figure 41: Migration of events in the (x,Q^2) and (z,Q^2) planes is shown on the upper plots for single tagged events using HERWIG Monte Carlo model. The base of an arrow is at the average generated x and Q^2 (z and Q^2) for a given bin. The head of the arrow is at the average reconstructed x and Q^2 (z and Q^2). Smearing of the variables x and z is shown on the bottom plots.

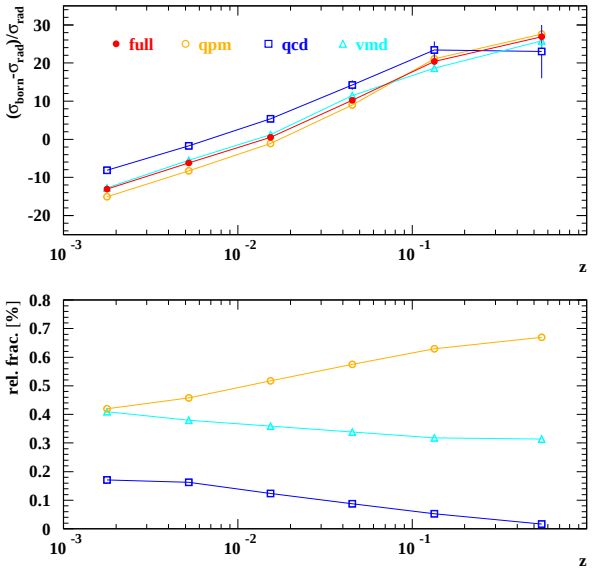

Figure 42: QED radiative corrections estimated with TWOGAM 2.04 Monte Carlo program in the phase space used for F_2^e measurement by OPAL [143]. The relative difference of non-radiative and radiative with respect to the radiative cross section is shown for $\langle Q^2 \rangle = 15$ GeV^2 as a function of z for different subprocesses generated by TWOGAM as well as for the weighted average. The relative size of the individual subprocesses is shown in bottom plot.

three average centre-of-mass energies of the data were generated separately. To each sample the experimental restrictions on the electron energy and polar angle, the minimum and maximum invariant mass and the anti-tag energy and angle were applied. The predicted ratio of the differential cross section for each bin of the analysis is used to correct the data, i.e. the measured differential cross section $\mathrm{d}\sigma_{\mathrm{ee}}/\mathrm{d}z$ is multiplied by the ratio of the non-radiative to the radiative cross sections predicted by TWOGAM. The radiative corrections with statistical errors, weighted with the luminosity of the data samples, are given in Table 8. In Fig. 42 we show the value of the radiative corrections as a function of z for different subprocesses generated by TWOGAM as well as for the weighted average. Also the relative contribution of the individual subprocesses to the total cross section is shown in the bottom plot.

The electron structure function F_2^e was obtained from the differential cross section $\mathrm{d}\sigma_{\mathrm{ee}}/\mathrm{d}z\,\mathrm{d}Q^2$ using Eq. 69. Although it is reasonable to measure the cross section in the phase space defined by the cuts on the scattered electron polar angle and its energy, the structure function F_2^e should be given as a function of z for an average value of Q^2. Therefore the structure function obtained from the cross section is further corrected to the bin-centre in the variable z and to the nominal value of $Q^2 = 15$ GeV^2, which is close to the average Q^2 in the high z range. The overal bin-centre correction is calculated as the average of GRV LO and SaS1D predictions for the correction from the average F_2^e over the bin in z and the range of Q^2 to the value of F_2^e at the nominal (x,$\langle Q^2\rangle$ =15 GeV^2) position. The luminosity weighted average values of bin-centre corrections and the nominal values of z and $\langle Q^2\rangle$ are given in Table 8. The errors on the bin-centre correction are obtained as a half of the difference between the predictions of GRV LO and SaS1D parameterisations. The measured electron structure function F_2^e and the cross section $\mathrm{d}\sigma_{\mathrm{ee}}/\mathrm{d}z$ do not need to be corrected for the P^2 effect (as in case of F_2^γ). However, the measured F_2^e should be compared with predictions which involve a dependence of F_2^γ on P^2. Most of parameterisations of F_2^γ available are only valid for $P^2 = 0$. Therefore all predictions used for the comparisons with measured F_2^e were corrected for the P^2 effect. The correction factor is defined as the ratio of $F_2^e(z, Q^2)$ obtained from the convolution of $F_2^\gamma(x, Q^2, P^2)$ and $\hat{f}_{\gamma^\star/e}(y, P^2)$ (see Eq. 70), and of $F_2^e(z, Q^2)$ obtained from the convolution of $F_2^\gamma(x, Q^2, P^2 = 0)$ and $\hat{f}_{\gamma^\star/e}(y, P^2)$.

z range	radiative cor. [%]	bin-centre cor. [%]
0.0009 - 0.00265	-12.62 ± 0.24	8.08 ± 0.53
0.00265 - 0.0078	-5.79 ± 0.21	-2.23 ± 0.05
0.0078 - 0.0230	0.82 ± 0.26	-4.22 ± 0.05
0.0230 - 0.0677	10.54 ± 0.34	-4.74 ± 0.09
0.0677 - 0.2000	20.78 ± 0.51	-4.41 ± 0.15
0.2000 - 0.9048	27.53 ± 0.95	2.59 ± 0.28

Table 8: The average values of the corrections which have been applied are listed. For a given bin in z the correction is the difference of the corrected and non corrected cross sections as a percentage of the non corrected cross section. For the details of how the correction have been estimated and the meaning of the errors see text.

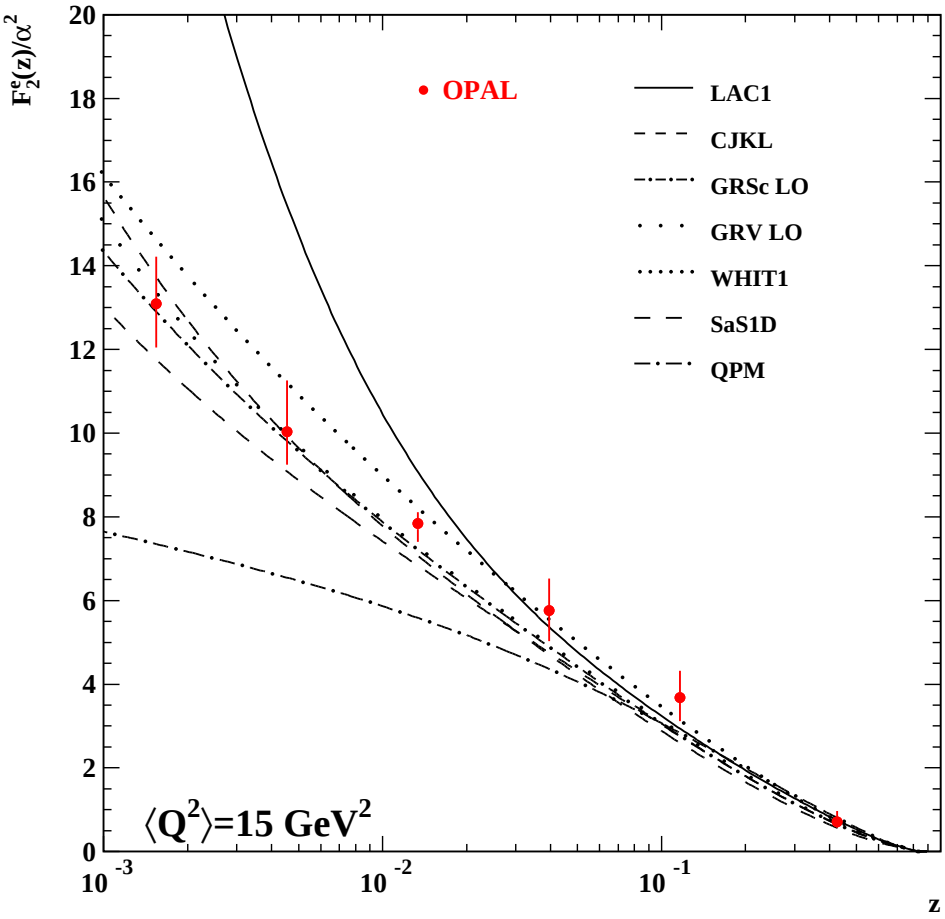

Figure 43: Electron structure function F_2^e divided by the fine structure constant squared shown as a function of z for an average $\langle Q^2 \rangle = 15$ GeV^2. The points represent the OPAL data with statistical (inner error bars) and total (outer error bars) errors. Predictions of several parameterisations are shown as curves.

The measured differential cross section $\mathrm{d}\sigma_{\mathrm{ee}}/\mathrm{d}z$ for the process $\mathrm{e^+e^-} \to \mathrm{e^+e^-}\gamma^\star\gamma \to \mathrm{e^+e^-X}$ in the phase space region defined in Table 7 and the measured structure function F_2^e for average $\langle Q^2 \rangle = 15$ GeV^2 are listed in Table 9 together with statistical and systematic errors. The systematic errors were estimated using essentially the same list of systematic checks as in the case of the measurement of F_2^γ described in Section 8.2.1 (the systematic error due to the P^2 effect and due to the check (8) are not applicable in the present analysis). The contribution from individual checks to the total systematic error are given in Table 10 as a percentage of the nominal value of F_2^e. The most significant contribution to the total systematic error comes from the energy scale uncertainty in the determination of the energy of the tagged electron. The effect of the modeling of the hadronic final state is only significant in the highest z bin. The electron structure function F_2^e measured by the OPAL experiment is shown in Fig. 43 and is listed in addition in Table 27. The data are compared to the predictions based on several parameterisations of F_2^γ convoluted with the photon flux according to Eq. 70. All theoretical predictions shown in Fig. 43 were corrected for the P^2

z		$\mathrm{d}\sigma/\mathrm{d}z$ [pb]	F_2^e/α^2
range	bin-centre		
0.0009 - 0.00265	0.00154	$6128 \pm 57\ ^{+518}_{-485}$	$13.10 \pm 0.12\ ^{+1.12}_{-1.04}$
0.00265 - 0.0078	0.00455	$2992 \pm 22\ ^{+280}_{-236}$	$10.04 \pm 0.08\ ^{+1.22}_{-0.79}$
0.0078 - 0.0230	0.01339	$857 \pm 8\ ^{+28}_{-47}$	$7.84 \pm 0.07\ ^{+0.26}_{-0.43}$
0.0230 - 0.0677	0.03946	$220 \pm 3\ ^{+30}_{-28}$	$5.76 \pm 0.09\ ^{+0.76}_{-0.73}$
0.0677 - 0.2000	0.11636	$48 \pm 1\ ^{+8}_{-7}$	$3.66 \pm 0.10\ ^{+0.64}_{-0.55}$
0.2000 - 0.9048	0.42539	$2.8 \pm 0.2\ ^{+1.0}_{-0.6}$	$0.71 \pm 0.03\ ^{+0.25}_{-0.13}$

Table 9: Results for the cross section $\mathrm{d}\sigma/\mathrm{d}z$ obtaineded in the phase space defined by $E' > 0.75E_\mathrm{b}$, $34 < \theta < 55$ mrad and $W > \sqrt{3}$ GeV and the structure function F_2^e/α^2 for the average $\langle Q^2 \rangle = 15$ GeV^2 measured by the OPAL experiment [143]. The first errors are statistical and the second systematic.

effect using average prediction of SaS1D and GRSc parameterisations of F_2^γ for the virtual photon and the method described above. The data clearly exclude the quark parton model (QPM). Also the rise as fast as predicted by the LAC1 parameterisation is disfavoured by the data. However, most of the modern predictions are in accord with the measured F_2^e.

The electron structure function F_2^e has been also measured at LEP by the DELPHI experiment [144]. The general procedure of extracting F_2^e from the single tagged events is similar to that applied in OPAL. The data samples used in the analysis correspond to integrated luminosities of 72 pb^{-1} accumulated by the DELPHI experiment at $\mathrm{e^+e^-}$ centre-of-mass energy $\sqrt{s_{\mathrm{ee}}} = 92.5$ GeV (LEP1), and of 487 pb^{-1} accumulated at several $\mathrm{e^+e^-}$ centre-of-mass energies in the range $\sqrt{s_{\mathrm{ee}}} = 189 - 209$ GeV (LEP2).

Single tagged events are selected by applying cuts on the scattered electrons and on the hadronic final state. A scattered electron is required to have energy $E' > 0.6E_\mathrm{b}$ and polar angle in the range $43.6 < \theta < 174.5$ mrad. This corresponds to the effective ranges of photon virtualities of $4.5 < Q^2 < 40$ GeV^2 at LEP1 and $16 < Q^2 < 80$ GeV^2 at LEP2. To ensure that the virtuality of the quasi-real photon is small, the highest energy cluster in the hemisphere opposite to the one containing the tagged electron must have an energy $E_a < 0.3E_\mathrm{b}$. The visible invariant mass W_{vis} is required to be greater than 3 GeV, and at least 3 tracks should be present in the hadronic final state. After these cuts, 2168 single tagged events were selected at LEP1, and 9697 events at LEP2 energies. Among them we expect 111 at LEP1 and 1027 at LEP2 background events, coming mainly from two photon production of tau pairs, four fermion final states and hadronic decays of Z^0 bosons. The data are corrected for detector effects using TWOGAM 2.03 Monte Carlo model.
The electron structure function F_2^e is obtained from the differential cross section $\mathrm{d}\sigma_{\mathrm{ee}}/\mathrm{d}z\mathrm{d}Q^2$ in the similar way as in the OPAL analysis. The cross section is measured in the phase space defined in Table 7. The electron structure function F_2^e is measured in several bins of Q^2, which effectively represent stronger cuts on the available phase space than the cuts listed in Table 7. The following ranges of Q^2 are choosen: $4.5 < Q^2 < 40$ GeV^2 at LEP1 energy, and four intervals at LEP2 energies: $16 < Q^2 < 20$ GeV^2, $20 < Q^2 < 30$ GeV^2, $30 < Q^2 < 50$ GeV^2 and $50 < Q^2 < 80$ GeV^2. The radiative corrections have been estimated

using TWOGAM 2.04 program. The size of the corrections and the estimation method are similar to that used by OPAL. The bin centre corrections are below 1% and were not applied to the data. The structure function F_2^e measured by the DELPHI experiment at LEP1 is listed in Table 28 and the one measured at LEP2 is shown in Fig. 44 and listed in Table 29. In Fig. 44 the data are compared to several theoretical predictions of F_2^e. For details see the caption of the figure. As in case of the OPAL measurement the measured F_2^e clearly disfavour QPM and steeply rising predictions like LAC1 (not shown), and due to large errors have no sufficient power to distinguish between the predictions shown in the figure.

Table 10: Systematic errors for F_2^e/α^2 as a function of z for the average $\langle Q^2 \rangle = 15$ GeV^2. The statistical error and the contributions to the systematic error from each of the sources are listed as a percentages of F_2^e/α^2.

z bin centre	F_2^e/α^2	total error		$\theta_{\min}-$	$\theta_{\min}+$	$E_{\mathrm{SW}}+$	$E_{\mathrm{SW}}-$	$E_{\mathrm{had}}+$	$E_{\mathrm{had}}-$	$W_{\min}-$	$W_{\min}+$	$W_{\max}+$	$W_{\max}-$
		stat.	sys.										
0.00154	13.10	0.9	$^{+8.5}_{-7.9}$	1.52	−1.44	−7.00	7.87	0.06	0.03	1.13	−1.41	0.45	−0.28
0.00455	10.04	0.8	$^{+12.2}_{-7.9}$	0.57	−0.62	−6.46	8.90	0.21	−0.27	2.15	−2.27	0.05	−0.06
0.01339	7.84	0.9	$^{+3.3}_{-5.5}$	0.30	−0.36	−2.66	−1.58	0.29	−0.25	2.50	−2.39	0.00	−0.02
0.03946	5.76	1.6	$^{+13.2}_{-12.7}$	0.37	−0.54	12.42	−11.73	0.48	−0.23	3.11	−2.35	0.00	0.00
0.11636	3.66	2.7	$^{+17.5}_{-15.0}$	0.26	−0.48	10.58	−4.36	0.59	0.00	2.85	−1.55	0.00	0.00
0.42539	0.71	4.2	$^{+35.2}_{-18.3}$	0.54	−0.43	21.85	3.90	0.22	−0.39	0.22	−4.71	0.00	0.00

z bin centre	F_2^e/α^2	total error		MC model	bin centre	rad. corr.	$N_{\mathrm{ch}} > 3$	$\lvert z_0\rvert-$	$\lvert z_0\rvert+$	$\lvert d_0\rvert-$	$\lvert d_0\rvert+$		
		stat.	sys.										
0.00154	13.10	0.9	$^{+8.5}_{-7.9}$	0.75	0.53	0.24	−1.39	−2.82	1.88	−0.51	0.45		
0.00455	10.04	0.8	$^{+12.2}_{-7.9}$	0.92	0.05	0.21	−2.73	−2.91	1.69	−0.52	0.27		
0.01339	7.84	0.9	$^{+3.3}_{-5.5}$	0.89	0.05	0.26	−1.64	−3.08	1.77	−0.63	0.41		
0.03946	5.76	1.6	$^{+13.2}_{-12.7}$	1.25	0.09	0.34	0.38	−3.40	1.58	−0.81	0.07		
0.11636	3.66	2.7	$^{+17.5}_{-15.0}$	2.10	0.15	0.51	−1.36	−4.35	3.00	−0.92	0.56		
0.42539	0.71	4.2	$^{+35.2}_{-18.3}$	11.64	0.28	0.95	2.63	−7.33	3.79	−0.64	0.00		

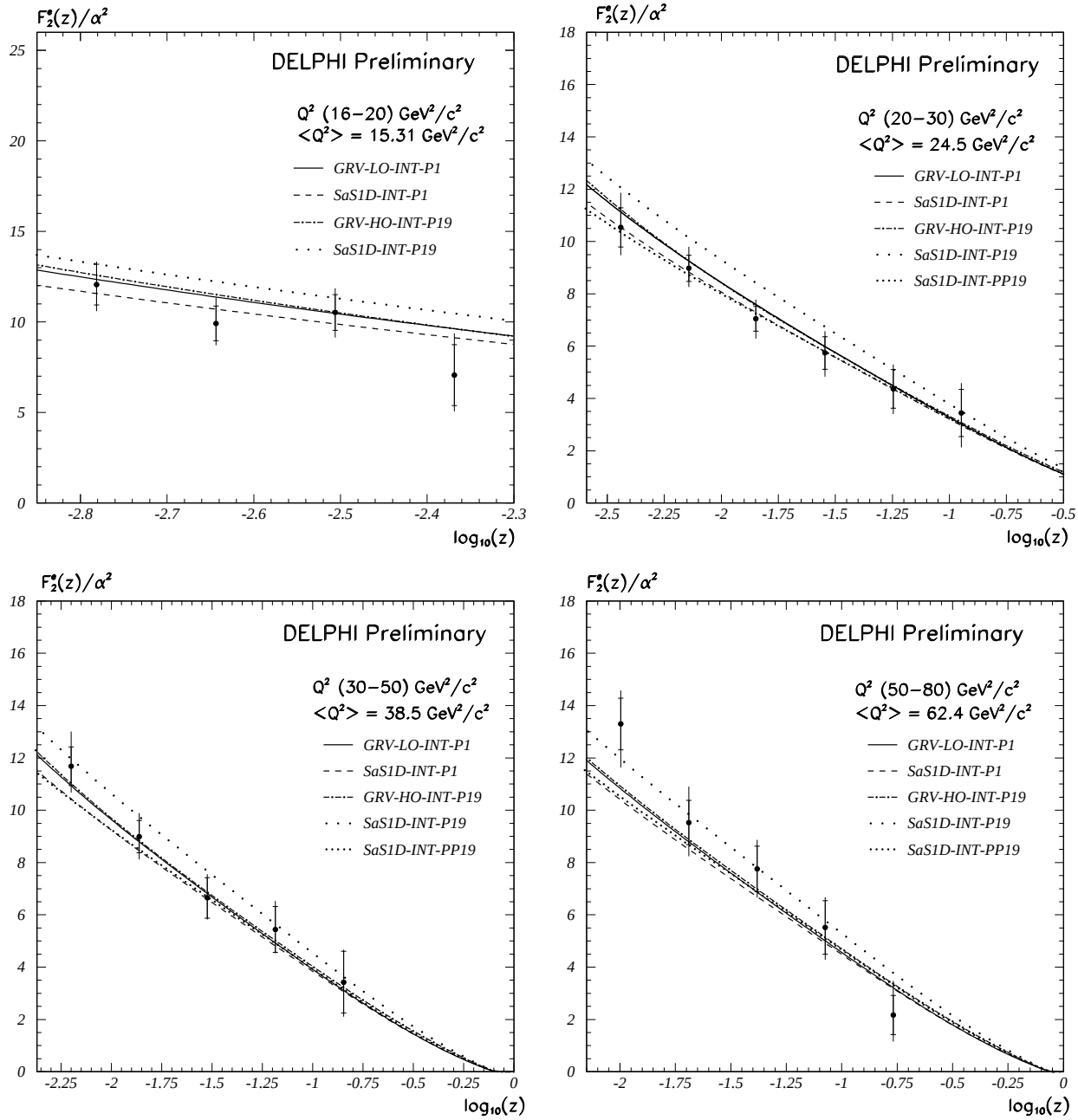

Figure 44: Electron structure function F_2^e divided by the fine structure constant squared is shown as a function of z in four intervals of Q^2 displayed together with the average values on the plots. The points represent the DELPHI LEP2 data with statistical (inner error bars) and total (outer error bars) errors. Predictions of several parameterisations are shown as curves. The predictions are obtained from the convolution of F_2^γ and the photon flux $\hat{f}_{\gamma^\star/e}(y, P^2)$ as given in Eq. 70. The integration over P^2 extends to 1 GeV^2 (INT-P1) or to 19 GeV^2 (INT-P19) in case when P^2 dependence is taken into account only in the photon flux, and to 19 GeV^2 (INT-PP19) in case of SaS1D parameterisation with P^2 dependence taken into account in both photon flux and F_2^γ.

9 Interactions of two virtual photons

In this Section we present the results on the structure of the highly virtual photon and on the structure of interactions of two highly virtual photons. The effective structure function of the virtual photon $F^{\gamma}_{\rm eff}$ can be measured in the kinematical region where $Q^2 \gg P^2 \gtrsim \Lambda$. If both photons have similar virtualities then the interference terms in the cross section (Eq. 13) can be large and there is no clear relation between the photon structure functions and the individual cross sections. In this situation the most proper measurements are the differential e^+e^- or total $\gamma^\star\gamma^\star$ cross sections. The effective structure function $F^{\gamma}_{\rm eff}$ has been measured so far only for the hadronic final state by the PLUTO and L3 experiments. Cross sections for the interactions of virtual photons have been measured for both leptonic (OPAL) and hadronic (OPAL, L3, ALEPH) final states.

9.1 Leptonic cross section for the scattering of two virtual photons

The differential cross section for the reaction $e^+e^- \to e^+e^- \mu^+\mu^-$, proceeding via the exchange of two highly virtual photons has been measured at LEP by the OPAL experiment [111]. The results of the measurement are shown in Fig. 45 and listed in Table 19. The measurements have been performed in two ranges of probe and target photon virtualities: $1.5 < Q^2 < 6$ GeV^2, $1.5 < P^2 < 6$ GeV^2 and $5 < Q^2 < 30$ GeV^2, $1.5 < P^2 < 20$ GeV^2. The data are compared with the predictions from the Vermaseren and GALUGA programs. The data are well described using the full cross section from Eq. 13. With the GALUGA program, it is possible to see the influence of the non-vanishing terms proportional to $\cos\bar{\phi}$ and $\cos 2\bar{\phi}$. If the terms are neglected, the predicted cross section grossly overestimates the measured cross section. This shows that both terms, $\tau_{\rm TT}$ and $\tau_{\rm TL}$, are present, mainly at $x > 0.1$, and that their contributions to the cross section are negative.

9.2 Effective hadronic structure function of virtual photon

The first measurement of the effective structure function of the virtual photon $F^{\gamma}_{\rm eff}$ has been performed by the PLUTO experiment [145]. The results of this measurement are presented in Fig. 46 and listed in Table 30. The average virtuality of the probe photons was $\langle Q^2 \rangle = 5$ GeV^2 and of the target photons $\langle P^2 \rangle = 0.35$ GeV^2. In Fig. 46a the measured structure function $F^{\gamma}_{\rm eff}$ as a function of x is compared with the predictions of $F^{\gamma}_{\rm eff}$ from the double virtual box diagram and with the predictions of the parameterizations GRSc and SaS1D for F^{γ}_2 and for $(F^{\gamma}_2 + 3/2F^{\gamma}_L)$, with F^{γ}_L calculated in all cases from the box diagram. In Fig. 46b the P^2 evolution of $F^{\gamma}_{\rm eff}$ measured by PLUTO is compared to the QPM predictions and to the predictions of the parameterizations GRSc and SaS 1D for $(F^{\gamma}_2 + 3/2F^{\gamma}_L)$, with F^{γ}_L calculated in all cases using the box diagram.

The only measurement of $F^{\gamma}_{\rm eff}$ at LEP has been performed by the L3 experiment [146]. The results of this measurement are shown in Fig. 47 and listed in Table 31. The average

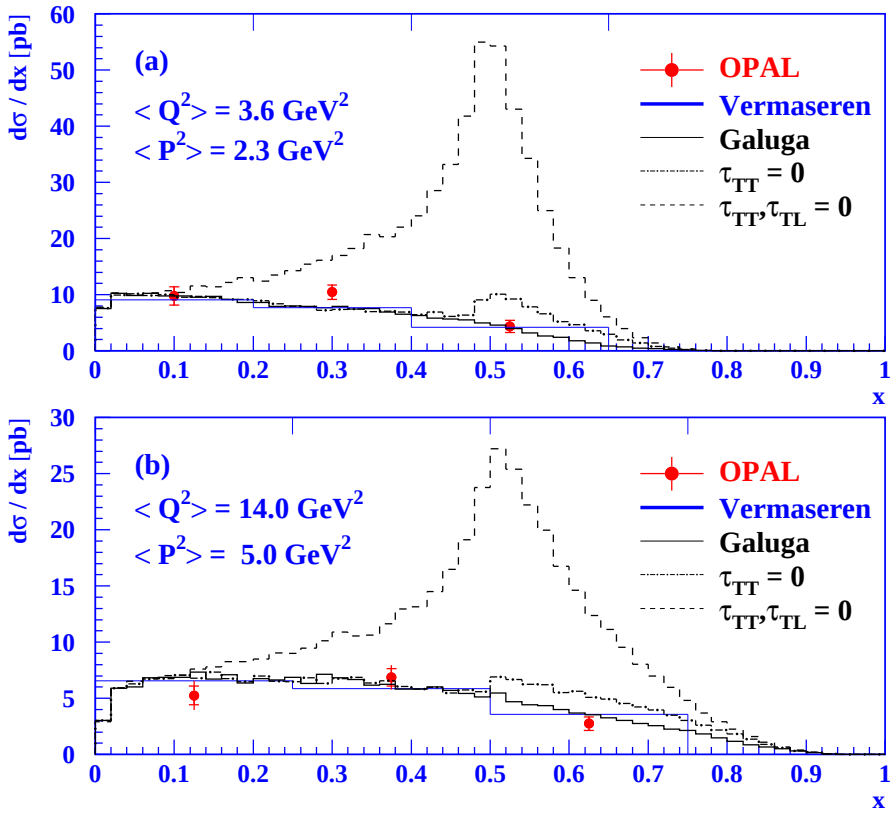

Figure 45: The measured differential cross sections $d\sigma/dx$ for two sets of average values of $\langle Q^2 \rangle = 3.6\,\mathrm{GeV}^2$, $\langle P^2 \rangle = 2.3\,\mathrm{GeV}^2$ and $\langle Q^2 \rangle = 14\,\mathrm{GeV}^2$, $\langle P^2 \rangle = 5\,\mathrm{GeV}^2$. The points represent the OPAL data with their statistical (inner error bars) and total errors (outer error bars). The full line denotes the differential cross section as predicted by the Vermaseren Monte Carlo using the same bins as for data. The additional three histograms represent the cross section calculations from Galuga Monte Carlo for three different scenarios: the full cross section (solid line), the cross section obtained for vanishing τ_{TT} (dot-dash) and the cross section obtained for vanishing τ_{TT} and τ_{TL} (dash). The tick marks at the top of the figures indicate the bin boundaries of the OPAL measurement.

virtualities of the photons are $\langle Q^2 \rangle = 120$ GeV^2 and $\langle P^2 \rangle = 3.7$ GeV^2. In Fig. 47a the measured structure function $F^{\gamma}_{\mathrm{eff}}$ as a function of x is compared with the predictions of $F^{\gamma}_{\mathrm{eff}}$ from the double virtual box diagram and with the predictions of the parameterizations GRSc and SaS1D for F^{γ}_2 and for $(F^{\gamma}_2 + 3/2F^{\gamma}_L)$. In Fig. 47b the P^2 evolution of $F^{\gamma}_{\mathrm{eff}}$ measured by L3 is compared to the QPM predictions and to the predictions of the parameterizations GRSc and SaS1D for $(F^{\gamma}_2 + 3/2F^{\gamma}_L)$. In all cases the longitudinal structure function F^{γ}_L is calculated using the box diagram approximation.

Within the present statistics, the measurements of $F^{\gamma}_{\mathrm{eff}}$ are in full agreement with the naive QPM predictions derived from the doubly virtual box diagram. Only the point at lowest x in the PLUTO measurement may be a sign of a QCD resumed parton content in the virtual photon. However, to firmly establish this, measurements at still lower values of x and with better experimental precision are necessary. The measurements lie above the predictions of F^{γ}_2 demonstrating that the effectively measured quantity is $(F^{\gamma}_2 + 3/2F^{\gamma}_L)$.

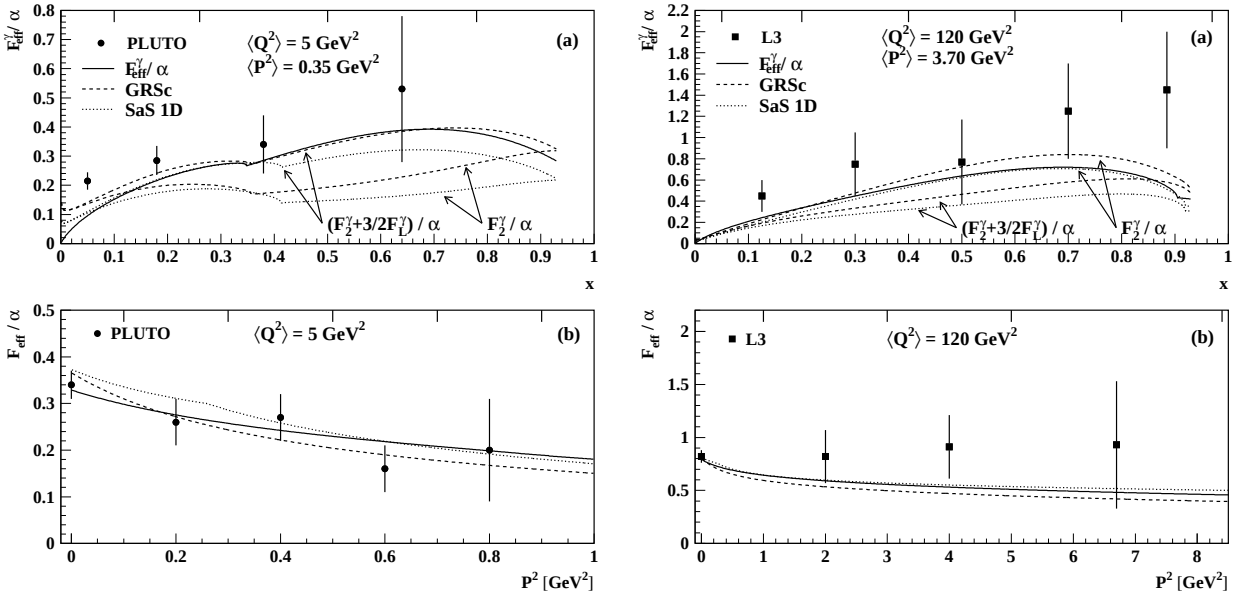

Figure 46: The effective structure function of the virtual photon $F_{\rm eff}^\gamma$ divided by the fine structure constant measured by the PLUTO experiment [145] is shown as a function of x (a) and as a function of P^2. Points represent the data with total errors. In (a) the curves are the predictions for $F_{\rm eff}^\gamma$ from the doubly virtual box diagram for massless partons (solid), and the predictions for F_2^γ and for $(F_2^\gamma + 3/2F_L^\gamma)$ from GRSc (dash) and SaS1D (dot) parameterisations, with F_L^γ always calculated from the box diagram. In (b) the curves are the predictions for $F_{\rm eff}^\gamma$ (solid) and for $(F_2^\gamma + 3/2F_L^\gamma)$ from GRSc (dash) and SaS 1D (dot) parameterisations, with box diagram calculations for massive quarks.

Figure 47: The effective structure function of the virtual photon $F_{\rm eff}^\gamma$ divided by the fine structure constant measured by the L3 experiment [146] is shown as a function of x (a) and as a function of P^2. The meaning of curves is the same as in Fig. 46.

The P^2 dependence of the PLUTO measurement suggests, as expected, a slow decrease with increasing P^2, but it is also consistent with a constant behaviour. The L3 measurement is even less conclusive.

9.3 Hadronic cross section for the $\gamma^\star\gamma^\star$ scattering process

The hadronic structure of interactions of virtual photons has been studied, using the reaction $e^+e^- \to e^+e^-$ hadrons, by three LEP experiments: OPAL [149], L3 [150, 151] and ALEPH [152]. The measurement of the hadronic cross section for interactions of two virtual photons at OPAL has been performed by the author of this paper. The measurements are based on double tagged events, where both scattered electrons are detected mostly in the small angle calorimeters. The first published measurement of this type has been performed by the L3 experiment [150] at e^+e^- centre-of-mass energies $\sqrt{s_{\rm ee}} = 91$ GeV and $\sqrt{s_{\rm ee}} = 183$ GeV.

However, the data in this analysis had been not corrected for QED radiative effects, which were found later to be very large. Therefore we do not discuss this first L3 measurement in the following. The next measurement by L3 as well as the measurements by OPAL and ALEPH have been performed at LEP2 energies, $\sqrt{s_{ee}} = 189 - 209$ GeV, with a luminosity weighted average of around $\sqrt{s_{ee}} = 198$ GeV. The total luminosities used by the experiments amount to 592.9 pb^{-1} (OPAL), 640 pb^{-1} (ALEPH) and 617 pb^{-1} (L3).

9.3.1 Event selection and background estimation

Double tagged two photon events were selected with the sets of cuts discussed below and with the values of the cuts specified in Table 11. In each experiment two electron candidates with sufficient energies E_i and within the specified range of polar angles θ_i must be observed. To ensure that the final state is a hadronic system and not a pair of leptons, at least three tracks ($N_{\rm ch}$) are required by OPAL and ALEPH, or five objects ($N_{\rm part}$) defined as tracks or isolated calorimeter clusters, by L3. In each analysis also a minimum visible invariant mass $W_{\rm vis}$ is required. It is reconstructed from tracks measured in the central tracking detectors and the position and energy of clusters measured in the electromagnetic and hadronic calorimeters. In order to ensure that the event is well contained in the detector and to reduce background from beam–gas interactions, it is required by OPAL that the z component of the total momentum vector of the event, $|\sum p_z|$, is less than 35 GeV, and that the total energy measured in the event is less than $2.2E_{\rm b}$. For the background reduction ALEPH requirs the total visible energy to be above $1.4E_{\rm b}$.
The following additional cuts were used only by OPAL. In order to restrict the number of electron candidates to exactly two, there should not be observed any additional single object with energy above $0.25E_{\rm b}$. To further suppress the beam-gas background a strict requirements on the vertex position in both z direction and in the plane perpendicular to the z-axis, have been set. Here $\langle z_0 \rangle$ is calculated as the error weighted average of the z coordinates of all tracks at the point of closest approach to the origin in the (r, ϕ) plane, and d_0 is the distance of the primary vertex from the beam axis.
Remaining Bhabha-like events (i.e. a Bhabha event with a random overlap of hadronic activity) were tagged in all experiments using the back-to-back topology of the scattered electrons and removed from the data samples.

With these cuts 179, 491 and 891 events were selected by OPAL, L3 and ALEPH, respectively. Among them we expect background events from two main sources. The first contribution is from e^+e^- processes containing scattered beam electrons in the final state observed in the detector, and the second stems from coincidences of e^+e^- processes without the electrons in the final state and with off-momentum electrons from beam–gas interactions faking the scattered electrons.

The background from e^+e^- reactions containing electrons in the final state, dominantly stems from the processes $e^+e^- \to e^+e^-\,\tau^+\tau^-$ and $e^+e^- \to e^+e^-\,e^+e^-$, and was estimated using the Vermaseren [73] (OPAL, L3) or PHOT02 [60] (ALEPH) Monte Carlo programs. The contribution from other e^+e^- backgrounds, such as $e^+e^- \to e^+e^-\,q\bar{q}$ and other processes leading to four fermion final states was found to be much less important. L3 reported a significant background from single-tagged two-photon processes with a cluster from the

OPAL	ALEPH	L3
$E_i > 0.4E_b$	$E_i > 0.3E_b$	$E_i > 40$ GeV
$34 < \theta_i < 55$ mrad	$35 < \theta_i < 55$ mrad	$30 < \theta_i < 66$ mrad
	$60 < \theta_i < 155$ mrad	
$N_{\rm ch} \geq 3$	$N_{\rm ch} \geq 3$	$N_{\rm part} \geq 5$
$W_{\rm vis} > 5$ GeV	$W_{\rm vis} > 3$ GeV	$W_{\rm vis} > 2.5$ GeV
$E_{\rm max} < 0.25E_b$		
$\lvert z_0\rvert < 4$ cm		
$\lvert d_0\rvert < 0.5$ cm		
$\frac{1}{2}\sum E < 1.1E_b$	$\frac{1}{2}\sum E > 0.7E_b$	
$\lvert\sum p_z\rvert < 35$ GeV		
rejection of Bhabha–like events		

Table 11: Selection cuts for double tagged events. For description of the variables see text.

hadronic final state misidentified as the second electron. This type of background was negligible in OPAL and ALEPH. The reason might be that the acceptance of the L3 small angle calorimeters start from a significantly lower polar angle than in the other two experiments.

Beam–gas interactions can result in off-momentum electrons observed in the detectors, faking final state electrons from the process $e^+e^- \to e^+e^-$ hadrons. Due to the LEP running conditions this kind of background was high in OPAL and ALEPH experiments and only negligible in case of L3. The details of the background estimation in OPAL are given below. A similar procedure was adopted by ALEPH. The background was estimated using a sample of Bhabha events, selected by requiring events with two back-to-back electrons in the SW calorimeters, which each have an energy of more than $0.7E_{\rm b}$, with $|\Delta r| < 0.5$ cm and $(\pi - 0.1) < |\Delta\phi| < \pi$ rad, where Δr and $\Delta\phi$ are the differences of the radial and azimuthal coordinates of the tagged electrons. Additional clusters in the SW detectors, which fulfill the criteria for electron candidates, but do not belong to the Bhabha event, are counted as off-momentum electrons. The probabilities to have an overlapping off-momentum electron with an event coming from the interaction region are determined for the left ($-z$) / right ($+z$) side of the detector separately and amount to 0.000715/0.00115 (1998), 0.00139 /0.00279 (1999) and 0.00117 /0.000671 (2000). The relative statistical precision of these probabilities is 2-3%. As the running conditions changed from year to year also the off-momentum background was changing accordingly. The background expectation is more than a factor two larger in 1999 than in the other years. Using the above overlap probabilities, and assuming that they are independent between the left and right side of the detector, we predict that there should be 14.6 events with 'double' overlaps in the Bhabha sample, which agrees well with the 19 events observed.

It is essential to check this method of estimating the background from off-momentum electrons on a different process. Here we used a sample of single-tagged two-photon events. The sample is selected with the same cuts as described for the double-tagged selection, except that only one scattered electron is required. The event properties are compared with the absolute prediction for the single-tagged plus background events. The single-tagged events are based on the HERWIG generator with the GRV [74] parameterisations of the photon structure function F_2^γ, which has been shown to describe the single-tagged cross-section [75]

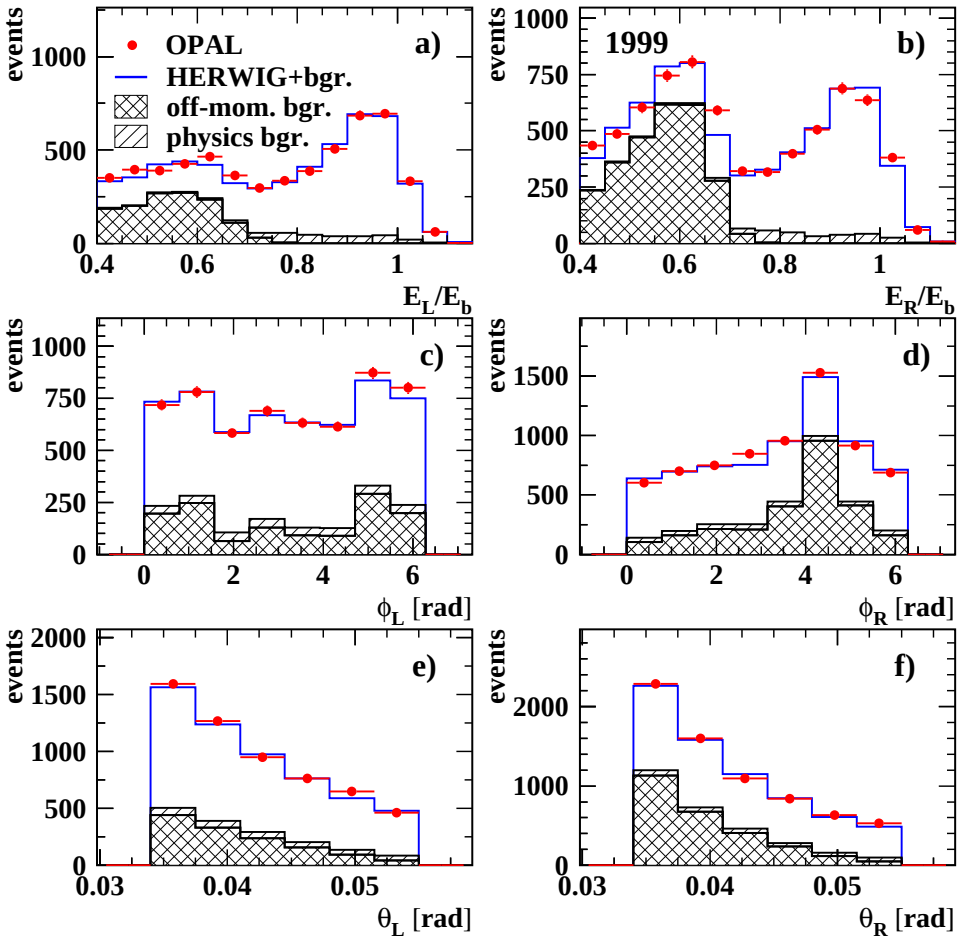

Figure 48: Off-momentum background in OPAL detector. Shown are distributions of the electron energy normalized to the energy of the beam electrons (a,b), electron azimuthal angle (c,d), and electron polar angle (e,f), shown separately for the left (L) and right (R) side of the OPAL detector, for selected single-tagged events in 1999. The histograms are the predictions for the single-tagged process from HERWIG, the off-momentum background contribution, and the background from other physics channels.

within about 10% for $E > 0.7E_{\rm b}$. The genuine single-tagged events are complemented by the physics background and by artificially created single-tagged events constructed by a combination of anti-tagged two-photon events generated by PHOJET with a cluster created by an off-momentum electron. The θ, ϕ and energy dependence of the electron clusters are given by the spectra of the additional clusters in Bhabha events.

Fig. 48 shows the 1999 OPAL data, which are expected to have the largest background from off-momentum overlaps, compared with the prediction resulting from the sum of HERWIG and the background, normalized to the luminosity of the data. Results are shown for θ, ϕ and energy of the scattered electron normalized to the energy of the beam electrons. Fig. 49 shows separately for the 1998, 1999 and 2000 OPAL data samples, the missing longitudinal momentum and missing transverse momentum in the event, calculated including the untagged electron, which has been assumed to have zero transverse momentum and an energy equal to the energy of the beam electrons. Both distributions have been normalized

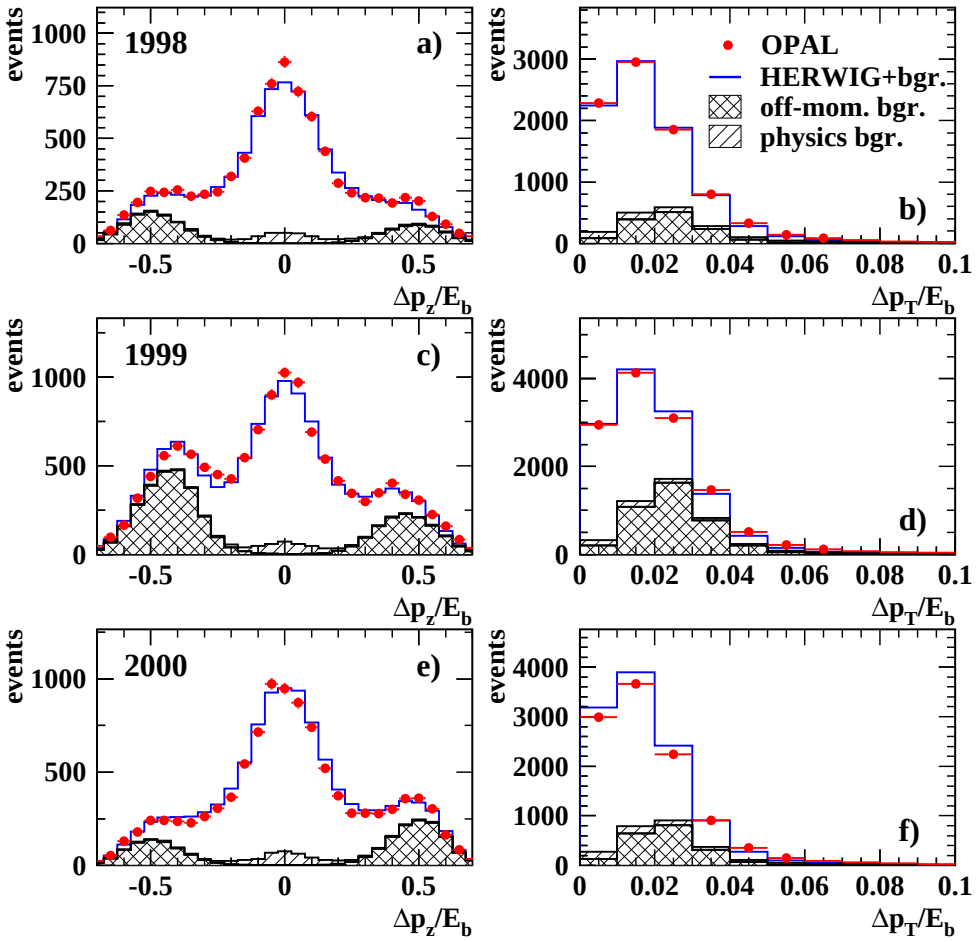

Figure 49: Off-momentum background in OPAL detector. Shown are distributions of the scaled missing longitudinal momentum (a,c,e) and the scaled missing transverse momentum (b,d,f) in single-tagged events for the different years. The meaning of the histograms are as defined in Fig. 48.

to the energy of the beam electrons. For energies below $0.6E_{\rm b}$ the off-momentum background clearly dominates and the observed angular dependences, especially in ϕ, clearly follow the expected shape. The agreement between data and prediction is very good for all variables examined, providing confidence that the background from overlap of off-momentum beam electrons is under control to a level of about 10%. The off-momentum background estimate was used to calculate the contribution of fake double-tagged events, resulting from the overlap of one background cluster with a single-tagged two-photon event and the overlap of two background clusters with an untagged event. In total 4.3, 15.2 and 4.6 overlap events are predicted in OPAL data for the 1998, 1999 and 2000 data samples.

The total expected background from all the sources discussed above amounts to 42.2, 87, 206.1, in case of OPAL, L3 and ALEPH, respectively.

9.3.2 Comparison with Monte Carlo models

PHOJET, TWOGAM, PYTHIA and PHOT02 Monte Carlo samples are used to correct the data for acceptance and resolution effects in OPAL, L3 and ALEPH experiments. It is therefore essential that the shape of all important distributions is well reproduced by these Monte Carlo simulations. Below a comparison is made of data distributions with predictions from the above Monte Carlo models. Variables calculated from the scattered electrons as well as variables calculated from the hadronic final state are studied. The integrated luminosities of the Monte Carlo samples exceed many times that of the data.

OPAL: All Monte Carlo distributions shown are normalized to the data luminosity. In Fig. 50 variables which are based on electron quantities, and the variables $x_{1,2}$, are compared with predictions of PHOJET and background estimates. All variables, the normalized electron energies $E_{1,2}/E_{\rm b}$, the polar angles $\theta_{1,2}$, the azimuthal angles $\phi_{1,2}$, and photon virtualities $Q^2_{1,2}$, are reasonably well described by the sum of the signal as predicted by PHOJET and the estimated background from overlaps with off-momentum electrons and other physics processes. Note that PHOJET does not contain any explicit effects from BFKL, which would show up in the region of low electron energies. Fig. 50e shows the logarithm of the ratio of the photon virtualities, $\log(Q^2_1/Q^2_2)$, of the two photons in an event. This distribution is peaked around zero, indicating that the Q^2 values of both photons are generally close to one another, which is ideal to test for BFKL effects. In Fig. 51 distributions are shown which characterize the hadronic final state in double-tagged two-photon events: the number of tracks, $N_{\rm ch}$, the visible hadronic invariant mass, $W_{\rm vis}$, the hadronic energy, $E_{\rm had}$, the variable $\overline{Y}$ as well as the sum of the longitudinal $\sum p_{\rm z}$ and transverse $\sum p_{\rm T}$ momenta. Within statistics, the agreement with PHOJET plus background estimates is reasonable.

L3: All Monte Carlo distributions shown are normalized to the number of data events. In Fig. 52 variables which are based on electron quantities, are compared with predictions of PHOJET, TWOGAM and background estimates. All variables, the normalized electron energies $E_i/E_{\rm b}$, the polar angles θ_i, the photon virtualities Q^2_i and their ratio $\ln(Q^2_1/Q^2_2)$ are reasonably well described by the sum of the signal as predicted by PHOJET or TWOGAM and the estimated background from other physics processes. However, TWOGAM gives slightly better description of the shape of θ_i and Q^2_i distributions. The distributions of the visible hadronic invariant mass $W_{\rm vis}$ calculated using the four-vectors of all measured particles (see Eq. 9) and the corresponding variable $\overline{Y}_{\rm vis}$ are compared to Monte Carlo predictions on Fig. 53a and 53b. The same quantities but calculated using the scattered electrons four-momenta (see Eq. 11), $W_{\rm ee}$ and $\overline{Y}_{\rm ee}$, are shown in Fig. 53c and 53d. In all cases a good agreement with both Monte Carlo models is observed. It should be pointed out here that due to undetected particles the distribution of $W_{\rm vis}$ (and in consequence $\overline{Y}_{\rm vis}$) is shifted towards smaller values, whereas the distribution of $W_{\rm ee}$ ($\overline{Y}_{\rm ee}$) extends to much higher values. However, as will be explained later, the distribution of $\overline{Y}_{\rm ee}$ is very sensitive to QED radiative corrections, which are large.

ALEPH: All Monte Carlo predictions shown are normalized to the data, that means the cross-section predicted by PYTHIA was reduced by 12% and the cross section predicted by

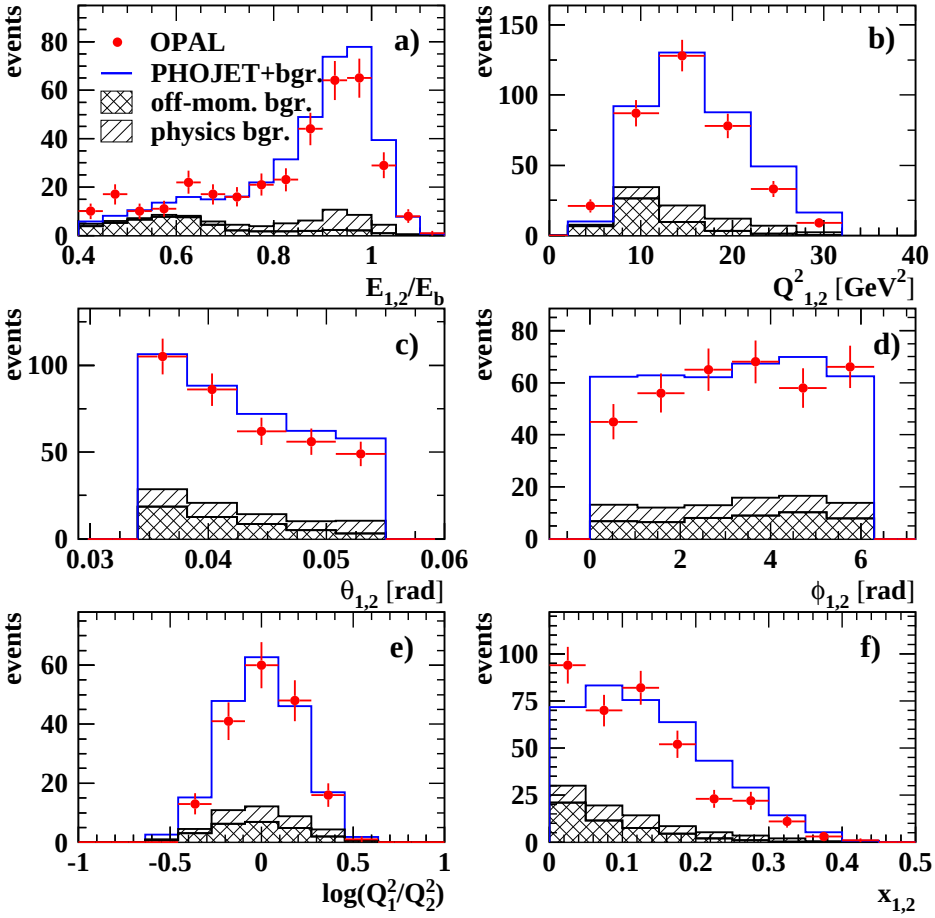

Figure 50: Comparison of OPAL data with Monte Carlo predictions. Shown are distributions of (a) the energies of the electrons, normalized to the beam energy, (b) the virtualities of both photons, (c) the polar angles of the electrons, (d) the azimuthal angles of the electrons, (e) the ratio of the photon virtualities and (f) the x values of double-tagged two-photon events. The histograms are the predictions for the double-tagged two-photon process from PHOJET1.10, the off-momentum background contribution, and the background from other physics channels.

PHOT02 was increased by 30%. In Fig. 54 we show the distributions of the normalized electron energies $E_{1,2}$, the polar angles $\theta_{1,2}$, the azimuthal angle between the electron scattering planes $\Delta\Phi$, the photon virtualities $Q^2_{1,2}$ and their ratio, the number of tracks $N_{\rm ch}$, the hadronic invariant mass (denoted as $W_{\gamma\gamma}$) and the variable $\overline{Y}$. Both Monte Carlo models, PYTHIA and PHOT02, describe the shape of the above variables in the data equally well. Only in case of the quantity $\Delta\Phi$, which in the data is flat, the prediction of PYTHIA is significantly better.

From the above Monte Carlo models used by the experiments to correct the data for detector effects only TWOGAM contains QED radiative corrections to the lepton lines. Therefore it is necessary to estimate independently the size of radiative corrections in double tagged events. We used TWOGAM and BDK [73] Monte Carlo generators which agree in

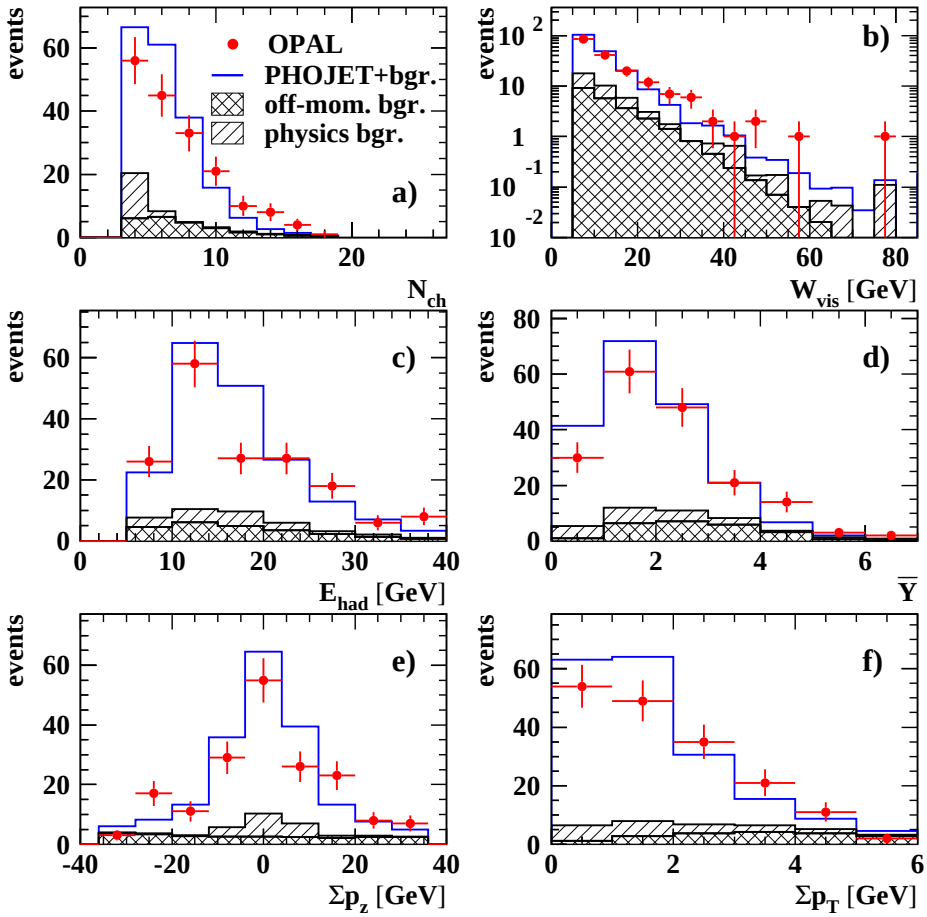

Figure 51: Comparison of OPAL data with Monte Carlo predictions. Shown are distributions of (a) the number of tracks of the hadronic final state, (b) the visible hadronic invariant mass, (c) the total hadronic energy (d) the variable $\overline{Y}$, (e) the missing longitudinal momentum and (f) the missing transverse momentum for double-tagged events. The PHOJET1.10 predictions and backgrounds contributions are as in Fig. 50.

description of radiative corrections for the process $e^+e^- \rightarrow e^+e^-\mu^+\mu^-$. The size of the radiative corrections depends on the variables used to calculate the kinematics, and also to some extent on the non-radiative cross-section. As an example we present the estimation of radiative corrections by the OPAL experiment. This study has been performed purely on the generator levels, without detector simulation. In radiative events the scattered electrons are combined with the closeby photons that would also not be resolved in the experimental setup (due to granularity of the calorimeters). The combined object is considered to be the observed electron and is used to calculate the kinematic variables. Hence the data are mainly sensitive to initial state radiation. The radiative corrections have been estimated in bins of $\overline{Y}$, as the ratio of the relative difference of the non-radiative and radiative cross sections with respect to the radiative cross section, while applying the experimental restrictions on the scattered electrons energies and polar angles as well as on the minimum invariant mass of the hadronic system. Figure 55 compares the effect of radiative corrections in two methods of calculating the variable $\overline{Y}$. The first method uses the hadronic final state to calculate W

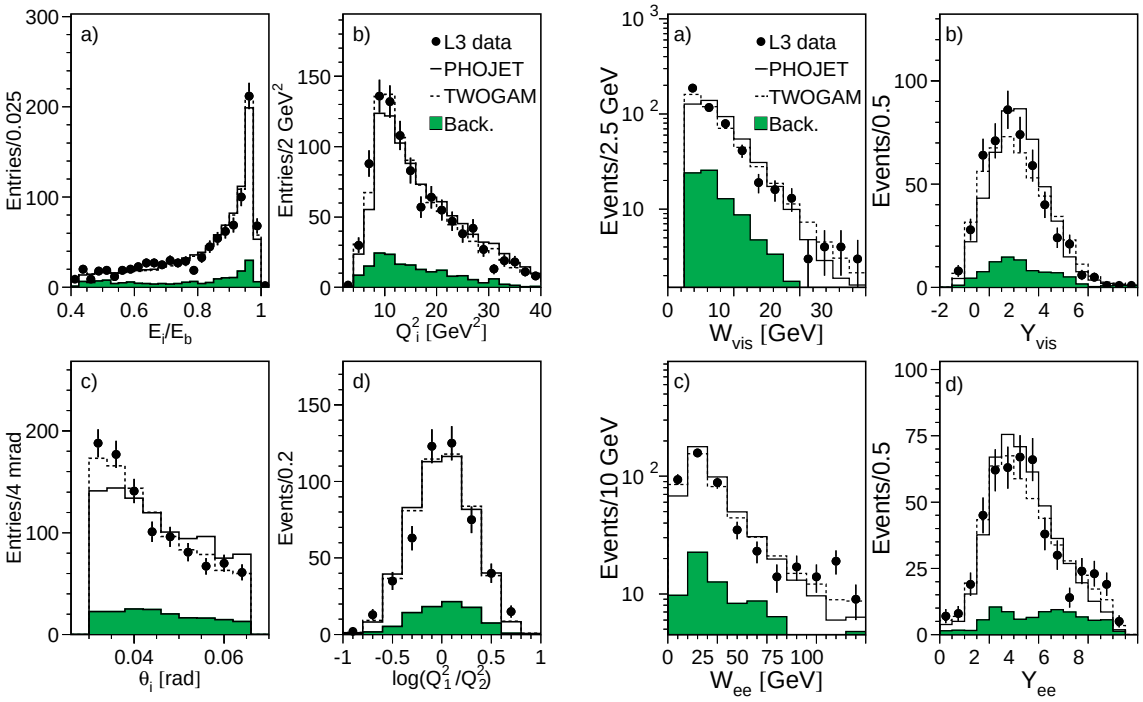

Figure 52: Comparison of L3 data with Monte Carlo predictions. Distributions of (a) the energies of the electrons, normalized to the beam energy, (b) the virtualities of both photons, (c) the polar angles of the electrons, (d) the ratio of the photon virtualities for double-tagged events. The histograms are the predictions for the double-tagged two-photon process from PHOJET and TWOGAM and background from other physics channels.

Figure 53: Comparison of L3 data with Monte Carlo predictions. Distributions of the measured two photon invariant mass W and the corresponding variable $\overline{Y}$, calculated from the detected particles in the hadronic final state (a,b) and from the scattered electrons (c,d). The PHOJET and TWOGAM predictions and background contributions are as in Fig. 52.

(Eq. 9). The second method uses the beam and scattered electrons to obtain W (Eq. 11). The predictions on the size of radiative corrections from different subprocesses generated by TWOGAM are shown separately. Also the predictions weighted with the relative cross sections of different subprocesses shown in Fig. 55c are shown in the figure. For the fully hadronic method the radiative corrections are small. However, for the electron method the corrections can be larger than 50% at large $\overline{Y}$ values. Obviously, measurements based on the electron kinematics cannot be compared with models or BFKL calculations in the region $\overline{Y} > 4$, unless radiative corrections have been applied. Since the actual size of the radiative corrections also depends on the non-radiative cross-section itself, in principle an iterative procedure would be required to extract the non-radiative cross-section. However, the present statistics of data do not permit such a procedure. In the analyses presented in this paragraph only the L3 experiment used the electron method to calculate W (and in consequence $\overline{Y}$) and corrected the data for radiative effects. OPAL and ALEPH used the fully hadronic method to calculate $\overline{Y}$ where the effects of radiative corrections are small.

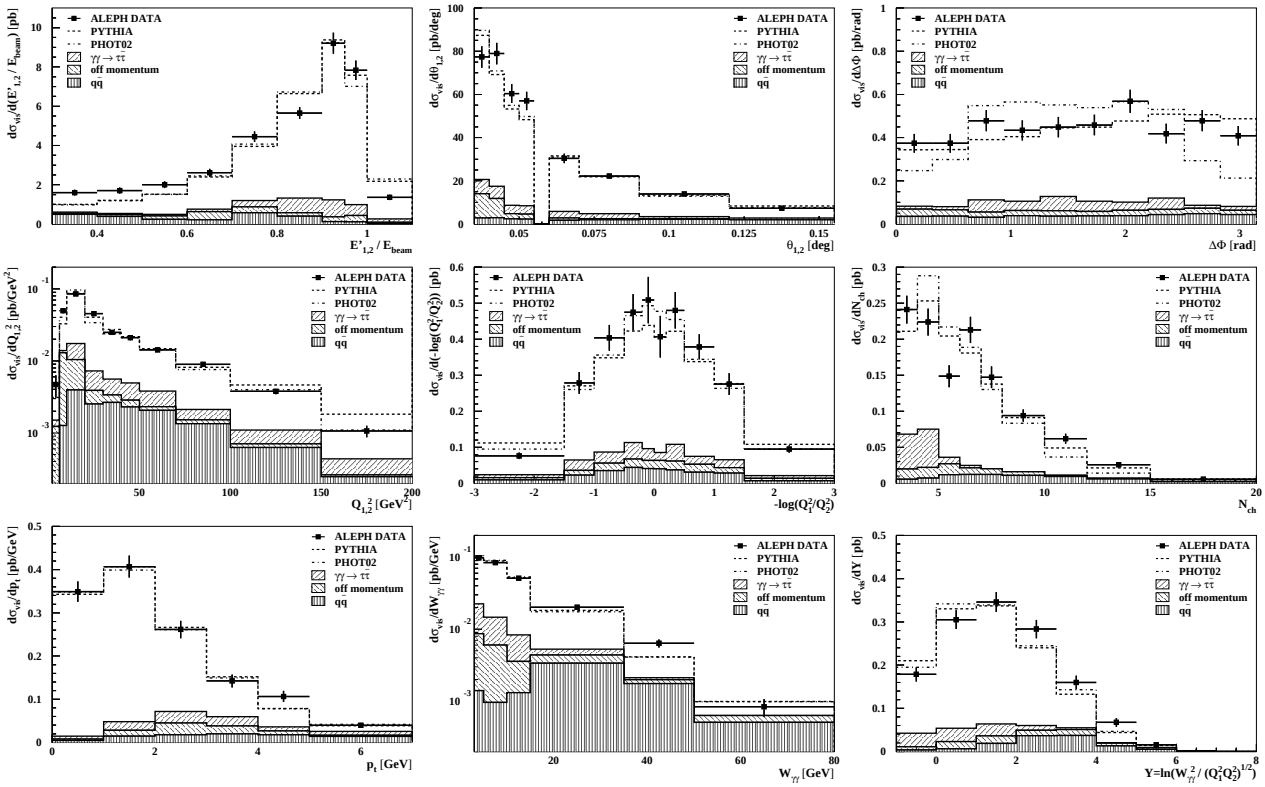

Figure 54: Comparison of ALEPH data with Monte Carlo predictions. Distributions of (a) the energies of the electrons, normalized to the beam energy, (b) the polar angles of the electrons, (c) the azimuthal angle between the electron scattering planes $\Delta\Phi$, (d) the virtualities of both photons, (e) the ratio of the photon virtualities, (f) the number of tracks, (g) total transverse momentum in the event, (h) the hadronic invariant mass and (i) the variable $\overline{Y}$, are shown for double tagged events. The histograms are the predictions for the double-tagged two-photon process from PYTHIA and PHOT02, the off-momentum background contribution, and the background from other physics channels.

9.3.3 Results

Several differential e^+e^- and total $\gamma^\star\gamma^\star$ cross sections have been measured by the experiments. Due to different geometrical acceptances of the detectors, the measurements have been performed in slightly different phase space regions presented in Table 12 (in order not to bias the measurements by model predictions the phase space in which the cross sections have been measured is close to the kinematical selection cuts used at the detector level). Below the main results obtained by OPAL, L3 and ALEPH will be presented in turn. Due to limited statistics in the data, a simple bin-by-bin method was applied to correct for detector and selection inefficiencies. The efficiency, $R_{\rm e}$, and purity, $R_{\rm p}$, are defined as:

$$R_{\rm e} = \frac{N^{\rm Det\otimes Had}}{N^{\rm Had}} \qquad\qquad R_{\rm p} = \frac{N^{\rm Det\otimes Had}}{N^{\rm Det}}$$

where $N^{\rm Det\otimes Had}$ is the number of events which are generated in a bin and measured in the same bin, $N^{\rm Had}$ is the number of events which are generated in a bin and $N^{\rm Det}$ is the number

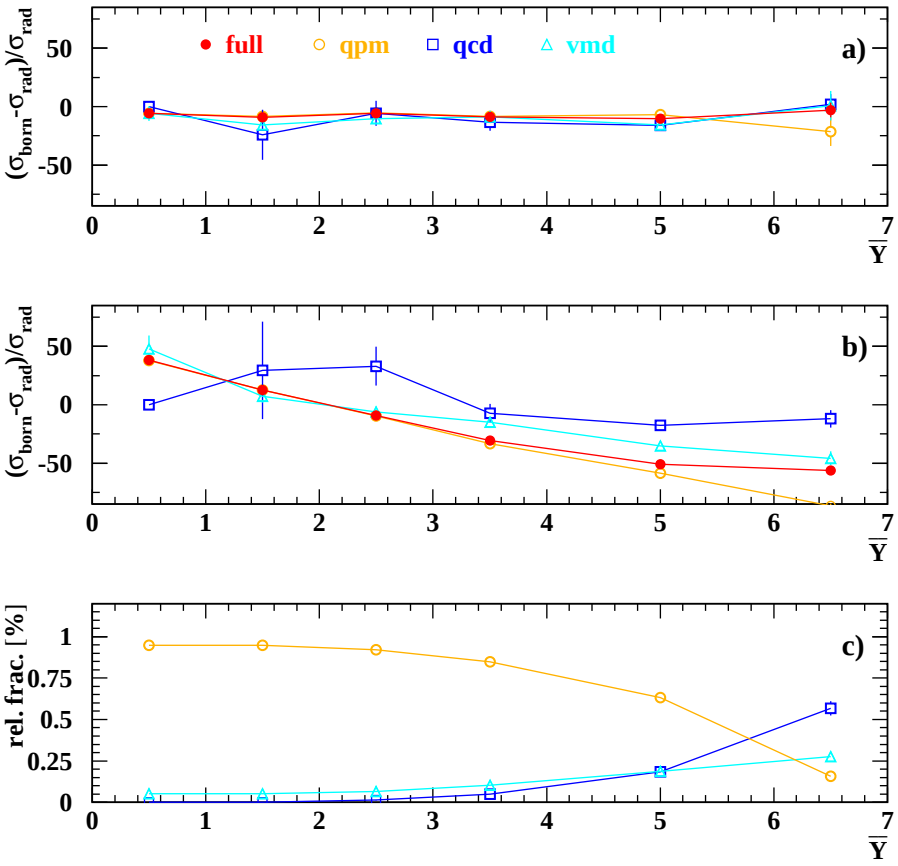

Figure 55: Radiative corrections for the process $e^+e^- \to e^+e^-$ hadrons as a function of $\overline{Y}$ for two different methods to calculate W: a hadronic method (a) and an electron method (b), as explained in the text. Shown are the relative differences of the non-radiative and radiative cross sections with respect to the radiative cross section as a function of $\overline{Y}$ for different subprocesses: QPM (open circle), QCD (open square) and VMD (open triangle) as well as for their weighted average (full circle). In (c) the relative fraction of different subprocesses, as predicted by TWOGAM, in the total cross section are shown as a function of $\overline{Y}$.

of events measured in a bin. In both definitions the terms 'generated' and 'measured' denote events which pass all selection cuts at the hadron or at the detector level, respectively. The correction factor $N^{\rm Had}/N^{\rm Det}$ is obtained by dividing purity by efficiency. For the W variable the purity is typically around 60% over the whole range, and the efficiency is in the range of 30-50%. Similar numbers are obtained for $\overline{Y}$ and x, while for the $\Delta\phi$ and Q^2 variables the efficiencies are around 60% and purities around 80%. The correction factor is typically around 1.5 and fairly constant. From the measurement of the differential cross-sections of the process $e^+e^- \to e^+e^-$ hadrons we extract the cross-sections for the reaction $\gamma^\star\gamma^\star \to$ hadrons as a function of the variable under study, using $L_{\rm TT}$ (see Eq. 72), obtained separately for each bin using Monte Carlo. Technically this was done by setting $\sigma_{\gamma^\star\gamma^\star} \equiv 1$ in GALUGA and integrating (Eq. 71) using only $L_{\rm TT}$ for each bin within the experimental phase space restrictions. The cross-sections for the reaction $\gamma^\star\gamma^\star \to$ hadrons predicted by the models are calculated using the same $L_{\rm TT}$ factors.

Phase space for the cross section measurements		
OPAL	ALEPH	L3
$E_i > 0.4E_b$	$E_i > 0.3E_b$	$E_i > 40$ GeV
$34 < \theta_i < 55$ mrad	$35 < \theta_i < 155$ mrad	$30 < \theta_i < 66$ mrad
$W > 5$ GeV	$W > 3$ GeV	$W > 5$ GeV

Table 12: Phase space used for the cross section measurements for the process $e^+e^- \to e^+e^-$ hadrons, by different LEP experiments.

The QPM cross-section for the process $e^+e^- \to e^+e^- q\bar{q}$, which corresponds to the diagram labelled F_0 in Fig. 20, was calculated with the GALUGA [65] program, which includes all terms from Eq. 13. The quark masses assumed are 0.325 GeV for uds and 1.5 GeV for c quarks. For the region of $W > 5$ GeV considered here, the cross-section depends only weakly on the chosen masses, e.g. the results for u and c quarks differ only slightly.

OPAL: Differential e^+e^- and total $\gamma^\star\gamma^\star$ cross-sections are obtained as functions of x, Q^2, W, and the azimuthal correlation between the two scattered electrons $\Delta\phi$. Here Q^2 refers to the maximum of Q_1^2 and Q_2^2, and x is the corresponding value of x_1 or x_2. For the comparison with BFKL predictions we also present the differential cross-section as a function of $\overline{Y}$. For all variables except Q^2 the results for the cross-sections of the reaction $\gamma^\star\gamma^\star \to$ hadrons are given at an average value of Q^2, $\langle Q^2 \rangle = 17.9$ GeV^2. The main contributions to the systematic errors come from changing the Monte Carlo model from PHOJET to PYTHIA (-16% change in the total cross-section), changing the cut on $N_{\rm ch}$ (-12%), and varying the lower cuts on W ($\pm 8\%$) and $\theta_{1,2}$ ($\pm 5\%$). The normalization uncertainty due to the luminosity measurement is less than 1% and has been neglected.

Radiative corrections are calculated with the program BDK [66]. As for the GALUGA Monte Carlo, the BDK program calculates the QPM cross-section with, in addition, initial and final state QED radiative corrections to the scattered electrons. It has been verified that the non-radiative cross-sections predicted by BDK and GALUGA agree with each other. GALUGA has more flexibility for calculating cross-sections and is therefore used to calculate the $L_{\rm TT}$ factors and QPM predictions. The results are presented in Fig. 56, 57 and 58 and in Table 32. In Fig. 56 we show the measured differential cross-section for the processes $e^+e^- \to e^+e^-$ hadrons and the cross-section for $\gamma^\star\gamma^\star \to$ hadrons as a function of x and Q^2. PHOJET better describes the data at lower x values, where the QPM prediction is too low. In contrast, in the large x region the QPM prediction is sufficient to account for the data. Fig. 57 shows the measured cross-sections as a function of W and $\Delta\phi$. The model predictions indicate a slightly different shape than is observed for the data. Studies for HERA have shown [76] that angular variables similar to $\Delta\phi$ can be sensitive to the presence of BFKL dynamics, but so far no calculations are available for $\gamma^\star\gamma^\star$ scattering. The data show that the $\Delta\phi$ behavior of the cross-section for the reaction $e^+e^- \to e^+e^-$ hadrons is flat, while the cross-section for the process $\gamma^\star\gamma^\star \to$ hadrons increases from $\Delta\phi = 0$ to $\Delta\phi = \pi$. PHOJET1.10 does not describe the $\Delta\phi$ distribution, whereas QPM reproduces the shape of the distribution. One should remark that the earlier version, PHOJET1.05, follows the data in both shape and normalization. In Fig. 58 we compare the measured cross-section for the processes $e^+e^- \to e^+e^-$ hadrons and $\gamma^\star\gamma^\star \to$ hadrons as a function of $\overline{Y}$

with the PHOJET Monte Carlo, the QPM calculation, the NLO calculation for the reaction $e^+e^- \to e^+e^- q\bar{q}$, and numerical BFKL calculations. The BFKL predictions are shown for the LO-BFKL [41] and a NLO-BFKL [42] calculation both using Y. Also shown is a (partial) HO-BFKL calculation [43] using $\overline{Y}$. All BFKL predictions are shown for Y or $\overline{Y} > 2$, except for the NLO-BFKL calculation which has been evaluated for $Y > 1$. Both PHOJET and QPM using massive quarks describe the data equally well. Also the NLO calculation for the reaction $e^+e^- \to e^+e^- q\bar{q}$, evaluated for five massless quarks and using $\Lambda_5^{\overline{\rm MS}} = 0.2275$ GeV, is in accord with the data. As can be seen from Table 13 the predicted differential cross-sections as functions of Y and $\overline{Y}$ are very different at small values, but get much closer at higher values. This is expected from the approximation made in Eq. 81. It means that at low values of $\overline{Y}$ the comparison of the experimental result with predictions based on Y is rather uncertain, whereas at high values the uncertainty from using different definitions is small. For all BFKL predictions shown the cross-section is significantly larger than the

Y or $\overline{Y}$	$d\sigma/d\overline{Y}$		$d\sigma/dY$	
range	LO	NLO	LO	NLO
0 – 1	0.071	0.065	0.015	0.014
1 – 2	0.135	0.128	0.149	0.138
2 – 3	0.087	0.089	0.111	0.122
3 – 4	0.041	0.047	0.047	0.053
4 – 6	0.010	0.013	0.011	0.014

Table 13: Predictions for the differential cross-section for the process $e^+e^- \to e^+e^- q\bar{q}$ as functions of $\overline{Y}$ and Y in LO and NLO using the calculation from [34].

PHOJET prediction for $\overline{Y} > 3$, and the differences increase with increasing $\overline{Y}$. The LO-BFKL calculation predicts a cross-section which is too large compared to the data. This LO-BFKL calculation (Bartels99) [41] already incorporates improvements compared to the original results [45] by including effects of the charm quark mass, the running of the strong coupling constant α_s and contribution of longitudinal photon polarization states. Hence BFKL effects as large as predicted by the LO-BFKL calculation are not in agreement with the data. BFKL cross-sections have been calculated to NLO (Kim99) [42], using the BLM [77] optimal scale setting. At the highest $\overline{Y}$ value the NLO-BFKL cross-section is a factor seven larger than the PHOJET prediction. The data lie in between these two predictions. Finally, the calculation (Kwiecinski) [43] contains the dominant contribution of the higher order corrections via the so-called consistency constraint, to all orders. Its prediction in the highest reachable $\overline{Y}$ range is about a factor two lower than for the NLO-BFKL calculation, and this prediction and PHOJET are roughly equally compatible with the data.

The total measured cross-section for the process $e^+e^- \to e^+e^-$ hadrons in phase space defined in Table 12, is 0.35 ± 0.04 (stat) $^{+0.04}_{-0.08}$ (sys) pb. The expected cross-section from PHOJET is 0.39 ± 0.02(stat) pb, while the GALUGA prediction for QPM using massive quarks is 0.27 ± 0.02(stat) pb, and the NLO predictions for the reaction $e^+e^- \to e^+e^- q\bar{q}$ using massless quarks is 0.35 pb.

L3: Differential e^+e^- and total $\gamma^\star\gamma^\star$ cross sections are obtained as functions of $Q^2 = \sqrt{Q_1^2\, Q_2^2}$, W and $\overline{Y}$. They are presented in Fig. 59 and Fig. 60 and listed in Table 35. The ranges

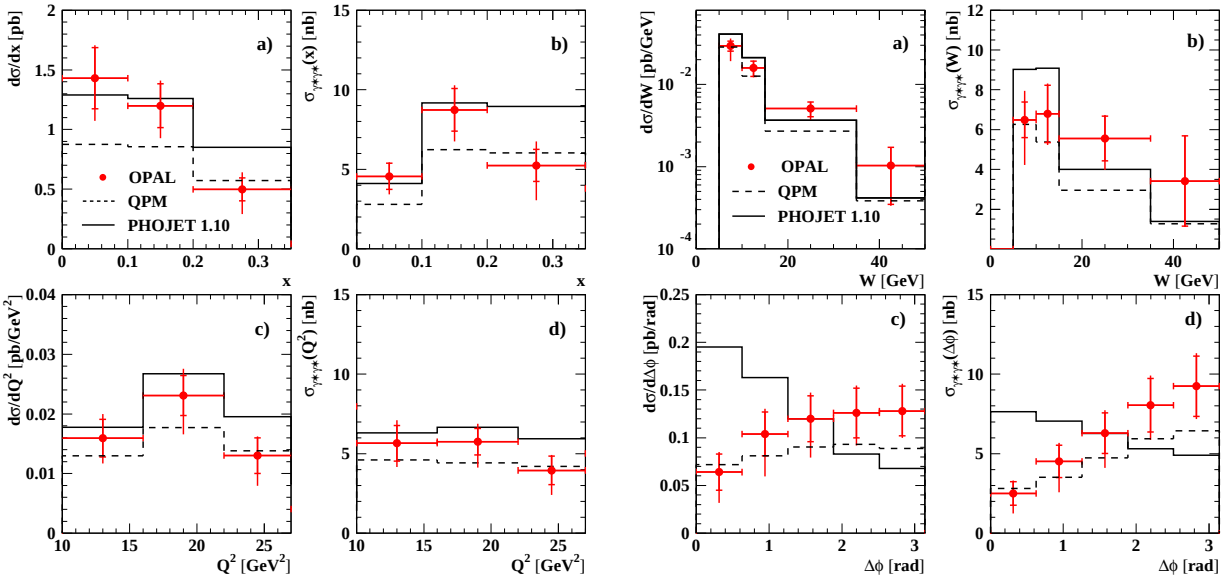

Figure 56: Cross-sections for the process $e^+e^- \to e^+e^-$ hadrons in the phase space region defined in Table 12, and for the process $\gamma^\star\gamma^\star \to$ hadrons, as functions of x for $\langle Q^2 \rangle = 17.9$ GeV^2 (a,b), and as functions of Q^2 (c,d). Data are shown as full dots in the centre of the bins. The inner error bars represent the statistical errors and the outer error bars represent statistical and systematic errors added in quadrature. The predictions of PHOJET1.10 are shown as solid lines, and those of QPM as dashed lines.

Figure 57: Cross-sections for the process $e^+e^- \to e^+e^-$ hadrons in the phase space region defined in Table 12, and for the process $\gamma^\star\gamma^\star \to$ hadrons for $\langle Q^2 \rangle = 17.9$ GeV^2, as functions of W (a,b) and $\Delta\phi$ (c,d). The meaning of symbols as in Fig. 56.

$10\,\mathrm{GeV}^2 < Q^2 < 32\,\mathrm{GeV}^2$, $5\,\mathrm{GeV} < W < 100\,\mathrm{GeV}$ and $2 < \overline{Y} < 7$ are investigated independently. An important difference between the L3 analysis and the analyses by OPAL and ALEPH is the calculation of W, which in case of L3 was obtained from the scattered electrons via Eq. 11. In consequence, in the L3 analysis the QED radiative corrections were large and were estimated by TWOGAM using the method described above. The systematic uncertainty on the cross sections due to the selection cuts is 5%. The uncertainty due to background estimation of single tagged events is 3.4%. The uncertainty due to Monte Carlo modeling is estimated as 6.4% by comparing PHOJET and TWOGAM with QED radiative corrections switched off. The uncertainty in the estimation of radiative corrections was determined as 3% by comparing the size of radiative corrections to the process $e^+e^- \to e^+e^- \mu^+\mu^-$ predicted by TWOGAM and RADCOR programs. The different contribution from QPM, VMD and QCD subprocesses as function od $\overline{Y}$ and W gives an additional systematic uncertainty. A 20% variation of the QCD component results in an uncertainty of 0.3% at low values and of 5.7% at large values of $\overline{Y}$ and W. This uncertainty is about 0.5% over the full Q^2 range. The cross section for the process $e^+e^- \to e^+e^-$ hadrons after applying QED radiative corrections are compared in Fig59 to the PHOJET Monte Carlo and to LO and NLO calculations of $\gamma^\star\gamma^\star \to q\bar{q}$ [34]. In these calculations the mass of quarks is set to zero and α is fixed to the value for on-shell photons. The calculations describe well the Q^2 depen-

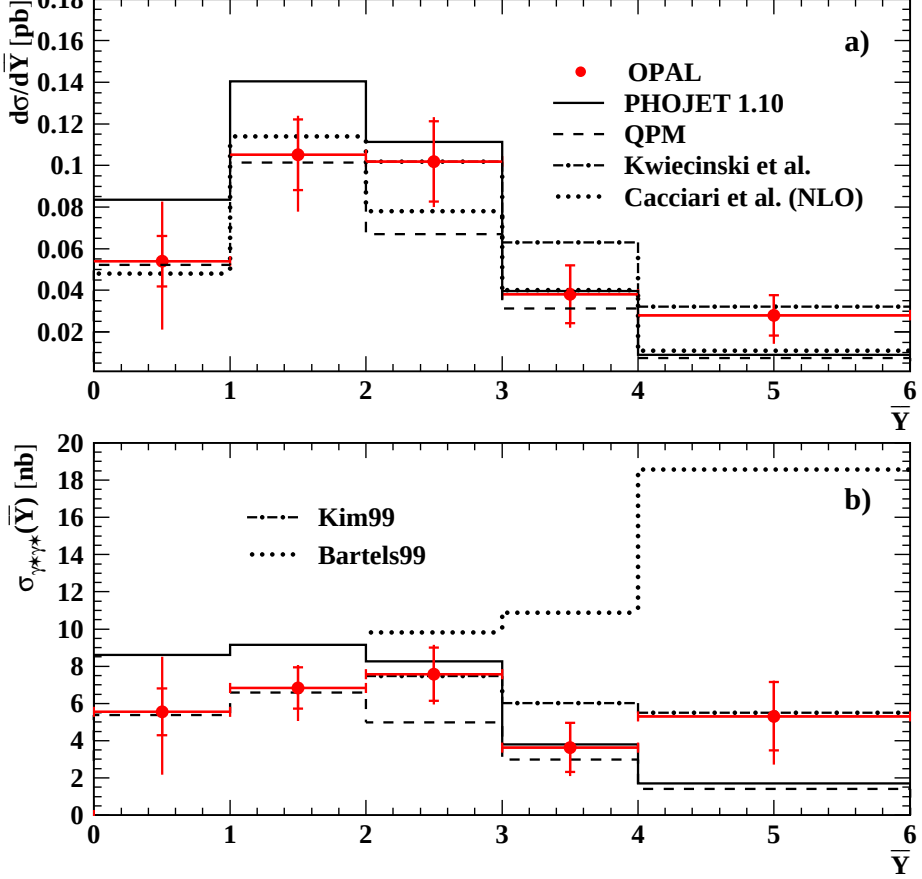

Figure 58: Cross-sections for the process $e^+e^- \to e^+e^-$ hadrons in the region $E_{1,2} > 0.4E_b$, $34 < \theta_{1,2} < 55$ mrad and $W > 5$ GeV, and the process $\gamma^\star\gamma^\star \to$ hadrons for $\langle Q^2 \rangle = 17.9$ GeV^2, as functions of $\overline{Y}$. Data are shown as full dots in the centre of the bins. The inner error bars represent the statistical errors and the outer error bars represent statistical and systematic errors added in quadrature. The predictions of PHOJET1.10 are shown as the solid lines, that of the NLO calculation of the process $e^+e^- \to e^+e^- q\bar{q}$ as dotted lines, and those of QPM as dashed lines. Three BFKL calculations are shown: a LO one from Bartels et al. (Bartels99), NLO from Kim et al. (Kim99) using Y, and the calculation from Kwieciński et al., using the consistency constraint calculated for $\overline{Y}$.

dence observed in data. For the W and $\overline{Y}$ distributions, the QPM calculations describe the data except in the last bin, where the measured cross section exceeds the predictions. Such an excess is expected if the resolved photon QCD processes become important at large $\overline{Y}$. The predictions of PHOJET, which includes the QPM and QCD processes in the framework of DGLAP equations, also describe the data. A similar behaviour may also be obtained by considering 'hard pomeron' contribution in the framework of BFKL theories, while LO BFKL calculations we found to exceed the experimental values by a large factor.

A fit of the form $f(Q^2) = A/Q^2$ predicted by perturbative QCD [45,46] to the measured $\gamma^\star\gamma^\star$ cross section as a function of Q^2 gives $A = 81.8 \pm 6.4$ nb/GeV^2 and χ^2/d.o.f. $= 1.2/3$. The average value of $\sigma_{\gamma^\star\gamma^\star}$ in the kinematical region given in Table 12 is 4.7 ± 0.4 nb.The NLO calculations [34] predict a decrease of $\sigma_{\gamma^\star\gamma^\star}$ as a function of W or $\overline{Y}$, which is inconsistent with the measurements at large values of W and $\overline{Y}$.

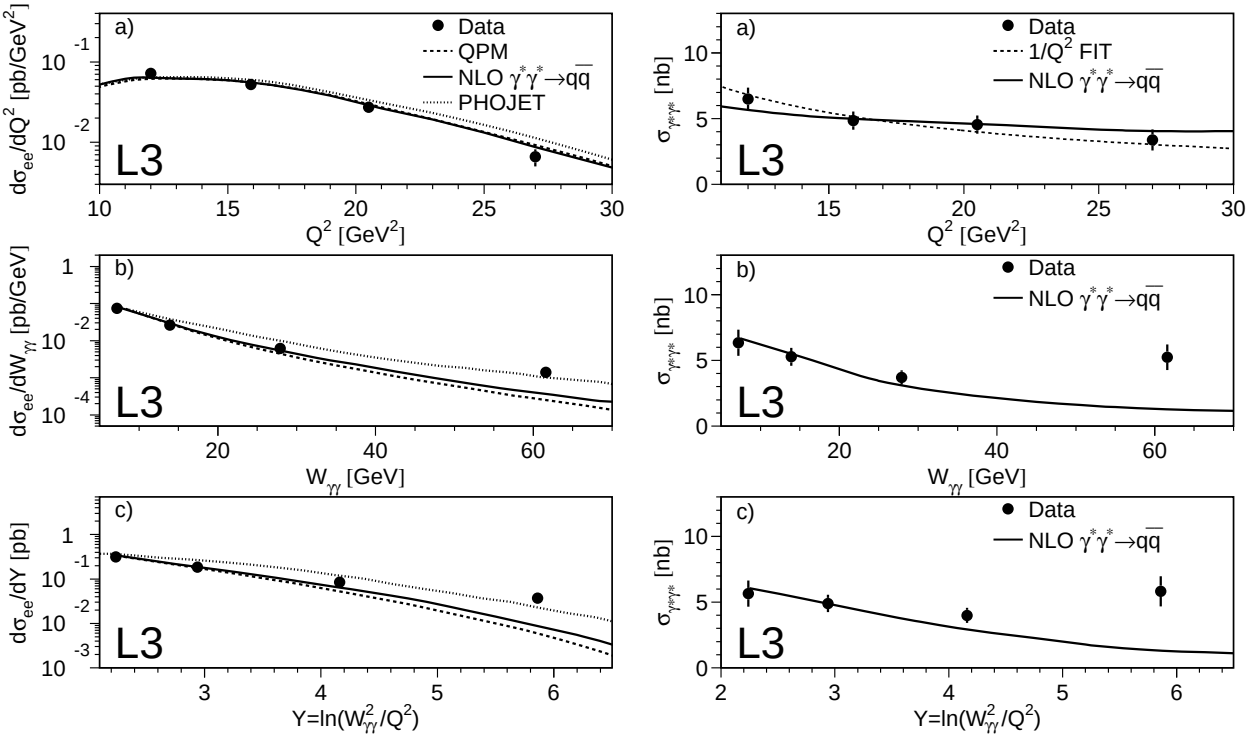

Figure 59: The differential cross section for the process $e^+e^- \to e^+e^-$ hadrons in the kinematical region defined in the text, measured by the L3 experiment. Points represent the data with statistical and systematic errors added in quadrature. The LO and NLO predictions of [34] for the process $\gamma^\star\gamma^\star \to q\bar{q}$ are displayed as the dashed and solid lines, respectively. The dotted line shows the prediction of the PHOJET Monte Carlo.

Figure 60: Cross section for the process $\gamma^\star\gamma^\star \to$ hadrons in the kinematical region defined in the text, measured by the L3 experiment. The dashed line represents the fit to the data described in the text. The NLO predictions of [34] for the process $\gamma^\star\gamma^\star \to q\bar{q}$ are displayed as the solid line.

ALEPH: Differential e^+e^- cross sections are obtained as functions of the energy of the scattered electrons scaled by the energy of beam electrons $E_{1,2}/E_b$, the polar angles $\theta_{1,2}$, the azimuthal angle between the two electron scattering planes $\Delta\Phi$, photon virtualities $Q^2_{1,2}$, two photon invariant mass $W_{\gamma\gamma}$ and the variable $\overline{Y}$. They are presented in Fig. 61 and listed in Table 33 and 34. In order to estimate the systematic effects caused by an imperfect detector simulation all subdetector resolutions were scaled by 10%. The uncertainty due to a possible shift in the energy scale of the small angle calorimeters was estimated by introducing an offset of 0.5 GeV to the measure energy. the polar and azimuthal angles of the scattered electrons were shifted by 0.25 mrad and 0.5 mrad, respectively. The cross sections of the background processes were changed conservatively by ±10%. The dependence on the Monte Carlo model used to correct the data was estimated using PHOT02 instead of PYTHIA. The systematic error was calculated as the quadratic sum of the three largest effects in each bin. The main contributions to the systematic error came from varying the resolutions for the

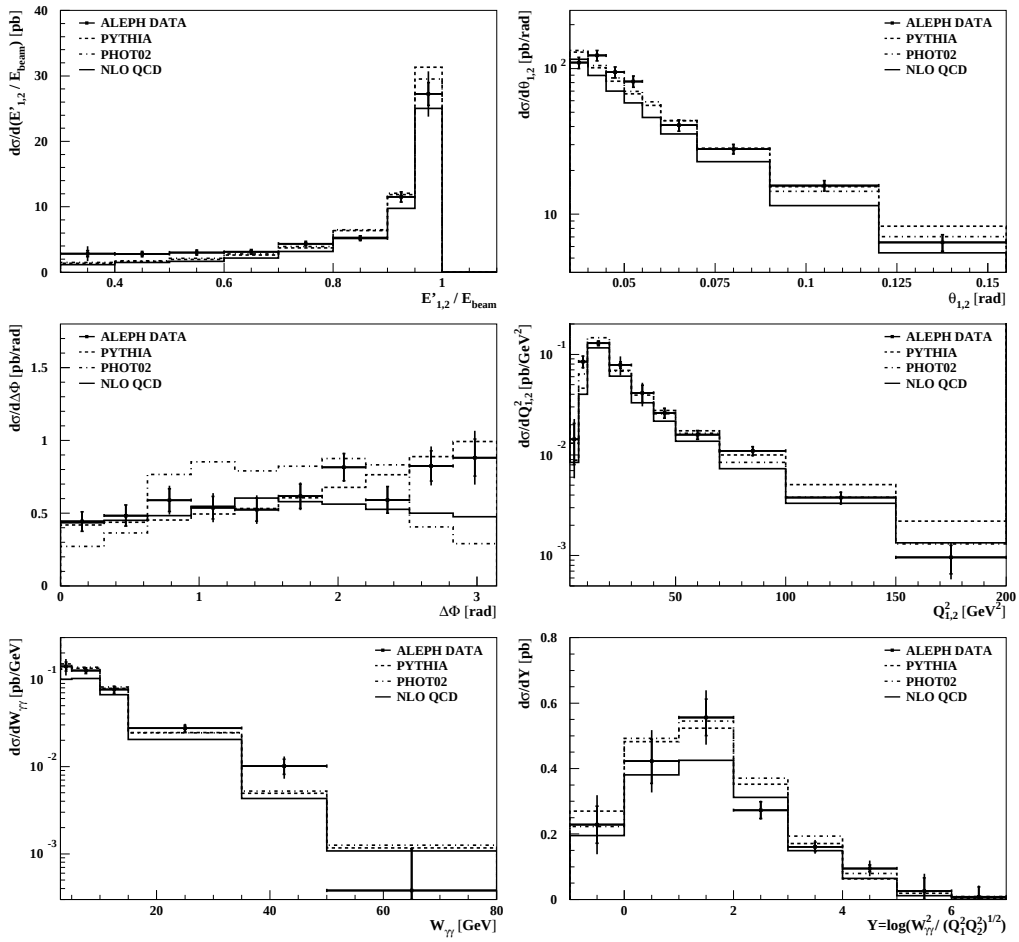

Figure 61: The differential cross section for the process $e^+e^- \to e^+e^-$ hadrons in the kinematical region defined in Table 12, measured by the ALEPH experiment. Points represent the data with statistical and systematic errors added in quadrature. The predictions of PYTHIA (dash), PHOT02 (dash-dot) and NLO predictions of [34] for the process $e^+e^- \to e^+e^- q\bar{q}$ (solid) are shown as histograms.

hadronic system and the tagged electron energy. The measured cross sections are compared with the PYTHIA and PHOT02 Monte Carlo models and with a NLO calculation of [34] for the process $e^+e^- \to e^+e^- q\bar{q}$. Due to the geometrical acceptance there is a gap in the measurement of the cross section as a function of $\theta_{1,2}$ between 55 mrad and 60 mrad. However, for the other measurements this gap has been interpolated with a Monte Carlo model. The presented differential cross sections are rather well described by the two Monte Carlo models and by the NLO calculation. The only exception is the azimuthal angle between electron scattering planes. In this case only PYTHIA gives a good description of the data. The NLO calculation underestimates the cross section at large angles, whereas PHOT02 does not describe the data.

Due to the large range of the possible polar angles of the scattered electrons in the ALEPH measurements, the virtualities of exchanged photons can be quite different, allowing for an evolution in transverse momenta of gluons emitted along the ladder in Fig. 19.

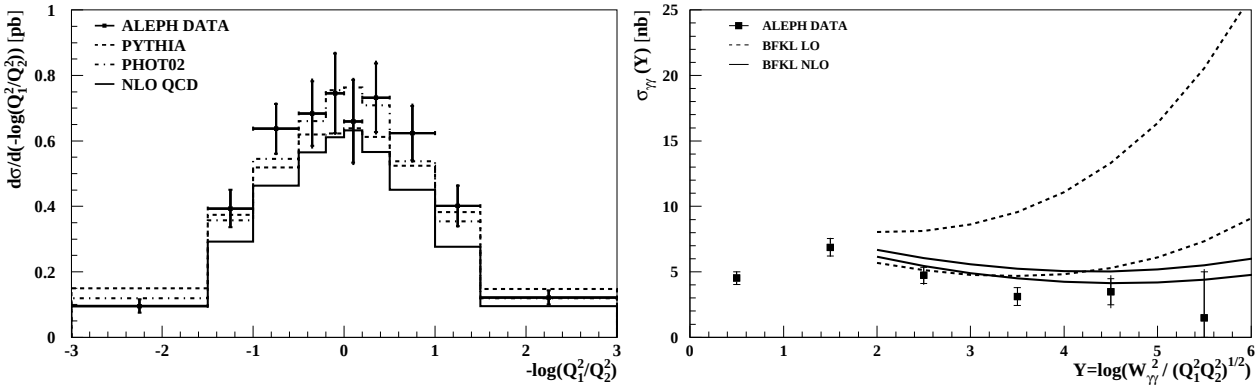

Figure 62: The differential cross section for the process $e^+e^- \to e^+e^-$ hadrons in the kinematical region defined in Table 12, measured by the ALEPH experiment, as a function of $\log Q_1^2/Q_2^2$. The meaning of symbols as in Fig. 61.

Figure 63: The total cross section for the process $\gamma^\star\gamma^\star \to$ hadrons measured by the ALEPH experiment, as a function of $\overline{Y}$. The data are compared with LO BFKL and NLO BFKL predictions, with the bands giving the uncertainty from the variation of the scale parameter s_0 from Q^2 to $10\,Q^2$ in LO and from Q^2 to $4\,Q^2$ in NLO.

This can be seen in Fig. 62 where the differential e^+e^- cross section as the function of the ratio of the virtualities of the exchanged photons in the phase space defined in Table 12 is presented. Therefore the above ALEPH results can not be compared with BFKL calculation. To enable this comparison a further cut has been applied, $|\log Q_1^2/Q_2^2| < 1$. The whole analysis, including the systematic error estimation, was redone with this additional cut. The agreement between the ALEPH data and the Monte Carlo simulations was on the same level as previously, while the data statistics was reduced by 40%. In Fig. 63 we present the $\gamma^\star\gamma^\star$ cross section as a function of $\overline{Y}$ in the phase space defined with cuts in Table 12 together with the additional cut on the photon virtualities, $|\log Q_1^2/Q_2^2| < 1$. The measured cross section is compared to LO and NLO BFKL calculations. The ranges denoting the LO and NLO calculations correspond to the variation of the scale parameter s_0 from Q^2 to $10\,Q^2$ or from Q^2 to $4\,Q^2$, respectively. The LO calculations overestimate the measured cross section even at lower values of $\overline{Y}$. The NLO calculation is consistent with the data (although some systematic shift is observed).

After the presentation of independent results obtained by different LEP experiments on the structure of interactions of virtual photons, it is time to ask whether they are consistent. It is not easy to compare them because the phase space of each measurement (see Table 12) is different, and also the observables for which the cross sections have been measured are not the same. Essentially the only quantity which can be compared is the differential e^+e^- cross section as a function of $\overline{Y}$. However, due to different phase space regions of the measurements it is necessary to use Monte Carlo models to 'correct' the measurements to the same phase space. We have chosen the phase space of the OPAL measurement and used PYTHIA (for ALEPH) and PHOJET (for L3) Monte Carlo programs to find the correction factors. The comparison is shown in Fig. 64. The original errors of the L3 and ALEPH

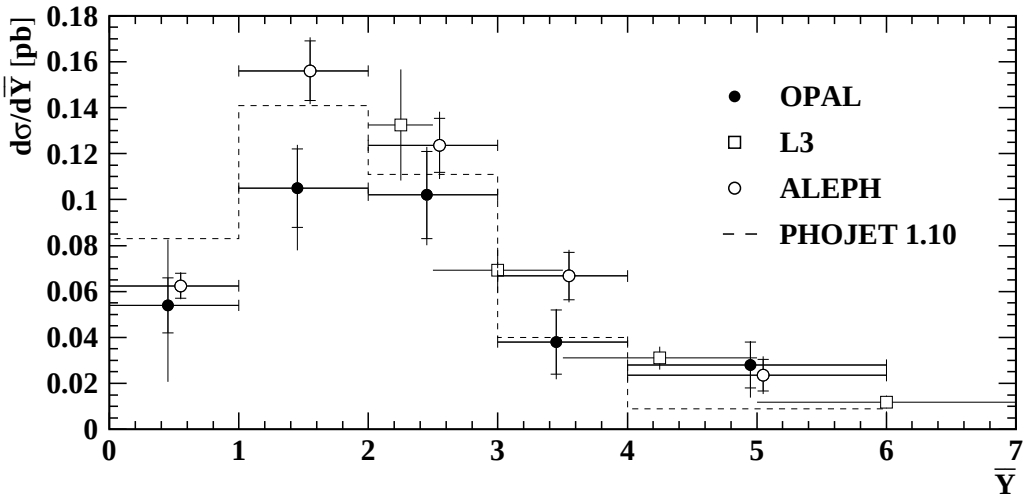

Figure 64: Comparison of the cross sections for the process $e^+e^- \to e^+e^-$ hadrons as a function of $\overline{Y}$ measured by different LEP experiments. The ALEPH and L3 data have been corrected to the phase space used in the OPAL measurement using Monte Carlo models as explained in the text.

measurements have been increased by the (small) statistical errors of the correction factors. One can conclude that the agreement between the LEP measurements is quite good. The data are consistent with PHOJET predictions which does not involve any BFKL like effects and with existing NLO or HO BFKL predictions. However, for unambigous confirmation of BFKL effects in interactions of two virtual photons one needs to acces higher values of $\overline{Y}$, which migh be possible only at a future linear collider.

10 Summary and outlook

In this review article we discussed in detail the theoretical foundations and the measurements of the QED and hadronic structure of the real and virtual photons as well as the hadronic structure of the electron. The paper is concentrated on the measurements performed at LEP experiments, although wherever similar measurements performed at other e^+e^- colliders exist, they are compared to the LEP results. The measurements at LEP have been performed at several e^+e^- centre-of-mass energies starting from $\sqrt{s_{ee}} \approx 92$ GeV at LEP1 phase (with integrated luminosities of about 100 pb^{-1} per experiment), and in the range $\sqrt{s_{ee}} = 161-209$ GeV at LEP2 phase (with integrated luminosities of above 600 pb^{-1} per experiment).

The measurements of the QED structure of the photon are based on full LEP1 statistics. Extending the measurements to LEP2 phase would reduce the errors by a factor of more than two, however this is not planed. Together with the measurements performed by the other experiments, the QED structure function of the quasi-real photon $F^{\gamma}_{2,\mathrm{QED}}$ has been measured in the range of average probe photon virtualities of $0.43 < \langle Q^2 \rangle < 130$ GeV^2. The effect of the small, but different from zero, virtuality of the target photon has been observed. Apart of $F^{\gamma}_{2,\mathrm{QED}}$, two other structure functions of the real photon, $F^{\gamma}_{\mathrm{A,QED}}$ and $F^{\gamma}_{\mathrm{B,QED}}$, have been measured at LEP for the first time. The QED structure of interactions of virtual photons has been also studied at LEP, and the importance of the contribution to the cross section of the interference terms, τ_{TT} and τ_{TL}, was observed. All these measurements are in a very good agreement with predictions of QED.

The hadronic structure function of the photon F^{γ}_2 has been measured at LEP using the full available statistics. Together with several measurements performed at other e^+e^- colliders, the data cover at present a broad range of average virtualities, $0.24 < \langle Q^2 \rangle < 780$ GeV^2 and reach as low x as approximatelly 10^{-3}. The data clearly disfavour the QPM predictions, and suggest a rise of F^{γ}_2 towards low values of x, as predicted by most of the modern parameterisations of F^{γ}_2. Using the broad range of $\langle Q^2 \rangle$, the Q^2 evolution of F^{γ}_2 was studied. The expected positive scaling violations for all values of x have been confirmed. The hadronic structure function of the photon has been also measured separately for charm quarks using full LEP2 statistics. The measured $F^{\gamma}_{2,c}$ agrees perfectly with perturbative QCD calculation at NLO for $x > 0.1$, and is above the predictions for $x < 0.1$.

As suggested by some theorists, the hadronic structure function of the electron F^e_2 has been recently measured at LEP. Because of the much better reconstruction of the variable z than the variable x, the measurement of F^e_2 does not require an unfolding procedure, which is needed for the measurement of F^{γ}_2. However, because the different predictions of the photon structure function lead to very similar electron structure functions, the measurement of F^e_2 does not have a better resolving power than the measurements of F^{γ}_2.

The hadronic structure of interactions of virtual photons have been studied in terms of the effective structure function of the virtual photon $F^{\gamma}_{\mathrm{eff}}$ and differential e^+e^- and total $\gamma^\star\gamma^\star$ cross sections. The measurements of $F^{\gamma}_{\mathrm{eff}}$ are in full agreement with the naive QPM model predictions derived from the doubly virtual box diagram. The measured P^2 dependence of $F^{\gamma}_{\mathrm{eff}}$, as expected, suggests a slow decrease with increasing P^2. The measurements of the cross sections for interactions of two highly virtual photons serve as an ideal tool to distinguish between DGLAP and BFKL dynamics of partons inside the photon, because the

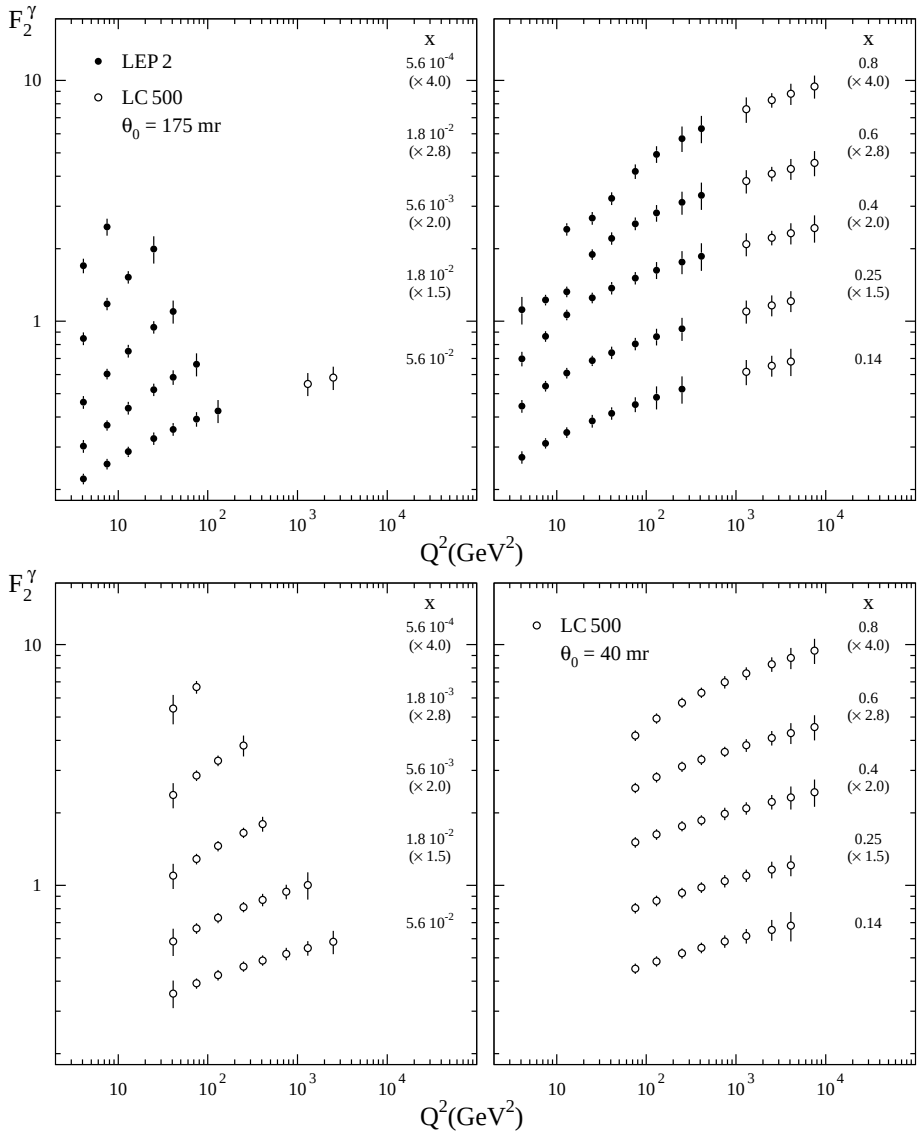

Figure 65: Simulated linear collider data for integrated luminosity 10 fb^{-1} at $\sqrt{s_{\rm ee}} = 500$ GeV if tagging is feasible for $\theta > 175$ mrad (upper plots) and for $\theta > 40$ mrad (bottom plots). The LEP2 points shown in the upper plots are simulated data points.

appropriate calculations do not involve any non-perturbative input. The measured cross section $\sigma_{\gamma^\star\gamma^\star}$ as a function of $\overline{Y}$ disfavours as steep rise of the cross section as predicted by the LO BFKL calculation. The data are consistent with NLO BFKL calculation. However, the NLO corrections are very large, and therefore higher order calculations are needed to make the perturbative BFKL calculations more credible.

The measurements of the photon structure functions are expected to be extended to higher values of Q^2 and to lower values of x at a future linear collider. The discussion of the physics goals for a linear collider can be found e.g. in [154, 155]. A future linear collider running in e^+e^- mode is expected to operate in the first phase at $\sqrt{s_{\rm ee}} = 500$ GeV and to

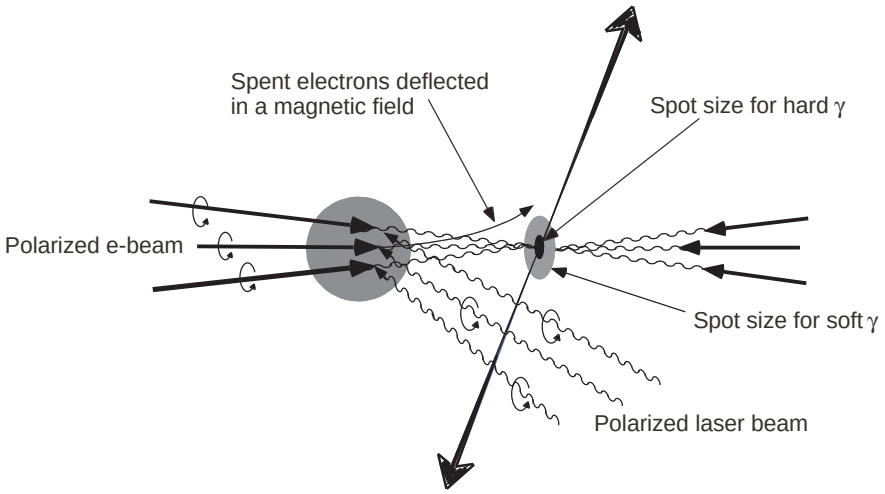

Figure 66: Creation of high energetic photons in the Compton backscattering process of laser photons off the beam electrons. The figure is taken from [158].

be able to accumulate an integrated luminosity of 100 fb^{-1} per year of operation. In the second phase the energy is expected to be rised to $\sqrt{s_{\rm ee}} = 2$ TeV. The background studies performed in [157] show that the amount of background per bunch crossing expected for the TESLA design is a factor of 10^6 higher than the number of two photon interactions with $W > 5$ GeV and with an average visible energy of 10 GeV. Most of background sources will lead to $\rm e^+e^-$ pair creation and to hadronic background, with most of particles produced in the forward regions of the detector. Therefore in each detector proposal the forward regions must be shielded with massive masks, which will make difficult, or even impossible, tagging electrons scattered at small angles. Electron tagging outside the mask, out of a cone of about 175 mrad will give access to a previously unexplored high Q^2 range, Fig. 65 [156], but will give neither overlap with LEP2 results nor sensitivity to the small x region. To achieve the overlap with LEP2 measurements, one needs an electron tagging device inside the shielding, down to about 40 mrad, Fig. 65. This is however still not sufficient to unfold structure functions in the region $x < 0.1$, since small x corresponds to large W^2, where an unknown part of the hadronic system disappears undetected in the forward direction.

In order to circumevent this problem the eγ laser backscattering mode is ideal. The method to produce a beam of high energetic photons from an electron beam by means of the Compton backscattering process is shown in Fig. 66. The photons produced by high intensity laser are brought into collision with the electron beams at distances of about $0.1 - 1$ cm from the interaction point. The photons are scattered into a small cone around the initial electron direction and receive a large fraction of the electron energy. Spent electrons are deflected in a magnetic field. The invariant mass of the electron photon system is expected to peak around $\sqrt{s_{\rm e\gamma}} \approx 0.8\sqrt{s_{\rm ee}}$ [154].

The partonic content of the quasi-real and virtual photons has been also extensively studied at the HERA collider mainly in photon-proton scattering and in deep inelastic electron-proton scattering. However the results obtained by the HERA experiments are beyond the scope of this review. The reader is refered to original publications or to review articles e.g. [6, 7, 11].

Acknowledgements

I would like to express my gratitude to Professor Danuta Kisielewska for her constant support and encouragement since the time when I first met her as a student of physics at AGH.
I would like to thank Richard Nisius and Albert de Roeck for the fruitful collaboration and useful discussions on several topics presented in this paper.
I am grateful to all the members of the OPAL Collaboration for discussions and friendly atmosphere during my stay at CERN as a postdoctoral fellow.
Last but not least, I would like to thank my parents for their support and understanding.

A Results on QED structure of the photon

In this Appendix we present the results on the QED photon structure functions $F^{\gamma}_{2,\mathrm{QED}}$, $F^{\gamma}_{\mathrm{A,QED}}$ and $F^{\gamma}_{\mathrm{B,QED}}$ obtained by the LEP experiments OPAL, DELPHI and L3 as well as by the other experiments including CELLO, PLUTO and TPC/2γ. In all cases the structure functions scaled by the fine structure constant are given. Depending on the measurement, both statistical and systematic errors or only statistical or total error are given.
Also the results of the measurement of the differential cross section $d\sigma/dx$ for the scattering of two virtual photons in the process $e^+e^- \to e^+e^- \mu^+\mu^-$ are listed.

CELLO $Q^2 = 1.2 - 39$ GeV^2 (9.5 GeV^2)			
x range	$\langle F^{\gamma}_{2,\mathrm{QED}}\rangle/\alpha$	$\pm\sigma_{stat}$	$\pm\sigma_{sys}$
0.00 - 0.10	0.222	±0.077	±0.018
0.10 - 0.20	0.426	±0.128	±0.032
0.20 - 0.30	0.562	±0.162	±0.045
0.30 - 0.40	0.511	±0.153	±0.039
0.40 - 0.50	0.597	±0.170	±0.049
0.50 - 0.60	0.571	±0.170	±0.046
0.60 - 0.70	0.545	±0.170	±0.046
0.70 - 0.80	1.202	±0.256	±0.095
0.80 - 0.90	1.057	±0.273	±0.085
0.90 - 1.00	1.185	±0.528	±0.092

PLUTO $Q^2 = 1 - 16$ GeV^2 (5.5 GeV^2)		
x range	$\langle F^{\gamma}_{2,\mathrm{QED}}\rangle/\alpha$	$\pm\sigma_{tot}$
0.00 - 0.10	0.081	±0.040
0.10 - 0.20	0.177	±0.048
0.20 - 0.30	0.532	±0.089
0.30 - 0.40	0.403	±0.105
0.40 - 0.50	0.532	±0.113
0.50 - 0.60	0.597	±0.161
0.60 - 0.70	0.952	±0.322
0.70 - 0.80	0.887	±0.444

TPC/2γ $Q^2 = 0.14 - 1.28$ GeV^2 (0.45 GeV^2)			
x range	$\langle F^{\gamma}_{2,\mathrm{QED}}\rangle/\alpha$	$\pm\sigma_{stat}$	$\pm\sigma_{sys}$
0.00 - 0.05	0.038	±0.010	±0.007
0.05 - 0.10	0.104	±0.010	±0.017
0.10 - 0.15	0.135	±0.017	±0.021
0.15 - 0.20	0.172	±0.021	±0.028
0.20 - 0.25	0.219	±0.031	±0.035
0.25 - 0.30	0.281	±0.042	±0.044
0.30 - 0.35	0.320	±0.042	±0.051
0.35 - 0.40	0.344	±0.037	±0.055
0.40 - 0.50	0.370	±0.042	±0.059
0.50 - 0.60	0.373	±0.037	±0.059
0.60 - 0.70	0.357	±0.037	±0.057
0.70 - 0.80	0.354	±0.037	±0.057
0.80 - 0.90	0.291	±0.031	±0.047
0.90 - 1.00	0.323	±0.068	±0.051

PLUTO $Q^2 = 10 - 160$ GeV^2 (40 GeV^2)		
x range	$\langle F^{\gamma}_{2,\mathrm{QED}}\rangle/\alpha$	$\pm\sigma_{tot}$
0.00 - 0.20	0.177	±0.113
0.20 - 0.40	0.565	±0.210
0.40 - 0.60	0.532	±0.241
0.60 - 0.80	1.532	±0.468
0.80 - 1.00	0.807	±0.581

Table 14: The average photon structure function $\langle F^{\gamma}_{2,\mathrm{QED}}\rangle/\alpha$ measured by the CELLO [114], PLUTO [115] and TPC/2γ [116] experiments. The numbers listed here are in all cases read off the published figures. For the consistency they are the same as given in [7]. The Q^2 range of each measurement, with the average value in parentheses, is given next to the experiment name. No information is avalible on the average $\langle P^2\rangle$ in those measurements.

OPAL $Q^2 = 1.5 - 3$ GeV^2 (2.2 GeV^2)			
x range	$F^\gamma_{2,\mathrm{QED}}/\alpha$	$\pm\sigma_{stat}$	$\pm\sigma_{sys}$
0.00 - 0.10	0.115	$\pm$0.007	$\pm$0.005
0.10 - 0.20	0.219	$\pm$0.010	$\pm$0.008
0.20 - 0.30	0.282	$\pm$0.012	$\pm$0.011
0.30 - 0.40	0.347	$\pm$0.015	$\pm$0.011
0.40 - 0.50	0.356	$\pm$0.017	$\pm$0.010
0.50 - 0.60	0.400	$\pm$0.020	$\pm$0.011
0.60 - 0.70	0.483	$\pm$0.025	$\pm$0.016
0.70 - 0.80	0.491	$\pm$0.031	$\pm$0.012
0.80 - 0.90	0.532	$\pm$0.034	$\pm$0.013
0.90 - 0.97	0.308	$\pm$0.032	$\pm$0.071

OPAL $Q^2 = 3 - 7$ GeV^2 (4.2 GeV^2)			
x range	$F^\gamma_{2,\mathrm{QED}}/\alpha$	$\pm\sigma_{stat}$	$\pm\sigma_{sys}$
0.00 - 0.10	0.108	$\pm$0.010	$\pm$0.016
0.10 - 0.20	0.237	$\pm$0.014	$\pm$0.009
0.20 - 0.30	0.320	$\pm$0.018	$\pm$0.012
0.30 - 0.40	0.378	$\pm$0.020	$\pm$0.011
0.40 - 0.50	0.373	$\pm$0.020	$\pm$0.010
0.50 - 0.60	0.421	$\pm$0.025	$\pm$0.012
0.60 - 0.70	0.519	$\pm$0.029	$\pm$0.013
0.70 - 0.80	0.556	$\pm$0.034	$\pm$0.011
0.80 - 0.90	0.601	$\pm$0.040	$\pm$0.013
0.90 - 0.97	0.470	$\pm$0.041	$\pm$0.051

OPAL $Q^2 = 6 - 10$ GeV^2 (8.4 GeV^2)			
x range	$F^\gamma_{2,\mathrm{QED}}/\alpha$	$\pm\sigma_{stat}$	$\pm\sigma_{sys}$
0.00 - 0.10	0.090	$\pm$0.012	$\pm$0.007
0.10 - 0.20	0.271	$\pm$0.022	$\pm$0.019
0.20 - 0.30	0.334	$\pm$0.029	$\pm$0.020
0.30 - 0.40	0.409	$\pm$0.033	$\pm$0.022
0.40 - 0.50	0.496	$\pm$0.038	$\pm$0.026
0.50 - 0.60	0.563	$\pm$0.043	$\pm$0.026
0.60 - 0.70	0.596	$\pm$0.049	$\pm$0.023
0.70 - 0.80	0.687	$\pm$0.056	$\pm$0.023
0.80 - 0.90	0.891	$\pm$0.072	$\pm$0.044
0.90 - 0.97	0.761	$\pm$0.074	$\pm$0.049

OPAL $Q^2 = 10 - 15$ GeV^2 (12.4 GeV^2)			
x range	$F^\gamma_{2,\mathrm{QED}}/\alpha$	$\pm\sigma_{stat}$	$\pm\sigma_{sys}$
0.00 - 0.10	0.095	$\pm$0.010	$\pm$0.007
0.10 - 0.20	0.264	$\pm$0.018	$\pm$0.014
0.20 - 0.30	0.319	$\pm$0.023	$\pm$0.014
0.30 - 0.40	0.428	$\pm$0.028	$\pm$0.020
0.40 - 0.50	0.446	$\pm$0.030	$\pm$0.018
0.50 - 0.60	0.558	$\pm$0.034	$\pm$0.023
0.60 - 0.70	0.698	$\pm$0.040	$\pm$0.030
0.70 - 0.80	0.770	$\pm$0.044	$\pm$0.026
0.80 - 0.90	0.871	$\pm$0.053	$\pm$0.033
0.90 - 0.97	0.795	$\pm$0.053	$\pm$0.044

OPAL $Q^2 = 15 - 30$ GeV^2 (21 GeV^2)			
x range	$F^\gamma_{2,\mathrm{QED}}/\alpha$	$\pm\sigma_{stat}$	$\pm\sigma_{sys}$
0.00 - 0.15	0.117	$\pm$0.028	$\pm$0.012
0.15 - 0.30	0.302	$\pm$0.039	$\pm$0.021
0.30 - 0.45	0.403	$\pm$0.051	$\pm$0.029
0.45 - 0.60	0.559	$\pm$0.058	$\pm$0.030
0.60 - 0.75	0.782	$\pm$0.070	$\pm$0.034
0.75 - 0.90	0.907	$\pm$0.080	$\pm$0.033
0.90 - 0.97	0.802	$\pm$0.103	$\pm$0.033

OPAL $Q^2 = 70 - 400$ GeV^2 (130 GeV^2)			
x range	$F^\gamma_{2,\mathrm{QED}}/\alpha$	$\pm\sigma_{stat}$	$\pm\sigma_{sys}$
0.00 - 0.40	0.343	$\pm$0.094	$\pm$0.034
0.40 - 0.60	0.578	$\pm$0.079	$\pm$0.052
0.60 - 0.80	0.936	$\pm$0.109	$\pm$0.063
0.80 - 0.90	1.125	$\pm$0.130	$\pm$0.057

Table 15: The photon structure function $F^\gamma_{2,\mathrm{QED}}/\alpha$ measured by the OPAL experiment [111]. The Q^2 range of each measurement, with the average value in parentheses, is given next to the experiment name. The average virtuality of the target photon in all the measurements is $\langle P^2 \rangle = 0.05$ GeV^2.

DELPHI $Q^2 = 2.4 - 51.2$ GeV^2 (12.5 GeV^2)			
x range	$\langle F^\gamma_{2,\mathrm{QED}}\rangle/\alpha$	$\pm\sigma_{stat}$	$\pm\sigma_{sys}$
0.00 - 0.10	0.106	$\pm$0.008	$\pm$0.023
0.10 - 0.20	0.273	$\pm$0.012	$\pm$0.012
0.20 - 0.30	0.426	$\pm$0.017	$\pm$0.012
0.30 - 0.40	0.515	$\pm$0.021	$\pm$0.012
0.40 - 0.50	0.573	$\pm$0.024	$\pm$0.004
0.50 - 0.60	0.645	$\pm$0.029	$\pm$0.003
0.60 - 0.70	0.743	$\pm$0.038	$\pm$0.021
0.70 - 0.80	0.942	$\pm$0.060	$\pm$0.053
0.80 - 1.00	1.152	$\pm$0.112	$\pm$0.094

L3 $Q^2 = 1.4 - 7.6$ GeV^2 (3.25 GeV^2)			
x range	$\langle F^\gamma_{2,\mathrm{QED}}\rangle/\alpha$	$\pm\sigma_{stat}$	$\pm\sigma_{sys}$
0.00 - 0.10	0.062	$\pm$0.006	$\pm$0.002
0.10 - 0.20	0.216	$\pm$0.015	$\pm$0.007
0.20 - 0.30	0.326	$\pm$0.022	$\pm$0.011
0.30 - 0.40	0.391	$\pm$0.026	$\pm$0.013
0.40 - 0.50	0.477	$\pm$0.028	$\pm$0.016
0.50 - 0.60	0.534	$\pm$0.029	$\pm$0.018
0.60 - 0.70	0.654	$\pm$0.035	$\pm$0.022
0.70 - 0.80	0.709	$\pm$0.037	$\pm$0.023
0.80 - 0.90	0.775	$\pm$0.046	$\pm$0.026
0.90 - 1.00	0.549	$\pm$0.069	$\pm$0.018

DELPHI $Q^2 = 45.9 - 752.8$ GeV^2 (120 GeV^2)			
x range	$\langle F^\gamma_{2,\mathrm{QED}}\rangle/\alpha$	$\pm\sigma_{stat}$	$\pm\sigma_{sys}$
0.00 - 0.20	0.387	$\pm$0.214	$\pm$0.015
0.20 - 0.40	0.464	$\pm$0.133	$\pm$0.051
0.40 - 0.60	0.673	$\pm$0.138	$\pm$0.049
0.60 - 0.80	0.984	$\pm$0.162	$\pm$0.026
0.80 - 1.00	1.508	$\pm$0.231	$\pm$0.044

Table 16: The average photon structure function $\langle F^\gamma_{2,\mathrm{QED}}\rangle/\alpha$ measured by the DELPHI [112] and by the L3 [113] experiments. The Q^2 range of each measurement, with the average value in parentheses, is given next to the experiment name. The average virtuality of the target photon in the DELPHI measurement is $\langle P^2\rangle = 0.025 \pm 0.005$ GeV^2 and $\langle P^2\rangle = 0.073 \pm 0.056$ GeV^2 for the samples with low and high Q^2, respectively, and in the L3 measurement $\langle P^2\rangle = 0.033$ GeV^2.

OPAL $Q^2 = 1.5 - 30$ GeV^2 $\langle Q^2\rangle = 5.4$ GeV^2			
x range	$F^\gamma_{2,\mathrm{QED}}/\alpha \pm\sigma_{stat} \pm\sigma_{sys}$	$F^\gamma_{\mathrm{A,QED}}/\alpha \pm\sigma_{stat} \pm\sigma_{sys}$	$F^\gamma_{\mathrm{B,QED}}/\alpha \pm\sigma_{stat} \pm\sigma_{sys}$
$x < 0.25$	0.249 $\pm$0.006 $\pm$0.008	0.039 $\pm$0.007 $\pm$0.003	0.029 $\pm$0.010 $\pm$0.003
0.25 $-$ 0.50	0.523 $\pm$0.011 $\pm$0.014	0.011 $\pm$0.016 $\pm$0.004	0.101 $\pm$0.025 $\pm$0.011
0.50 $-$ 0.75	0.738 $\pm$0.017 $\pm$0.019	$-$0.122 $\pm$0.021 $\pm$0.006	0.121 $\pm$0.041 $\pm$0.017
0.75 $< x$	0.871 $\pm$0.027 $\pm$0.021	$-$0.201 $\pm$0.033 $\pm$0.013	0.063 $\pm$0.056 $\pm$0.018

L3 $Q^2 = 1.4 - 7.6$ GeV^2 $\langle Q^2\rangle = 3.35$ GeV^2			
x range	$F^\gamma_{2,\mathrm{QED}}/\alpha \pm\sigma_{tot}$	$F^\gamma_{\mathrm{A,QED}}/\alpha \pm\sigma_{tot}$	$F^\gamma_{\mathrm{B,QED}}/\alpha \pm\sigma_{tot}$
0.00 $-$ 0.25	0.090 $\pm$0.008	0.014 $\pm$0.024	0.008 $\pm$0.010
0.25 $-$ 0.50	0.404 $\pm$0.016	0.036 $\pm$0.032	0.090 $\pm$0.021
0.50 $-$ 0.75	0.597 $\pm$0.020	$-$0.126 $\pm$0.052	0.168 $\pm$0.040
0.75 $-$ 1.00	0.731 $\pm$0.032	$-$0.174 $\pm$0.062	0.089 $\pm$0.045

Table 17: The photon structure functions $F^\gamma_{\mathrm{A,QED}}/\alpha$ and $F^\gamma_{\mathrm{B,QED}}/\alpha$ measured by the OPAL [111] and L3 [113] experiments. Due to sligthly diffeent definition of $F^\gamma_{\mathrm{A,QED}}$ in the L3 publication, the original numbers for $F^\gamma_{\mathrm{A,QED}}$ given in Table 2 in [113] have been multiplied by -2.

OPAL $Q^2 = 1.5 - 30$ GeV^2 $\langle Q^2 \rangle = 5.4$ GeV^2						
x range	$F^\gamma_{\mathrm{A,QED}}/F^\gamma_{\mathrm{2,QED}}$	$\pm\sigma_{stat}$	$\pm\sigma_{sys}$	$\frac{1}{2}F^\gamma_{\mathrm{B,QED}}/F^\gamma_{\mathrm{2,QED}}$	$\pm\sigma_{stat}$	$\pm\sigma_{sys}$
$x < 0.25$	0.176	$\pm$0.031	$\pm$0.010	0.075	$\pm$0.025	$\pm$0.008
$0.25 - 0.50$	0.018	$\pm$0.028	$\pm$0.008	0.099	$\pm$0.024	$\pm$0.010
$0.50 - 0.75$	-0.171	$\pm$0.029	$\pm$0.007	0.081	$\pm$0.027	$\pm$0.011
$0.75 < x$	-0.228	$\pm$0.037	$\pm$0.014	0.037	$\pm$0.033	$\pm$0.011

L3 $Q^2 = 1.4 - 7.6$ GeV^2 $\langle Q^2 \rangle = 3.35$ GeV^2						
x range	$F^\gamma_{\mathrm{A,QED}}/F^\gamma_{\mathrm{2,QED}}$	$\pm\sigma_{stat}$	$\pm\sigma_{sys}$	$\frac{1}{2}F^\gamma_{\mathrm{B,QED}}/F^\gamma_{\mathrm{2,QED}}$	$\pm\sigma_{stat}$	$\pm\sigma_{sys}$
$0.00 - 0.25$	0.159	$\pm$0.040	$\pm$0.034	0.046	$\pm$0.012	$\pm$0.012
$0.25 - 0.50$	0.087	$\pm$0.071	$\pm$0.056	0.111	$\pm$0.019	$\pm$0.038
$0.50 - 0.75$	-0.210	$\pm$0.102	$\pm$0.057	0.141	$\pm$0.026	$\pm$0.048
$0.75 - 1.00$	-0.236	$\pm$0.091	$\pm$0.079	0.061	$\pm$0.019	$\pm$0.030

DELPHI $Q^2 = 2.4 - 51.2$ GeV^2 $\langle Q^2 \rangle = 12.5$ GeV^2				
x range	$F^\gamma_{\mathrm{A,QED}}/F^\gamma_{\mathrm{2,QED}}$	$\pm\sigma_{tot}$	$\frac{1}{2}F^\gamma_{\mathrm{B,QED}}/F^\gamma_{\mathrm{2,QED}}$	$\pm\sigma_{tot}$
$x < 0.20$	0.135	$\pm$0.043	0.004	$\pm$0.027
$0.20 - 0.40$	0.140	$\pm$0.035	0.077	$\pm$0.026
$0.40 - 0.60$	0.038	$\pm$0.044	0.099	$\pm$0.035
$0.60 < x$	-0.263	$\pm$0.059	0.182	$\pm$0.040

Table 18: The photon structure function ratios $F^\gamma_{\mathrm{A,QED}}/F^\gamma_{\mathrm{2,QED}}$ and $\frac{1}{2}F^\gamma_{\mathrm{B,QED}}/F^\gamma_{\mathrm{2,QED}}$ measured by the OPAL [111], L3 [113] and DELPHI [112] experiments. Due to sligthly diffeent definition of $F^\gamma_{\mathrm{A,QED}}$ in the L3 publication, the original numbers for $F^\gamma_{\mathrm{A,QED}}$ given in Table 2 in [113] have been multiplied by -2. In case of DELPHI the total error given is a sum in quadrature of statistical and systematic errors.

OPAL $\langle Q^2 \rangle = 3.6$ GeV^2 $\langle P^2 \rangle = 2.3$ GeV^2			
x range	$d\sigma/dx$	$\pm\sigma_{stat}$	$\pm\sigma_{sys}$
0.00 - 0.20	9.77	$\pm$1.62	$\pm$1.80
0.20 - 0.40	10.45	$\pm$1.26	$\pm$1.39
0.40 - 0.65	4.34	$\pm$1.07	$\pm$1.09

OPAL $\langle Q^2 \rangle = 14$ GeV^2 $\langle P^2 \rangle = 5$ GeV^2			
x range	$d\sigma/dx$	$\pm\sigma_{stat}$	$\pm\sigma_{sys}$
0.00 - 0.25	5.26	$\pm$0.82	$\pm$1.29
0.25 - 0.50	6.87	$\pm$0.78	$\pm$1.08
0.50 - 0.75	2.75	$\pm$0.60	$\pm$0.63

Table 19: The cross section for the scattering of two virtual photons in the process $e^+e^- \to e^+e^-\mu^+\mu^-$ measured by the OPAL experiment [111].

B Results on hadronic structure of the photon

In this Appendix we present the results on the hadronic photon structure function F_2^γ obtained by the LEP experiments OPAL, ALEPH, DELPHI and L3 as well as by the other experiments including AMY, CELLO, JADE, PLUTO, TASSO, TOPAZ and TPC/2γ. In all cases the structure functions scaled by the fine structure constant are given. Depending on the measurement, both statistical and systematic errors or only statistical or total error are given.

AMY			
$Q^2 = 3.5 - 12$ GeV^2		$\langle Q^2 \rangle = 6.8$ GeV^2	
x range	F_2^γ	$\pm\sigma_{stat}$	$\pm\sigma_{sys}$
0.015 - 0.125	0.337	$\pm$0.030	$\pm$0.044
0.125 - 0.375	0.302	$\pm$0.040	$\pm$0.029
0.375 - 0.620	0.322	$\pm$0.049	$\pm$0.084
$Q^2 = 25 - 220$ GeV^2		$\langle Q^2 \rangle = 73$ GeV^2	
x range	F_2^γ	$\pm\sigma_{stat}$	$\pm\sigma_{sys}$
0.125 - 0.375	0.65	$\pm$0.08	$\pm$0.06
0.375 - 0.625	0.60	$\pm$0.16	$\pm$0.03
0.625 - 0.875	0.65	$\pm$0.11	$\pm$0.08
$Q^2 > 110$ GeV^2		$\langle Q^2 \rangle = 390$ GeV^2	
x range	F_2^γ	$\pm\sigma_{stat}$	$\pm\sigma_{sys}$
0.120 - 0.500	0.94	$\pm$0.23	$\pm$0.10
0.500 - 0.800	0.82	$\pm$0.16	$\pm$0.11

TOPAZ			
$Q^2 = 3 - 10$ GeV^2		$\langle Q^2 \rangle = 5.1$ GeV^2	
x range	F_2^γ/α	$\pm\sigma_{stat}$	$\pm\sigma_{sys}$
0.010 - 0.076	0.33	$\pm$0.02	$\pm$0.05
0.076 - 0.200	0.29	$\pm$0.03	$\pm$0.03
$Q^2 = 10 - 30$ GeV^2		$\langle Q^2 \rangle = 16$ GeV^2	
x range	$\langle F_2^\gamma \rangle/\alpha$	$\pm\sigma_{stat}$	$\pm\sigma_{sys}$
0.020 - 0.150	0.60	$\pm$0.08	$\pm$0.06
0.150 - 0.330	0.56	$\pm$0.09	$\pm$0.04
0.330 - 0.780	0.46	$\pm$0.15	$\pm$0.06
$Q^2 = 45 - 130$ GeV^2		$\langle Q^2 \rangle = 80$ GeV^2	
x range	$\langle F_2^\gamma \rangle/\alpha$	$\pm\sigma_{stat}$	$\pm\sigma_{sys}$
0.060 - 0.320	0.68	$\pm$0.26	$\pm$0.05
0.320 - 0.590	0.83	$\pm$0.22	$\pm$0.05
0.590 - 0.980	0.53	$\pm$0.21	$\pm$0.05

JADE		
$Q^2 = 10 - 55$ GeV^2		$\langle Q^2 \rangle = 24$ GeV^2
x range	F_2^γ	$\pm\sigma_{tot}$
0.000 - 0.100	0.51	$\pm$0.15
0.100 - 0.200	0.29	$\pm$0.12
0.200 - 0.400	0.34	$\pm$0.10
0.400 - 0.600	0.59	$\pm$0.12
0.600 - 0.900	0.23	$\pm$0.12
$Q^2 = 30 - 220$ GeV^2		$\langle Q^2 \rangle = 100$ GeV^2
x range	F_2^γ	$\pm\sigma_{tot}$
0.100 - 0.300	0.52	$\pm$0.23
0.300 - 0.600	0.75	$\pm$0.22
0.600 - 0.900	0.90	$\pm$0.27

TASSO		
$Q^2 = 7 - 70$ GeV^2		$\langle Q^2 \rangle = 23$ GeV^2
x range	F_2^γ/α	$\pm\sigma_{tot}$
0.020 - 0.200	0.366	$\pm$0.089
0.200 - 0.400	0.670	$\pm$0.086
0.400 - 0.600	0.722	$\pm$0.104
0.600 - 0.800	0.693	$\pm$0.116
0.800 - 0.980	0.407	$\pm$0.222

Table 20: The photon structure function F_2^γ/α measured by the AMY [123,124], JADE [125], TOPAZ [130] and TASSO [128] experiments. The Q^2 range of each measurement, with the average value in parentheses, is given next to the experiment name. The quoted numbers for the JADE and TASSO measurements have been taken from the RAL database, which were read off the figures in the original publications and contain probably only the total errors.

TPC/2γ			
$Q^2 = 0.2 - 0.3$ GeV^2		$\langle Q^2 \rangle = 0.24$ GeV^2	
x range	F_2^γ/α	$\pm\sigma_{stat}$	$\pm\sigma_{sys}$
0.000 - 0.020	0.084	$\pm$0.005	$\pm$0.001
0.020 - 0.060	0.074	$\pm$0.008	$\pm$0.001
0.060 - 0.180	0.062	$\pm$0.013	$\pm$0.001
$Q^2 = 0.3 - 0.5$ GeV^2		$\langle Q^2 \rangle = 0.38$ GeV^2	
x range	F_2^γ/α	$\pm\sigma_{stat}$	$\pm\sigma_{sys}$
0.000 - 0.020	0.113	$\pm$0.007	$\pm$0.001
0.020 - 0.055	0.118	$\pm$0.011	$\pm$0.001
0.055 - 0.111	0.171	$\pm$0.021	$\pm$0.002
0.111 - 0.243	0.151	$\pm$0.028	$\pm$0.002
$Q^2 = 0.5 - 1$ GeV^2		$\langle Q^2 \rangle = 0.71$ GeV^2	
x range	F_2^γ/α	$\pm\sigma_{stat}$	$\pm\sigma_{sys}$
0.000 - 0.028	0.117	$\pm$0.006	$\pm$0.001
0.028 - 0.065	0.130	$\pm$0.010	$\pm$0.001
0.065 - 0.121	0.170	$\pm$0.017	$\pm$0.002
0.121 - 0.340	0.133	$\pm$0.013	$\pm$0.002

TPC/2γ			
$Q^2 = 1 - 1.6$ GeV^2		$\langle Q^2 \rangle = 1.3$ GeV^2	
x range	F_2^γ/α	$\pm\sigma_{stat}$	$\pm\sigma_{sys}$
0.000 - 0.050	0.107	$\pm$0.013	$\pm$0.001
0.050 - 0.126	0.184	$\pm$0.021	$\pm$0.002
0.126 - 0.215	0.215	$\pm$0.034	$\pm$0.003
0.215 - 0.507	0.102	$\pm$0.031	$\pm$0.002
$Q^2 = 1.8 - 4$ GeV^2		$\langle Q^2 \rangle = 2.8$ GeV^2	
x range	F_2^γ/α	$\pm\sigma_{stat}$	$\pm\sigma_{sys}$
0.000 - 0.080	0.134	$\pm$0.018	$\pm$0.002
0.080 - 0.156	0.234	$\pm$0.031	$\pm$0.003
0.156 - 0.303	0.198	$\pm$0.042	$\pm$0.002
0.303 - 0.600	0.160	$\pm$0.033	$\pm$0.002
$Q^2 = 4 - 6.6$ GeV^2		$\langle Q^2 \rangle = 5.1$ GeV^2	
x range	F_2^γ/α	$\pm\sigma_{stat}$	$\pm\sigma_{sys}$
0.021 - 0.199	0.224	$\pm$0.034	$\pm$0.003
0.199 - 0.359	0.373	$\pm$0.057	$\pm$0.005
0.359 - 0.740	0.300	$\pm$0.044	$\pm$0.004

PLUTO			
$Q^2 = 1.5 - 3$ GeV^2		$\langle Q^2 \rangle = 2.4$ GeV^2	
x range	F_2^γ/α	$\pm\sigma_{stat}$	$\pm\sigma_{sys}$
0.016 - 0.110	0.183	$\pm$0.014	$\pm$0.046
0.110 - 0.370	0.263	$\pm$0.026	$\pm$0.039
0.370 - 0.700	0.222	$\pm$0.064	$\pm$0.033
$Q^2 = 3 - 6$ GeV^2		$\langle Q^2 \rangle = 4.3$ GeV^2	
x range	F_2^γ/α	$\pm\sigma_{stat}$	$\pm\sigma_{sys}$
0.030 - 0.170	0.218	$\pm$0.014	$\pm$0.055
0.170 - 0.440	0.273	$\pm$0.020	$\pm$0.041
0.440 - 0.800	0.336	$\pm$0.044	$\pm$0.050
$Q^2 = 6 - 16$ GeV^2		$\langle Q^2 \rangle = 9.2$ GeV^2	
x range	F_2^γ/α	$\pm\sigma_{stat}$	$\pm\sigma_{sys}$
0.060 - 0.230	0.300	$\pm$0.027	$\pm$0.075
0.230 - 0.540	0.340	$\pm$0.029	$\pm$0.051
0.540 - 0.900	0.492	$\pm$0.069	$\pm$0.074

PLUTO			
$Q^2 = 18 - 100$ GeV^2		$\langle Q^2 \rangle = 45$ GeV^2	
x range	F_2^γ/α	$\pm\sigma_{stat}$	$\pm\sigma_{sys}$
0.100 - 0.250	0.360	$\pm$0.170	$\pm$0.036
0.250 - 0.500	0.400	$\pm$0.120	$\pm$0.040
0.500 - 0.750	0.770	$\pm$0.160	$\pm$0.077
0.750 - 0.900	0.840	$\pm$0.260	$\pm$0.084
$Q^2 = 1.5 - 16$ GeV^2		$\langle Q^2 \rangle = 5.3$ GeV^2	
x range	F_2^γ/α	$\pm\sigma_{stat}$	$\pm\sigma_{sys}$
0.035 - 0.072	0.216	$\pm$0.015	$\pm$0.054
0.072 - 0.174	0.258	$\pm$0.010	$\pm$0.065
0.174 - 0.319	0.222	$\pm$0.025	$\pm$0.056
0.319 - 0.490	0.329	$\pm$0.037	$\pm$0.049
0.490 - 0.650	0.439	$\pm$0.052	$\pm$0.066
0.650 - 0.840	0.361	$\pm$0.076	$\pm$0.054

Table 21: The photon structure function F_2^γ measured by the TPC/2γ [129] and PLUTO [126,127] experiments. The Q^2 range of each measurement, with the average value in parentheses, is given next to the experiment name. The quoted numbers for F_2^γ/α with the statistical errors have been taken from the RAL database. The quoted systematic errors in case of TPC/2γ measurements amount to 11% for the regions $0.2 < Q^2 < 1$ GeV^2 with $x < 0.1$ and $1 < Q^2 < 7$ GeV^2 with $x < 0.2$, and to 14% elsewhere [129], and in case of PLUTO the systematic error amounts to 10% for data at $\langle Q^2 \rangle = 45$ GeV62 [127], and to 25/15% for data at lower $\langle Q^2 \rangle$ and for below/above $x = 0.2$, respectively [126].

OPAL			
$Q^2 = 6 - 8$ GeV^2		$\langle Q^2 \rangle = 7.5$ GeV^2	
x range	F_2^γ/α	$\pm\sigma_{stat}$	$\pm\sigma_{sys}$
0.001 - 0.091	0.28	±0.02	$^{+0.03}_{-0.10}$
0.091 - 0.283	0.32	±0.02	$^{+0.08}_{-0.13}$
0.283 - 0.649	0.38	±0.04	$^{+0.06}_{-0.21}$
$Q^2 = 8 - 30$ GeV^2		$\langle Q^2 \rangle = 14.7$ GeV^2	
x range	F_2^γ/α	$\pm\sigma_{stat}$	$\pm\sigma_{sys}$
0.006 - 0.137	0.38	±0.01	$^{+0.06}_{-0.13}$
0.137 - 0.324	0.41	±0.02	$^{+0.06}_{-0.03}$
0.324 - 0.522	0.41	±0.03	$^{+0.08}_{-0.11}$
0.522 - 0.836	0.54	±0.05	$^{+0.31}_{-0.13}$
$Q^2 = 60 - 400$ GeV^2		$\langle Q^2 \rangle = 135$ GeV^2	
x range	F_2^γ/α	$\pm\sigma_{stat}$	$\pm\sigma_{sys}$
0.100 - 0.300	0.65	±0.09	$^{+0.33}_{-0.06}$
0.300 - 0.600	0.73	±0.08	$^{+0.04}_{-0.08}$
0.600 - 0.800	1.72	±0.10	$^{+0.81}_{-0.07}$
$Q^2 = 6 - 11$ GeV^2		$\langle Q^2 \rangle = 9.0$ GeV^2	
x range	F_2^γ/α	$\pm\sigma_{stat}$	$\pm\sigma_{sys}$
0.020 - 0.100	0.33	±0.03	$^{+0.06}_{-0.06}$
0.100 - 0.250	0.29	±0.04	$^{+0.04}_{-0.05}$
0.250 - 0.600	0.39	±0.08	$^{+0.30}_{-0.10}$
$Q^2 = 11 - 20$ GeV^2		$\langle Q^2 \rangle = 14.5$ GeV^2	
x range	F_2^γ/α	$\pm\sigma_{stat}$	$\pm\sigma_{sys}$
0.020 - 0.100	0.37	±0.03	$^{+0.16}_{-0.01}$
0.100 - 0.250	0.42	±0.05	$^{+0.04}_{-0.14}$
0.250 - 0.600	0.39	±0.06	$^{+0.10}_{-0.11}$
$Q^2 = 20 - 40$ GeV^2		$\langle Q^2 \rangle = 30$ GeV^2	
x range	F_2^γ/α	$\pm\sigma_{stat}$	$\pm\sigma_{sys}$
0.050 - 0.100	0.32	±0.04	$^{+0.11}_{-0.02}$
0.100 - 0.350	0.52	±0.05	$^{+0.06}_{-0.13}$
0.350 - 0.600	0.41	±0.09	$^{+0.20}_{-0.05}$
0.600 - 0.800	0.46	±0.15	$^{+0.39}_{-0.14}$

OPAL			
$Q^2 = 40 - 100$ GeV^2		$\langle Q^2 \rangle = 59$ GeV^2	
x range	F_2^γ/α	$\pm\sigma_{stat}$	$\pm\sigma_{sys}$
0.050 - 0.100	0.37	±0.06	$^{+0.28}_{-0.07}$
0.100 - 0.350	0.44	±0.07	$^{+0.08}_{-0.07}$
0.350 - 0.600	0.48	±0.09	$^{+0.16}_{-0.10}$
0.600 - 0.800	0.51	±0.14	$^{+0.48}_{-0.02}$
$Q^2 = 1.1 - 2.5$ GeV^2		$\langle Q^2 \rangle = 1.86$ GeV^2	
x range	F_2^γ/α	$\pm\sigma_{stat}$	$\pm\sigma_{sys}$
0.0025 - 0.0063	0.27	±0.03	$^{+0.05}_{-0.07}$
0.0063 - 0.0200	0.22	±0.02	$^{+0.02}_{-0.05}$
0.0200 - 0.0400	0.20	±0.02	$^{+0.09}_{-0.02}$
0.0400 - 0.1000	0.23	±0.02	$^{+0.03}_{-0.05}$
$Q^2 = 2.5 - 6.6$ GeV^2		$\langle Q^2 \rangle = 3.76$ GeV^2	
x range	F_2^γ/α	$\pm\sigma_{stat}$	$\pm\sigma_{sys}$
0.0063 - 0.0200	0.35	±0.03	$^{+0.08}_{-0.08}$
0.0200 - 0.0400	0.29	±0.03	$^{+0.06}_{-0.06}$
0.0400 - 0.1000	0.32	±0.02	$^{+0.07}_{-0.05}$
0.1000 - 0.2000	0.32	±0.03	$^{+0.08}_{-0.04}$
$Q^2 = 400 - 2350$ GeV^2		$\langle Q^2 \rangle = 780$ GeV^2	
x range	F_2^γ/α	$\pm\sigma_{stat}$	$\pm\sigma_{sys}$
0.15 - 0.40	0.93	±0.10	$^{+0.14}_{-0.11}$
0.40 - 0.70	0.87	±0.10	$^{+0.05}_{-0.15}$
0.70 - 0.98	0.97	±0.17	$^{+0.16}_{-0.23}$
$Q^2 \simeq 7 - 14$ GeV^2		$\langle Q^2 \rangle = 10.2$ GeV^2	
x range	F_2^γ/α	$\pm\sigma_{stat}$	$\pm\sigma_{sys}$
0.0009 - 0.0050	0.545	±0.016	$^{+0.066}_{-0.071}$
0.0050 - 0.0273	0.349	±0.007	$^{+0.030}_{-0.033}$
0.0273 - 0.1496	0.315	±0.006	$^{+0.023}_{-0.024}$
0.1496 - 0.8187	0.417	±0.008	$^{+0.052}_{-0.052}$
$Q^2 \simeq 14 - 33$ GeV^2		$\langle Q^2 \rangle = 20$ GeV^2	
x range	F_2^γ/α	$\pm\sigma_{stat}$	$\pm\sigma_{sys}$
0.0015 - 0.0074	0.626	±0.019	$^{+0.123}_{-0.129}$
0.0074 - 0.0369	0.395	±0.008	$^{+0.047}_{-0.051}$
0.0369 - 0.1827	0.380	±0.006	$^{+0.019}_{-0.022}$
0.1827 - 0.9048	0.500	±0.008	$^{+0.067}_{-0.066}$

Table 22: The photon structure function F_2^γ measured by the OPAL experiment [131, 132]. The Q^2 range of each measurement, with the average value in parentheses, is given next to the experiment name. The quoted numbers for F_2^γ/α with the statistical and systematic errors have been taken from the published tables.

ALEPH			
$Q^2 = 6 - 13$ GeV^2	$\langle Q^2 \rangle = 9.9$ GeV^2		
x range	F_2^γ/α	$\pm\sigma_{stat}$	$\pm\sigma_{sys}$
0.005 - 0.080	0.30	$\pm$0.02	$\pm$0.02
0.080 - 0.200	0.40	$\pm$0.03	$\pm$0.07
0.200 - 0.400	0.41	$\pm$0.05	$\pm$0.09
0.400 - 0.800	0.27	$\pm$0.13	$\pm$0.09
$Q^2 = 13 - 44$ GeV^2	$\langle Q^2 \rangle = 20.7$ GeV^2		
x range	F_2^γ/α	$\pm\sigma_{stat}$	$\pm\sigma_{sys}$
0.009 - 0.120	0.36	$\pm$0.02	$\pm$0.05
0.120 - 0.270	0.34	$\pm$0.03	$\pm$0.11
0.270 - 0.500	0.56	$\pm$0.05	$\pm$0.10
0.350 - 0.890	0.45	$\pm$0.11	$\pm$0.05
$Q^2 = 35 - 3000$ GeV^2	$\langle Q^2 \rangle = 284$ GeV^2		
x range	F_2^γ/α	$\pm\sigma_{stat}$	$\pm\sigma_{sys}$
0.03 - 0.35	0.65	$\pm$0.10	$\pm$0.09
0.35 - 0.65	0.70	$\pm$0.16	$\pm$0.19
0.65 - 0.97	1.28	$\pm$0.26	$\pm$0.26

ALEPH			
$Q^2 \simeq 10 - 29$ GeV^2	$\langle Q^2 \rangle = 17.3$ GeV^2		
x range	F_2^γ/α	$\pm\sigma_{stat}$	$\pm\sigma_{sys}$
0.0020 - 0.0110	0.43	$\pm$0.016	$\pm$0.115
0.0110 - 0.0338	0.27	$\pm$0.014	$\pm$0.049
0.0338 - 0.0787	0.35	$\pm$0.015	$\pm$0.041
0.0787 - 0.1487	0.35	$\pm$0.015	$\pm$0.028
0.1487 - 0.2429	0.39	$\pm$0.016	$\pm$0.034
0.2429 - 0.3624	0.46	$\pm$0.018	$\pm$0.041
0.3624 - 0.5074	0.40	$\pm$0.021	$\pm$0.149
0.5074 - 0.7000	0.18	$\pm$0.019	$\pm$0.235
$Q^2 \simeq 29 - 250$ GeV^2	$\langle Q^2 \rangle = 67.2$ GeV^2		
x range	F_2^γ/α	$\pm\sigma_{stat}$	$\pm\sigma_{sys}$
0.0060 - 0.0362	0.57	$\pm$0.027	$\pm$0.145
0.0362 - 0.0950	0.43	$\pm$0.027	$\pm$0.039
0.0950 - 0.1811	0.47	$\pm$0.029	$\pm$0.041
0.1811 - 0.2907	0.50	$\pm$0.031	$\pm$0.031
0.2907 - 0.4204	0.60	$\pm$0.036	$\pm$0.038
0.4204 - 0.5714	0.66	$\pm$0.038	$\pm$0.077
0.5714 - 0.7356	0.65	$\pm$0.055	$\pm$0.126
0.7356 - 0.9600	0.66	$\pm$0.060	$\pm$0.137

Table 23: The photon structure function F_2^γ measured by the ALEPH experiment [131,132]. The Q^2 range of each measurement, with the average value in parentheses, is given next to the experiment name. The quoted numbers for F_2^γ/α with the statistical and systematic errors have been taken from the published tables.

DELPHI			
$Q^2 = 4 - 30$ GeV^2	$\langle Q^2 \rangle = 12$ GeV^2		
x range	F_2^γ/α	$\pm\sigma_{stat}$	$\pm\sigma_{sys}$
0.003 - 0.080	0.21	$\pm$0.03	$\pm$0.06
0.080 - 0.213	0.41	$\pm$0.04	$\pm$0.05
0.213 - 0.428	0.45	$\pm$0.05	$\pm$0.05
0.428 - 0.847	0.45	$\pm$0.11	$\pm$0.10

DELPHI			
$Q^2 = 4 - 30$ GeV^2	$\langle Q^2 \rangle = 12$ GeV^2		
x range	F_2^γ/α	$\pm\sigma_{stat}$	$\pm\sigma_{sys}$
0.003 - 0.046	0.24	$\pm$0.03	$\pm$0.07
0.046 - 0.117	0.41	$\pm$0.05	$\pm$0.08
0.117 - 0.350	0.46	$\pm$0.17	$\pm$0.09

DELPHI			
$Q^2 =$ ..... GeV^2	$\langle Q^2 \rangle = 5.2$ GeV^2		
x range	F_2^γ/α	$\pm\sigma_{stat}$	$\pm\sigma_{sys}$
0.001 - 0.020	0.283	$\pm$0.011	$\pm$0.026
0.020 - 0.100	0.203	$\pm$0.014	$\pm$0.024
0.100 - 0.500	0.212	$\pm$0.020	$\pm$0.033
$Q^2 =$ ..... GeV^2	$\langle Q^2 \rangle = 12.7$ GeV^2		
x range	F_2^γ/α	$\pm\sigma_{stat}$	$\pm\sigma_{sys}$
0.001 - 0.020	0.446	$\pm$0.015	$\pm$0.027
0.020 - 0.100	0.317	$\pm$0.018	$\pm$0.013
0.100 - 0.300	0.286	$\pm$0.034	$\pm$0.015
0.300 - 0.800	0.362	$\pm$0.015	$\pm$0.029
$Q^2 =$ ..... GeV^2	$\langle Q^2 \rangle = 28.5$ GeV^2		
x range	F_2^γ/α	$\pm\sigma_{stat}$	$\pm\sigma_{sys}$
0.020 - 0.100	0.413	$\pm$0.030	$\pm$0.035
0.100 - 0.300	0.346	$\pm$0.015	$\pm$0.034
0.300 - 0.800	0.488	$\pm$0.037	$\pm$0.033

DELPHI			
$Q^2 =$ ..... GeV^2	$\langle Q^2 \rangle = 19$ GeV^2		
x range	F_2^γ/α	$\pm\sigma_{stat}$	$\pm\sigma_{sys}$
0.001 - 0.020	0.438	$\pm$0.013	$\pm$0.063
0.020 - 0.100	0.317	$\pm$0.010	$\pm$0.029
0.100 - 0.300	0.293	$\pm$0.007	$\pm$0.061
0.300 - 0.800	0.341	$\pm$0.026	$\pm$0.042
$Q^2 =$ ..... GeV^2	$\langle Q^2 \rangle = 40$ GeV^2		
x range	F_2^γ/α	$\pm\sigma_{stat}$	$\pm\sigma_{sys}$
0.001 - 0.020	0.632	$\pm$0.010	$\pm$0.051
0.020 - 0.100	0.428	$\pm$0.007	$\pm$0.064
0.100 - 0.300	0.351	$\pm$0.018	$\pm$0.092
0.300 - 0.800	0.487	$\pm$0.017	$\pm$0.119
$Q^2 =$ ..... GeV^2	$\langle Q^2 \rangle = 101$ GeV^2		
x range	F_2^γ/α	$\pm\sigma_{stat}$	$\pm\sigma_{sys}$
0.001 - 0.020	0.930	$\pm$0.106	$\pm$0.131
0.020 - 0.100	0.585	$\pm$0.034	$\pm$0.084
0.100 - 0.300	0.425	$\pm$0.020	$\pm$0.101
0.300 - 0.800	0.704	$\pm$0.031	$\pm$0.094
$Q^2 =$ ..... GeV^2	$\langle Q^2 \rangle = 700$ GeV^2		
x range	F_2^γ/α	$\pm\sigma_{stat}$	$\pm\sigma_{sys}$
0.010 - 0.300	0.797	$\pm$0.090	$\pm$0.226
0.300 - 0.800	0.962	$\pm$0.052	$\pm$0.111

Table 24: The photon structure function F_2^γ measured by the DELPHI experiment [131,132]. The two measurements at $\langle Q^2 \rangle = 12$ GeV^2 are not independent, but use the same data which are unfolded for four bins on a linear scale in x, and for three bins on a logarithmic scale for $x < 0.35$. The quoted numbers for F_2^γ/α with the statistical and systematic errors have been taken from the published tables.

L3			
$Q^2 = 1.2 - 3$ GeV^2	$\langle Q^2 \rangle = 1.9$ GeV^2		
x range	F_2^γ	$\pm\sigma_{stat}$	$\pm\sigma_{sys}$
0.002 - 0.005	0.184	$\pm$0.009	$\pm$0.049
0.005 - 0.010	0.179	$\pm$0.007	$\pm$0.022
0.010 - 0.020	0.176	$\pm$0.006	$\pm$0.016
0.020 - 0.030	0.191	$\pm$0.008	$\pm$0.005
0.030 - 0.050	0.193	$\pm$0.008	$\pm$0.009
0.050 - 0.100	0.185	$\pm$0.007	$\pm$0.026
$Q^2 = 3 - 9$ GeV^2	$\langle Q^2 \rangle = 5$ GeV^2		
x range	F_2^γ	$\pm\sigma_{stat}$	$\pm\sigma_{sys}$
0.005 - 0.010	0.307	$\pm$0.021	$\pm$0.094
0.010 - 0.020	0.282	$\pm$0.014	$\pm$0.045
0.020 - 0.040	0.263	$\pm$0.011	$\pm$0.021
0.040 - 0.060	0.278	$\pm$0.013	$\pm$0.007
0.060 - 0.100	0.270	$\pm$0.012	$\pm$0.009
0.100 - 0.200	0.252	$\pm$0.011	$\pm$0.045
$Q^2 = 9 - 13$ GeV^2	$\langle Q^2 \rangle = 10.8$ GeV^2		
x range	F_2^γ	$\pm\sigma_{stat}$	$\pm\sigma_{sys}$
0.01 - 0.10	0.30	$\pm$0.02	$\pm$0.03
0.10 - 0.20	0.35	$\pm$0.03	$\pm$0.02
0.20 - 0.30	0.30	$\pm$0.04	$\pm$0.11

L3			
$Q^2 = 13 - 18$ GeV^2	$\langle Q^2 \rangle = 15.3$ GeV^2		
x range	F_2^γ	$\pm\sigma_{stat}$	$\pm\sigma_{sys}$
0.01 - 0.10	0.37	$\pm$0.02	$\pm$0.03
0.10 - 0.20	0.42	$\pm$0.04	$\pm$0.02
0.20 - 0.30	0.42	$\pm$0.05	$\pm$0.07
0.30 - 0.50	0.35	$\pm$0.05	$\pm$0.15
$Q^2 = 18 - 30$ GeV^2	$\langle Q^2 \rangle = 23.1$ GeV^2		
x range	F_2^γ	$\pm\sigma_{stat}$	$\pm\sigma_{sys}$
0.01 - 0.10	0.40	$\pm$0.03	$\pm$0.04
0.10 - 0.20	0.44	$\pm$0.04	$\pm$0.04
0.20 - 0.30	0.47	$\pm$0.05	$\pm$0.02
0.30 - 0.50	0.44	$\pm$0.05	$\pm$0.12

L3			
$Q^2 = 40 - 500$ GeV^2	$\langle Q^2 \rangle = 120$ GeV^2		
x range	F_2^γ/α	$\pm\sigma_{stat}$	$\pm\sigma_{sys}$
0.05 - 0.20	0.66	$\pm$0.08	$\pm$0.06
0.20 - 0.40	0.81	$\pm$0.08	$\pm$0.08
0.40 - 0.60	0.76	$\pm$0.12	$\pm$0.07
0.60 - 0.80	0.85	$\pm$0.14	$\pm$0.08
0.80 - 0.98	0.91	$\pm$0.19	$\pm$0.09

Table 25: The photon structure function F_2^γ measured by the L3 experiment [135, 136, 146]. The Q^2 range of each measurement, with the average value in parentheses, is given next to the experiment name. In the published tables two sets of numbers are given, one obtained by an unfolding based on PHOJET Monte Carlo and the other based on the TWOGAM Monte Carlo. The numbers quoted numbers here for F_2^γ/α are those obtained from PHOJET with the statistical errors. The systematic error is calculated from the quadratic sum of the systematic error for the result based on PHOJET and the difference bbetween the results obtained from PHOJET and from TWOGAM.

OPAL $\langle Q^2 \rangle = 20$ GeV^2			
x range	$\sigma^{D^\star}$ [pb]	$\sigma(\mathrm{e^+e^-} \to \mathrm{e^+e^-c\bar{c}\,X})$ [pb]	$F_{2,c}^\gamma/\alpha$
0.0014 - 0.10	$3.1 \pm 1.0 \pm 0.5$	$43.8 \pm 14.3 \pm 6.3 \pm 2.8$	$0.180 \pm 0.059 \pm 0.026 \pm 0.012$
0.1000 - 0.87	$2.6 \pm 0.9 \pm 0.3$	$26.2 \pm 8.8 \pm 3.2 \pm 1.3$	$0.084 \pm 0.028 \pm 0.010 \pm 0.004$

Table 26: Measurement of the cross section $\sigma^{D^\star}$ in the restricted region, the cross section $\sigma(\mathrm{e^+e^-} \to \mathrm{e^+e^-c\bar{c}\,X}$, extrapolated using Monte Carlo and the structure function $F_{2,c}^\gamma/\alpha$ at $Q^2 = 20$ GeV^2 by the OPAL experiment [142]. For the measurements the quoted errors are due, respectively, statistics, systematics and extrapolation.

C Results on hadronic structure of the electron

In this Appendix we present the results on the hadronic structure function of the electron F_2^e measured by the OPAL and DELPHI experiments. In all cases the structure function scaled by the fine structure constant squared is given.

OPAL $\langle Q^2 \rangle = 15$ GeV^2			
z		$\mathrm{d}\sigma/\mathrm{d}z$ [pb]	F_2^e/α^2
range	bin-centre		
0.0009 - 0.00265	0.00154	$6141 \pm 57\ ^{+525}_{-533}$	$13.14 \pm 0.12\ ^{+1.21}_{-1.07}$
0.00265 - 0.0078	0.00455	$2996 \pm 22\ ^{+279}_{-280}$	$10.04 \pm 0.08\ ^{+0.90}_{-0.81}$
0.0078 - 0.0230	0.01339	$857 \pm 8\ ^{+34}_{-48}$	$7.84 \pm 0.07\ ^{+0.45}_{-0.53}$
0.0230 - 0.0677	0.03946	$221 \pm 3\ ^{+30}_{-28}$	$5.69 \pm 0.09\ ^{+0.60}_{-0.63}$
0.0677 - 0.2000	0.11636	$48 \pm 1\ ^{+9}_{-7}$	$3.43 \pm 0.10\ ^{+0.60}_{-0.56}$
0.2000 - 0.9048	0.42539	$2.8 \pm 0.2\ ^{+1.2}_{-0.6}$	$0.71 \pm 0.04\ ^{+0.23}_{-0.15}$

Table 27: Results for the cross section $\mathrm{d}\sigma/\mathrm{d}z$ obtaineded in the phase space defined by $E' > 0.75E_\mathrm{b}$, $34 < \theta < 55$ mrad and $W > \sqrt{3}$ GeV and the structure function F_2^e/α^2 for the average $\langle Q^2 \rangle = 15$ GeV^2 measured by the OPAL experiment [143]. The first errors are statistical and the second systematic.

DELPHI $\langle Q^2 \rangle = 8.9$ GeV^2	
z range	F_2^e/α^2
0.00398 - 0.01000	$6.98\ ^{+0.41}_{-0.43}$
0.01000 - 0.02512	$5.45\ ^{+0.39}_{-0.42}$
0.02512 - 0.06310	$3.58\ ^{+0.52}_{-0.49}$
0.06310 - 0.15849	$1.77\ ^{+0.59}_{-0.62}$
0.15849 - 0.39811	$0.21\ ^{+0.65}_{-0.71}$

Table 28: Results for F_2^e/α^2 obtained for the average $\langle Q^2 \rangle = 8.9$ GeV^2 measured by the DELPHI experiment [144] at LEP1 energy. Only the total erro is available. There is no error due to model dependence.

DELPHI	$\langle Q^2 \rangle = 15.3$ GeV^2
z range	F_2^e/α^2
0.00151 - 0.00204	$12.06 \pm 1.68\ ^{+1.59}_{-0.93}$
0.00204 - 0.00275	$9.92 \pm 0.98\ ^{+0.90}_{-0.93}$
0.00275 - 0.00372	$10.52 \pm 0.96\ ^{+1.07}_{-0.93}$
0.00372 - 0.00500	$7.06 \pm 1.12\ ^{+0.61}_{-0.93}$

DELPHI	$\langle Q^2 \rangle = 24.5$ GeV^2
z range	F_2^e/α^2
0.00295 - 0.00575	$10.54 \pm 0.75\ ^{+0.70}_{-0.96}$
0.00575 - 0.01122	$8.98 \pm 0.50\ ^{+0.57}_{-0.62}$
0.01122 - 0.02188	$7.05 \pm 0.48\ ^{+0.56}_{-0.66}$
0.02188 - 0.04266	$5.74 \pm 0.62\ ^{+0.53}_{-0.59}$
0.04266 - 0.08318	$3.36 \pm 0.74\ ^{+0.65}_{-0.51}$
0.08318 - 0.16218	$3.44 \pm 0.90\ ^{+1.09}_{-0.75}$

DELPHI	$\langle Q^2 \rangle = 38.5$ GeV^2
z range	F_2^e/α^2
0.00490 - 0.01047	$11.68 \pm 0.74\ ^{+1.11}_{-0.69}$
0.01047 - 0.02239	$8.99 \pm 0.62\ ^{+0.66}_{-0.52}$
0.02239 - 0.04786	$6.65 \pm 0.77\ ^{+0.46}_{-0.30}$
0.04786 - 0.10233	$5.44 \pm 0.88\ ^{+0.65}_{-0.23}$
0.10233 - 0.21878	$3.42 \pm 1.18\ ^{+0.39}_{-0.61}$

DELPHI	$\langle Q^2 \rangle = 62.4$ GeV^2
z range	F_2^e/α^2
0.00794 - 0.01585	$13.30 \pm 0.99\ ^{+0.81}_{-1.34}$
0.01585 - 0.03162	$9.53 \pm 0.84\ ^{+1.10}_{-0.97}$
0.03162 - 0.06310	$7.75 \pm 0.86\ ^{+0.70}_{-0.65}$
0.06310 - 0.12589	$5.51 \pm 1.02\ ^{+0.52}_{-0.69}$
0.12589 - 0.25119	$2.17 \pm 0.75\ ^{+1.06}_{-0.69}$

Table 29: Results for F_2^e/α^2 obtained in four intervals of Q^2 with the average values of $\langle Q^2 \rangle = 15.3$, 24.5, 38.5 and 62.4 GeV^2 measured by the DELPHI experiment [144] at LEP2 energies. The first error is statistical and the second systematic. There is no error due to model dependence.

D Results on hadronic structure of the virtual photon

In this Appendix we present the results on the photon hadronic structure function F_2^γ obtained by the LEP experiments OPAL, ALEPH, DELPHI and L3 as well as by the other experiments including AMY, CELLO, JADE, PLUTO, TASSO, TOPAZ and TPC/2γ. In all cases the structure functions scaled by the fine structure constant are given. Depending on the measurement, both statistical and systematical errors or only statistical or total error are given.

PLUTO		
$\langle Q^2\rangle = 5$ GeV^2 $\langle P^2\rangle = 0.35$ GeV^2		
$\langle x\rangle$	x range	$F_{\rm eff}^\gamma/\alpha \pm\sigma_{tot}$
0.05	0.00 - 0.10	0.22 $\pm$0.04
0.19	0.10 - 0.28	0.27 $\pm$0.07
0.39	0.28 - 0.50	0.35 $\pm$0.11
0.63	0.50 - 0.76	0.54 $\pm$0.25

PLUTO	
$\langle Q^2\rangle = 5$ GeV^2	
$\langle P^2\rangle$	$F_{\rm eff}^\gamma/\alpha \pm\sigma_{tot}$
0.0	0.35 $\pm$0.04
0.2	0.26 $\pm$0.05
0.4	0.26 $\pm$0.05
0.6	0.16 $\pm$0.05
0.8	0.20 $\pm$0.12

Table 30: Effective structure function $F_{\rm eff}^\gamma$ scaled by the fine structure constant measured by the PLUTO experiment [145]. The structure function is given as a function of x for virtual photons at $\langle P^2\rangle = 0.35$ GeV^2, $\langle Q^2\rangle = 5$ GeV^2 and as a function of P^2 for $\langle Q^2\rangle = 5$ GeV^2. The point at $P^2 = 0$ was taken from [122]. The values given in the tables have been read out from the figures in the above publications.

L3		
$\langle Q^2\rangle = 120$ GeV^2 $\langle P^2\rangle = 3.7$ GeV^2		
$\langle x\rangle$	x range	$F_{\rm eff}^\gamma/\alpha \pm\sigma_{stat} \pm\sigma_{sys}$
0.13	0.05 - 0.20	0.42 $\pm$0.16 $\pm$0.05
0.30	0.20 - 0.40	0.71 $\pm$0.24 $\pm$0.09
0.50	0.40 - 0.60	0.72 $\pm$0.34 $\pm$0.09
0.70	0.60 - 0.80	1.27 $\pm$0.51 $\pm$0.16
0.89	0.80 - 0.98	1.48 $\pm$0.66 $\pm$0.19

L3	
$\langle Q^2\rangle = 120$ GeV^2 $0.05 < x < 0.98$	
$\langle P^2\rangle$	$F_{\rm eff}^\gamma/\alpha \pm\sigma_{stat} \pm\sigma_{sys}$
0.0	0.83 $\pm$0.06 $\pm$0.08
2.0	0.87 $\pm$0.25 $\pm$0.11
3.9	1.00 $\pm$0.32 $\pm$0.13
6.4	1.02 $\pm$0.70 $\pm$0.13
3.7	0.94 $\pm$0.19 $\pm$0.12

Table 31: Effective structure function $F_{\rm eff}^\gamma$ scaled by the fine structure constant measured by the L3 experiment [146]. The structure function is given as a function of x for virtual photons at $\langle P^2\rangle = 3.7$ GeV^2, $\langle Q^2\rangle = 120$ GeV^2 and as a function of P^2 for $\langle Q^2\rangle = 120$ GeV^2, $0.05 < x < 0.98$. In the last row in the right table the structure function value averaged over whole P^2 range is given.

OPAL							
$\langle x \rangle$	x range	$d\sigma_{ee}/dx$	$\pm\sigma_{stat}$	$\pm\sigma_{sys}$	$\sigma_{\gamma^\star\gamma^\star}$	$\pm\sigma_{stat}$	$\pm\sigma_{sys}$
		[pb]			[nb]		
0.06	0.0 - 0.1	1.46	± 0.27	$^{+0.11}_{-0.26}$	4.66	± 0.85	$^{+0.33}_{-0.83}$
0.15	0.1 - 0.2	1.22	± 0.20	$^{+0.10}_{-0.19}$	8.92	± 1.42	$^{+0.71}_{-1.39}$
0.26	0.2 - 0.35	0.55	± 0.11	$^{+0.11}_{-0.20}$	5.76	± 1.10	$^{+1.18}_{-2.10}$
$\langle Q^2 \rangle$	Q^2 range	$d\sigma_{ee}/dQ^2$	$\pm\sigma_{stat}$	$\pm\sigma_{sys}$	$\sigma_{\gamma^\star\gamma^\star}$	$\pm\sigma_{stat}$	$\pm\sigma_{sys}$
[GeV^2]	[GeV^2]	[pb/GeV^2]			[nb]		
13.6	10 - 16	0.016	± 0.003	$^{+0.002}_{-0.003}$	5.63	± 1.23	$^{+0.77}_{-1.05}$
18.9	16 - 22	0.026	± 0.004	$^{+0.003}_{-0.006}$	6.37	± 0.91	$^{+0.75}_{-1.56}$
24.4	22 - 27	0.013	± 0.003	$^{+0.001}_{-0.003}$	3.91	± 0.89	$^{+0.36}_{-0.98}$
$\langle W \rangle$	W range	$d\sigma_{ee}/dW$	$\pm\sigma_{stat}$	$\pm\sigma_{sys}$	$\sigma_{\gamma^\star\gamma^\star}$	$\pm\sigma_{stat}$	$\pm\sigma_{sys}$
[GeV^2]	[GeV^2]	[pb/GeV^2]			[nb]		
7.2	5 - 10	0.031	± 0.004	$^{+0.0053}_{-0.0098}$	6.79	± 0.96	$^{+1.17}_{-2.15}$
12.4	10 - 15	0.017	± 0.004	$^{+0.0012}_{-0.0015}$	7.11	± 1.51	$^{+0.52}_{-0.63}$
20.6	15 - 35	0.005	± 0.001	$^{+0.0004}_{-0.0010}$	5.53	± 1.14	$^{+0.38}_{-1.11}$
41.5	35 - 50	0.001	± 0.001	$^{+0.0001}_{-0.0001}$	3.10	± 2.06	$^{+0.29}_{-0.43}$
$\Delta\phi$	$\Delta\phi$ range	$d\sigma_{ee}/d\Delta\phi$	$\pm\sigma_{stat}$	$\pm\sigma_{sys}$	$\sigma_{\gamma^\star\gamma^\star}$	$\pm\sigma_{stat}$	$\pm\sigma_{sys}$
[rad]	[rad]	[pb]			[nb]		
0.31	0.00 - 0.63	0.081	± 0.022	$^{+0.010}_{-0.032}$	3.18	± 0.84	$^{+0.40}_{-1.25}$
0.94	0.63 - 1.26	0.098	± 0.024	$^{+0.012}_{-0.035}$	4.25	± 1.03	$^{+0.51}_{-1.53}$
1.57	1.26 - 1.89	0.130	± 0.026	$^{+0.013}_{-0.036}$	6.84	± 1.38	$^{+0.68}_{-1.88}$
2.20	1.89 - 2.51	0.117	± 0.026	$^{+0.011}_{-0.020}$	7.44	± 1.67	$^{+0.70}_{-1.25}$
2.83	2.51 - 3.14	0.132	± 0.028	$^{+0.009}_{-0.010}$	9.56	± 2.02	$^{+0.68}_{-0.76}$
$\overline{Y}$	$\overline{Y}$ range	$d\sigma_{ee}/d\overline{Y}$	$\pm\sigma_{stat}$	$\pm\sigma_{sys}$	$\sigma_{\gamma^\star\gamma^\star}$	$\pm\sigma_{stat}$	$\pm\sigma_{sys}$
		[pb]			[nb]		
0.5	0 - 1	0.059	± 0.013	$^{+0.029}_{-0.033}$	6.11	± 1.34	$^{+2.95}_{-3.42}$
1.5	1 - 2	0.105	± 0.018	$^{+0.007}_{-0.021}$	6.84	± 1.17	$^{+0.43}_{-1.39}$
2.5	2 - 3	0.108	± 0.020	$^{+0.009}_{-0.011}$	7.99	± 1.51	$^{+0.69}_{-0.83}$
3.5	3 - 4	0.040	± 0.014	$^{+0.003}_{-0.009}$	3.78	± 1.38	$^{+0.32}_{-0.84}$
5.0	4 - 6	0.026	± 0.010	$^{+0.003}_{-0.010}$	4.97	± 1.82	$^{+0.49}_{-1.81}$

Table 32: The differential cross-section for the process $e^+e^- \to e^+e^-$ hadrons and the total cross section for the process $\gamma^\star\gamma^\star \to$ hadrons in the region $E_{1,2} > 0.4E_b$, $34 < \theta_{1,2} < 55$ mrad and $W > 5$ GeV, as a function of x, Q^2, W, $\Delta\phi$ and $\overline{Y}$. The average value of x, Q^2, W and the central value for $\Delta\phi$ and $\overline{Y}$ in a bin, value of the bin boundaries, value of the cross-section with statistical and systematic errors, are given.

ALEPH			
e_{tag} range	$d\sigma_{ee}/de_{tag}$	$\pm\sigma_{stat}$	$\pm\sigma_{sys}$
	[pb]		
0.30 - 0.40	2.85	±0.47	±1.03
0.40 - 0.50	2.78	±0.39	±0.30
0.50 - 0.60	3.01	±0.37	±0.32
0.60 - 0.70	3.12	±0.36	±0.10
0.70 - 0.80	4.36	±0.36	±0.21
0.80 - 0.90	5.19	±0.36	±0.27
0.90 - 0.95	11.51	±0.78	±0.40
0.95 - 1.00	27.24	±1.75	±2.99
θ range [rad]	$d\sigma_{ee}/d\theta$ [pb/rad]	$\pm\sigma_{stat}$	$\pm\sigma_{sys}$
0.035 - 0.040	110.11	±9.63	±3.92
0.040 - 0.045	122.18	±9.94	±3.01
0.045 - 0.050	94.71	±8.01	±2.47
0.050 - 0.055	81.16	±7.08	±2.73
0.060 - 0.070	40.57	±3.63	±1.65
0.070 - 0.090	28.08	±2.14	±0.92
0.090 - 0.120	15.81	±1.29	±0.55
0.120 - 0.155	6.49	±0.84	±0.27
Q^2 range [GeV^2]	$d\sigma_{ee}/dQ^2$ [pb/GeV^2]	$\pm\sigma_{stat}$	$\pm\sigma_{sys}$
2 - 6	0.0133	±0.0062	±0.0056
6 - 10	0.0852	±0.0112	±0.0059
10 - 20	0.1290	±0.0070	±0.0052
20 - 30	0.0785	±0.0056	±0.0161
30 - 40	0.0415	±0.0081	±0.0073
40 - 50	0.0263	±0.0030	±0.0013
50 - 70	0.0160	±0.0016	±0.0004
70 - 100	0.0111	±0.0011	±0.0008
100 - 150	0.0038	±0.0005	±0.0003
150 - 200	0.0010	±0.0003	±0.0002

ALEPH			
$\Delta\phi$ range [rad]	$d\sigma_{ee}/d\Delta\phi$ [pb/rad]	$\pm\sigma_{stat}$	$\pm\sigma_{sys}$
0.00 - 0.31	0.45	±0.07	±0.02
0.31 - 0.63	0.49	±0.07	±0.02
0.63 - 0.94	0.58	±0.08	±0.06
0.94 - 1.26	0.54	±0.08	±0.07
1.26 - 1.57	0.53	±0.08	±0.06
1.57 - 1.88	0.62	±0.08	±0.05
1.88 - 2.20	0.82	±0.09	±0.03
2.20 - 2.51	0.58	±0.09	±0.03
2.51 - 2.83	0.83	±0.10	±0.08
2.83 - 3.14	0.88	±0.13	±0.14
W range [GeV^2]	$d\sigma_{ee}/dW$ [pb/GeV^2]	$\pm\sigma_{stat}$	$\pm\sigma_{sys}$
3 - 5	0.1409	±0.0164	±0.0257
5 - 10	0.1263	±0.0095	±0.0033
10 - 15	0.0763	±0.0072	±0.0032
15 - 35	0.0276	±0.0023	±0.0023
35 - 50	0.0102	±0.0020	±0.0021
50 - 80	0.0005	$^{+0.0010}_{-0.0005}$	±0.0020
x range	$d\sigma_{ee}/dx$ [pb]	$\pm\sigma_{stat}$	$\pm\sigma_{sys}$
0.00 - 0.05	17.71	±1.38	±2.00
0.05 - 0.10	14.48	±1.05	±1.13
0.10 - 0.15	11.97	±0.95	±0.77
0.15 - 0.20	8.20	±0.79	±0.44
0.20 - 0.25	6.62	±0.72	±0.56
0.25 - 0.30	7.31	±0.70	±0.43
0.30 - 0.40	3.71	±0.36	±0.22
0.40 - 0.50	2.19	±0.28	±0.14
0.50 - 1.00	0.42	±0.06	±0.09

Table 33: The differential cross-section for the process $e^+e^- \to e^+e^-$ hadrons and the total cross section for the process $\gamma^\star\gamma^\star \to$ hadrons in the region $E_{1,2} > 0.4E_b$, $34 < \theta_{1,2} < 55$ mrad and $W > 5$ GeV, as a function of x, Q^2, W, $\Delta\phi$ and $\overline{Y}$. The average value of x, Q^2, W and the central value for $\Delta\phi$ and $\overline{Y}$ in a bin, value of the bin boundaries, value of the cross-section with statistical and systematic errors, are given.

ALEPH									
$\overline{Y}$ range	$d\sigma_{ee}/d\overline{Y}$	$\pm\sigma_{stat}$	$\pm\sigma_{sys}$	$d\sigma_{ee}/d\overline{Y}$	$\pm\sigma_{stat}$	$\pm\sigma_{sys}$	$\sigma_{\gamma^\star\gamma^\star}$	$\pm\sigma_{stat}$	$\pm\sigma_{sys}$
	[pb]			[pb]			[nb]		
-1.0 - 0.0	0.224	±0.028	±0.031	0.142	±0.022	±0.015	2.0	±0.3	±0.2
0.0 - 1.0	0.437	±0.039	±0.015	0.321	±0.034	±0.014	4.5	±0.5	±0.2
1.0 - 2.0	0.542	±0.045	±0.022	0.385	±0.038	±0.014	6.9	±0.7	±0.3
2.0 - 3.0	0.422	±0.040	±0.030	0.232	±0.030	±0.019	4.7	±0.6	±0.4
3.0 - 4.0	0.227	±0.035	±0.017	0.115	±0.025	±0.008	3.1	±0.7	±0.2
4.0 - 5.0	0.117	±0.026	±0.024	0.073	±0.021	±0.016	3.5	±1.0	±0.8
5.0 - 6.0	0.026	$^{+0.040}_{-0.020}$	±0.013	0.012	$^{+0.028}_{-0.012}$	±0.010	1.5	$^{+3.5}_{-1.5}$	±1.3
6.0 - 7.0	0.008	$^{+0.030}_{-0.008}$	±0.005	0.005	$^{+0.024}_{-0.005}$	±0.004	2.5	$^{+12.}_{-2.5}$	±2.0

Table 34: The differential cross-section for the process $e^+e^- \to e^+e^-$ hadrons and the total cross section for the process $\gamma^\star\gamma^\star \to$ hadrons in the region $E_{1,2} > 0.4E_b$, $34 < \theta_{1,2} < 55$ mrad and $W > 5$ GeV, as a function of x, Q^2, W, $\Delta\phi$ and $\overline{Y}$. The average value of x, Q^2, W and the central value for $\Delta\phi$ and $\overline{Y}$ in a bin, value of the bin boundaries, value of the cross-section with statistical and systematic errors, are given.

L3									
$\langle Q^2\rangle$	Q^2 range	$d\sigma_{ee}/dQ^2$	$\pm\sigma_{stat}$	$\pm\sigma_{sys}$	$\pm\sigma_{rad}$	$\sigma_{\gamma^\star\gamma^\star}$	$\pm\sigma_{stat}$	$\pm\sigma_{sys}$	$\pm\sigma_{rad}$
[GeV^2]	[GeV^2]	[pb/GeV^2]				[nb]			
12.0	10 - 14	0.0718	±0.0070	±0.0061	±0.0022	6.49	±0.64	±0.55	±0.20
15.9	14 - 18	0.0522	±0.0057	±0.0044	±0.0016	4.84	±0.53	±0.41	±0.15
20.5	18 - 24	0.0273	±0.0033	±0.0023	±0.0008	4.54	±0.55	±0.39	±0.14
27.0	24 - 32	0.0066	±0.0014	±0.0006	±0.0002	3.38	±0.74	±0.29	±0.10
$\langle W\rangle$	W range	$d\sigma_{ee}/dW$	$\pm\sigma_{stat}$	$\pm\sigma_{sys}$	$\pm\sigma_{rad}$	$\sigma_{\gamma^\star\gamma^\star}$	$\pm\sigma_{stat}$	$\pm\sigma_{sys}$	$\pm\sigma_{rad}$
[GeV^2]	[GeV^2]	[pb/GeV^2]				[nb]			
7.2	5 - 10	0.0747	±0.0096	±0.0063	±0.0023	6.34	±0.82	±0.54	±0.19
13.9	10 - 20	0.0263	±0.0024	±0.0022	±0.0008	5.27	±0.49	±0.45	±0.16
27.9	20 - 40	0.0062	±0.0007	±0.0005	±0.0003	3.71	±0.40	±0.32	±0.16
61.6	40 - 100	0.0014	±0.0002	±0.0001	±0.0001	5.24	±0.79	±0.45	±0.34
$\overline{Y}$	$\overline{Y}$ range	$d\sigma_{ee}/d\overline{Y}$	$\pm\sigma_{stat}$	$\pm\sigma_{sys}$	$\pm\sigma_{rad}$	$\sigma_{\gamma^\star\gamma^\star}$	$\pm\sigma_{stat}$	$\pm\sigma_{sys}$	$\pm\sigma_{rad}$
		[pb]				[nb]			
2.2	2.0 - 2.5	0.315	±0.048	±0.027	±0.009	5.65	±0.86	±0.48	±0.17
2.9	2.5 - 3.5	0.184	±0.018	±0.016	±0.006	4.90	±0.48	±0.42	±0.16
4.2	3.5 - 5.0	0.085	±0.009	±0.007	±0.004	3.99	±0.42	±0.34	±0.19
5.9	5.0 - 7.0	0.037	±0.006	±0.003	±0.002	5.82	±0.97	±0.49	±0.37

Table 35: The differential cross-section for the process $e^+e^- \to e^+e^-$ hadrons and the total cross section for the process $\gamma^\star\gamma^\star \to$ hadrons in the region $E_{1,2} > 0.4E_b$, $34 < \theta_{1,2} < 55$ mrad and $W > 5$ GeV, as a function of x, Q^2, W, $\Delta\phi$ and $\overline{Y}$. The average value of x, Q^2, W and the central value for $\Delta\phi$ and $\overline{Y}$ in a bin, value of the bin boundaries, value of the cross-section with statistical and systematic errors, are given.

References

[1] Particle Data Group, K. Hagiwara et al., *Review of particle physics*, Phys. Rev. **D66** (2002) 010001.

[2] J. Chýla, *Hard Collisions of Photons: Plea for a Common Language*, Prag Univ. Report PRA-HEP-01-01, hep-ph/0102100.

[3] J.J. Sakurai, Ann. Phys. **11** (1960) 1.

[4] G.A. Schuler and T. Sjöstrand, Phys. Lett. **300** (1993) 169, Nucl. Phys. **B407** (1993) 539.

[5] G.A. Schuler and T. Sjöstrand, Z. Phys. **C73** (1997) 677.

[6] M. Krawczyk, A. Zembrzuski, M. Staszel, Phys. Rep. **345** (2001) 265.

[7] R. Nisius, Phys. Rep. **332** (2000) 165.

[8] V.M. Budnev, I.F. Ginzburg, G.V. Meledin and V.G. Serbo, Phys. Rep. **15** (1975) 181.

[9] I. Schienbein, Annals Phys. **301** (2002) 128.

[10] M. Erdmann, Springer Tracts in Modern Physics **138**, 1997, Springer Verlag.

[11] M. Klasen, Rev. Mod. Phys. **74** (2002) 1221.

[12] Ch. Berger, W. Wagner, Phys. Rep. **C15** (1975) 181.

[13] H. Abramowicz et al., Int. J. Modern Phys. **A8** (1993) 1005.

[14] Physics at LEP2, G. Altarelli, T. Sjöstrand, F. Zwirmer (Eds.), Vol. 1 and 2, CERN 96-01.

[15] S. Todorova-Nová et al., *Event generators for $\gamma\gamma$ physics*, in Reports of the working groups on precision calculations for LEP2 physics, S. Jadach, G. Passarino, R. Pittau (Eds.), CERN 2000-009, p.219.

[16] L. Lönnblad et al. in Ref. [14] Vol. 2, p.201.

[17] R. Battacharya, G. Grammer Jr., J. Smith, Phys. Rev. **D15** (1977) 3267.

[18] P. Kessler, Il Nuovo Cimento **17** (1960) 809.

[19] C.F. von Weizsäker, Z. Phys. **88** (1934) 612,
E.J. Williams, Phys. Rev. **45** (1934) 729.

[20] C.T. Hill, G.G Ross, Nucl. Phys. **B148** (1979) 373.

[21] T. Uematsu, T.F. Walsh, Phys. Lett. **101B** (1981) 263, Nucl. Phys. **B199** (1982) 93.

[22] G. Rossi, Phys. Rev. **D29** (1984) 852, UC San Diego Report UCSD-10P10-227 (unpublished).

[23] I. Schienbein, Univ. Dortmund Report DO-TH-2001-17 (unpublished).

[24] M. Glück, E. Reya, M. Stratmann, Nucl. Phys. **B422** (1994) 37.

[25] M. Stratmann, Univ. Dortmund Report DO-TH-1996-24 (unpublished).

[26] E. Laenen, S. Riemersma, J. Smith, W.L. van Neerven, Phys. Rev. **D49** (1994) 5753.

[27] M. Glück, E. Reya, I. Schienbein, Phys. Rev. **D60** (1999) 054019.

[28] W.A. Bardeen, A.J. Buras, D.W. Duke, T. Muta, Phys. Rev. **D18** (1978) 3998, G. Altarelli, R.K. Ellis, G. Martinelli, Nucl. Phys. **B157** (1979) 461.

[29] W.A. Bardeen, A.J. Buras, Phys, Rev. **D20** (1979) 166, Phys, Rev. **D21** (1980) 2041(E).

[30] G. Curci, W Furmanski, R. Petronzio, Nucl. Phys. **B175** (19980) 27.

[31] W Furmanski, R. Petronzio,Phys. Lett. **B97** (1980) 437.

[32] M. Fontannaz, E. Pilon, Phys. Rev. **D45** (1992) 382.

[33] J. Chýla, Phys. Lett. **B488** (2000) 289.

[34] M. Cacciari, V. Del Duca, S. Frixione, Z. Trocsanyi, JHEP (2001) 0102.

[35] R. Engel, Z. Phys. **C66** (1995) 203, R. Engel and J. Ranft, Phys. Rev. **D54** (1996) 4246.

[36] E.A. Kuraev, L.N. Lipatov and V.S. Fadin, Sov. Phys. JETP**45** (1977) 199, Ia. Balitski and L.N. Lipatov, Sov. J. Nucl. Phys. **28** (1978) 822.

[37] B. Badelek, K. Charchula, M. Krawczyk, J.Kwiecinski, Rev. Mod. Phys. **64** (1992) 927.

[38] C.R. Schmidt, *Review of BFKL*, Michigan State Univ. preprint MSUHEP-10615, C.R. Schmidt, Phys. Rev. **D60** (1999) 074003.

[39] G.P. Salam, Acta Phys.Polon. **B30** (1999) 3679.

[40] A. De Rujula, S.L. Glashow, H.D. Politzer, S.B. Treiman, F. Wilczek, A. Zee, Phys. Rev. **D10** (1974) 1649.

[41] J. Bartels, C. Ewerz and R. Staritzbichler, Phys. Lett. **B492** (2000) 56.

[42] S.J. Brodsky et al., JETP Lett. **70** (1999) 155, V.T. Kim, L.N. Lipatov, G.B. Pivovarov, IITAP-99-013, hep-ph/9911228, V.T. Kim, L.N. Lipatov, G.B. Pivovarov, IITAP-99-014, hep-ph/9911242.

[43] J. Kwiecinski and L. Motyka, Phys. Lett. **B462** (1999) 203,
J. Kwiecinski and L. Motyka, Eur. Phys. J. **C18** (2000) 343.

[44] L3 Collaboration, M. Acciarri et al., Phys. Lett. **B453** (1999) 333.

[45] J. Bartels, A. De Roeck and H. Lotter, Phys. Lett. **B389** (1996) 742,
J. Bartels, A. De Roeck, H. Lotter and C. Ewerz, *The $\gamma^\star\gamma^\star$ Total Cross-Section and the BFKL pomeron at the 500 GeV e^+e^- Linear Collider*, DESY 97-123E, hep-ph/9710500,
S.J. Brodsky, F. Hautmann and D.E. Soper, Phys. Rev. **D56** (1997) 6957.

[46] A. Donnachie, H.G. Dosch, M. Rueter, Eur. Phys. J **C13** (2000) 141.

[47] ZEUS Collaboration, J. Breitweg et al., Eur. Phys. J. **C6** (1999) 239,
H1 Collaboration, C. Adloff et al., Nucl. Phys. **B538** (1999) 3,
H1 Collaboration, C. Adloff et al., Phys. Lett. **B462** (1999) 440.

[48] S.J. Brodsky, F. Hautmann and D.E. Soper, Phys. Rev. Lett. **78** (1997) 803.

[49] A. Białas, W. Czyż and W. Florkowski, Eur. Phys. J. **C2** (1998) 683.

[50] M. Boonekamp, A. De Roeck, C. Royon and S. Wallon, Nucl. Phys. **B555** (1999) 540.

[51] G. Altarelli and G. Parisi, Nucl. Phys. **B126** (1977) 298,
V.N. Gribov and L.N. Lipatov, Sov. J. Nucl. Phys. **15** (1972) 438,
L.N. Lipatov, Sov. J. Nucl. Phys. **20** (1975) 94,
Y.L. Dokshitzer, Sov. Phys. JETP. **46** (1977) 641.

[52] M. Ciafaloni, D. Colferai and G.P. Salam, Phys. Rev. **D60** (1999) 114036,
M. Ciafaloni, D. Colferai, Phys. Lett. **B452** (1999) 372.

[53] J.R. Forshaw, D.A. Ross and A. Saboi Vera, Phys. Lett. **B455** (1999) 273.

[54] R.S. Thorne, Phys. Rev. **D60** (1999) 054031.

[55] G. Altarelli, R.D. Ball and S. Forte, Nucl. Phys. **B599** (2001) 383.

[56] I.F. Ginzburg and V.G. Serbo, Phys. Lett. **B109** (1982) 231.

[57] T. Sjöstrand, Comp. Phys. Comm. **82** (1994) 74,
T. Sjöstrand, LUND University Report, LU-TP-95-20 (1995).

[58] C. Friberg and T. Sjöstrand, JHEP **09** (2000) 010.

[59] G. Marchesini et al., Comp. Phys. Comm. **67** (1992) 465.

[60] ALEPH Collaboration, D. Buskulic et al., Phys. Lett. **B313** (1993) 509.

[61] TOWGAM v.2.04, L. Lönnblad et al. in Ref. [14] Vol. 2, p. 224.

[62] J. Fujimoto et al., Comput. Phys. Commun. 100 (1997) 128.

[63] The LEP Working Group for Two-Photon Physics, ALEPH, L3 and OPAL Collaborations, *Comparison of Deep Inelastic Electron-Photon Scattering Data with the HERWIG and PHOJET Monte Carlo Models*, CERN-EP-2000-109, hep-ex/0010041.

[64] OPAL Collaboration, G. Abbiendi et al., Eur. Phys. J. **C14** (2000) 199.

[65] G.A. Schuler, Comp. Phys. Comm. **108** (1998) 279.

[66] F.A. Berends, P.H. Daverveldt and R. Kleiss, Nucl. Phys. **B253** (1985) 421.

[67] F.A. Berends, P.H. Daverveldt and R. Kleiss, Comp. Phys. Comm. **40** (1986) 271, 285, 309.

[68] F.A. Berends, P.H. Daverveldt and R. Kleiss, Nucl. Phys. **B264** (1986) 243.

[69] OPAL Collaboration, K. Ahmet et al., Nucl. Instr. and Meth. **A305** (1991) 275,
OPAL Collaboration, P.P. Allport et al., Nucl. Instr. and Meth. **A324** (1993) 34,
OPAL Collaboration, P.P. Allport et al., Nucl. Instr. and Meth. **A346** (1994) 476,
OPAL Collaboration, B.E. Anderson et. al., IEEE Trans.Nucl.Sci. **41** (1994) 845.

[70] P.P. Allport et al., Nucl. Instr. Meth. **A324** (1993) 34.

[71] M. Hauschild et al., Nucl. Instr. Meth. **A379** (1996) 436.

[72] OPAL Collaboration, G. Alexander et al., Phys. Lett. **B377** (1996) 181.

[73] J.A.M. Vermaseren, Nucl. Phys. **B229** (1983) 347,
J. Smith, J.A.M. Vermaseren, G. Grammer Jr., Phys. Ref. **D15** (1977) 3280,
J.A.M. Vermaseren, J. Smith, G. Grammer Jr., Phys. Ref. **D19** (1979) 137.

[74] M. Glück, E. Reya and A. Vogt, Phys. Rev. **D45** (1992) 3986,
M. Glück, E. Reya and A. Vogt, Phys. Rev. **D46** (1992) 1973.

[75] OPAL Collaboration, G. Abbiendi et al., Eur. Phys. J. **C18** (2000) 15.

[76] J. Bartels, V. Del Duca and M. Wüsthoff, Z. Phys. **C76** (1997) 75.

[77] S.J. Brodsky, G.P. Lepage and P.B. Mackenzie, Phys. Rev. **D28** (1983) 228.

[78] J.A.Lauber, L.Lönnblad, M.H. Seymour, in Proceedings of Photon'97, 10-15 May, 1997, eddited by A. Buijs and F.C. Erné, World Scientific, 1998, pp. 52-56,
S. Cartwright, M.H.Seymour et al., J. Phys. **G24** (1998) 457

[79] T. Sjöstrand, Comp. Phys. Comm. **39** (1986) 347,
T. Sjöstrand, M. Bengtsson, Comp. Phys. Comm. **43** (1987) 367,
T. Sjöstrand, Comp. Phys. Comm. **82** (1994) 74.

[80] A. Capella, U. Sukhatme, C.I. Tan, J. Tran Thanh Van, Phys. Rep. **236** (1994) 225.

[81] H. Plothow-Besch, PDFLIB, User's Manual, CERN Program Library entry W5051,
H. Plothow-Besch, Comp. Phys. Comm. **75** (1993) 396.

[82] M. Landrø, K.J. Mork, H.A. Olsen, Phys. Rev. **D36** (1987) 44,
F.A. Berends, P.H. Daverveldt, R. Kleiss, Nucl. Phys. **B253** (1985) 441.

[83] R. Bhattacharya, G. Grammer, J. Smith, Phys. Rev. **D15** (1977) 3267.

[84] R. Nisius, M.H. Seymour, Phys. Lett. **B452** (1999) 409.

[85] N. Arteaga, C. Carimalo, P. Kessler, S. Ong, Phys. Rev. **D52** (1995) 4920.

[86] T.F. Walsh, P.M. Zerwas, Nucl. Phys. **B41** (1972) 551.

[87] T.F. Walsh, P.M. Zerwas, Phys. Lett. **B44** (1973) 195.

[88] E. Witten, Nucl. Phys. **B120** (1977) 189.

[89] E. Laenen and G.A. Schuler, Phys Lett. **B374** (1996) 217,
E. Laenen and G.A. Schuler, *Model-independent QED corrections to photon structure function measurements*, in Proceedings of Photon'97, 10-15 May, 1997, eddited by A. Buijs and F.C. Erné, World Scientific, 1998, pp. 57-62.

[90] A. Höcker, V. Kartvelishvili, Nucl. Inst. and Meth. **A372** (1996) 469.

[91] V. Blobel, *Unfolding methods in high energy physics experiments*, DESY-84-118 (1984),
V. Blobel, *Regularized unfolding for high energy physics experiments, RUN program manual*, unpublished (1996).

[92] M. Drees, K. Grassie, Z. Phys. **C28** (1985) 451.

[93] H. Abramowicz, K. Charchuła, A. Levy, Phys. Lett. **B269** (1991) 458.

[94] K. Hagiwara, M. Tanaka, I. Watanabe, Phys. Rev. **D51** (1995) 3197.

[95] P. Aurenche, J.-P. Guillet, M. Fontannaz, Z. Phys. **C64** (1994) 621.

[96] F. Cornet, P. Jankowski, M. Krawczyk, A. Lorca, A new five flavour LO analysis and parametrization of parton distributions in the real photon, DESY-02-118.

[97] Wu-Ki Tung, S. Kretzer, C. Schmidt, J. Phys. **G28** (2002) 983.

[98] L.E. Gordon, J.K. Storrow, Z. Phys. **C56** (1992) 307.

[99] L.E. Gordon, J.K. Storrow, Nucl. Phys. **B489** (1997) 405.

[100] M. Glück, E. Reya, I. Schienbein, Eur. Phys. J. **C10** (1999) 313.

[101] M. Glück, E. Reya, M. Stratmann, Phys. Rev. **D51** (1995) 3220.

[102] G.A. Schuler, T. Sjöstrand, Z. Phys. **C68** (1995) 607,
G.A. Schuler, T. Sjöstrand, Phys. Lett. **B300** (1993) 169,
G.A. Schuler, T. Sjöstrand, Nucl. Phys. **B407** (1993) 539.

[103] G.A. Schuler, T. Sjöstrand, Phys. Lett. **B376** (1996) 193.

[104] W. Słomiński, J. Szwed, Phys. Lett. **B387** (1996) 861,
W. Słomiński, J. Szwed, Acta Phys. Polon. **B27** (1996) 1887.

[105] W. Słomiński, J. Szwed, Acta Phys. Polon. **B29** (1998) 1253.

[106] W. Słomiński, Acta Phys. Polon. **B30** (1999) 369.

[107] W. Słomiński, J. Szwed, Eur. Phys. J. **C22** (2001) 123.

[108] ALEPH Collaboration, D. Decamp et al., Nucl. Instrum. Meth. **A294** (1990) 121,
ALEPH Collaboration, D. Decamp et al., Nucl. Instrum. Meth. **A303** (1991) 393 (erratum),
ALEPH Collaboration, D. Buskulic et al., Nucl. Instrum. Meth. **A360** (1995) 481.

[109] DELPHI Collaboration P. Aarnio et al., Nucl. Instr. Meth. **A303** (1991) 233,
DELPHI Collaboration P. Abreu et al., Nucl. Instr. Meth. **A378** (1996) 57.

[110] L3 Collaboration, B. Adeva et al., Nucl. Instr. Meth. **A289** (1990) 35,
L3 Collaboration, J.A. Bakken et al., Nucl. Instr. Meth. **A275** (1989) 81,
L3 Collaboration, O. Adriani et al., Nucl. Instr. Meth. **A323** (1992) 109,
L3 Collaboration, M. Acciari et al., Nucl. Instr. Meth. **A351** (1994) 300.

[111] OPAL Collaboration, G. Abbiendi et al., Eur. Phys. J. **C11** (1999) 409.

[112] DELPHI Collaboration, P. Abreu et al., Eur. Phys. J. **C19** (2001) 15.

[113] L3 Collaboration, M. Acciarri et al., Phys. Lett. **B438** (1998) 363.

[114] CELLO Collaboration, H.J. Behrend et al., Phys. Lett. **B126** (1983) 384.

[115] PLUTO Collaboration, C. Berger et al., Z. Phys. **C27** (1985) 249.

[116] TPC/2γ Collaboration, M.P. Cain et al., Phys. Lett. **B147** (1984) 232.

[117] OPAL Collaboration, R. Akers et al., Z. Phys. **C60** (1993) 593,
OPAL Collaboration, K. Ackerstaff et al., Z. Phys. **C74** (1997) 49.

[118] DELPHI Collaboration, P. Abreu et al., Z. Phys. **C69** (1996) 223.

[119] C. Brew, *Muonic structure functions of the photon*, in Proceedings of Photon'97, 10-15 May, 1997, eddited by A. Buijs and F.C. Erné, World Scientific, 1998, pp. 21-26, ALEPH Collaboration.

[120] TPC/2γ Collaboration, D. Bintinger et al., Phys. Rev. Lett. **54** (1985) 763.

[121] TPC/2γ Collaboration, H. Aihara et al., Phys. Rev. Lett. **58** (1987) 97.

[122] PLUTO Collaboration, C. Berger et al., Phys. Lett. **B107** (1981) 168.

[123] AMY Collaboration, S.K. Sahu et al., Phys. Lett. **B346** (1995) 208.

[124] AMY Collaboration, T. Kojima et al., Phys. Lett. **B400** (1997) 395.

[125] JADE Collaboration, W. Bartel et al., Z. Phys. **C24** (1984) 231.

[126] PLUTO Collaboration, C. Berger et al., Phys. Lett. **B142** (1984) 111.

[127] PLUTO Collaboration, C. Berger et al., Nucl. Phys. **B281** (1987) 365.

[128] TASSO Collaboration, M. Althoff et al., Z. Phys. **C31** (1986) 527.

[129] TPC/2γ Collaboration, H. Aihara et al., Z. Phys. **C34** (1987) 1.

[130] TOPAZ Collaboration, K. Muramatsu et al., Phys. Lett. **B332** (1994) 477.

[131] ALEPH Collaboration, D. Barate et al., Phys. Lett. **B458** (1999) 152.

[132] ALEPH Collaboration, A. Heister et al., Eur. Phys. J. **C** (2003) 145.

[133] DELPHI Collaboration, P. Abreu et al., Z. Phys. **C69** (1996) 223.

[134] DELPHI Collaboration, T. Allmendinger et al., *Study of the hadronic photon structure function at LEP2*, CERN-EP-2003-018, submitted to Eur. Phys. J. **C**.

[135] L3 Collaboration, M. Acciari et al., Phys. Lett. **B436** (1998) 403.

[136] L3 Collaboration, M. Acciari et al., Phys. Lett. **B447** (1999) 147.

[137] OPAL Collaboration, K. Ackersttaff et al., Z. Phys. **C74** (1997) 33.

[138] OPAL Collaboration, K. Ackersttaff et al., Phys. Lett. **B411** (1997) 387.

[139] OPAL Collaboration, K. Ackersttaff et al., Phys. Lett. **B412** (1997) 225.

[140] OPAL Collaboration, G. Abbiendi et al., Phys. Lett. **B533** (2002) 207.

[141] OPAL Collaboration, G. Abbiendi et al., Eur. Phys. J. **C16** (2000) 579.

[142] OPAL Collaboration, G. Abbiendi et al., Phys. Lett. **B539** (2002) 13.

[143] OPAL Collaboration, G. Abbiendi et al., *Measurement of the electron and photon structure functions in deep inelastic* eγ *and* ee *Scattering at LEP*, to be published in Eur. Phys. J. **C**.

[144] B. Muryn, T. Szumlak, W. Słomiński, J. Szwed, *Measurement of the electron structure function F_2^e at LEP1 and LEP2 energies*, in Proceedings of Photon'03, 10-15 April, 2003, eddited by F. Anulli, S. Braccini and G. Pancheri., to be published in Nuclear Physics B, Proceedings Supplement.

[145] PLUTO Collaboration, C. Berger et al., Phys. Lett. **B142** (1984) 119.

[146] L3 Collaboration, M. Acciarri et al., Phys. Lett. **B483** (2000) 373.

[147] S. Frixione, M.L. Magnano, P. Nason, G. Ridolfi, Phys. Lett. **B319** (1993) 339.

[148] T. Carli, Int. J. Mod. Phys. **A17** (2002) 3185.

[149] OPAL Collaboration, G. Abbiendi et al., Eur. Phys. J. **C24** (2002) 17.

[150] L3 Collaboration, M. Acciarri et al., Phys. Lett. **B453** (1999) 333.

[151] L3 Collaboration, P. Achard et al., Phys. Lett. **B531** (2002) 39.

[152] ALEPH Collaboration, A. Heister et al., *Study of hadronic final states from double tagged $\gamma\gamma$ events at LEP*, CERN-EP-2003-025, submitted to Eur. Phys. J. **C**.

[153] I.F. Ginzburg, G.L. Kotkin, S.L. Panfil, V.G. Serbo, V.I. Telnov, Nucl. Instr. Meth. **219** (1984) 5.

[154] V.I. Telnov, Int. J. Mod. Phys. **A13** (1988) 2399.

[155] E. Accomando et al., Phys. Rep. **229** (1998) 1.

[156] D.J. Miller, A. Vogt, in Proc. e^+e^- Collisions at TeV energies: The physical potential, eddited by P.M. Zerwas, Annecy–Gran Sasso–Hamburg, 1995, DESY 96-123D.

[157] D. Schulte, *Study of electromagnetic and hadronic background in the interaction region of the TESLA collider*, DESY-TESLA 97-08, 1997.

[158] C. Adolphsen et al., *Zeroth-order design report for the Next Linear Collider*, SLAC-474, 1996.